

0 0 1 0 5 5 0 4 1 2

UC-4
LBL-9981c.1



Lawrence Berkeley Laboratory

UNIVERSITY OF CALIFORNIA

RECEIVED
LAWRENCE
BERKELEY LABORATORY

FEB 25 1980

LIBRARY AND
DOCUMENTS SECTION

Materials & Molecular Research Division

ABSOLUTE PHOTODISSOCIATION QUANTUM YIELDS OF NO_3 AND N_2O_5
BY TUNABLE LASER FLASH PHOTOLYSIS-RESONANCE FLUORESCENCE

Frank Magnotta
(Ph.D. thesis)

November 1979

For Reference

Not to be taken from this room



Prepared for the U.S. Department of Energy under Contract W-7405-ENG-48

LBL-9981c.1

DISCLAIMER

This document was prepared as an account of work sponsored by the United States Government. While this document is believed to contain correct information, neither the United States Government nor any agency thereof, nor the Regents of the University of California, nor any of their employees, makes any warranty, express or implied, or assumes any legal responsibility for the accuracy, completeness, or usefulness of any information, apparatus, product, or process disclosed, or represents that its use would not infringe privately owned rights. Reference herein to any specific commercial product, process, or service by its trade name, trademark, manufacturer, or otherwise, does not necessarily constitute or imply its endorsement, recommendation, or favoring by the United States Government or any agency thereof, or the Regents of the University of California. The views and opinions of authors expressed herein do not necessarily state or reflect those of the United States Government or any agency thereof or the Regents of the University of California.

TABLE OF CONTENTS

Abstract	v
I. Introduction	1
A. Photochemistry of NO_3	2
B. The Structure and Thermochemistry of NO_3	3
C. Photochemistry and Thermochemistry of N_2O_5	5
II. Experimental Methods and Apparatus	8
A. Methods	8
1. Simulation of Chemical System	9
2. Measurement of Reactants and Products	15
3. Consideration of Interferences	22
4. Interpretation of Data	24
B. Apparatus	27
1. Photolytic Source	27
2. Detection of N_2O_5 and HNO_3	30
3. Detection of Nitric Oxide and Oxygen Atoms	31
4. Detection of Nitrogen Dioxide	34
5. Signal Processing	37
C. Gases and Flow System	39
III. Experimental Procedures and Data	44
A. Visible and Ultraviolet Cross Section Measurements of NO_2 and NOCl	45
B. Joulemeter Calibration-- NO_2 and NOCl Actinometry	50
C. Calibration of NO and NO_2 Detection Systems	69
D. Quantum Yield Determinations	84

1. Oxygen Atom Calibration by NO_2 Photolysis	87
2. Oxygen Atom Quantum Yield Measurements from NO_3 Photolysis	101
3. Nitric Oxide Calibration by NO_2 Photolysis	111
4. Nitric Oxide Quantum Yield Measurements from NO_3 Photolysis	118
5. Oxygen Atom Quantum Yield Measurements from N_2O_5 Photolysis	138
E. Detection of $\text{O}_2(^1\Sigma_g^+)$ and $\text{NO}_3(^2\text{B}_2)$ Fluorescence	140
F. Nitrogen Dioxide Two Photon Cross Sections	145
G. Rate of the $\text{O} + \text{NO}_2$ Reaction	151
H. Calculation of Laser Heating	152
IV. Results and Discussion	156
A. NO_3 Cross Sections	156
B. Quantum Yield Determinations	158
1. Nitric Oxide and Oxygen Atom Measurements from NO_3 Photolysis	158
2. Nitric Oxide and Oxygen Atom Measurements from N_2O_5 Photolysis	176
C. Detection of $\text{O}_2(^1\Sigma_g^+)$ and $\text{NO}_3(^2\text{B}_2)$ Fluorescence	177
D. Correlation of Reactant and Products	179
E. Nitrogen Dioxide Two Photon Cross Sections	183
V. Summary	188
Acknowledgments	189
Appendices	190
References	214

ABSOLUTE PHOTODISSOCIATION QUANTUM YIELDS OF NO₃ AND N₂O₅
BY TUNABLE LASER FLASH PHOTOLYSIS-RESONANCE FLUORESCENCE

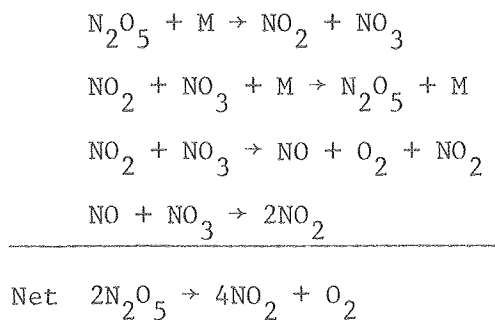
Frank Magnotta

Materials and Molecular Research Division,
Lawrence Berkeley Laboratory and Department of Chemistry,
University of California, Berkeley, California 94720

ABSTRACT

This study investigated the channel specific absolute photofragmentation quantum yields of NO_3 as a function of wavelength in the visible, and N_2O_5 in the ultraviolet. The technique of tunable laser flash photolysis was coupled with a real time product diagnostic, namely atomic and molecular resonance fluorescence spectroscopy.

Low levels of NO_3 were maintained in an ozone-free system by carefully controlled unimolecular thermal decomposition of N_2O_5 in N_2 at a total pressure of 10 torr. Through the mechanism



N_2O_5 (and HNO_3) concentrations were measured by infrared absorption spectroscopy, while NO_2 levels were determined by the technique of

laser induced fluorescence. These measurements, combined with the N_2O_5 equilibrium constant measured by Graham,⁹ resulted in determination of the NO_3 concentration.

Representative of the two possible photolytic channels are NO and O, which were measured by detecting resonantly scattered vacuum ultraviolet radiation from microwave powered discharge lamps. Absolute calibration was achieved by in situ ultraviolet photolysis of NO_2 , occurring naturally in the reaction mixture.

Results of NO_3 photolysis experiments from 4700–6850 Å indicate that oxygen atom is the major product and is produced in the wavelength range between 4700 and 6350 Å. Nitric oxide production occurred from 5860 and 6280 Å and was always less than O atom at each wavelength. The maximum quantum yields for O and NO are

$$\phi_{\text{O}}(\text{max}) = 1.00 \quad \text{at } \lambda \text{ 5850 Å}$$

$$\phi_{\text{NO}}(\text{max}) = 0.32 \quad \text{at } \lambda = 5920 \text{ Å}$$

Average primary quantum yields for each species, were in acceptable agreement with those obtained by Graham,⁹ who used a molecular modulation technique and broadband illumination.

$$\phi_{\text{O}}(\text{ave.}) = 0.68 \quad 4700 \leq \lambda \leq 6350 \text{ Å}$$

$$\phi_{\text{NO}}(\text{ave.}) = 0.18 \quad 5860 \leq \lambda \leq 6280 \text{ Å}$$

NO_3 absorption cross sections at two wavelengths were found to be higher than those obtained by Graham⁹ (at 1 atmosphere), by a factor of 1.46. Quantum yield values, averaged over each nm, combined with these NO_3 cross sections, and a tabulation of the solar flux in the

lower atmosphere⁸⁹ resulted in the following photodissociation coefficients at a solar zenith angle of 0°:

$$j(O + NO_2) = 0.18 \pm 0.018 \text{ sec}^{-1}$$

$$j(NO + O_2) = 0.022 \pm 0.002 \text{ sec}^{-1}$$

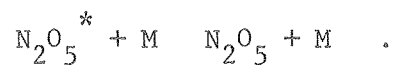
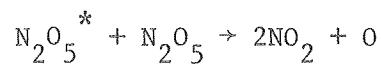
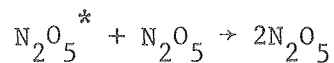
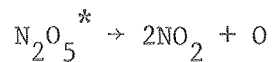
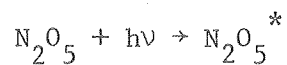
The quantum yield for O atom production is ≈ 0.97 at the energetic threshold calculated by Graham⁹ ($5800 \pm 30 \text{ Å}$) and falls off rapidly at lower energies. The nitric oxide channel falls off rapidly towards the blue as the $O + NO_2$ threshold energy is approached.

The two photon photolytic behavior of NO_3 was investigated across the wavelength region where the total one-photon quantum yield varies from one to zero. The two large absorption features, identified as the (0,0), (1,0) vibrational bands, were found to display considerable two photon activity.

The primary photoproducts from ultraviolet photolysis of N_2O_5 ($2900 < \lambda < 300 \text{ Å}$) include an oxygen atom, with NO not being produced to any appreciable extent, with an upper limit determined to be

$$\phi_{NO}(N_2O_5) \leq 0.11$$

For N_2O_5 photolysis, ϕ_O values were found to vary with N_2O_5 concentration, in excellent agreement with the recent results of Connell¹⁷ who suggested the following mechanism



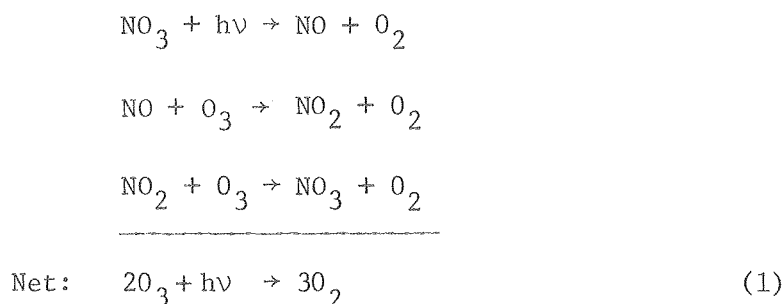
Two photon cross sections for NO_2 were measured at several visible wavelengths, and used to correct one- and two-photon quantum yield data obtained in the high laser energy region. The rate constant for the reaction of $\text{O} + \text{NO}_2$ was measured and found to be

$$k_{\text{O},\text{NO}_2} = 1.03 \pm 0.008 \times 10^{-11} \text{ cm}^3 \cdot \text{molecule}^{-1} \cdot \text{sec}^{-1}$$

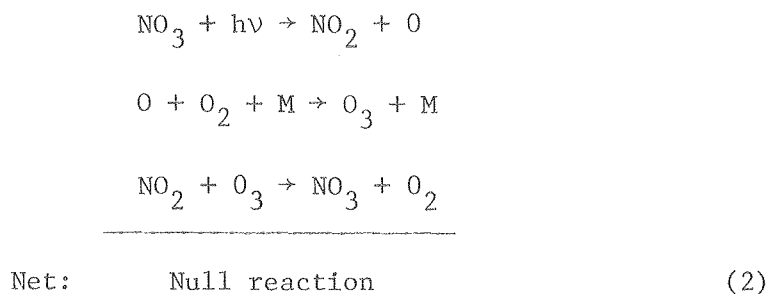
which is higher than, but agrees within the error limits of the recommended value.⁸⁶

I. Introduction

The photochemistry of the nitrate free radical (NO_3) is potentially important in the balance of ozone in the troposphere and lower stratosphere.¹ NO_2 and ground state oxygen atom, $\text{O}(^3\text{P})$ are energetically possible products for light of wavelengths less than 5800 \AA while NO and O_2 could be produced at any wavelength below $8.0 \text{ }\mu\text{m}$. If the photolysis products are NO and O_2 , the net effect is catalytic destruction of ozone:



However, the alternative products lead to no net chemical reaction:



Very little is known concerning the nature of the intense absorption spectrum of NO_3 which begins near 7000 \AA and extends across the visible wavelengths into the near ultraviolet. The purpose of this work was to investigate several aspects of NO_3 photodissociation dynamics and to determining primary products, primary quantum yields, and hence branching ratios as a function of wavelength.

A secondary goal was to extend the methods and techniques developed to study the photochemical decomposition products of dinitrogen pentoxide (N_2O_5) in the ultraviolet region where it exhibits a continuous absorption beginning at around 3800 Å, extending smoothly with decreasing wavelength to beyond 2100 Å. The photochemistry of this absorption may contribute to the lifetime of N_2O_5 in the stratosphere and to possible reduction of ozone by several mechanisms.

A. Photochemistry of NO_3

The visible absorption spectrum of NO_3 has been studied by Sprenger² as a function of ozone and nitrogen pentoxide concentrations. However no cross sections could be determined. Jones and Wulf³ also studied the visible NO_3 spectrum produced by reaction of ozone with NO_2 . This work was later reinvestigated by Ramsay⁴ under high dispersion who concluded that the observed diffuseness indicates predissociation. He identified a short progression beginning with the strong zero-zero transition at 6626 Å as a symmetric stretch with approximately 950 cm^{-1} intervals, extending to 5590 Å. Some fifteen or more weaker bands were also observed but unassigned. Apparently,¹²⁻¹⁴ NO_3 formed in X-irradiated crystals and solution exhibits a second absorption system, with a maximum in the vicinity of 3300 Å. However this absorption has not been verified in the gas phase. Scott and Davidson⁵ measured visible cross sections for NO_3 in a high temperature shock tube, found the absorption spectrum to change with temperature and extrapolated their results to obtain a cross section of $8.4 \times 10^{-19}\text{ cm}^2\text{ molecule}^{-1}$ (base e) at 6520 Å.

B. The Structure and Thermochemistry of NO₃

The NO_3 free radical is important in several gas phase reaction mechanisms, but relatively little is known about its structure or electronic states. Walsh¹⁵ predicted that the molecule has D_{3h} symmetry and a ${}^2A_2'$ ground electronic state. Semiempirical calculations by Olsen and Burnelle¹⁴ however, predicts a Y-shaped structure with a 2B_2 ground state. Furthermore, they showed that the 6600 Å transition should be the allowed, Z-polarized ${}^2B_2 \leftarrow {}^2B_2$ transition. This is in agreement with the observation by Chantry¹² that in irradiated urea nitrate crystals, the NO_3 transition is polarized in the molecular plane and with their measured oscillator strength of $f \sim 0.013$. The transition calculated in the near ultraviolet region is ${}^2A_1 ({}^2E') \leftarrow {}^2B_2$ and also allowed. Again Chantry¹²

has estimated its oscillator strength in NO_3 at 0.009, in agreement with this interpretation.

Several products are energetically possible in the region of strong NO_3 visible absorption. If one product is the ground vibrational states of NO ($^2\Pi_{3/2,1/2}$) then the calculated maximum wavelengths for various excited O_2 products are:

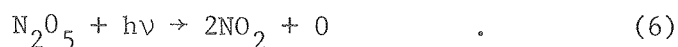
O_2	$\lambda_{\text{cutoff}}(\text{nm})$	
$3\Sigma_g^-$	8000	
$1\Delta_g$	1100	
$1\Sigma_g^+$	700	
$3\Sigma_u^+$	269	(3)

Since the absorption spectrum originates just below 700 nm, it is tempting to postulate that the products are NO and O_2 ($^1\Sigma_g^+$). If so, the wavelengths that can produce these products in various excited vibrational states are:

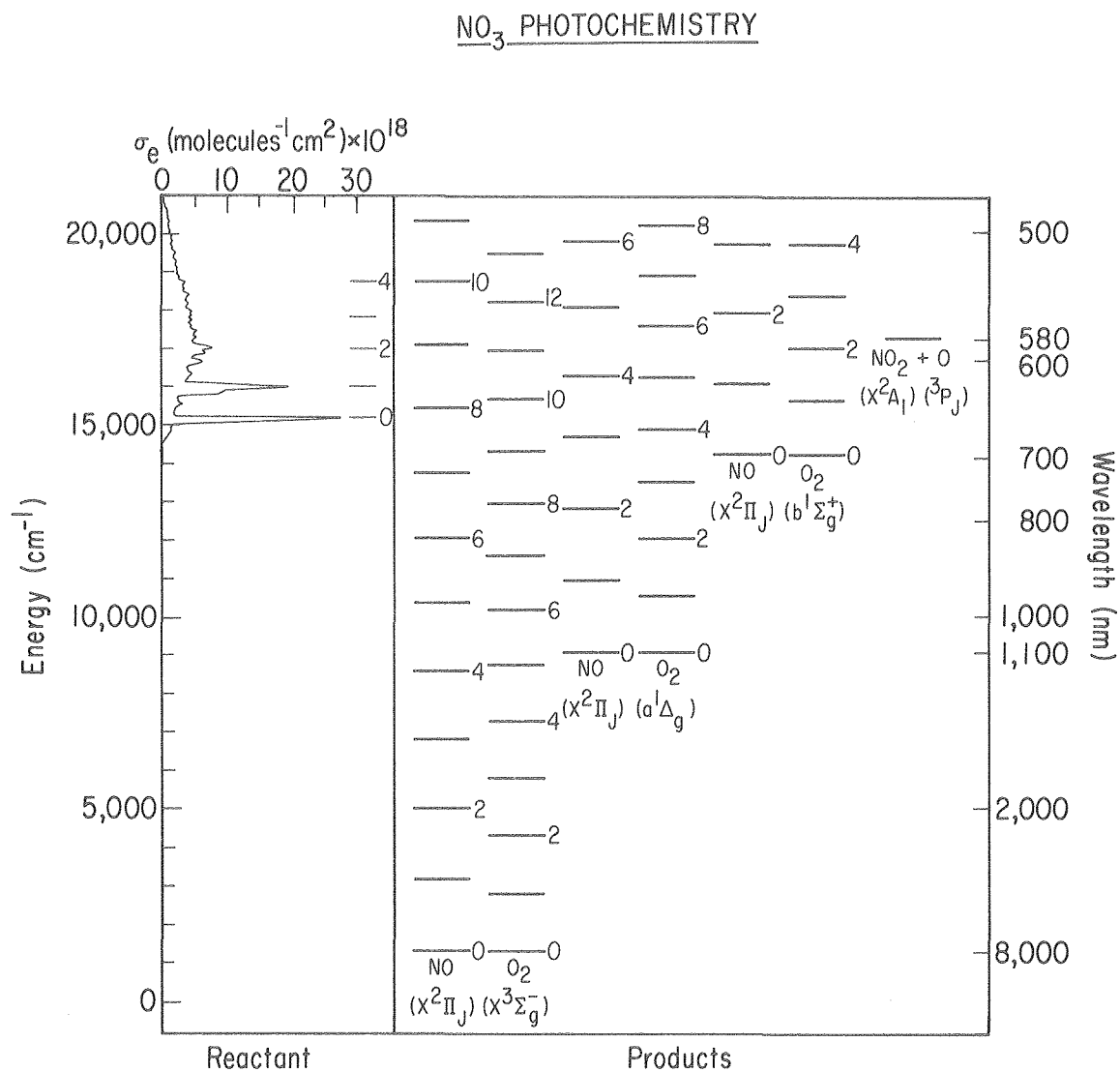
$\text{NO}(^2\Pi_{3/2,1/2})$	$\text{O}_2(^1\Sigma_g^+)$	$\lambda(\text{nm})$	
0	0	700	
0	1	637	
1	0	619	
0	2	586	
2	0	555	
1	1	569	(4)

C. Photochemistry and Thermochemistry of N_2O_5 :
$$\text{N}_2\text{O}_5 + h\nu \rightarrow 2\text{NO}_2 + 1/2 \text{O}_2 \quad (5)$$

Most recently Connell,¹⁷ observing the disappearance of N_2O_5 by illumination with 254 nm radiation in the presence of N_2 or O_2 buffer gas, showed the primary photolytic step to be

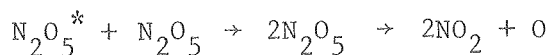
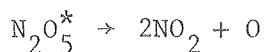


The quantum yield was found to be dependent on both N_2O_5 and buffer



XBL 791-7839A

Figure 1. Spectroscopy and thermochemistry of NO₃ photodissociation. The left hand panel displays the reactant electronic absorption spectrum while the right-hand panel displays electronic and vibronic state energetics for the possible photofragments.

$$\text{N}_2\text{O}_5 + h\nu \rightarrow \text{N}_2\text{O}_5^*$$


The calculated maximum wavelengths for photolysis are

<u>Products</u>	<u>$\lambda_{\text{cutoff}}(\text{nm})$</u>
$\text{NO}_2 + \text{NO}_3$	1300
$\text{NO}_2 + \text{NO}_2 + \text{O}$	401
$\text{NO} + \text{NO}_2 + \text{O}_2$	1125

(8)

Since the ultraviolet absorption commences around 380 nm, all three possibilities are energetically allowed. Utilizing the techniques developed to ascertain the primary photolytic products in NO_3 , the relative abundances of the second two channels was investigated in this study.

II. Experimental Methods and Apparatus

A. Methods

The choice of spectroscopic detection methods utilized in this study required careful consideration, due in part to the complexity of the reaction mixture needed to generate the NO_3 reactant, but mainly due to the fact that both reactant and products are transient species. To differentiate product channels, O atom and NO were chosen since their counterparts (NO_2 and O_2) were usually present in concentrations much larger than NO_3 itself. The further complication of utilizing a system containing ozone to generate NO_3 ($\text{O}_3 + \text{NO}_2 \rightarrow \text{NO}_3 + \text{O}_2$) was avoided due to its concomitant production of O atom in the visible region of interest.

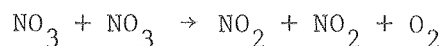
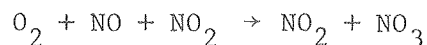
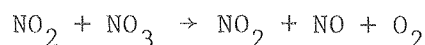
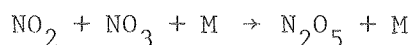
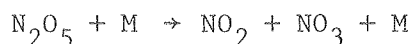
The previously discussed experiments of Graham⁹ and Connell¹⁷ both utilized frequency domain techniques, observing reactants and products in low level steady state conditions, inferring by kinetic modeling techniques as to mechanism and primary products. For systems as complex as N_2O_5 , these experimental methods are well suited and generally the only ones available.

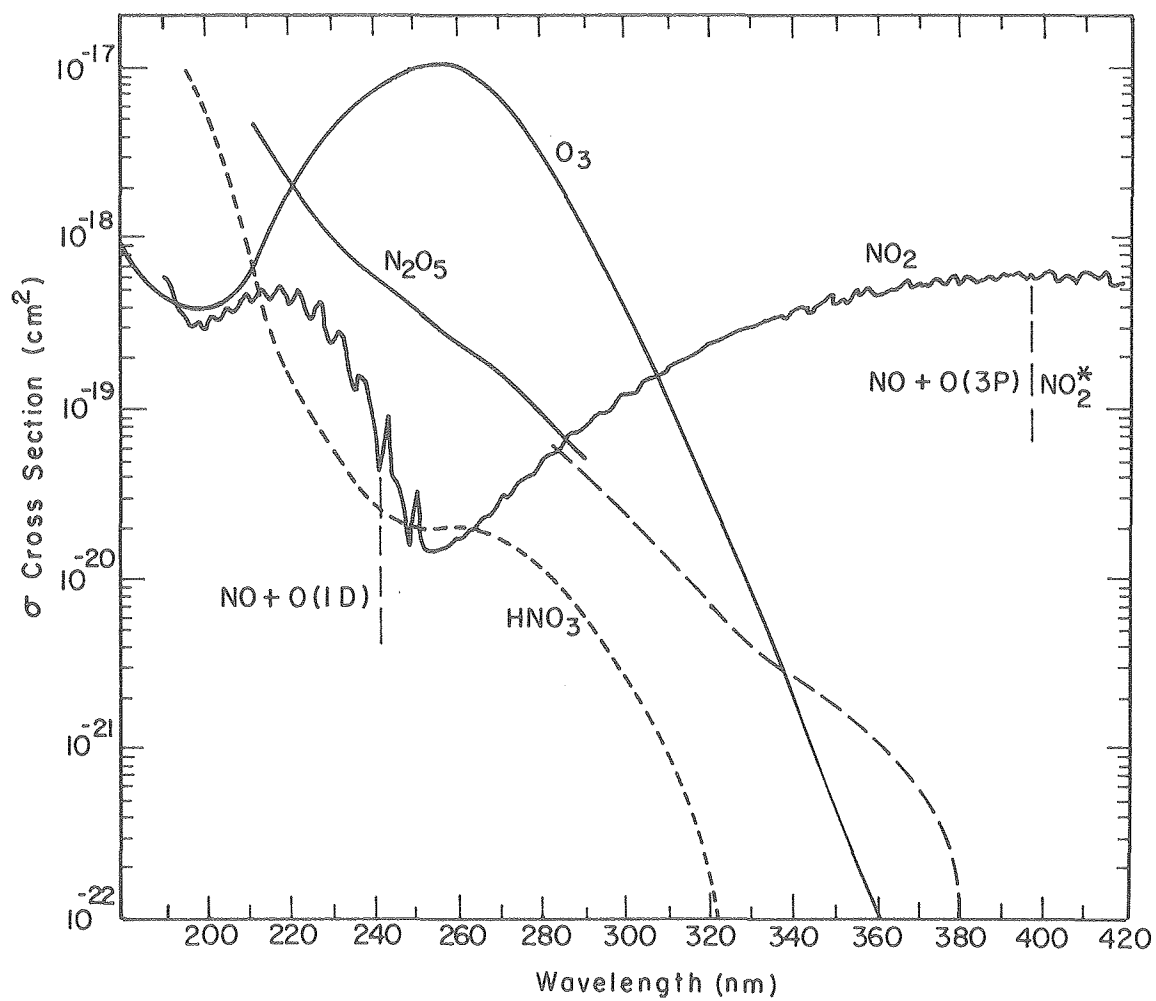
However by a fortuitous coincidence of experimentally controllable variables, it was possible to structure the present work around the time domain, utilizing tunable laser flash photolysis for excitation and atomic and molecular resonance fluorescence as a real time product diagnostic. Furthermore, reactant concentrations were ascertained by a combination of infrared absorption (N_2O_5 and HNO_3) and laser induced fluorescence (NO_2). Extrapolation of product decay profiles back to zero time was the measured experimental

quantity. The product channels were internally calibrated on an absolute basis by ultraviolet photolysis of ambient NO_2 in the reaction mixture itself.

1. Simulation of Chemical System

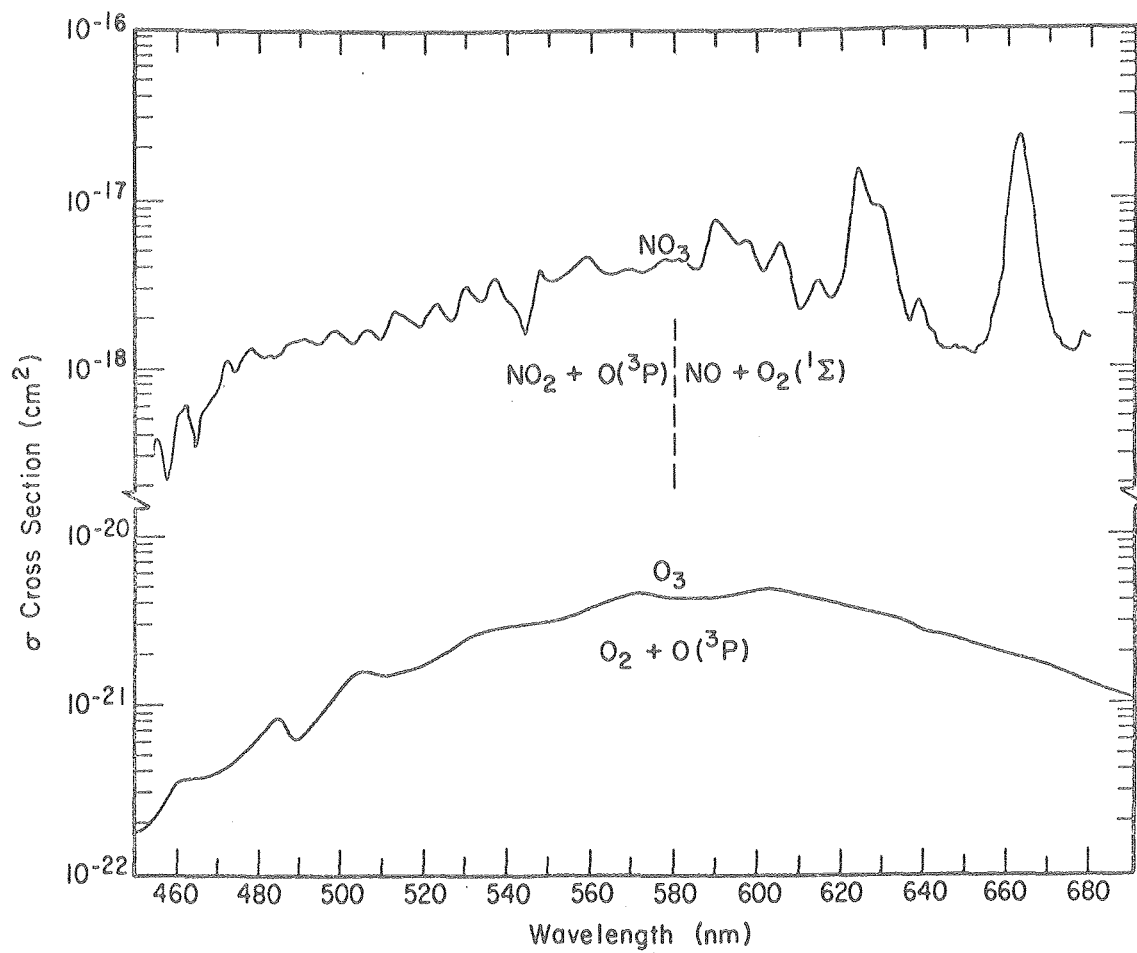
Prior to design or construction of the apparatus, the chemical system involved was simulated utilizing a numerical integration package (CHEMK),^{19,60} since exact analytical expressions for the complete chemical mechanism cannot generally be derived. The application of the gear method (as discussed by Hindmarsh²⁰) to numerically integrate a set of stiff differential equations uses the complete set of differential rate expressions describing the chemical system to generate concentration versus time profiles for each species. This simulation program was run on the CDC 7600 computer located at the Lawrence Berkeley Laboratory. The chemical species involved include N_2O_5 , NO_2 , NO_3 , O , NO , HNO_3 , O_2 and carrier gas. Survey absorption spectra¹⁰ of these components are shown in Figure 2 and 3. The complete set of differential rate expressions includes thirty reactions and is reproduced in Appendix A. A simplified mechanism representing the most important reactions is:





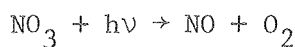
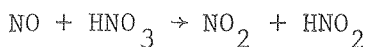
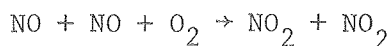
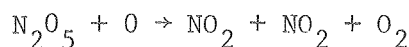
XBL76I-6356

Figure 2. Ultraviolet and near ultraviolet absorption spectra of NO_2 , N_2O_5 , O_3 and HNO_3 .



XBL 7910-12205

Figure 3. Visible absorption spectra of NO₃ and O₃.

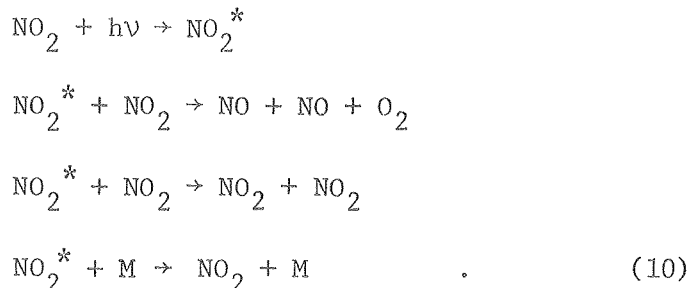


Pertinent features of this reaction scheme involve the unimolecular decomposition of N_2O_5 and equilibrium, followed by an NO_3 destroying reaction and its reverse reaction. Further loss of NO_3 occurs by self-reaction. Beginning with N_2O_5 , free of NO_2 , the system evolves in time with equal concentrations of NO_2 and NO_3 , towards equilibrium. Mainly due to reaction of $\text{NO}_2 + \text{NO}_3 \rightarrow \text{NO} + \text{NO}_2 + \text{O}_2$ after equilibrium, the NO_3 begins to decline and the NO_2 increase. Any initially present NO_2 depresses the maximum obtainable NO_3 . Hence, the first two constraints to appear are to minimize NO_2 contamination of N_2O_5 , and to flow N_2O_5 from source to photolysis cell in a time period slightly longer than the equilibrium time, thus maximizing NO_3 . The fast reaction of $\text{NO} + \text{NO}_3$ is fortuitous since it acts to suppress background nitric oxide to levels significantly lower ($< 10^{10}$ molecules/cm³) than that produced from photolysis of the ambient NO_3 ($\sim 2 \times 10^{12}$ molecules/cm³), allowing product detection to go unhampered by large background signals.

Two heterogeneous reactions known to occur involve ever-present traces of water with N_2O_5 , leading to nitric acid and subsequent reaction of $HNO_3 + NO$ to produce $HNO_2 + NO_2$. These reactions are both negligibly slow in the gas phase.^{21,22} Fortunately HNO_3 is not photolysed by light above about 3200 Å and its products are $HO + NO_2$, which are not detected by either O or NO detection system. This is important since the N_2O_5 photolysis experiments were performed at $\lambda < 3100$ Å, and NO, O absolute calibrations at $\lambda = 3518$ Å. Careful conditioning and flaming of vacuum line components kept HNO_3 levels to below 8%, (typically 5%). The second heterogeneous reaction leads to HNO_2 , which does absorb at 3518 Å and produces $HO + NO$. However using exaggerated estimates for the heterogeneous rate, coupled to the fact that ambient NO concentrations are very low and dominantly controlled by reaction with NO_3 , showed that HNO_2 levels are considerably below NO_2 levels utilized for calibration purposes ($NO_2 + h\nu \rightarrow NO + O$). The photolytic reactions of NO_3 are quickly followed by $NO + NO_3 \rightarrow NO_2 + NO_2$ in the case of NO production and by $O + NO_2 \rightarrow NO + O_2$ and $O + NO_3 \rightarrow NO_2 + O_2$, when O is produced.

Very large fractions of NO_3 can be photolysed without disturbing the relative concentrations of the major cell constituents, since NO_3 is a minor specie present and NO_2 and O_2 from its photolysis contribute little to the ambient levels already present. This is important because the absolute sensitivity of both O and NO detection systems are somewhat dependent on relative concentrations of the major cell constituents. Figures 2 and 3 show that N_2O_5 absorption does not interfere with NO_3 photolysis, but NO_2 does. While NO_2 does not photodissociate directly above 398 nm, excited state

reactions of NO_2 have been shown to occur from 458 to 630 nm.²³



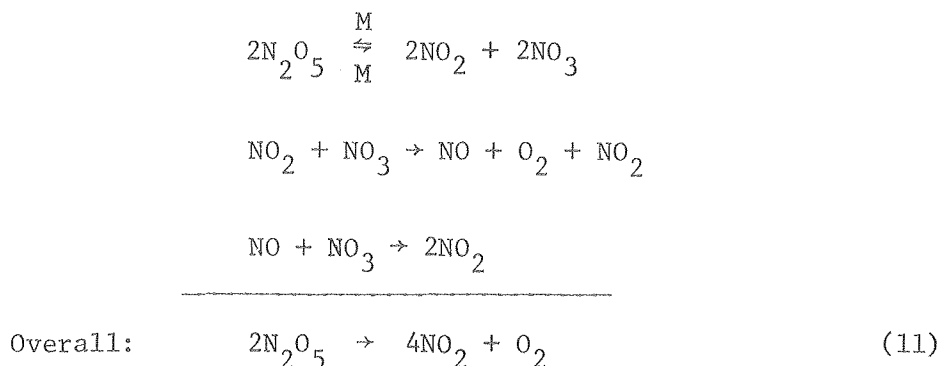
These reactions were included in the total reaction set, and modeling results indicated that, even at the highest laser fluence utilized in this study, negligible NO is produced. This is primarily due to the very rapid quenching step, since the concentration ratio of buffer to NO_2 was typically $10^4/1$.

In situ calibration, utilizing ultraviolet photolysis of NO_2 , was performed at $\lambda = 3518.3 \text{ \AA}$ (ambient phase match wavelength for the RD^*A frequency-doubling crystal), which minimized product contribution from N_2O_5 photolysis to less than 0.1%. Conversely quantum yield experiments involving N_2O_5 were performed at $\lambda \leq 3100 \text{ \AA}$ to minimize contribution from NO_2 photolysis, which typically was below 5% and easily corrected for.

Variations in N_2O_5 and buffer gas concentration, flow rates, saturator temperature, laser flash intensity and repetition rate, were computer modeled in order to determine an optimum set of operating parameters. Considerations and trade-offs included the following. The flow rate must be rapid enough to (a) flush the photolysis cell between laser pulses, (b) minimize NO_2 formation in the saturator and infrared detection cell and (c) prevent change in NO_2 concentration between the photolysis cell and the

2. Measurement of Reactants and Products

The nitrate free radical is highly reactive and cannot be prepared in large quantities. It occurs in thermal equilibrium with di-nitrogen pentoxide, with subsequent loss of N_2O_5 by further reactions, resulting finally in NO_2 and O_2



The equilibrium constant⁹ and rate constants^{17,18} for forward and reverse reactions in the unimolecular decomposition of N_2O_5 are known, as are the infrared and ultraviolet cross sections for N_2O_5 .⁹ In a flowing mixture of N_2O_5 and buffer gas, typical optical densities of NO_3 (in a 10 cm path length) were $\leq 10^{-5}$, making direct optical detection difficult.

In this study the concentration of NO_3 was obtained from the observed concentrations of NO_2 and N_2O_5 and from the equilibrium constant. The N_2O_5 infrared absorption cross section⁹ at 1246 cm^{-1} was used to determine a cross section for an equally strong absorption at 743 cm^{-1} , the later wavelength being preferred for various reasons. First, "nitration" of most commonly used infrared window materials occurs around 1200 cm^{-1} , slowly with time, presumably from contact with HNO_3 (or N_2O_5 itself) and results in decreased optical transmission. The 1246 cm^{-1} band also contains a marginal interference from an overlapping HNO_3 absorption, but at 743 cm^{-1} , N_2O_4 is the only interfering species and its concentration is negligible. Finally, the 743 cm^{-1} region is spectrally clean of absorbances from either CH_4 or SF_6 used as alternative buffer gases in this work.

The low ($\approx 10^{13}$ molecules/cm³) concentration of NO₂ in the cell was measured by the technique of laser induced fluorescence. A helium-cadmium laser was chosen to excite NO₂ in a strongly absorbing region below its dissociation limit, the subsequent visible fluorescence detected by conventional photon counting techniques. The very rapid deactivation rate of excited NO₂ with the nitrogen buffer gas and the large ratio of buffer gas to cell constituents resulted in the fluorescence signal being independent of variations in or absolute concentrations of these constituents. The only possible interference would result from NO₃, however its concentration-cross section product at 4416 Å is a factor of ~ 20 lower than that of NO₂, and NO₃ is in a mainly dissociative region at this wavelength. Flow rates were adjusted to prevent possible photolysis of NO₃ (or NO₂ from the reaction of NO₂^{*} with NO₂) which might interfere with NO₂ detection. Furthermore the detector itself was located close to, but following the main photolysis cell. Modeling results showed that differences in NO₂ concentration in flowing from photolysis cell to fluorescence detector was less than 0.25%.

NO₃ photolysis products were measured by a real time diagnostic, namely fluorescence excited by microwave powered resonance lamps. Such lamps provide versatile excitation sources, since they generally use the species to be monitored in the lamp itself. As a result of the need for specific kinetic rate constants dealing with atmospheric reactions as well as direct monitoring of atmospheric species, a wide variety of vacuum ultraviolet (VUV) lamps has been developed,²⁴ capable of detecting both stable and reactive species.

Some attributes of this detection method are relatively strong intensities (10^{13} - 10^{14} photons/cm²/sec) usually concentrated in one or more narrow emission lines. The nature of this line source makes detection very specific, and the relatively large absorption cross sections of atomic species (some approaching the wavelength of the absorbed light) result in its high sensitivity. In fluorescence, typical particle concentrations are detected over a range of 10^9 - 10^{12} cm⁻³ between which the observed fluorescence is linear with concentration. The application of a VUV lamp source allows use of solar blind photomultiplier tube detectors, which are not affected by scattered light from the laser pulse. Finally, it is a direct physical measurement of concentration which involves none of the potentially serious problems associated with the use of secondary chemical reactions to analyze for products (e.g., chemiluminescence or conversion to secondary products). In addition, errors arising from sampling and manipulation of products prior to analysis are eliminated since detection occurs in the reaction cell. The use of VUV radiation is also the most serious disadvantage of the technique due to the possibility of lamp photolysis of reactant or product, which dictates further the use of a flow system.

The high sensitivity of resonance fluorescence detection of atomic oxygen is well recognized and has become a standard monitoring technique in chemical kinetic studies.²⁵ The O atom resonance triplet, 3S_1 - $^3P_{2,1,0}$ consists of lines at 1302, 1305, and 1306 Å which are theoretically in the intensity ratio 5:3:1. However its line source is generally somewhat, to severely, reversed. The line

Detection sensitivity was maximized by varying O_2 concentrations in helium or argon while observing scattered radiation from a flowing mixture of nitrogen atoms in excess NO ($N + NO \rightarrow N_2 + O$), from a second microwave discharge. While increasing the O_2 content of the lamp directly increased the lamp emission intensity (as measured by a VUV monochromator with 0.3 Å resolution) the lines evidently become severely reversed with increasing O_2 , since the maximum O fluorescence intensity occurred with a pure helium discharge. Various tanks of helium were tested as sources of O resonance radiation, resulting in a sensitivity⁻¹ of $\sim 5 \times 10^6$ (molecules/cm³)/(count/sec).

Considerable effort was spent in development of a usable NO resonance lamp, since several of its properties severely reduce its sensitivity compared to atomic resonance lamps. The absorption spectrum at room temperature is highly structured from 1300 to 2300 Å, consisting of bands consisting of the $\gamma(A^2\Sigma^+ - X^2\Pi)$, $\beta(B^2\Pi - X^2\Pi)$, $\delta(C^2\Pi - X^2\Pi)$, and $\epsilon(D^2\Sigma^+ - X^2\Pi)$ systems. The only lines suitable for fluorescence scattering are the low-lying vibrational states of the γ and ϵ systems, the rest being predissociated. The generally accepted value for the radiative lifetimes of these vibrational levels is about 2×10^{-7} sec.^{27,28} O_2 (as well as most other inert buffer gases) is a rapid quencher $k_{v'=0,3} = 1.6 \times 10^{-10}$, $k_{v'=1} =$

$1.7 \times 10^{-10} \text{ cm}^3 \text{ molecule}^{-1} \text{ sec}^{-1}$), whereas N_2 is 2000-fold less effective²⁹ and was chosen as the primary buffer in this study. Vibrational relaxation is slow and requires about 790 and 220 collisions, respectively, to induce the $v' = 1 \rightarrow 0$ and $v' = 3 \rightarrow 2$ transitions.³⁰ Fluorescence for each system consists of γ band progressions, the intensities of which are controlled by the respective Franck-Condon factors.^{32,33} A literature and experimental survey was made of common nonreactive buffer gases, capable of fast quenching of ground state vibrational states of NO but not the electronic states (responsible for the observed fluorescence signal) resulting in methane as the only viable candidate.³¹ The relative half-life for quenching $v'' = 1$ in these experiments was 23 msec/16 μsec for N_2/CH_4 respectively, while the concomitant reduction in fluorescence signal was $\leq 25\%$. Methane buffer was utilized to ascertain the presence of vibrationally excited nitric oxide in this study.

Typical absorption cross sections in the more strongly fluorescing system are on the order of $10^{-17} \text{ cm}^2/\text{molecule}$, while fractional overlap (at 700 K) between lamp source and room temperature NO is about 2%²⁴ (compared to $\sim 50\%$ for oxygen atoms). Furthermore the fluorescence efficiency at 10 torr for NO is 0.27 vs. 0.77 for atomic oxygen. These considerations reduce the inherent sensitivity of NO to O by a factor of $\sim 3 \times 10^3$ (assuming equal source intensities). Furthermore Graham⁹ found the average quantum yield ratio of NO to O to be about 0.28, decreasing the relative sensitivities even further.

Conventional methods of detecting low levels of nitric oxide have revolved around observing fluorescence from excited NO_2 upon reaction of NO with ozone. This system could not be used since ozone produces atomic oxygen upon photolysis in the visible region, and furthermore fluorescence from excited NO_2 would require detection with phototubes not blind to scattered laser radiation. Diode lasers are available to excite NO in the vicinity of $5.3 \mu\text{m}$. However the absorption cross sections fall in the range of 7×10^{-21} to $2 \times 10^{-18} \text{ cm}^2$, which are far too low for the sensitive detection needed in this study.

Several metal vapor and hollow cathode lamps display near-coincidences to various ro-vibrational lines of NO (e.g., Se, Zn, Cd^+ , Te and Ge). Perhaps the most widely studied is the Cd^+ source which has a $+0.45 \text{ cm}^{-1}$ separation from the $v' = 1, k' = 13, R_{11}(25/2)$ γ band of NO at $46,618.1 \text{ cm}^{-1}$ (vac). This lamp was tested in the present system, but the active 2145 \AA line is about 25 times weaker than the accompanying Cd 2290 \AA line which makes up a progression of nine active emission lines that contributes uselessly to the background scattered radiation. It has been noted that, at low pressures, NO absorbs γ radiation band emission from an NO discharge more strongly by a factor of 40 than it absorbs the Cd^+ line.³⁴

Considerable effort was made to maximize and optimize a nitric oxide resonance lamp. Discharges of NO, NO_2 , N_2O with and without various buffers were screened at varying microwave powers and lamp pressures. However it was found that 600 m torr of breathing quality air resulted in the maximum signal, presumably due to the

lack of a NO or NO₂ absorbing layer in the lamp prior to the discharge. This coupled to an optimized optical detection system (see Section IIB), resulted in nitric oxide sensitivities⁻¹ of $\sim 4 \times 10^7$ molecules·cm⁻³/count·sec⁻¹, only a factor of 10 lower than the oxygen atom system. Details concerning detectivity and spectral parameters of this lamp are also contained in Section IIB.

3. Consideration of Interferences

Superficially, it appears that there is little or no reason to suspect that the detection systems described should perturb the chemical system being studied. However a more detailed analysis of possible interactions and interferences between the various diagnostic systems and the chemistry involved is given here.

Of primary concern is the selectivity and specificity of each detector. Since two photolytic channels are open concurrently, it is important that the oxygen detector not detect nitric oxide or vice-versa. This has been avoided by specifying photomultiplier tubes, with non-overlapping wavelength response limited to the species in question. This is necessary since the nitric oxide lamp generates atomic oxygen lines, and the helium lamp contains a finite nitrogen impurity which generates NO lines. Another concern was to maximize signal and minimize perturbation of the cell constituents. Such considerations include (a) line or band attenuation by cell constituents, (b) quenching of excited state (fluorescing) species and (c) line or band photolysis of cell constituents.

Calculation of signal attenuation of either O or NO shows a maximum optical density of ~ 0.03 , mainly due to N₂O₅ absorption at either 2144 Å or 1302 Å (assuming a cross section of 10^{-17} cm² molecule⁻¹).

Similarly, attenuation is not a factor in detection of NO_2 , the maximum optical density being $\sim 10^{-4}$. Linearity of both NO and NO_2 signal with concentration has been demonstrated over the ranges encountered in this work (Section IIIA). Clyne and Bemand³⁵ have shown that the maximum optical density, due to atomic oxygen self-absorption, is $\sim 1.5 (k_0 l)$ in all three emission lines before noticeable loss of linearity occurs. This limits the maximum O concentration to $\lesssim 2.5 \times 10^{12}$.

Quenching of excited state species has also been shown to be low in the case of O and NO. The fluorescence quantum yield for oxygen atom is 0.81 and buffer gas limited, hence variations in cell constituents are not important (10 torr total pressure was used throughout the study). Similarly, the NO fluorescence efficiency is 0.96 and is controlled by N_2O_5 assuming gas kinetic quenching and typical N_2O_5 concentrations. Doubling the N_2O_5 concentration decreases ϕ_f to 0.93. The long radiative lifetime of excited NO_2 and very efficient quenching by N_2 sets its quantum efficiency at 1.7×10^{-3} at 10 torr of nitrogen, making it completely insensitive to changes in mole fraction.

Considering photolysis from spectroscopic photon sources, the calculated loss of NO_2 due to irradiation by 10 mw of helium-cadmium laser radiation is $\sim 2 \times 10^4 \text{ molecules} \cdot \text{cm}^{-3} \cdot \text{sec}^{-1}$ due to reaction of $\text{NO}_2^* + \text{NO}_2$. The NO lamp integrated source intensity of $\sim 10^{14} \text{ photons} \cdot \text{cm}^{-2} \cdot \text{sec}^{-1}$ can photolyze $4 \times 10^{10} \text{ molecules} \cdot \text{cm}^{-3}$ of N_2O_5 (a $10^{-2}\%$ loss), assuming typical flow rates and an aperture time of 0.1 sec. This sets an approximate detection limit (at $S/N=1$) for atomic oxygen. The O lamp with similar integrated intensity

produces the same limiting constraints assuming an N_2O_5 cross section of $10^{-17} \text{ cm}^2 \cdot \text{molecule}^{-1}$ at 1300 \AA .

4. Interpretation of Data

In this work the initial concentration of product following flash photolysis was measured versus wavelength and correlated to the pulse energy, NO_3 cross section and reactant concentration. A simplified derivation of the expression utilized to interpret the data is given here. A more detailed derivation, demonstrating that the measured quantum yield is independent of temporal beam profile, is given in Appendix B.³⁶ For a system



$$\frac{dB}{dt} = I_a \phi = I_0 \sigma_A A \phi \quad (13)$$

when the system is optically thin and

$$\int_0^t dB = \int_0^t I_0 \sigma_A A dt \quad (14)$$

The time dependence of A is

$$\frac{dA}{dt} = -I_a = -I_0 \sigma_A A \quad (15)$$

or

$$A = A_0 e^{-E\sigma}$$

where

$$\int_0^t I_0 dt \quad (16)$$

is the laser fluence,

Now

$$B = \sigma \phi A_0 \int_0^t I_0 e^{-E\sigma} dt \quad . \quad (17)$$

Changing variables let $dE = I_0 dt$ so that

$$B = \sigma \phi A_0 \int e^{-E\sigma} dE \quad (18)$$

and

$$B = \phi A_0 (1 - e^{-E\sigma}) \quad . \quad (19)$$

The quantum yield is calculated from signal averaging many laser shots to achieve the desired photon counting statistics.

Rearranging,

$$\phi_{(B,C)\lambda} = \sum_{\text{shots}} \frac{[B,C]_{t=0}}{[A]_{t=0} [1 - \exp(-E_{\text{laser}} \sigma_A)]} \quad . \quad (20)$$

In the high energy limit,

$$[1 - \exp(-E\sigma_A)] \rightarrow 1 \quad , \quad (21)$$

and the absolute energy and cross section need not be measured. This condition is contingent upon a very fast dissociative channel such that saturation effects do not compete, a good assumption for small molecular species.^{37,38} The amount of photolysis occurring ($N_0 - N$) is simply given by

$$\ln \left(\frac{N_0}{N} \right) = E\sigma \quad (22)$$

(for optically thin samples).

These expressions have been verified by numerical integration procedures, and found to describe precisely the behavior of the chemical system.

Due to the large visible cross sections of NO_3 and availability of correspondingly intense laser pulses, use was made of this high energy limit condition to determine NO quantum yields, whereas 0 quantum yields could easily be obtained in the low energy linear regime $\left(\lim_{E\sigma \rightarrow 0} (1 - e^{-E\sigma}) \rightarrow E\sigma \right)$ due to enhanced signal sensitivity and overall yield. One NO experiment was also performed in the low energy regime (at the cost of an inordinate number of required laser shots and subsequent degradation of laser components).

During a typical NO quantum yield experiment, the laser firing sequence was begun along with the triggering control for the multi-channel analyser, and $2^9 - 2^{10}$ shots are totalized as a time profile in four memory quadrants (4096 channels). The first quadrant contained mainly signal information, while the remaining 3 quadrants were always located $\geq 20 \tau_{1/2}$ in time and contained the baseline, which was subsequently subtracted off. Following the photolysis period, the digital information was transferred to either magnetic tape or punched tape.

Subsequent data analysis of the temporal profiles of NO counts versus time was accomplished by performing a linear least square regression on points 0-10, 0-20, 0-30, ... 0-100, and calculating both slopes and intercepts. Then a second linear least square fit of number of points used versus intercept (or slope) was run, weighting each set by the number of points used, to get the "0-points" intercept ($t=0$).

The temporal profile is represented by a curve in which the NO signal first increases, then decays with time. This behavior has been shown (see Section IIID-4) to be due to subsequent reaction of $O + NO_2 \rightarrow NO + O_2$ followed by loss of NO, by reaction with NO_3 and diffusion out of the viewing zone. An analytic expression describing this temporal behavior was not readily obtainable, due to several competing terms involving replenishment of NO_3 in the initially depleted photolysis region by diffusion, depletion of ambient NO formed from NO_3 photolysis by reaction with a time varying NO_3 concentration, and diffusion of NO out of the viewing zone. These parameters would also be a function of laser excitation wavelength and percent photolysis. The above data reduction paradigm obviates determination of these parameters, and was found to reproducibly extract slope and intercept information with good precision.

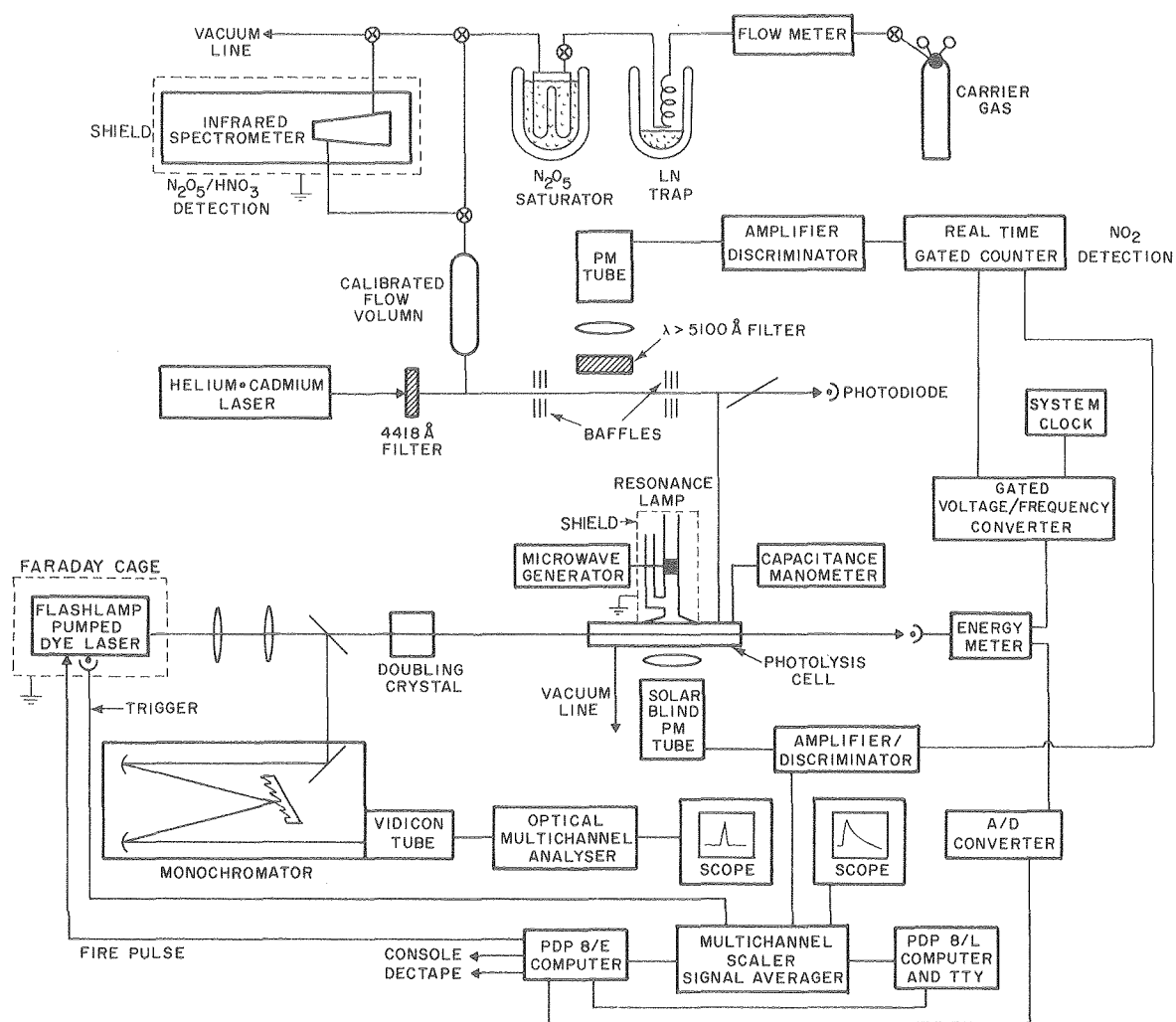
The decay of O signal shows no initial buildup, and can be represented by a single exponential decay over ≥ 2 lifetimes. Slopes and intercepts from such decay curves were extracted by a non-linear (exponential) least squares routine after baseline subtraction, performed on line prior to data transfer to archival storage media.

B. Apparatus

A schematic of the apparatus is shown in Figure 4, the components of which are described below.

1. Photolytic Source

A flash lamp pumped dye laser capable of producing 1-2 joules of visible radiation in a 400 ns long pulse, was the source of photolysis. The somewhat modified laser was of commercial design,



XBL 791-8065A

Figure 4. Schematic diagram of experimental apparatus.

a Phased-Radiation (Phase-R) 2100-B equipped with an 18 mm ID coaxial flash lamp. A second intra-annular pyrex tube of 8 mm ID provided a channel of flowing water between the lamp discharge and the dye (triax configuration). This served as a shockwave absorber and reduced heat build-up to the dye and laser tube wall, thereby reducing schlieren effects, thermal lensing and divergence. The use of a triax, while reducing output energy, allowed an increased repetition rate of 5 fold to one shot every 4 seconds, and increased the ultraviolet doubling efficiency considerably due to a more nearly gaussian beam profile. The beam was dispersed by either triple brewster angle prisms or a 1200 line/mm high energy (PTR optics) grating, operating in Littrow configuration. By adjusting the cavity length it was usually possible to approximate the laser bandwidth ($\sim 5 \text{ \AA}$) to the resolution used by Graham⁹ to measure NO_3 cross sections; however this depended on the gain characteristics of the dye, and the location on the gain profile and was not totally under control, with some narrowing in bandwidth occurring in low gain media.

By using passive thermal control, the temperature differential between dye and triax water was kept to within $4/1000^\circ\text{C}$, again necessary to eliminate schlieren and thermal lensing effects, and resulted in a half angle divergence in the far field of 0.4 milliradians. Thermal control consisted of passing dye and water from two separate stainless steel circulating baths at 2 gallons/minute through 1000 feet of stainless steel tubing immersed in a 55 gallon tank of agitated room-temperature water. Differential temperatures were continuously monitored with in-line thermistors at the input to the lamp, by a wheatstone bridge and digital voltmeter. Various

dyes were used in methanol to cover the wavelength range 4700-7100 Å. Frequency doubling was achieved by extracavity angle tuned ADP (cut to 3000 Å max) and an RD^{*}A temperature of tuned crystal ($\lambda_{2\nu} = 3518.3 \text{ Å} - 20.0^\circ\text{C}$), each delivering between 1-3 mJ of ultraviolet energy per pulse. The fundamental was eliminated by appropriate ultraviolet transmitting, visible absorbing blocking filters and energy attenuation achieved with volume absorbing neutral density filters.

A pellicle split off approximately 8% of the beam and directed it through a 1 meter monochromator onto the face of a PAR 1205D vidicon tube from which an optical multichannel analyser (OMA) displayed bandwidth and wavelength on a CRT with a resolution of 0.4 Å/channel. For performing wavelength determinations, suitable gate pulses from the OMA, fired the laser and triggered the vidicon face electron beam scan some 20 μs following the laser pulse, and thus avoiding RFI pickup from the laser spark gap. During photolysis experiments, the laser fire pulse was derived from external sources using either a digital delay generator, oscilloscope trigger or computer derived signal. The remaining beam passed through an aperature into the photolysis cell and terminated on a pyroelectric joulemeter. The laser was enclosed in a grounded metal clad room (Faraday cage) to shield the diagnostics and computers from RFI pickup.

2. Detection of N_2O_5 and HNO_3

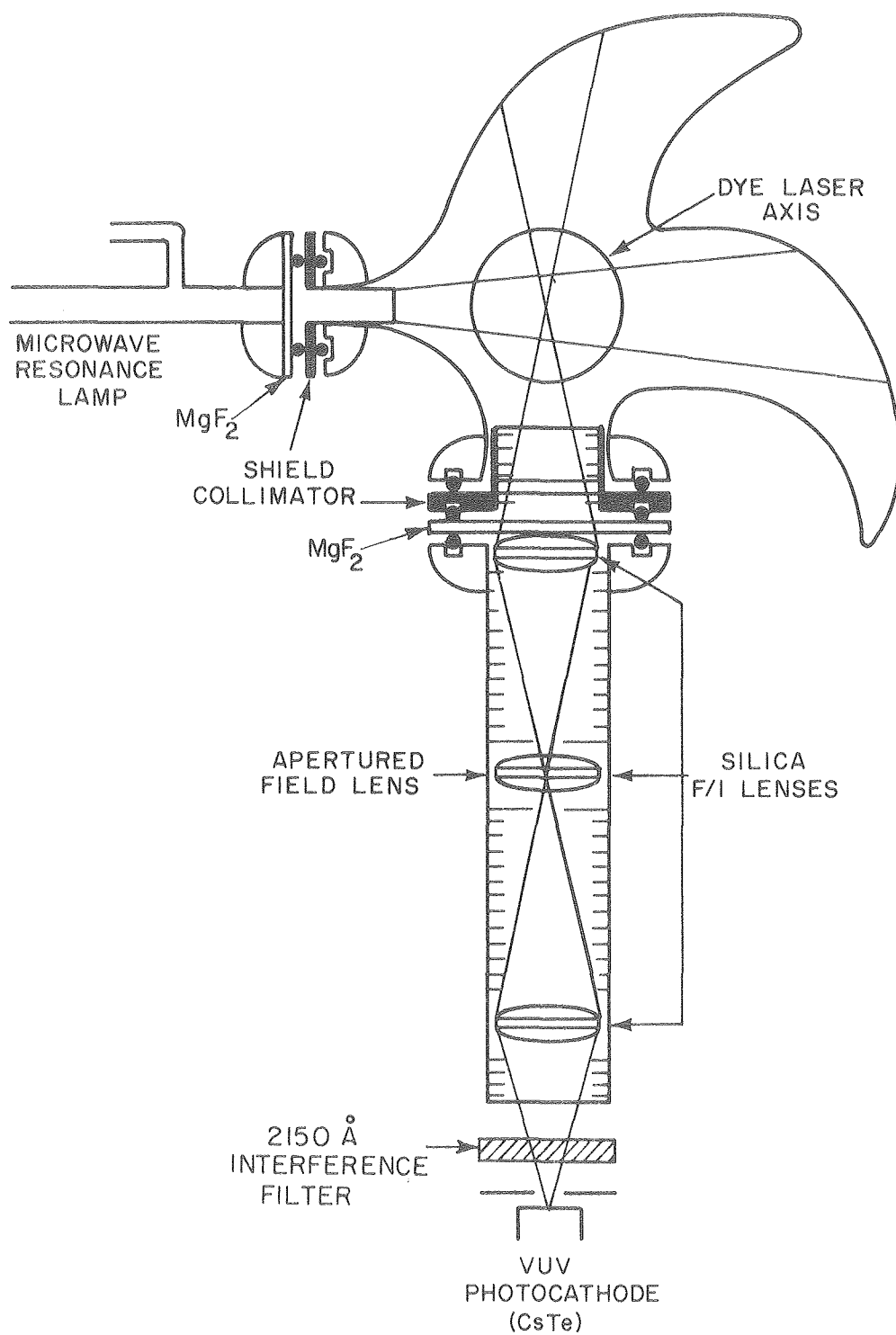
A Beckman Instruments IR-7 double beam infrared spectrophotometer was employed to continuously monitor N_2O_5 and periodically check HNO_3 concentrations. The infrared cell fitted with silver

chloride windows exactly confined the beam which entered at $\sim 2 \times 3$ mm and exited at $\sim 0.5 \times 1.5$ mm. This served to maximize sensitivity and decrease volume (and flow time) such that a minimum amount of NO_2 buildup occurred during flow through. The instrument was located physically close to the N_2O_5 saturator and clad in grounded aluminum foil to reduce pick-up from the microwave (resonance lamp) generator. The resolution was maintained at 2.0 cm^{-1} to match that used by Graham⁹ in determining N_2O_5 and HNO_3 cross sections; however the poorly resolved PQ and R branch maxima were rather insensitive to resolution.

3. Detection of Nitric Oxide and Oxygen Atoms

A schematic of the NO (and atomic oxygen) detection system is shown in Figure 5. The microwave lamp designed after Watson³⁹ consisted of a #9 O-ring joint fitted with a gas inlet close to the lamp window, minimizing self-reversal. A 2 mm thick VUV quality magnesium fluoride window was sealed to the lamp with Torr-seal low-vapor-pressure epoxy around the perimeter of the window, minimizing exposure and possible degradation of the epoxy by VUV radiation. Lithium fluoride windows, while displaying higher transmission to O atom resonance lines, were found to quickly F-center with time, causing rapid deterioration in sensitivity. Two black anodized aluminum shield collimators were fitted to prevent light from piping into the cell from the lamp connection or out of the cell from wall absorption, greatly reducing scattered light.

The photolysis cell consisted of a 3.8 cm diameter, 10 cm long laser path and two large perpendicular Wood's horns facing the lamp and photomultiplier tube. A solid state Analog Devices (AD-581)



XBL 791-8063A

Figure 5. Schematic of NO ($f/2$) and 0 optical detection system.

temperature transducer with digital-readout was attached to a copper band that was movable along the laser axis of the cell but confined to areas not occupied by the Wood's horn. A larger #13 O-ring joint served as the optical exit port with three (f/1) Suprasil-1 lenses imaging the reaction zone onto a 3/8" aperatured VUV cesium teluride photomultiplier tube. A 2150 Å band pass interference filter (220 Å FWHM-25% T) passed resonantly scattered $\gamma(A^2\Sigma^+-X^2\Pi)NO$ fluorescence, blocking both ultraviolet laser light (from NO_2 calibration photolysis) and possible O resonance lines. The optical path was thoroughly lined with baffles to further reduce scattered light. The cell and optical collection tube were externally blackened, and cell volume minimized, again to decrease N_2O_5 loss or NO_2 buildup during flow through.

To detect O radiation the Suprasil lenses were removed, a solar blind cesium iodide VUV photomultiplier tube fitted and the optical path evacuated to $< 10 \mu m$ pressure. Both CsTe and CsI tubes were operated in the negative high voltage cathode configuration for photon counting applications and housed in magnetically and RF shielded housings to minimize interference from external sources of RFI. Dark current at room temperature was generally less than 10 counts/sec.

The microwave source was a stabilized Burdick model MW/200 Medical Diathermy operating at 2.45 GHz, coupled to the lamp by a standard Evenson microwave cavity. The cavity and lamp were totally enclosed in a copper wire cage with braided ground, to reduce microwave leakage and subsequent pick-up by the infrared spectrometer.

Current stabilization of the magnetron was achieved by an in-house circuit modification, shown in Figure 6. After 1 hour warm-up period, no current drift was detectable within the 0.05% resolution of the instrumentation. Careful air cooling of the microwave discharge region in the lamp also minimized fluctuations. This type of long term stability distinguishes this application of VUV resonance emission from its use in reaction kinetics and as a photochemical source.

4. Detection of Nitrogen Dioxide

The technique of laser induced molecular fluorescence was chosen to measure NO_2 concentrations in the 10^{12} - 10^{13} molecule $\cdot\text{cm}^{-3}$ range. The instrumentation developed was similar in principle but much simplified in design to that recently developed by the Aerospace Corporation.⁴⁰⁻⁴³ Important characteristics of the method are (1) absence of interference by other cell constituents, (2) high sensitivity, (3) ease of calibration, and (4) linearity of response.

The instrument consisted of an apertured 4416 Å (33%T, 34 Å FWHM-B.W.) interference filter which passed the lasing line from a 10 mW Liconix 401 helium-cadmium laser while blocking the red light emitted by the laser plasma. (A schematic is shown in Figure 7). Internal light baffles were secured by two standard ultra-torr fittings on either end of a non-fluorescing fused silica tube. Since most glass filters absorbing scattered blue laser light fluoresce strongly in the red, a liquid filter cell with silica windows containing 304g/liter of $\text{Na}_2\text{Cr}_2\text{O}_7 \cdot 2\text{H}_2\text{O}$ was used between the active fluorescing region and the photomultiplier tube. This solution strongly absorbed scattered 4416 Å laser light⁴² without

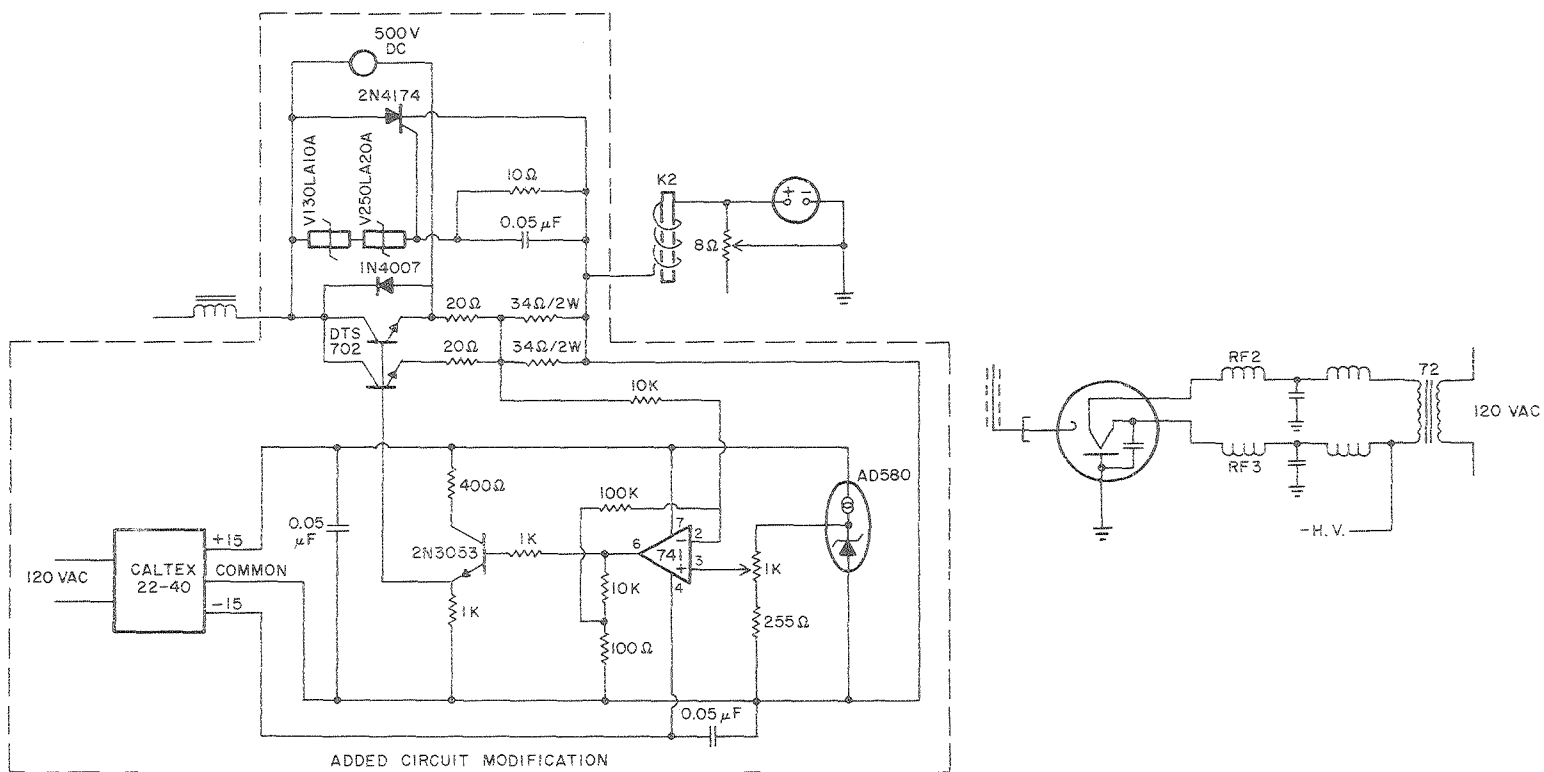
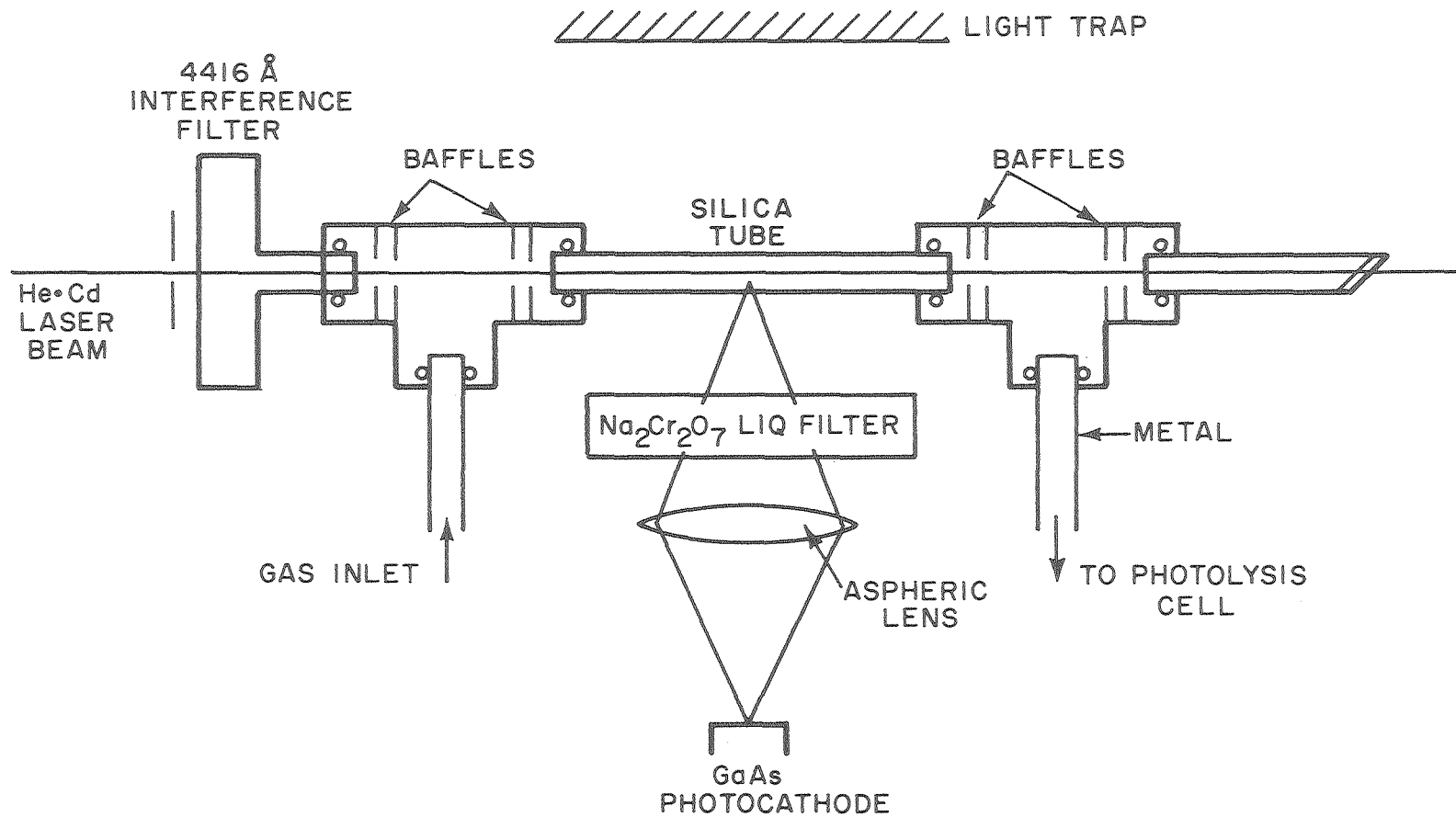


Figure 6. Schematic of microwave diathermy magnetron stabilization circuit.



XBL 791-8055 A

Figure 7. Schematic of nitrogen dioxide detector.

A 60 mm diameter, f/0.72 aspheric lens gathered the fluorescence emission and focused it onto the face of a magnetically and RF shielded (RCA 31034-A) GaAs photomultiplier tube. This tube was similarly operated in the negative high voltage cathode configuration. The output pulses of the PMT, cooled ($\approx -20^{\circ}\text{C}$) by blowoff from a heated liquid nitrogen dewar, were fed to a wideband high-gain amplifier/discriminator (Pacific Photometrics AD/4). The output of this amplifier consists of standard 10 nsec. pulses of -0.75 V amplitude which were terminated into 50Ω and fed to a 110 MHz gated counter (Heathkit-IM.4110). Typical background counts with flowing nitrogen at 10 torr were ~ 80 c/sec, and sensitivities approached that of the more highly sophisticated Aerospace instrument (see Section IIC). The physical placement of the detector could easily be altered to sample the flow stream either before or after the photolysis cell, insuring negligible NO_2 concentration variations during flow-through.

In early experiments, resonance fluorescence signals from the solar blind photomultiplier tubes were fed into a high gain amplifier/discriminator (P.A.R. 1120), then into a pulse pile-up counter, of in-house design (Appendix C). This unit was capable of storing up to 4 pulses and gating them out synchronously at 1, 5, or 10 MHz, acting as a prescaler at high counting rates. A high speed counter

was also built (Appendix D) storing up to 4 bits of information at a rate of 1 μ s per channel (and 32 channels wide). Two 4 bit FIFO's, upon a command pulse, dumped all 32 channels into an 8080 microprocessor with 1K of solid state memory (Appendix E). This unit was interfaced to a teletype and paper tape punch.

Because of limited memory and lack of versatility in data processing capability, this signal processing equipment was subsequently replaced by a Nicolet Instruments Model 1074 hardwired signal averager (Fabritek) operating in the multichannel scaling mode. All or part of the 4K of 18 bit word memory could be filled at a maximum scan rate of 1 μ sec/channel. Also the amplifier/discriminator-prescaler was updated with a PAR 1121 unit interfaced to a PAR 1120 data console, modified with an ECL/TTL converter and high speed (LH 0042) line driver, which terminated into 50 Ω at the multichannel scaler. Initial data manipulation was performed with a PDP 8/L computer, which was interfaced to the Fabritek and a PDP 8/E computer via an interprocessor buffer. Slope and intercept information from this initial analysis was then further processed on a PDP 11/10 computer with 24K of 16 bit memory.

Pulse energy measurements were obtained with a pulse intensity integrating "spectrally flat" pyroelectric joulemeter (Gen-Tec-ED200), equipped with a peak reading sample and hold and digital display. Analog signals from each pulse were fed into a gated voltage to frequency converter and continuously counted throughout the duration of the experiment. A clock controlled the V/F gate and timed the signal acquisition period. This information provided an extremely precise ($\sim 0.25\%$) measurement of average pulse energy per shot. The

V/F converter was insensitive to RFI from the laser spark gap as was the pyroelectric joulemeter transducer.

C. Gases and Flow System

The carrier and lamp gases used in this study were supplied by Lawrence Berkeley Laboratory. Calibration mixtures of NO and NO₂ in N₂ were analyzed reagent grade supplied by the Matheson Company. The following typical impurity levels were quoted by the suppliers. (see following table).

NO of 99.0% purity from the Matheson Company was purified (by the method of Hughes⁴⁴) by passing the stream slowly through a U-tube containing degassed silica gel maintained at -77°C. Samples of the purified sample were diluted to one atmosphere at concentration levels similar to that supplied commercially. The pressure dependent cross section at ~1 atm and 2262.9 Å (0,0-γ transition) was determined using a (Varian Instruments) Cary 118C UV/Visible spectrophotometer in a 9.95 cm path length quartz cell, at a resolution of 2.0 Å. An apparent average cross section of $2.04 \times 10^{-18} \text{ cm}^2 \cdot \text{molecule}^{-1}$ (base ε) was measured.

Two tanks of nominally 102 ppm and 1030 ppm NO/N₂ were analyzed under these exact conditions at the beginning and the end of the study to check for long term change in mole fraction. Both tank gas mixtures contained a small amount of NO₂ impurity, which was measured with the NO₂ laser induced fluorescence detector, converted to an absorbance at 2262.9 Å, and subtracted from the NO absorbance.

The following analysis were obtained:

	<u>Nominal Concentration</u>	
	<u>102 ppm</u>	<u>1030 ppm</u>
Start of study:	103.2 ppm	1007 ppm
Finish of study:	104.3 ppm	1006 ppm

	High Dry Nitrogen ^a	Nitrogen ^{b,c}	High Dry Oxygen ^a	Ultra high Purity ^b Oxygen ^b	Breathing Quality Air ^e	Extra Pure Helium ^a	Methane ^a	NO ^c	NO ₂ ^c	NOCL ^b
N ₂	99.999%	99.998%	500 ppm	25 ppm	78.08%	1.0 ppm	<i>f</i>	0.5%	--	"low"
O ₂	1.5 ppm	8.0 ppm	99.5%	99.99%	19.95%	0.2 ppm	<i>f</i>	--	--	"low"
He	--	--	--	--	--	99.998%	--	--	--	--
H ₂ O	1.5 ppm	5.0 ppm	1.5 ppm	<6 ppm	19 ppm	0.3 ppm	<i>f</i>	--	0.06%	--
CO ₂	--	1.0 ppm	10 ppm	7 ppm	--	0.1 ppm	<i>f</i>	0.2%	--	--
Ar	5 ppm	10 ppm	4000 ppm	60 ppm	--	0.1 ppm	<i>f</i>	--	--	--
Ne	--	--	--	--	--	14 ppm	<i>f</i>	--	--	--
THC ^d	--	<0.10 ppm	<i>f</i>	16 ppm	--	--	99.99	--	--	--
NO	--	--	--	--	--	--	--	99.2%	<5 ppm	--
NO ₂	--	--	--	--	--	--	--	0.05%	99.9%	0.5%
K + Xe	--	--	--	17 ppm	--	--	--	--	--	--
N ₂ O	--	--	--	2 ppm	--	--	--	0.05%	--	"ppm"
NOCL	--	--	--	--	--	--	--	--	Nil	99.2%

^a LBL issue.

^b Matheson Gas Company.

^c Used in gas mixtures from Matheson Co.

^d Total hydrocarbons as CH₄.

^e Ohio Hospital Supply (Airco Company).

^f Total <100 ppm (including ethane, ethylene and C₃ and higher hydrocarbons.

These tank gas mixtures were used to calibrate the nitric oxide lamp sensitivity before and after each experiment.

NO_2 of 99.5 purity from Matheson Company was liquified and stored in the dark. Several samples were then treated by either bubbling O_2 through them or simply storing them for 3-4 days under one atmosphere of O_2 at ~ 273 K, in order to oxidize residual NO. Solid samples were transferred several times after freeze thaw pump cycles to remove trapped oxygen. The resulting clear crystalline solid was stored at 196K.

Several samples of the variously purified crystals were taken both from solid and liquid phase material, and diluted with N_2 to concentration levels similar to that supplied in the NO_2/N_2 tank mixture. Accurate cross sections were obtained (see Section IIIA) at 1 atmosphere total pressure for use both in subsequent actinometry studies and tank gas calibration. A nominal mixture of 100 ppm NO_2/N_2 was analysed by ultraviolet absorption at 3900 \AA at 1 atmosphere in a 296 cm long path cell, again at the beginning and end of this study. A slow flow of the mixture was maintained to prevent adsorption losses on the walls of the cell. The tank concentration remained invariant throughout the study to the precision of the measurement and an average value of $1.15 \pm .02$ ppm was obtained. No correction for N_2O_4 was necessary in this measurement. This tank of NO_2/N_2 was used to calibrate the NO_2 fluorescence detector both before and after each experiment.

Dinitrogen pentoxide was prepared utilizing the method of Schott and Davidson.⁵ High dry oxygen was purified by passing through a silica tube with copper turnings at 900 K, then through a column of

5% palladium on an alumina substrate at 620K to convert any hydrogen impurities to CO_2 and water. It then passed through columns of ascarite and P_2O_5 -coated glass beads to remove CO_2 and water, then through a U-tube packed with silica gel at 196K for further drying. The flow was split into two streams, one passing to an Ozone Research and Equipment Company silent discharge ozonator which converted about 7% of the oxygen to ozone. The second stream was bubbled through liquid $\text{NO}_2/\text{N}_2\text{O}_4$ at 273K, then past a flow regulating needle valve, and was then mixed with the ozone stream. The flow rates were adjusted such that the brown color of NO_2 was totally absent after the junction, and ozone could be detected at the exhaust. The resulting N_2O_5 was condensed in a pyrex storage finger, held at 196K, until the NO_2 in the bubbler was exhausted. The oxygen was pumped off of the resulting needle-shaped crystals, and the N_2O_5 was stored at 196K until use. Infrared analysis detected less than 1% NO_2 and typically < 5-8% HNO_3 formed from heterogeneous reaction of N_2O_5 with water adsorbed on the walls of the manifold and trap. No detectable ozone was trapped out with the N_2O_5 ; upper limits were measured at < 0.1%.

N_2O_5 preparation took place in a glass manifold fitted with Westef and Kontes high-vacuum greaseless Teflon stopcocks with Viton-O rings. Connections were made with greaseless stainless steel ultra-torr fittings, and the manifold evacuated with a liquid nitrogen trapped oil diffusion pump. NO_2 purifications and all other gas manipulations took place in a similar vacuum line but equipped with glass-bore Westef greaseless stopcocks to prevent NO_2 absorption into and permeation from the standard teflon stopcocks.

During a typical experiment, a large Pyrex saturator at 244K was charged in the dark with a small layer of N_2O_5 from the storage trap. A stream of 3.0 psig-high dry nitrogen was flowed through tandem hasting electronic mass flowmeters into a stainless steel coil suspended above a pool of liquid nitrogen, and into the saturator. From there the flow could be diverted either through the Beckman IR-7 spectrophotomer IR cell, or around it and through a flow rate regulating needle valve where a pressure drop to $\gtrsim 10$ torr occurred. The gas stream now entered a calibrated flow volumn of approximately 443 cc in order to re-establish equilibrium between N_2O_5 , NO_2 , and NO_3 . The flow now entered the photolysis cell where the pressure was measured by a Bartron MKS Model 310 AHS-100 capacitance manometer, then on through and directly into the NO_2 fluorescence detector, after which it was pumped out through a liquid nitrogen trap to a Welch Duo-Seal mechanical pump.

III. Experimental Procedures and Data

Evaluation of quantum yields involved measurement of the following experimental quantities and use of various constants. For instance, to determine oxygen atom quantum yields, the following quantities are needed

$$\phi_0 = \frac{[O]_{NO_3}}{\frac{K_{EQ}[N_2O_5]}{[NO_2]} \left(E_{vis}^i \cdot \sigma_{NO_3} \right) \left(\frac{\text{dwell time}}{\text{channel}} \right) \left(\frac{\text{laser}}{\text{shots}} \right)} \times \frac{[NO_2] \left(E_{UV}^i \cdot \sigma_{NO_2} \right) \phi_{NO_2} \left(\frac{\text{dwell time}}{\text{channel}} \right) \left(\frac{\text{laser}}{\text{shots}} \right)}{[O]_{NO_2}} \quad (22)$$

The left hand term is the experimentally defined measurement from NO_3 photolysis, and the right-hand term the calibration factor derived from the in situ ultraviolet photolysis of NO_2 . Combining terms

$$\phi_0 = \frac{[O]_{NO_3}}{K_{EQ}[N_2O_5] (E_{vis}^i \cdot \sigma_{NO_3})} \times \frac{\left(\frac{ABS^2}{\sigma_{NO_2} \cdot L^2} \right) (E_{UV}^i \phi_{NO_2})}{[O]_{NO_2}} \quad (23)$$

E^i is the laser intensity directly behind the photolysis cell entrance window for the UV and visible beams. The NO_2 concentration enters the expression squared, and the ratio E_{UV}^i/E_{vis}^i contains any deviations from spectral flatness in the pyroelectric joulemeter as well as differences in window transmissions in the UV and visible.

In this work we have defined the ratio E_{UV}^i/E_{vis}^i by actinometry and window transmission measurements and the values of σ_{NO_2} and σ_{NO_3} have been refined. The temperature dependent equilibrium constant and N_2O_5 infrared cross sections obtained by Graham⁹ were used, allowing correction for an observed local heating effect due to the resonance lamps.

A. Visible and Ultraviolet Cross Section Measurements for NO_2 and $NOCl$

In order to determine the relative sensitivity of the pyro-electric joulemeter to visible and ultraviolet light, bulk laser photolysis was performed (Section III-B) using NO_2 and $NOCl$ as gas phase actinometers. A literature search revealed moderate disagreements in both $NOCl$ ⁴⁵⁻⁴⁸ and NO_2 ^{10,49-51} cross sections, hence they were redetermined in this work at the wavelengths of interest.

Harker⁵¹ has reported measurements of NO_2 absorption cross sections (and quantum yields) in the 3750-4200 Å region. These measurements agree well with those of Graham⁹ but are 4-10% larger than values reported by Bass.⁴⁹ Hall and Blacet⁵⁰ measured cross sections which were 10-20% higher than Bass in the 2500-4100 Å region. While cross sections in this region are somewhat resolution dependent, the discrepancy is in the wrong direction to explain these results. Corrections due to the presence of N_2O_4 must also be made, but by utilizing low partial pressures and/or long path lengths, these corrections are very small.

Samples of variously purified NO_2 were taken both from the solid and liquid phases and transferred to a 10 cm long, NO_2 conditioned, all

quartz cell fitted with a greaseless glass bore Westef stopcock. The ultraviolet absorption was determined at 3000.0, 3518.3 and 3900.0 Å, at ~300 mtorr pressure. The resolution of the Cary 118C spectrophotometer, a prism instrument, was wavelength dependent and is recorded in Table 1. Attempts to closely match the resolution used by Harker and Graham were made, and the increase in cross section with increasing resolution (at these three wavelengths) was noted. The average value of six separate measurements at "high resolution" and eight at "low resolution" are given. Pressure measurements were made with an MKS Baratron capacitance manometer (which was previously checked against a similar unit), and the absorption cell was evacuated between measurements. No difference in cross section was observed between samples obtained from solid or liquid $\text{NO}_2/\text{N}_2\text{O}_4$, nor was the method of purification shown to be important. Corrections for N_2O_4 are unnecessary at 3900 Å and very minor at 3518 Å and 3000 Å for the conditions used.

The results indicate good agreement with Graham⁹ at 3000 Å, and an increasing divergence as NO_2 structure increases (from 3000 to 3900 Å) accentuating the importance of resolution. Graham's values at 6.7 Å resolution match values from this work at ~1 Å suggesting that Graham was possibly working at greater resolution than indicated. Harker's value at 3900 Å (1 Å resolution) agrees well with this work, but Bass' values appear consistently low at even higher resolution, possibly due to NO_2 loss in the stainless steel cell used in that study.

Samples of NOCl of 99% typical purity, from Matheson Company, were degassed at liquid nitrogen temperatures and distilled three times from 196K to 77K, to remove possible NO_2 ⁵³ impurity. During

TABLE 1. NO₂ cross sections^(f) * 10¹⁹, (base e) cm²/molecule (corrected f/N₂O₄)^(e,f)

Source	FWHM Resolution (Å)	Wavelength		
		3000 Å	3518 Å	3900 Å
This work ^(a)	0.6	1.29±0.025		
	1.16		4.79±0.41	
	1.56			6.50±0.063
This work ^(b)	2.6	1.29±0.013		
	5.0		4.62±0.013	
	6.7			6.22±0.023
Graham, <u>et al.</u> ⁹	6.7	1.33	4.73	6.51
Bass, <u>et al.</u> ⁴⁹	0.15 ⇄ 0.4	1.17	4.28	6.00
Harker, <u>et al.</u> ⁵¹	1	(d)	(d)	6.50

(a) 0.020 slit - Average of 6 measurements

(b) 0.087 slit - Average of 8 measurements

(c) read f/graph

(d) Not measured

(e) [N₂O₄] ≈ 0.27%

(f) Values

(g) Correction from Verhoek and Daniels⁵²

each distillation, the first and last fractions of the sample were discarded. Any residual Cl_2 or NO (with vapor pressures of ~ 50 and 4000 torr at 196K) could be easily separated from the NOCl (VP ~ 10 torr at 196K) by this procedure.

NOCl is susceptible to photochemical decomposition throughout the visible and ultraviolet region,⁵⁴ and extreme care was exercised to prevent loss due to ambient light. Optical densities were invariant with time, and the thermal decomposition was calculated^{54,55} to be $\sim 3.5 \times 10^3$ molecules/cm³/sec under the conditions used.

The absorption spectrum of NOCl is continuous throughout the ultraviolet and visible region, resulting in little dependence of cross section on resolution except near 6000 Å where some diffuse structure began to appear. The earlier work of Goodeve⁴⁷ does not agree with more recent studies by Takacs,⁴⁵ Ballash,⁴⁶ or Martin⁴⁸, Table 2 (possibly due to variation in sensitivity of the photographic plates with wavelength used in that study). The results of the present measurement agrees most closely with those of Ballash and Martin. The results of Takacs may be biased by systematic error, since the ratio of those values to the other studies is relatively constant. The disagreement of this work with Ballash at 2200 Å may be due to a wavelength error in the previous study, since this wavelength is on the side of a steep, broad absorption peak. The wavelength calibration of the Cary-118C was checked against NO absorption peaks in this wavelength region, and agreement to within 0.5 Å was found. The cross sections determined in this work were utilized for subsequent actionometry and NO₂ flash photolysis calibrations.

Table 2. NOCl cross sections ($\text{cm}^2/\text{molecule-base e}$)

Source	Wavelength				
	2200 Å ^(a)	3000 Å	3518 Å	4700 Å	6000 Å
This work ^(c)	$9.20 \pm .083 \times 10^{-18}$	$1.020 \pm .004 \times 10^{-19}$	$1.455 \pm .009 \times 10^{-19}$	$2.830 \pm .006 \times 10^{-20}$	$3.587 \pm .041 \times 10^{-21}$
Takacs, <u>et al.</u> ⁴⁵	1.07×10^{-17}	8.67×10^{-20}	1.18×10^{-19}	(b)	(b)
Ballash, <u>et al.</u> ⁴⁶	1.27×10^{-17}	1.03×10^{-19}	1.38×10^{-19}	2.75×10^{-20}	(b)
Goodeve, <u>et al.</u> ^{47(d)}	2.74×10^{-18}	6.63×10^{-20}	1.19×10^{-19}	2.02×10^{-20}	3.59×10^{-21}
Martin, <u>et al.</u> ^{48(d)}	(b)	9.45×10^{-20}	1.41×10^{-19}	(b)	(b)

(a) On side of broad steep absorption peak.

(b) Not measured.

(c) Average of 4 or more determinations @ 0.02 mm slit.

(d) Read from graph.

B. Joulemeter Calibration —NO₂ and NOCl Actinometry

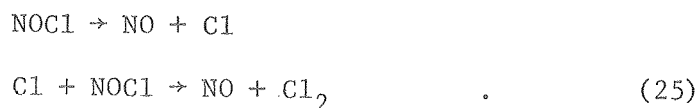
NO₂ and NOCl were employed as gas-phase actinometers to calibrate the laser joulemeter at 3000, 3518 and 6000 Å. Bulk flash photolysis was carried out in two quartz cells of 43.3 cm³ and 82.7 cm³ volume as a function of time, and decay of starting material was monitored by absorption (Cary 118C). Total laser fluence was measured with the joulemeter-gated voltage/frequency converter. Visible fundamental radiation was totally blocked in the ultraviolet photolysis runs (by two 7-54 Corning filters at 6000 Å, and 2-Hoya "Peak 320" filters and one Corning 7-60 filter at 7036.6 Å). Extensive tests were performed to insure that no transient bleaching or leak through of fundamental radiation was occurring. A 1.00 cm² aperture was used at the cell input window to prevent possible off axis laser modes from inducing photolysis and missing the clear aperture of the joulemeter (4.15 cm² area). Non-uniform response across the detector face was found to be negligible within the precision of the measurement (1-2%). In visible photolysis, a wavelength calibrated neutral density filter was used to prevent damage to the joulemeter surface, and its orientation was adjusted to prevent reflected laser light from re-entering the photolysis cell.

Between each 100-200 laser shots, the photolysis cell was removed from a clamped mount and inserted into the sample beam of the Cary for measurement. Blank runs in which the laser beam was blocked were made periodically to insure that flashlamp leakage to the room was not contributing to the photolysis, and to check for reproducibility in absorption measurements and cell placement. Both photolysis cells

and tubulation were externally blackened, and endcaps used during transport from laser to spectrometer. The percent transmission of the empty cell was determined before and after each run, and the double beam spectrometer baseline monitored continuously. All gas samples photolysed were optically thin (max $< 6\%$ absorption in 10 cm path) at the pressures used. The fraction photolysed was plotted versus $(1 - e^{-E\sigma})$, resulting in a slope equal to the total observed quantum yield. In both NOCl and NO₂, the primary quantum yield was equal to half the slope because of the rapid ensuing secondary reactions



and



The fraction photolyzed is easily shown to be equal to

$$\frac{\ln(I_t/I_{full})}{\ln(I_{mt}/I_{full})} \quad (26)$$

and is independent of the cross section at the monitoring wavelength.

In performing actinometry experiments it is important to properly ascertain the incident intensity (I_0^i) directly behind the entrance window. It is usually assumed that the fraction of I_0^i transmitted by the sample is equal to the ratio I_t/I_0 , i.e., the transmitted

intensity full versus empty. However this is only true for optically thick samples. Light not absorbed in the first pass through the cell is partially reflected at the rear window, making an additional pass through the sample. An additional fraction of this is also absorbed and a fraction of the reflected light is re-reflected, and so on. Approximate correction factors for this effect are given in Calvert and Pitts,⁵⁶ and exact corrections calculated in this work, and presented in Appendix F. This derivation closely parallels previous calculations by Hunt,⁵⁷ Dignam,⁵⁸ and Ravies.⁵⁹ The results of this calculation show that

$$I_0^i = \frac{\left(\frac{T}{1-R(1-\alpha)} \right)}{\left(\frac{T^2(1-\alpha)}{1-(1-\alpha)^2 R^2} \right)} \quad (26)$$

where

T = each window transmission

R = each window reflection

α = sample absorption

I_t = measured transmitted intensity .

From empty cell measurements ($\alpha = 0$),

$$\frac{I_t}{I_0} = \frac{T^2}{(1-R^2)} \quad (27)$$

In these calculations, it is assumed that $T+R+A = 1$, and furthermore that no measurable absorption (or scattering) by the Suprasil-1 windows used occurred ($A = 0$).

It has been fairly well established⁶¹⁻⁶³ that the primary quantum yield for NO₂ below 3660 Å is ≥ 0.96 and probably 1.0. The results of flash photolysis actinometry experiments at 3000.0 Å and 3518.3 Å, for a total of 1000 laser shots, are given in Tables 3 and 4. The laser fluence was corrected for I_0^i and for the volume-to-length ratio of the cell, and the fraction photolysed plotted versus $(1-e^{-E\sigma})$ in Figure 8. NO₂ decay was monitored at 3900 Å, and both experiments produced straightline behavior which went through the origin. The half slope values show that:

$$E_{\text{laser}}^{3000 \text{ Å}} (\text{actual}) = 0.587 \cdot E_{\text{measured}}$$

$$E_{\text{laser}}^{3518 \text{ Å}} (\text{actual}) = 0.577 \cdot E_{\text{measured}}$$

which represents a 42% absolute error factor in the Gentec Joulemeter calibration. Subsequent correspondence with Gentec confirmed "an average +40% error in these units".

Since the NO₂ run at 3518.3 Å was the least optically thin sample photolysed ($\sim 6\%$ absorption), the data were subjected to further analysis. In the case where the NO₂ decay is pathlength dependent,

$$\frac{d[\text{NO}_2]}{dt} = -2\sigma I(\ell)_\lambda \Phi_\lambda [\text{NO}_2] \quad (27)$$

employing a Beer's Law dependence on pathlength for absorption of the photolysis radiation, allows this expression to be integrated with respect to both time and reaction pathlength to produce

$$\Phi_\lambda = \frac{\ln\{\frac{\exp(\sigma_\lambda [\text{NO}_2]_i) - 1}{\exp(\sigma_\lambda [\text{NO}_2]_f) - 1}\}}{2\sigma_\lambda E_0^i} \quad (28)$$

Table 3. NO₂ Actinometry--Bulk photolysis @ 3000.0 Å

$$[\text{NO}_2]/[\text{N}_2] = 0.563 \text{ torr}/47.28 \text{ torr total}$$

% Transmission @ 3900.0 Å	% Transmission Baseline	(c) E _{laser} (mJ/cm ²)	Fraction Photolysed (d)	(1-e ^{-Eσ})
85.49 ^(a)	100.01	0	0	0
76.82 ^(b)	100.01	0	0	0
77.07	100.02	109.5	.02101	.02478
77.17	100.01	162.5	.03092	.03646
77.30	100.02	233.1	.04414	.05204
77.39	100.02	310.5	.0538	.06348

(a) Empty cell.

(b) Full cell.

(c) (number shots × E_{total} × 1.2079)/8.266

(d) λ_{monitor} = 3900 Å
 Slope/2 = 0.589 ± 0.014
 Incpt = 0.00053 ± 0.00046
 R² = 0.9980

Table 4. NO₂ Actinometry--Bulk photolysis @ 3518.3 Å

[NO₂]/[N₂] = 0.419 torr/45.30 torr total (N₂)

—— % Transmission ——		(c) E _{laser} (total) mJ/cm ²	Fraction Photolysed (d)	$\left(1 - e^{-E\sigma_{\text{NO}_2}}\right)$	[NO ₂] × 10 ⁻¹⁶	$\text{LN} \left\{ \frac{(\exp(\sigma[\text{NO}_2]_i) - 1)}{(\exp(\sigma[\text{NO}_2]_f) - 1)} \right\}$
@ 4000 Å	Baseline					
84.48 ^{a)}	98.85	0	0	0	0	--
77.21 ^{b)}	98.85	0	0	0	1.350	0.0000
77.35	98.84	20.55	.02013	.01717	1.323	0.02042
77.52	98.85	45.36	.04453	.03751	1.290	0.04569
77.72	98.86	77.21	.07316	.06301	1.251	0.07617
77.90	98.85	105.19	.09887	.08485	1.216	0.1043
78.04	98.85	128.28	.1188	.1025	1.189	0.1272
84.48 ^{a)}	98.85	--	--	--	0	--

(a) Empty cell.

(b) Full cell.

(c) $\frac{\# \text{ shots} \times E_{\text{total}} \times 1.245}{8.266}$

(d) λ monitor = 3900 Å

$I_0^1/I_t = 1.245$

slope/2 = 0.577±.0032

INCPT = 0.00067±0.00041

R² = 0.99991

Slope/2σ = 0.587±0.0023

INCPT = 0.00030±0.00042

R² = 0.99992

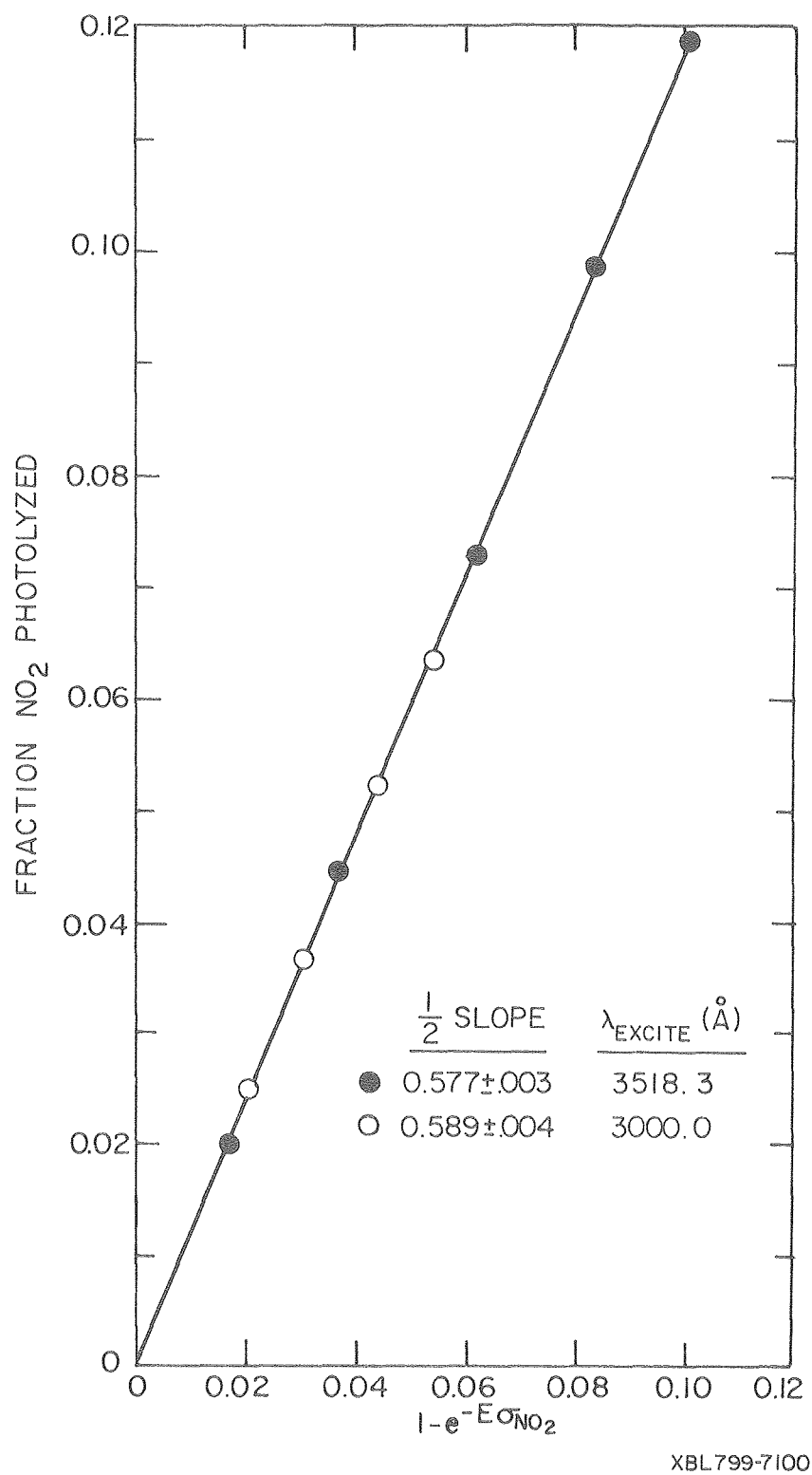
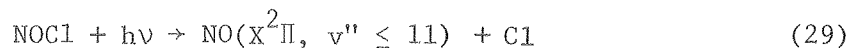


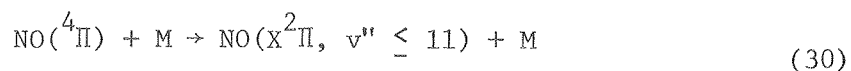
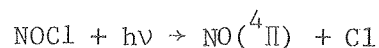
Figure 8. Actinometry results for NO_2 photolysis at 3518.3 and 3000.0 \AA .

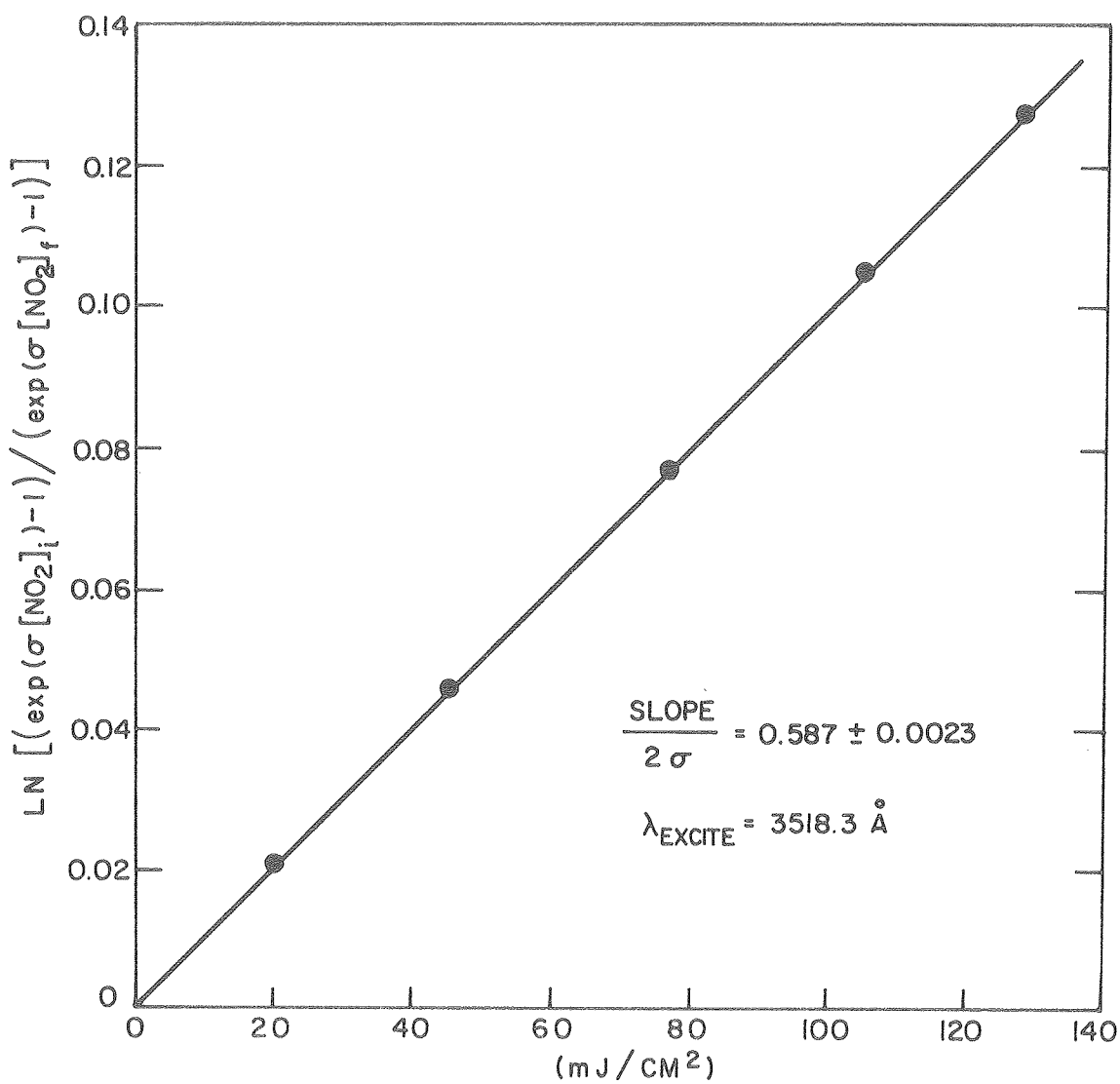
A plot of the numerator versus laser fluence now results in a slope equal to the photometer correction factor times 2σ . Treatment of the $\lambda = 3518.3 \text{ \AA}$ data in this way is given in Table 4 and plotted in Figure 9. The new correction factor of 0.587 is slightly higher than in Figure 8 and matches that at $\lambda = 3000.0 \text{ \AA}$. A similar calculation using the $\lambda 3000.0 \text{ \AA}$ data produced no change, since its absorption is a factor of 6 lower. While the correspondence of results is most likely fortuitous (i.e., the joulemeter surface coefficients of reflection are not equal at 3000.0 and 3518.3 \AA --see Appendix G), the calculation does demonstrate the applicability of the optically thin assumption in using Eq. (20).

NOCl is possibly the only viable gas-phase actinometer covering a wavelength region from 6400 \AA into the vacuum ultraviolet, displaying continuous absorption over most of that region. The photochemistry of NOCl was first investigated quantitatively by Kistiakowsky.⁶⁴ He determined the quantum yield of NOCl decomposition to be 2.0 over the range of 3650 to 6300 \AA , by following manometrically the course of the reaction. However, at 3650 \AA , a value of 2.7 was obtained and considered to be an experimental artifact. Basco and Norrish^{65,66} observed vibrationally excited nitric oxide (with $v'' \leq 11$) from NOCl photolysis either from the primary process at $\lambda \geq 2600 \text{ \AA}$



or through $\text{NO}(^4\Pi)$

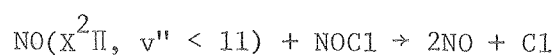




XBL799-7098

Figure 9. Actinometry results for NO_2 photolysis at 3518.3 \AA , for optically thick conditions.

Vibrationally excited NO was not found however when the flash was filtered through pyrex. These vibrationally excited NO molecules possess enough energy to further react with NOCl

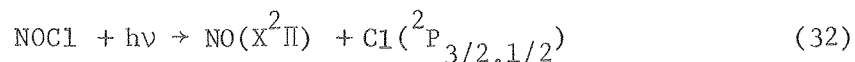


followed quickly by



hence increasing the maximum possible quantum yield to 4. Wayne⁶⁸ carried out NOCl photolysis at 2537 Å and found a mean quantum yield value of 1.96 ± 0.08 at various pressures of NOCl and buffer gas.

Nathanson⁶⁷ confirmed the quantum yield for NOCl disappearance to be 2.0 over the range of 4090–5460 Å and showed it to be independent of a 14-fold change in [NOCl] and a 50-fold excess of N₂ or CO₂. Re-evaluation of photolysis data and more accurate thermal data^{69,70} now favors⁵⁶ the primary dissociative process

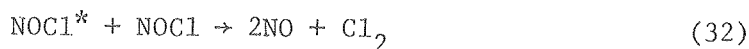
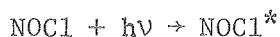


over the entire visible and ultraviolet region with a wavelength cutoff of $\lambda \leq 7600 \text{ Å}$.

Samples of NOCl were subjected to flash photolysis in a manner similar to the NO₂ experiments. To avoid complication from products an observation wavelength with a large cross section but in a region clear of NO or Cl₂ absorption was chosen. The loss of NOCl under 6000.0 Å photolysis was monitored at 4720.0 Å, and the UV-photolysis at 3518.3 and 3000.0 Å monitored at 2200 Å. Like NO₂, the final NOCl photodissociation products are stable with respect to recombination

with a calculated⁵⁴ rate (at the maximum fraction dissociated of 4×10^6 molecules/cm³·sec.

Photolysis at 6000.0 Å in both the small and large quartz cell displayed the expected behavior (Table 5 and Figure 10) and a half slope equal to 0.55, in good agreement with the ultraviolet NO₂ photolysis results, as expected for a spectrally flat pyroelectric transducer. However, analogous exposures at $\lambda = 3518.3$ Å resulted in a linear plot following an initial curvature in both cells, and photolysis at $\lambda = 3000.0$ Å resulted in a curved plot with a non-zero intercept. Both curves approached a half slope value of 0.85 at large total energy absorbed. (Tables 6 and 7, and Figures 11 and 12). This result in the ultraviolet is reminiscent of that observed by Kistiakowsky,⁶⁴ but which has not since been repeated in this wavelength range. It appears that the vibrationally excited nitric oxide mechanism is probably not operating due to the results of Basco⁶⁵ using Pyrex filtered light. However, a second mechanism involving collision induced dissociation is a possibility, analogous to that proposed by Connell¹⁷ to account for N₂O₅ photodissociation.



This behavior could be explainable equally well by a substantial NO₂ or Cl₂ impurity, but cross section measurements done in conjunction with these experiments rule this out. A detailed investigation of this result was not pursued further in light of the correspondence between NOCl photolysis in the red, NO₂ in the ultraviolet, and an approximate curve of surface coefficient of reflection versus wavelength of the

Table 5. NOCl Actinometry--Bulk photolysis @ 6000.0 Å

[NOCl] = 14.50 torr (large cell)

—— % Transmission ——		c) E _{laser} (J/cm ²)	Fraction Photolysed	1-e ^{-Eσ_{NOCl}}
@ 4720.0 Å	Baseline			
86.05 ^{a)}	100.02	0	0	0
76.30 ^{b)}	100.00	0	0	0
76.62	100.02	3.167	.03423	.03352
76.99	100.03	3.179	.07481	.06613
77.34	100.04	2.904	0.1124	.09487
77.68	100.05	2.965	0.1488	0.1233
78.04	100.05	3.237	0.1871	0.1533
86.08 ^{a)}	100.05	--	--	--

a) Empty cell.

b) Full cell.

c) (# shots × E total * 1.1704)/8.266

Volume/Length = 8.266

I₀ⁱ/I_t = 1.1704

Table 5 (continued) [NOC1] = 14.25 torr (small cell)

——% Transmission—— @ 4720.0 Å		^{d)} E _{laser} (J/cm ²)	Fraction Photolysed	1-e ^{-Eσ_{NOC1}}
Baseline				
85.84 ^a	101.66	0	0	0
74.95 ^b	101.68	0	0	0
74.95 ^b	101.65	0	0	0
76.43	101.65	14.14	0.157	.141
77.36	101.65	9.55	0.254	.225
78.03	101.65	7.28	0.323	.284
78.915	101.65	12.05	0.414	.371
79.53	101.65	9.85	0.476	.434
84.89 ^a	101.65	-	-	-

d) # shots × E total * 1.150/4.432

$$I_0^i/I_t = 1.150$$

Combined Data:

$$\text{Slope}/2 = 0.55 \pm 0.02$$

$$\text{INCPT} = 0.0036 \pm 0.0068$$

$$R^2 = 0.9987$$

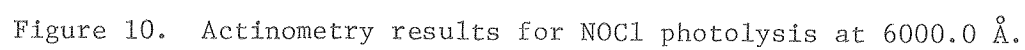


Table 6. NOCl Actinometry--Bulk Photolysis @ 3518.3 Å

[NOCl] = 387 m torr (large cell)

——% Transmission—— @ 2200 Å		c) E _{laser} (mJ/cm ²)	Fraction Photolysed	(1-e ^{-Eσ})
Baseline				
64.16 ^a	98.19	0	0	0
20.68 ^b	89.19	0	0	0
21.00	98.17	21.64	.0136	.0055
21.32	98.12	41.69	.0269	.0105
21.43	98.13	57.05	.0324	.0143
21.59	98.15	69.35	.0380	.0174
21.71	98.14	81.74	.0428	.0205
64.22 ^a	98.16	-	-	-

a) Empty cell.

b) Full cell.

c) (# shots × E total * 1.192)/8.266.

Table 6 (continued) [NOC1] = 318 m torr (small cell)

——% Transmission—— @ 2200 Å		d) E _{laser} (mJ/cm ²)	Fraction Photolysed	(1-e ^{-Eσ})
	Baseline			
46.85	99.65	0	0	0
46.85	99.70	0	0	0
18.46	99.68	0	0	0
18.90	99.68	38.91	.0259	.0100
19.16	99.67	74.04	.0405	.0189
19.38	99.67	102.90	.0528	.0260
19.71	99.67	146.20	.0709	.0367
19.98	99.65	179.66	.0855	.0449

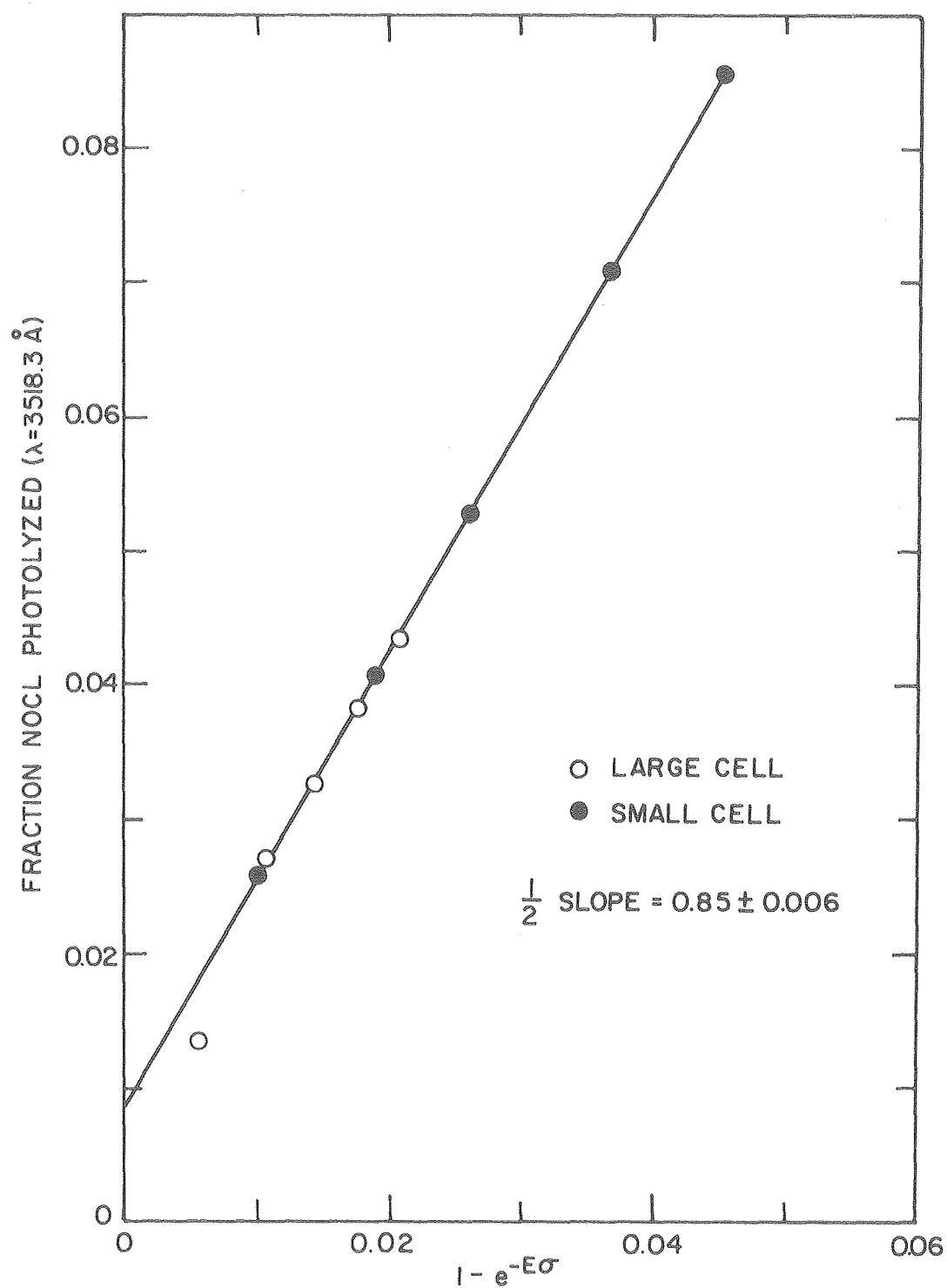
d) # shots × E total × 1.287/4.432.

Combined Results (excluding first point — see graph):

$$\text{Slope}/2 = 0.854 \pm 0.006$$

$$\text{INCPT} = 0.0084 \pm 0.003$$

$$R^2 = 0.9996$$



XBL 799-7096

Figure 11. Actinometry results for NOCl photolysis at 3518.3 Å.

Table 7. NOCl Actinometry--Bulk Photolysis @ 3000 Å
 [NOCl] = 459 m torr

— % Transmission —		$E_{\text{laser}}^{c)}$ (mJ/cm ²)	Fraction Photolysed	$1 - e^{-E\sigma}$
@ 2200 Å	Baseline			
65.62 ^{a)}	100.02	0	0	0
16.28 ^{b)}	100.02	0	0	0
16.60	100.02	42.28	.0141	.00647
16.72	100.04	77.57	.0191	.01187
16.90	100.05	124.33	.0268	.01884
17.15	100.03	167.58	.0373	.02531
17.40	100.03	207.58	.0478	.03126

a) Empty cell

b) Full cell

c) (# shots × E_{total} × 1.190)/8.266

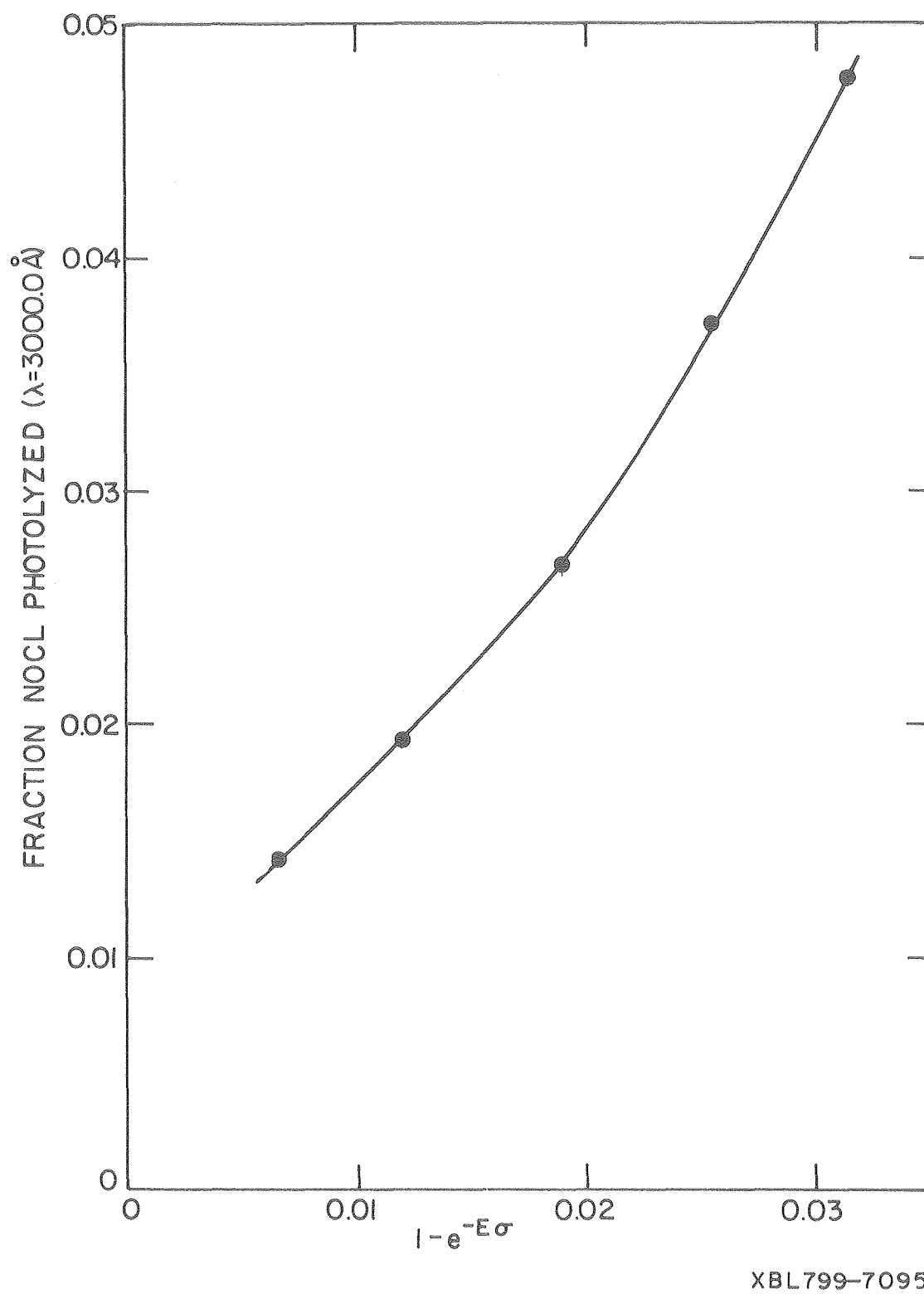


Figure 12. Actinometry results for NOCl at 3000.0 \AA .

Joulemeter transducer (supplied by Gentec-Appendix G) indicating reasonable spectral linearity.

C. Calibration of NO and NO₂ Detection Systems

The spectral output of the NO discharge consists of strong γ band emission ($A\Sigma^{2+} - X^2\Pi$) in the 2260 Å region and a less intense $\epsilon(D^2\Sigma^+ - X^2\Pi)$ system at higher energies (~ 1960 Å). Weaker emission from mainly predissociated levels of the $\beta(B^2\Pi - X^2\Pi)$ and $(C^2\Pi - X^2\Pi)$ are also observed but not useful for spectroscopic detection of NO. Both γ and ϵ system emission was investigated as possible excitation bands for nitric oxide detection, and the γ bands chosen due to resulting higher achieved sensitivity.

The unfiltered lamp output (at ~ 2 Å resolution) of the γ emission system is shown in Figure 13. It consists of strong emission terminating in the $X^2\Pi$, $v''=0$ level. Due to nested potential wells, emission from A_0^0 , A_1^1 and A_2^2 nearly coincide as do A_0^1 , A_1^2 , etc. Hot band emission lies to the low energy side of the A_0^0 band, and contributes to the scattered background radiation. Transmission through the $\lambda = 2150$ Å interference filter used to select resonance emission from the A_0^0 and A_0^1 lines is also shown.

The nitric oxide emission spectrum excited by the 1900-2300 Å γ system is shown in Figure 14, showing strong fluorescence from A_0^0 and A_0^1 , which was isolated and utilized to detect NO in this study. Attempts to utilize emission from non-resonant transitions at longer wavelengths ($\lambda > 2300$ Å) substantially reduced scattered background radiation but resulted in overall lower sensitivity. The excitation spectrum from dispersed resonance lamp radiation is shown in Figure 15. Detectivity

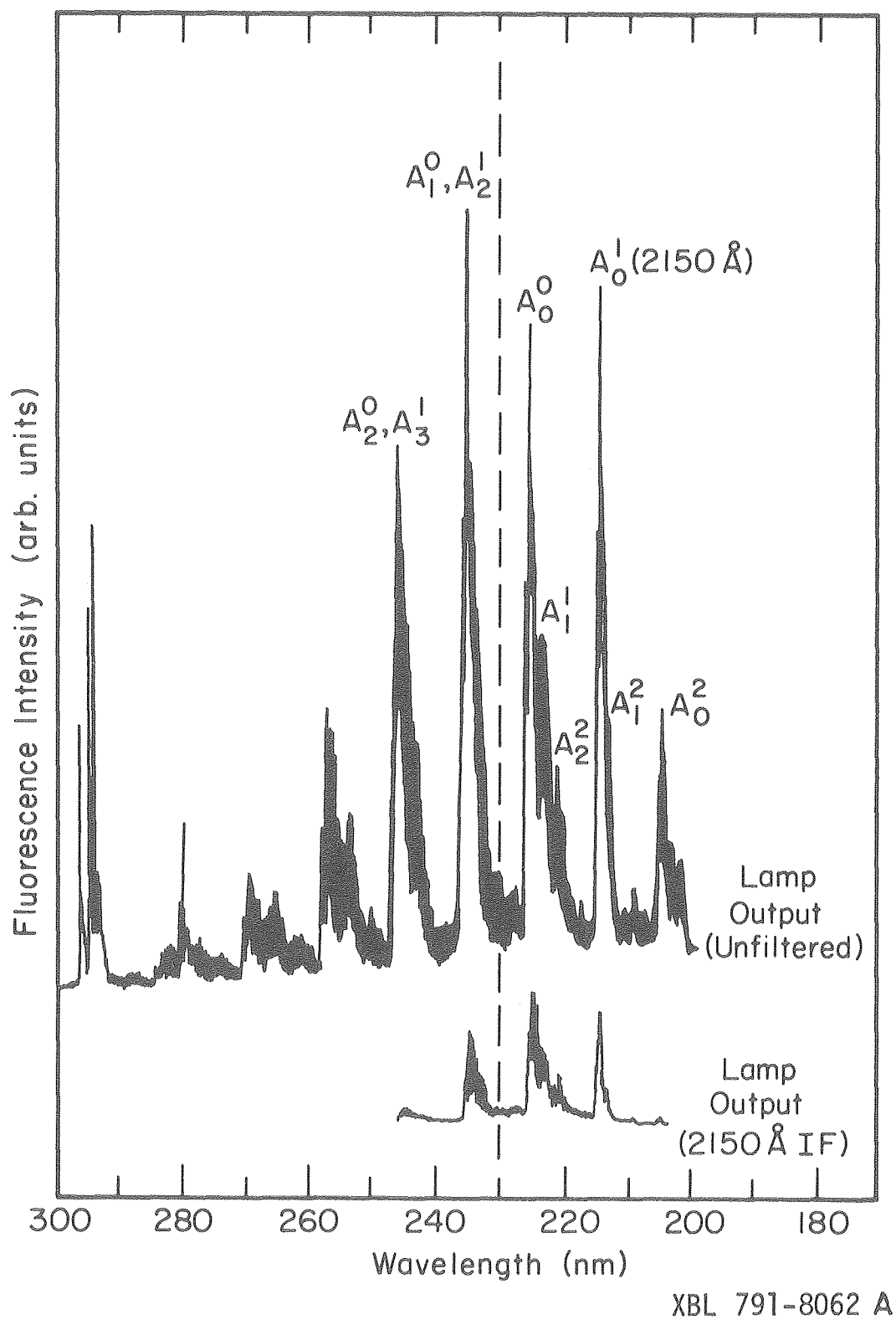


Figure 13. Spectrum of NO resonance lamp.

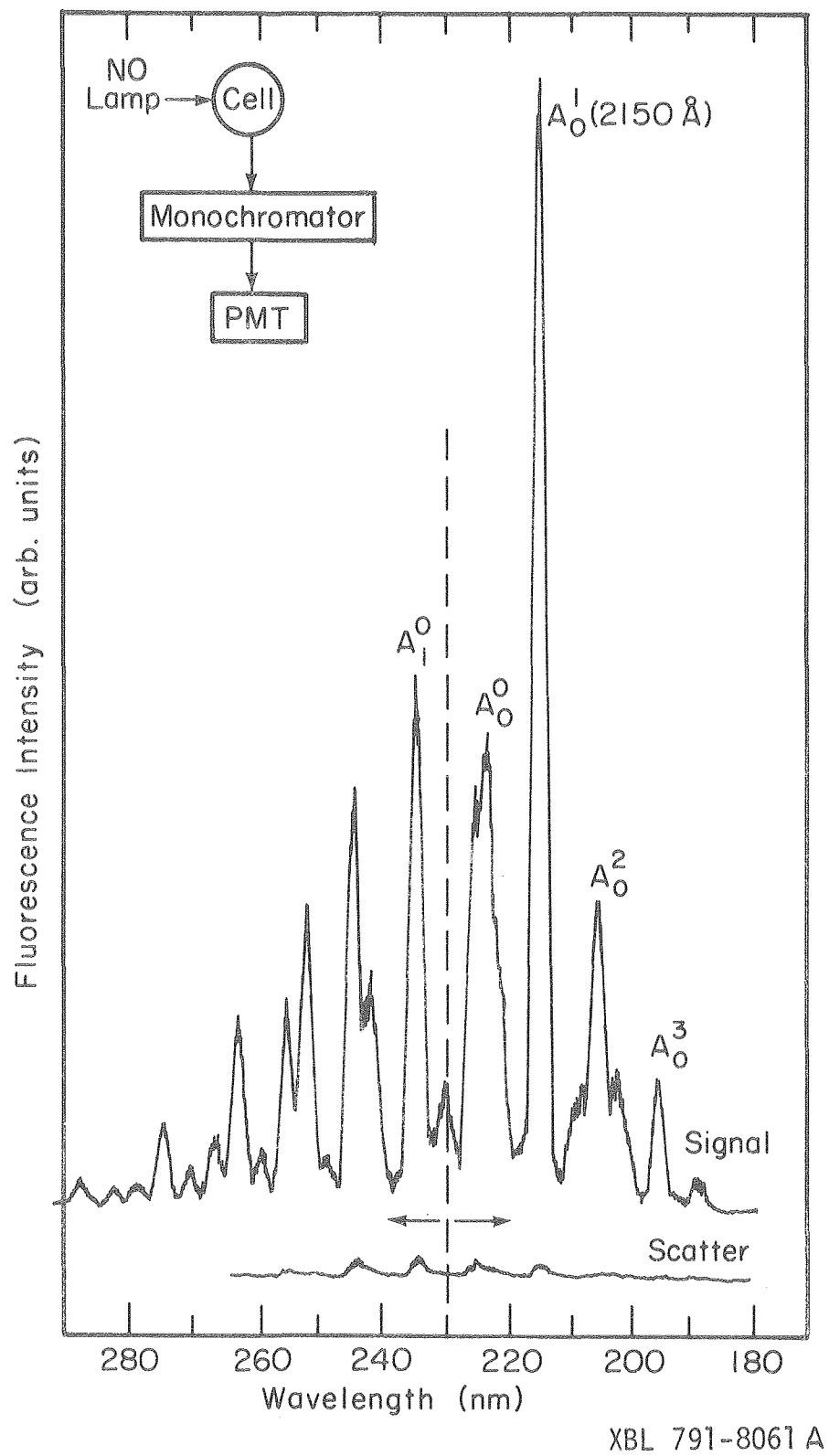
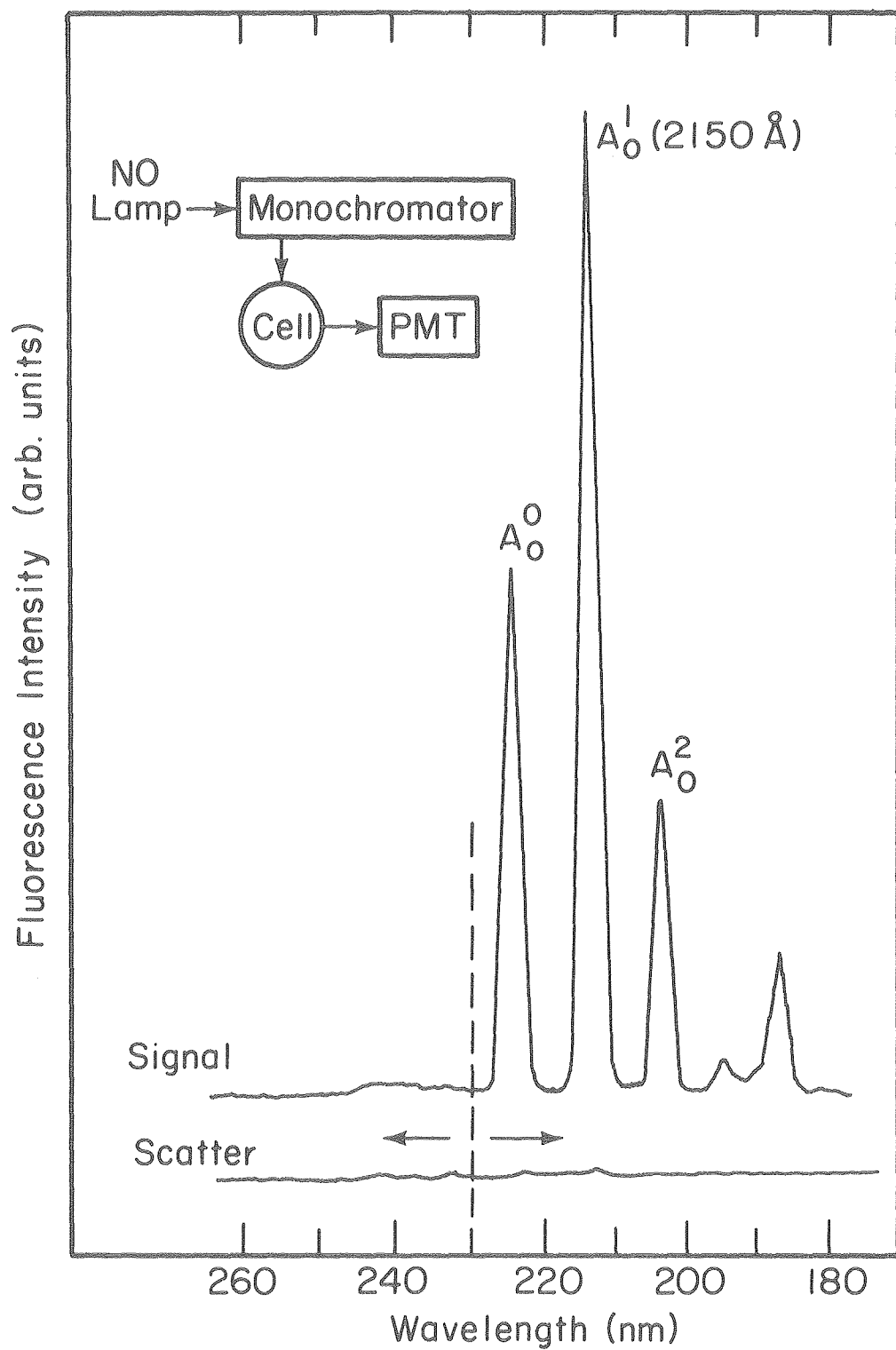


Figure 14. Emission spectrum of NO excited by the 1900-2300 Å γ system.



XBL 791-8064 A

Figure 15. Excitation spectrum of NO excited by dispersed resonance lamp.

limits, from configurations in which the 2150 Å interference filter was placed either at the lamp or the photomultiplier, were virtually identical. The majority of NO experiments were performed with a filtered photomultiplier tube, which served a dual function in blocking scattered ultraviolet laser radiation during NO₂ photolysis calibration runs.

Bulk calibration and demonstration of linearity was performed over the concentration region encountered during NO₃ photolysis experiments. Samples of purified NO were diluted with N₂ in three liter bulbs, and subsequently flowed through the photolysis cell at 10 torr total pressure. The signal count rate was observed for five 10-second gated intervals. Similarly, 50 seconds of background counts were measured and subtracted, to produce the calibration plot shown in Figure 16 (Table 8). Linear behavior is expected from consideration of the fluorescence quenching efficiency and should continue (in the absence of N₂O₅) out to $\sim 10^{14}$ molecules/cm³, due to the low absorption cross sections and lack of substantial self-reversal and radiation trapping. This is in contrast to atomic systems which typically exhibit larger cross sections ($\sim 10^{-14}$ cm²) and become nonlinear above $\sim 2 \times 10^{12}$ particles·cm⁻³. The fluorescence intensity is given by

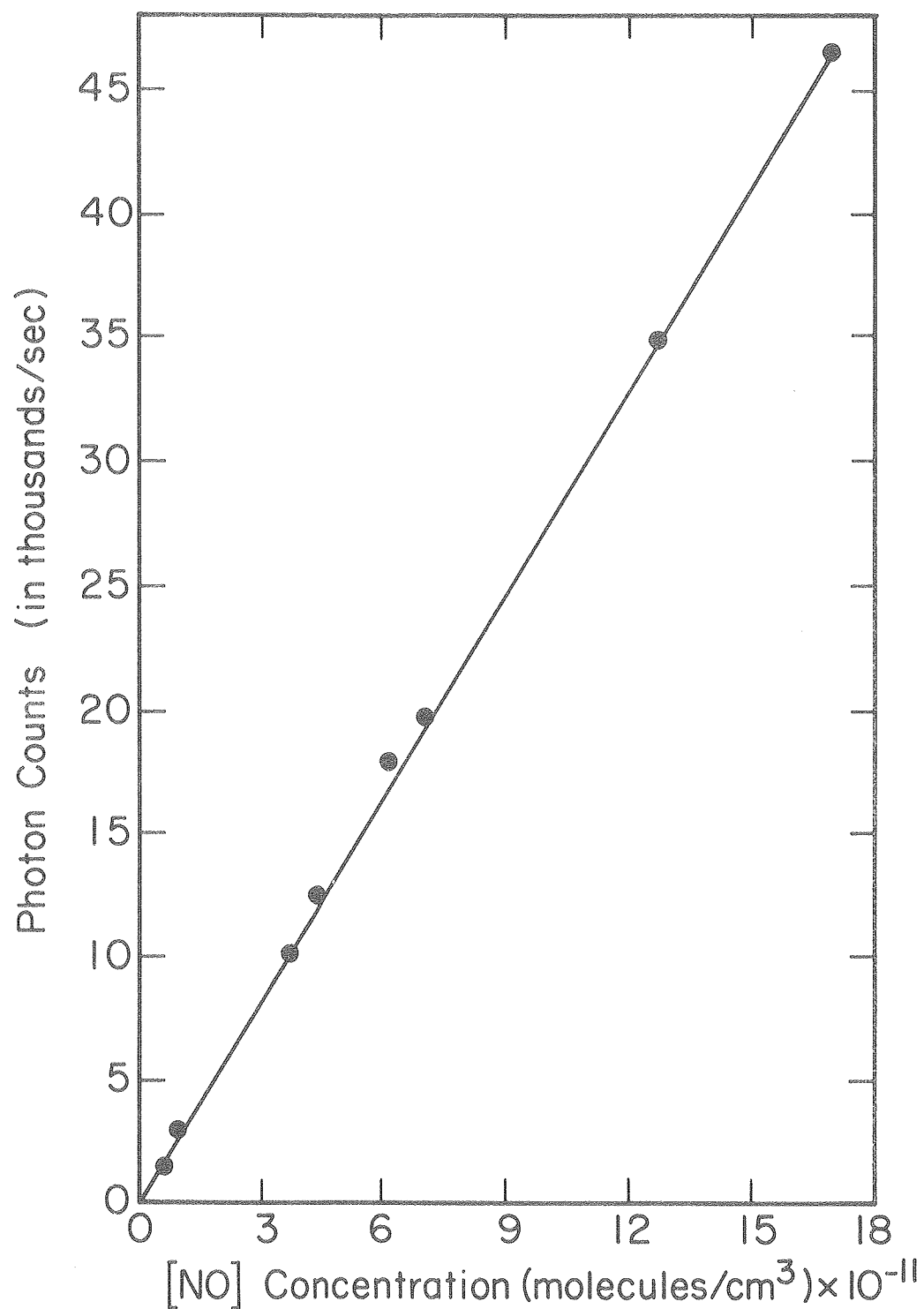
$$I_f = I_a \phi_f \approx I_0 \sigma_{NO} [NO] \phi_f \quad (34)$$

where

$$\phi_f = \left(1 + \frac{k_q}{k_f} [N_2] + \frac{k_q}{k_f} [NO] + \frac{k_q}{k_f} [NO_2] + \frac{k_q}{k_f} [M] \right)^{-1} \quad (35)$$

Table 8. NO Detector Calibration

Corrected Count Rate (Hz) $\times 10^{-3}$	[NO] Concentration (molecules \cdot cm $^{-3}$) $\times 10^{-1}$
1.45	0.583
3.03	0.927
10.0	3.72
12.4	4.46
17.9	6.22
19.6	7.09
34.9	12.7
46.5	17.0



XBL 791-8060A

Figure 16. Plot of NO detector calibration.

Assuming maximum gas kinetic quenching of excited NO by $M = N_2O_5$, suitable quenching values for N_2 , NO_2 , and NO,^{71,28,30} and typically encountered concentrations:

$$\phi_f = (1 + .0071 + .00012 + .0043 + .0323)^{-1} = 0.96 \quad (36)$$

For Poisson statistics, the signal to noise ratio is given by⁷²

$$S/N = \frac{R_S \sqrt{\Delta t_{OBS}}}{\sqrt{R_S + 2R_B}} \quad (37)$$

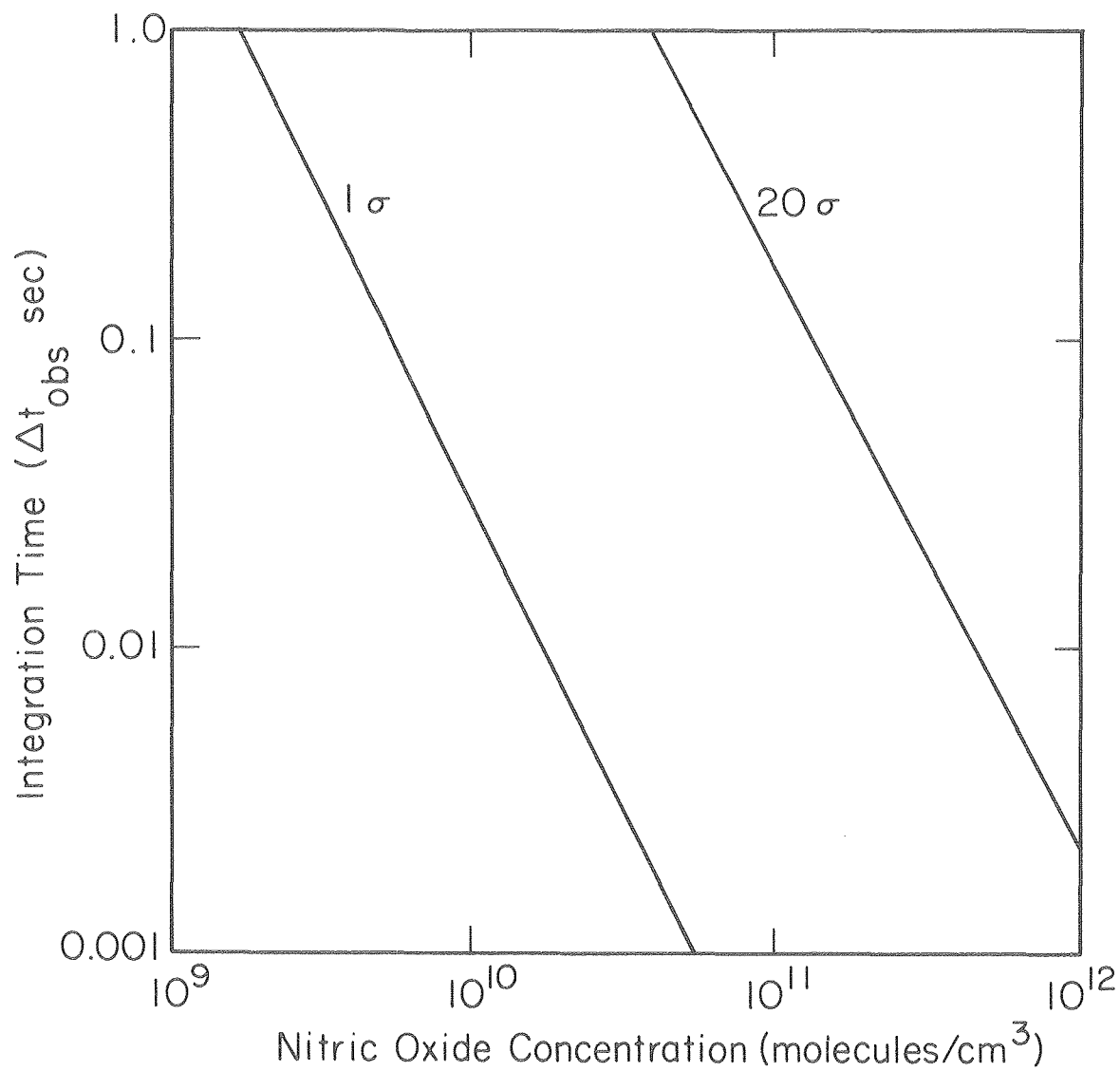
and the standard deviation (σ_S) by:

$$\sigma_S = \left(\frac{R_S + R_B}{\Delta t_{OBS}} \right)^{1/2} \quad (38)$$

where R_S = signal count rate

R_B = background count rate .

From the observed signal levels, expected detector sensitivities can be calculated at various levels of uncertainty. A plot of detector sensitivity (obtained at 50 second integration times) versus integration time is shown in Figure 17 in which 1σ and 20σ contours (10% error at 95% confidence) are plotted. The detectivity level for NO at 1000 seconds integration time is shown to be $\sim 10^8$ molecules/cm³; however, the apparent usable integration times during a flash photolysis experiment are quite short (< 2 ms), requiring multiple flashes to achieve the desirable counting statistics, at the NO concentration levels produced. At 50 seconds integration times, the standard deviation of the calibration sensitivity was < 0.3%, at concentrations



XBL 791-8058 A

Figure 17. NO detector sensitivity.

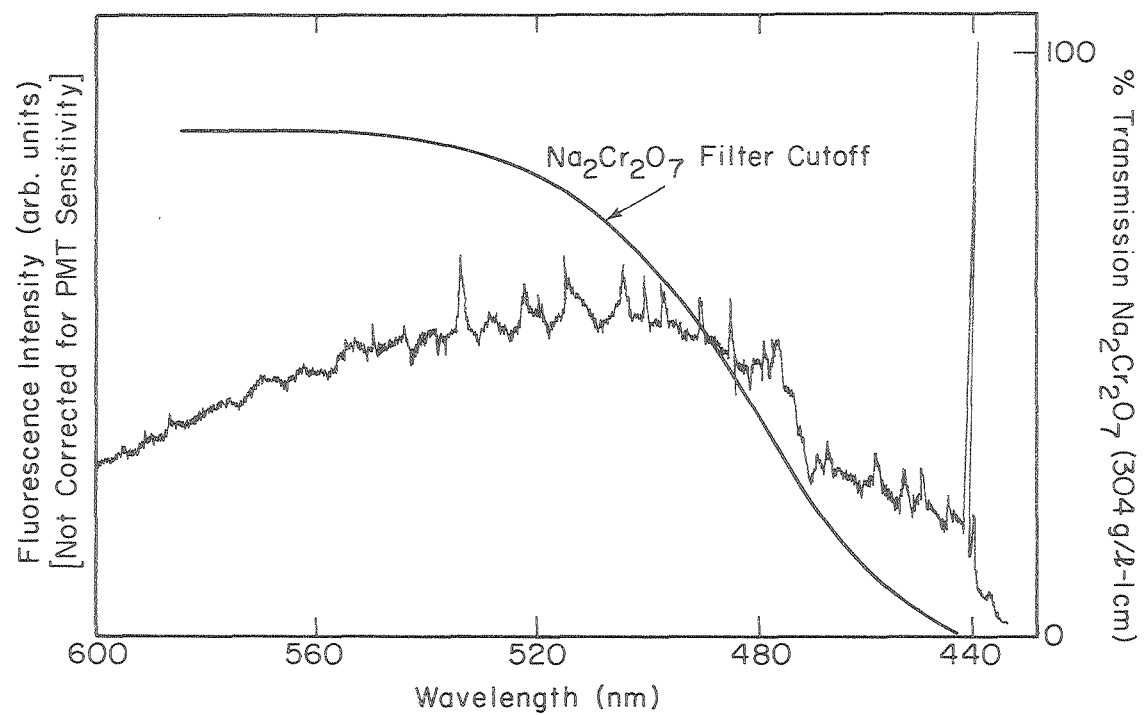
of 3.7×10^{13} molecules cm^{-3} .

Having demonstrated linearity over the experimentally determined concentration region, single point "bulk" calibrations using 103 ppm and/or 1030 ppm gas mixtures were performed at 10 torr total N_2 pressure before and after each experiment to establish relative lamp sensitivity. Actual system calibration for both NO and oxygen atoms was performed using laser flash photolysis of NO_2 , which established the response under identical experimental conditions of collection geometry and cell constituent concentrations. The long-term* variation of the nitric oxide detection system with time is shown in Table 9. The very slow decrease in sensitivity was possibly due to F centering, nitration, or physical contamination of the optical components. The short term stability was excellent, and the drift was below the detection limit at 10 seconds of integration time.

The NO_2 emission spectrum excited by helium cadmium laser radiation at 4416 Å (Figure 18) consists of small vibrational features, on top of a broad continuum which persists into the near infrared. The percent transmission of the $\text{Na}_2\text{Cr}_2\text{O}_7$ liquid filter used to block scattered laser radiation is also shown. The RCA 31034A gallium arsenide photomultiplier tube used was sensitive across the entire visible region, out to $\sim 8900 \text{ Å}$.

Demonstration of linearity is shown in Figure 19 and Table 10, in which corrected signal count rate is plotted versus NO_2 concentration at 10 torr total pressure of N_2 . In a similar fashion to the NO calibration procedure, purified NO_2 samples were expanded into 3 liter bulbs and diluted with nitrogen. Signal count rates were accumulated for 5, 10-second gate intervals from which 50 seconds

*i.e., during the course of the study

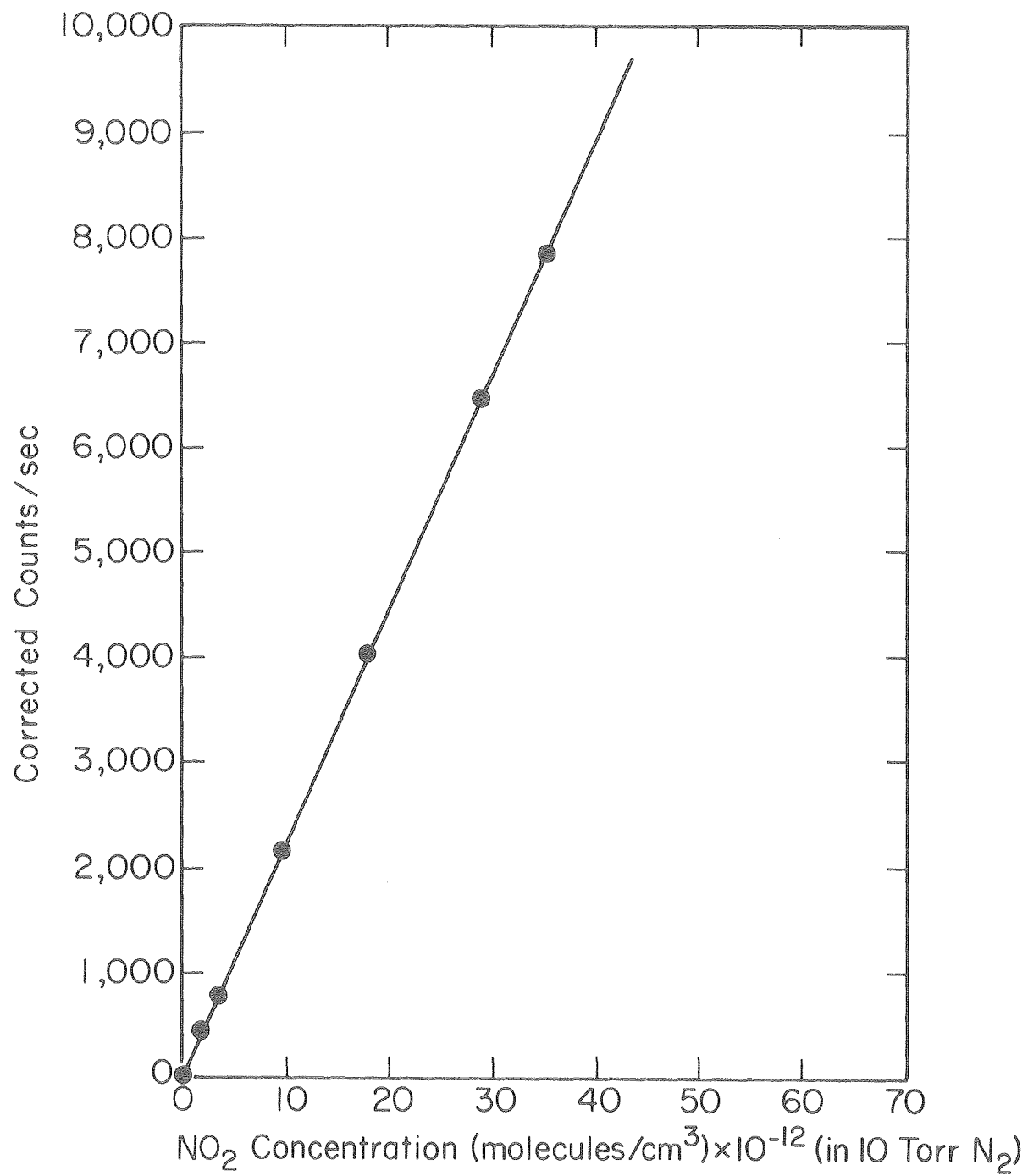


XBL 791-8059A

Figure 18. NO₂ fluorescence spectrum as excited by He•Cd radiation (at 4416 Å).

Table 9. Long Term Nitric Oxide Resonance Fluorescence Sensitivity⁻¹

Run Number	Sensitivity ⁻¹ $\left(\frac{\text{molecules} \cdot \text{cm}^{-3}}{\text{counts/sec} \times 10^{-7}} \right)$
22	4.13
21	4.30
20	4.11
19	4.01
18	4.02
17	3.97
16	3.98
15	3.90
14	4.00
13	3.91
12	3.78
11	3.76
9	3.50
8	3.54
7	3.50
12 (CH ₄ buffer)	4.62
10 (CH ₄ buffer)	4.62



XBL 791-8056A

Figure 19. NO₂ fluorescence detector signal versus concentration.

of background (10 torr N_2) were subtracted. The quenching behavior of NO_2 was predominated by the nitrogen buffer gas ($k_q(N_2) = 2 \times 10^{-11}$ molecules $^{-1} \cdot cm^3 \cdot sec^{-1}$) under the experimental conditions used, and signal was demonstrated to be substantially independent of pressure (at fixed mole fraction). Calculation of the fluorescence efficiency

$$\phi_f = k_R \left(k_R + k_{N_2}(N_2) + k_{NO_2}(NO_2) + k_{N_2O_5}(N_2O_5) \right)^{-1} \quad (39)$$

Again assuming a gas kinetic quenching rate for N_2O_5 and typically encountered concentrations,

$$\phi_f = (1 + 600 + 0.15 + 1.1)^{-1} = 1.7 \times 10^{-3} \quad (40)$$

Linearity in signal with increasing NO_2 concentration is expected to extend to $\sim 3 \times 10^{15}$ (1% deviation) and indeed a sample of 3.83×10^{15} NO_2/N_2 (at 10 torr) demonstrated linear behavior as shown below:

Table 11. Measured $[NO_2]$ Concentration.

Nominal Concentration	Measured		Count Rate
	Fraction	Molecules/cm ³	Percent NO_2
1.08%	1.19%	3.83×10^{15}	5.76×10^5
100 ppm	1.15 ppm	3.70×10^{13}	5.78×10^5

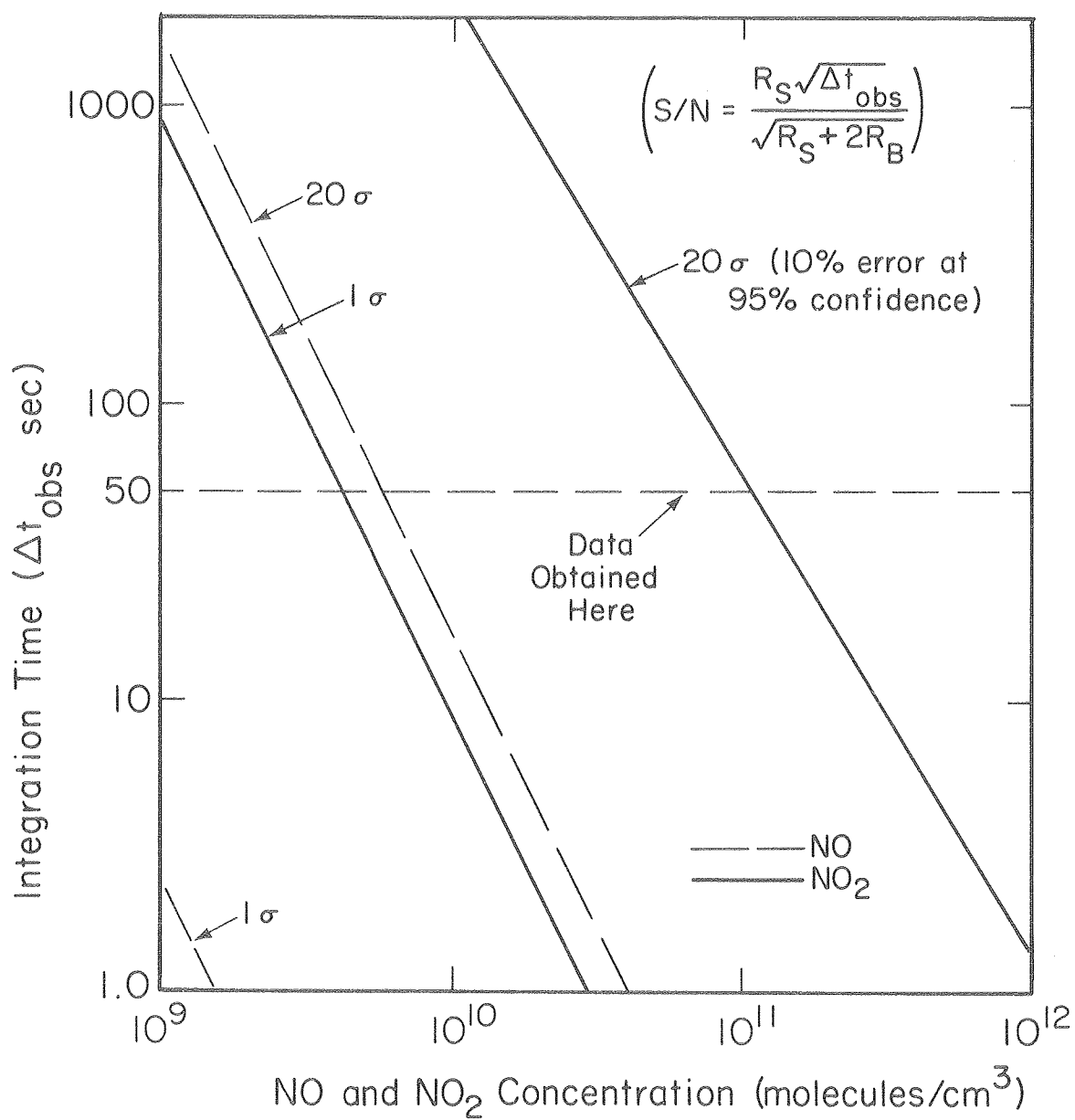
Long term variation in sensitivity was shown to be due to decay of the laser tube output intensity. Short term (~ 12 hours) stability was better than 0.5% after a 2-hour warm-up period of the entire system. The signal count rate standard deviation at 3.7×10^{13} particles/cm³ was typically $\leq 0.2\%$, at 10 second integration times.

A plot of integration time versus NO_2 concentration is shown in Figure 20, along with 1 σ and 20 σ contours. Analogous sensitivity of NO is also shown at integration times of 1-100 seconds for comparison. Absolute detectivity of NO_2 is shown to be $\sim 10^9$ molecules/cm³ at 1000 sec integration time, a factor of 10 lower than for the NO detection system.

A comparison of theoretically calculated detection limits for NO, O, and NO_2 with measured detectivities is shown in Table 12. Assuming a signal to noise ratio of 1 and an equivalent noise input of 5×10^{-18} watts, signal levels were calculated considering an f/2 collection efficiency, typical pmt quantum yields, fluorescence efficiency, lamp factors, and sample concentration, the details of which parallel a treatment given by Schofield.²⁴ The measured detectivity of each system developed for this study meets or exceeds that calculated. The oxygen atom detectivity level is usually limited by lamp photolysis of oxygen containing species, in this case N_2O_5 . The measured sensitivity of the NO lamp system is considerably better than that calculated with a cadmium ion lamp of similar source intensity.

D. Quantum Yield Determinations

A typical quantum yield experiment entailed stabilization of infrared spectrometer, resonance fluorescence lamp, photomultiplier tubes and electronics, helium cadmium laser, and NO_2 detection electronics, usually overnight, prior to a run. A small portion of N_2O_5 was then transferred to the two-way saturator at 248K, and a flow of dried N_2 started and allowed to come to (concentration) equilibrium.



XBL 791-8057A

Figure 20. NO + NO₂ detector sensitivity.

Table 12. Measured vs. calculated detection limits.

	NO*	O	NO ₂
Source Intensity	1×10^{14}	1×10^{14}	1×10^{16}
Source Wavelength	2144 Å	1302 Å	4416 Å
σ (cm ²)	$\sim 10^{-17}$	3.6×10^{-13}	5.4×10^{-19}
Fractional Overlap (source @ 700°K)	$\sim 2\%$	$\sim 50\%$?
ϕ_f (Fluorescent Efficiency)	0.96	0.77	1.7×10^{-3}
D.C. Detection Limit (f/2 optics)	$5 \times 10^{10} \text{ cm}^{-3*}$	$1.4 \times 10^7 \text{ cm}^{-3}$	$5 \times 10^9 \text{ cm}^{-3}$
Measured Detectivity (D.C.)	1.7×10^9 ** @ (1 sec)	$\leq 5 \times 10^{10}$ *** @ (1 sec)	$9 \times 10^8 \text{ cm}^{-3}$ @ 1000 sec
Measured Dark Count (Scattered Light)	3300 CPS	Not Limiting	80 CPS
One count/sec =	$3 \times 10^7 \text{ cm}^{-3}$	$2 \times 10^3 \text{ cm}^{-3}$	$3 \times 10^9 \text{ cm}^{-3}$

* Using Cd⁺ Lamp and 262 nm \pm 10 Detection Band** Using NO Lamp and 215 \pm 10 nm Detection Band (1 CPS = $3 \times 10^7 \text{ cm}^{-3}$)*** With N₂O₅ Background Photolysis Limit (Max)Calculated @ S/N = 1; Noise = 5×10^{-18} Watts (ENI)

$$S = \underbrace{\frac{\Omega_f f \theta}{4\pi}}_{\text{detector factor}} * \underbrace{\frac{k_f}{k_f + k_d + k_Q[Q] + \dots}}_{\text{fluorescence efficiency}} * \underbrace{I_s a_s \Omega_s}_{\text{source factor}} * \underbrace{\sigma N \ell}_{\text{absorption}}$$

Fresh laser dye was charged into the circulator reservoir and flowed through the lamp, to allow thermal equilibration with the flowing triax water. The absolute wavelength calibration of the OMA was checked with either neon or mercury lamps. The laser wavelength was selected using the OMA for each run, due to a large non-reproducibility in the laser grating micrometer drive. Prior to laser firing, O or NO background, and NO₂ signal count rates were recorded along with cell temperature and % N₂O₅ transmission (which was measured continuously). The gated voltage to frequency converter was reset and the laser firing sequence begun. After sufficient signal to noise has been achieved, the same parameters were remeasured after the firing sequence has terminated. Wavelengths were run in random order thereafter, throughout the gain profile of the particular dye chosen, covering each NO₃ peak and valley (peaks from Ramsay,⁴ valleys from Graham¹⁰, Table 13). Absolute calibrations were determined by switching dyes and frequency doubling 7036.6 Å radiation to photolyse a small fraction of the NO₂ present in the N₂O₅ flow.

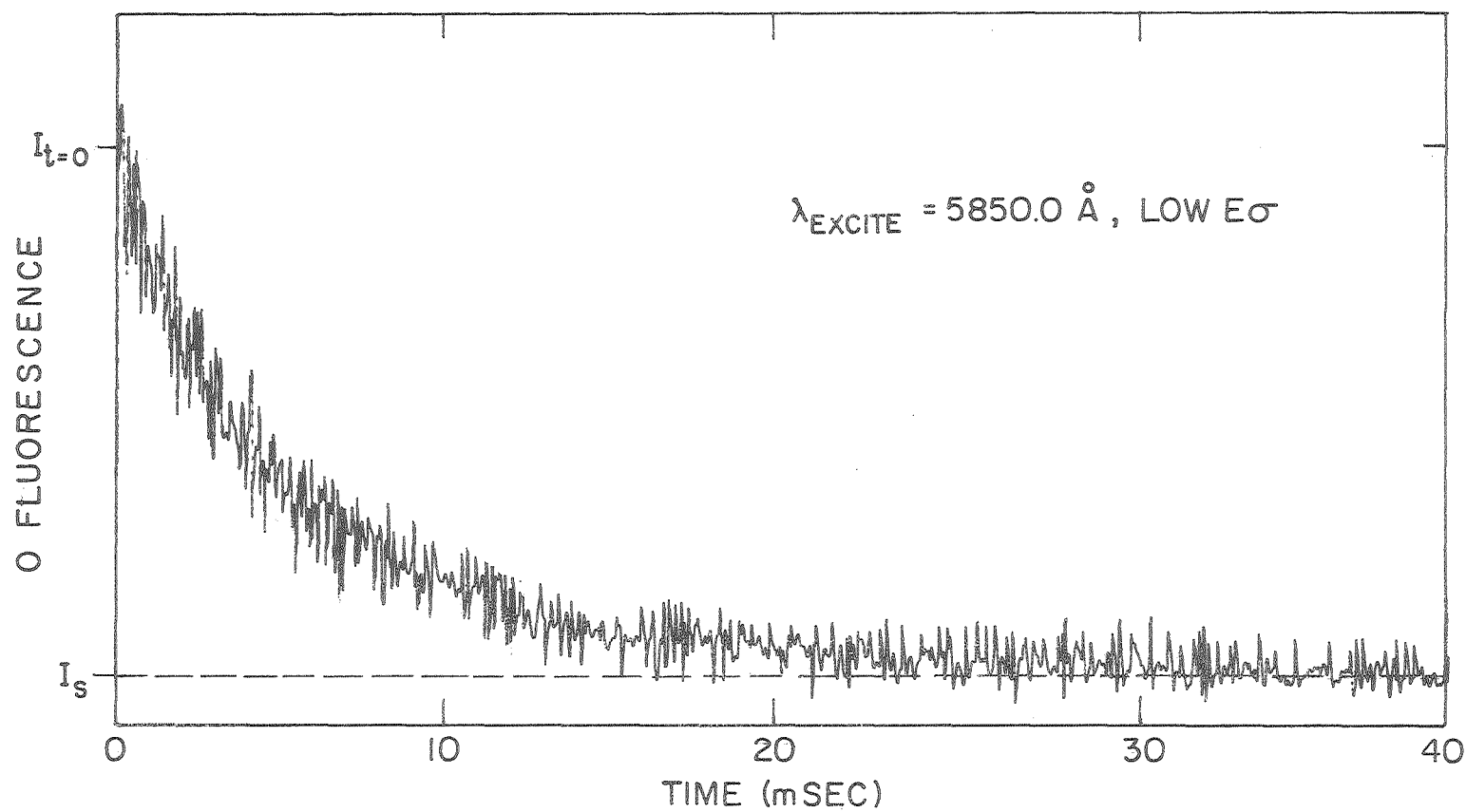
Typical oxygen atom decay curves at $\lambda = 5850.0 \text{ Å}$ (maximum quantum yield) are shown in the low E σ (Figure 21) and high E σ (Figure 22) regimes, which indicates the maximum signal to noise ratios encountered. Decay constants and intercepts were obtained with an exponential least square fit over two or three half-lives with resulting standard deviations of 3-5% for intercepts and 5-10% for slopes.

1. Oxygen Atom Calibration

The ratio of oxygen atoms produced from NO₂ and NO₃ was found to vary with resonance lamp intensity, which indicated that either photolysis from the lamp was occurring or a local temperature gradient

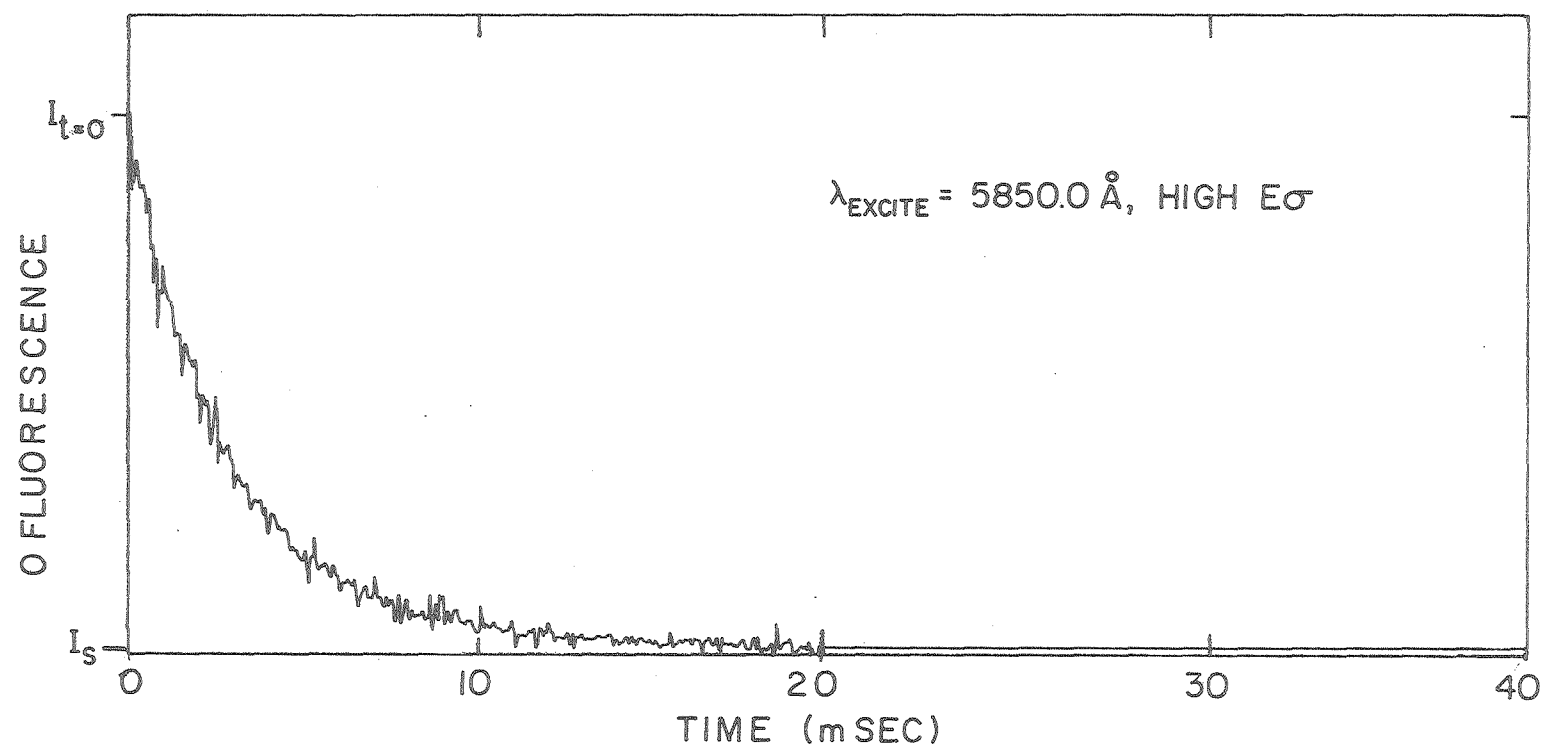
Table 13. NO_3 Absorption Peaks (Ramsay⁴)

	cm^{-1}	\AA	\AA
	(vac)	(vac)	air
Strong			
ν_1 Progression:	15089	6627.3	6625.5
	16039	6234.8	6233.1
	16965	5894.5	5892.9
	17886	5591.0	5589.5
Weaker			
	16537	6047.0	6045.3
	16776	5960.9	5959.3
	17197	5815.0	5813.4
	17329	5770.7	5769.1
	17375	5655.4	5753.8
	17576	5689.6	5688.0
	17668	5660.0	5658.4
	18261	5476.2	5474.7
	18638	5365.4	5363.9
	18903	5290.2	5288.7
	19164	5218.1	5216.7



XBL 799-7106

Figure 21. Typical O fluorescence signal decay vs. time at 5850.0 Å and low $E\sigma$ regime.



XBL799-7105

Figure 22. Typical O fluorescence signal delay vs. time at 5850 Å and high $E\sigma$ regime.

was present, causing fluctuations in the NO_2 and NO_3 concentrations. The difference in NO_2 concentration between having the lamp off and on with N_2O_5 flowing varied from 7-10%; whereas the oxygen atom "background" signal increased only slightly ($\sim 0.2\%$) when N_2O_5 was added to the nitrogen flow. The maximum increase in NO_2 observed with the lamp on represents $\leq 0.1\%$ loss of N_2O_5 . This and previous work¹⁷ indicate that the major photolytic channel for N_2O_5 destruction results in $2\text{NO}_2 + \text{O}$. Flowing NO_2 alone had virtually no effect in increasing the oxygen background signal, and no change in NO_2 fluorescence signal was evident with the lamp on or off. The alternate explanation to N_2O_5 photolysis could indicate that the lamp was producing a local thermal gradient which affects the N_2O_5 equilibrium concentrations and hence the normalized signal ratios. In order to determine the role of lamp intensity on signal ratios, an experiment was performed in which the signal ratio was determined in the limit of zero lamp intensity.

The normalized signal is defined as a relative quantum yield for each species:

$$\text{N.S.} = \frac{[\text{O}]_{\text{NO}_2}}{[\text{NO}_2](1-e^{-E\sigma})\left(\frac{\text{dwell time}}{\text{channel}}\right)(\# \text{ shots})} \quad (41)$$

The ratio of normalized signals at the lamp intensity used throughout the study is shown in Table 14. The ratio of normalized signals as a function of lamp intensity is given in Table 15 and plotted in Figure 23. In order to determine the limiting slope at zero lamp intensity, the oxygen signal from NO_3 is plotted vs. that from NO_2 , and the curve fit to a quadratic expression (Figure 24). Setting the

Table 14. NO_2/NO_3 Oxygen Atom Signal Ratio Calibration

$$\lambda_{\text{laser}}(\text{NO}_2) = 3518.3 \text{ \AA}$$

$$\lambda_{\text{laser}}(\text{NO}_3) = 5850.0 \text{ \AA}$$

$$[\text{NO}_2]_{\text{ave}} \sim 3 \times 10^{13} \text{ molecules} \cdot \text{cm}^{-3}$$

Normalized [O] signal from (in molecules cm^{-3}):			
Run #	[NO_2]	[NO_3]	Ratio
			$\frac{\text{NO}_2 \text{ N.S.}}{\text{NO}_3 \text{ N.S.}}$
28:	11.98	28.66	0.418
32:	19.37	46.15	
	18.40	50.07	
	18.65	41.57	
		<u>48.82</u>	
(Average)	18.81	45.65	<u>0.412</u>
0.413 \pm 0.037 Wt. Average			

Table 15. Oxygen Atom Signal from NO_2 and NO_3 vs. Lamp Intensity

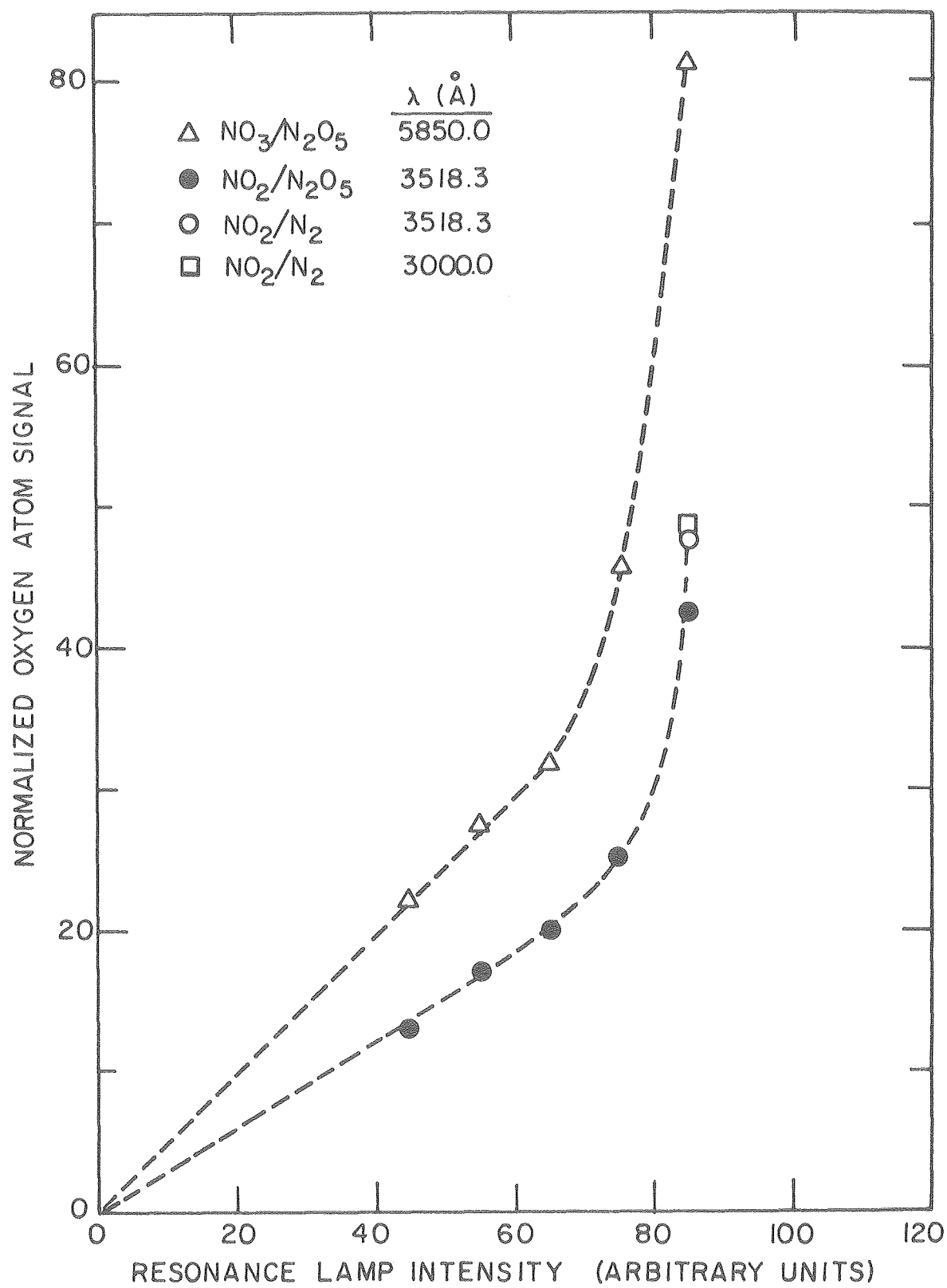
$$\frac{[\text{NO}_2]_{\text{ave}}}{[\text{N}_2]} = \frac{1.4 \times 10^{14} \text{ molecules} \cdot \text{cm}}{3.22 \times 10^{17} \text{ molecules} \cdot \text{cm}^{-3}}$$

Lamp Intensity (Arbitrary Units)	Normalized Oxygen Signal From	
	NO_2 (in N_2O_5) @ $\lambda = 3518.3 \text{ \AA}$	NO_3 (in N_2O_5) @ $\lambda = 5850.0 \text{ \AA}$
45	13.05	22.40
55	17.11	27.21
65	20.09	31.93
75	25.16	45.51
85	42.64	81.22
85	47.63 ^{a)}	
84	48.36 ^{b)}	

Notes: Pure $[\text{NO}_2]/[\text{N}_2] = 3.71 \times 10^{13}/3.22 \times 10^{17}$

a) 3518.3 \AA

b) 2925.0 \AA



XBL 799-7087

Figure 23. Plot of O fluorescence signal intensity vs. lamp intensity.

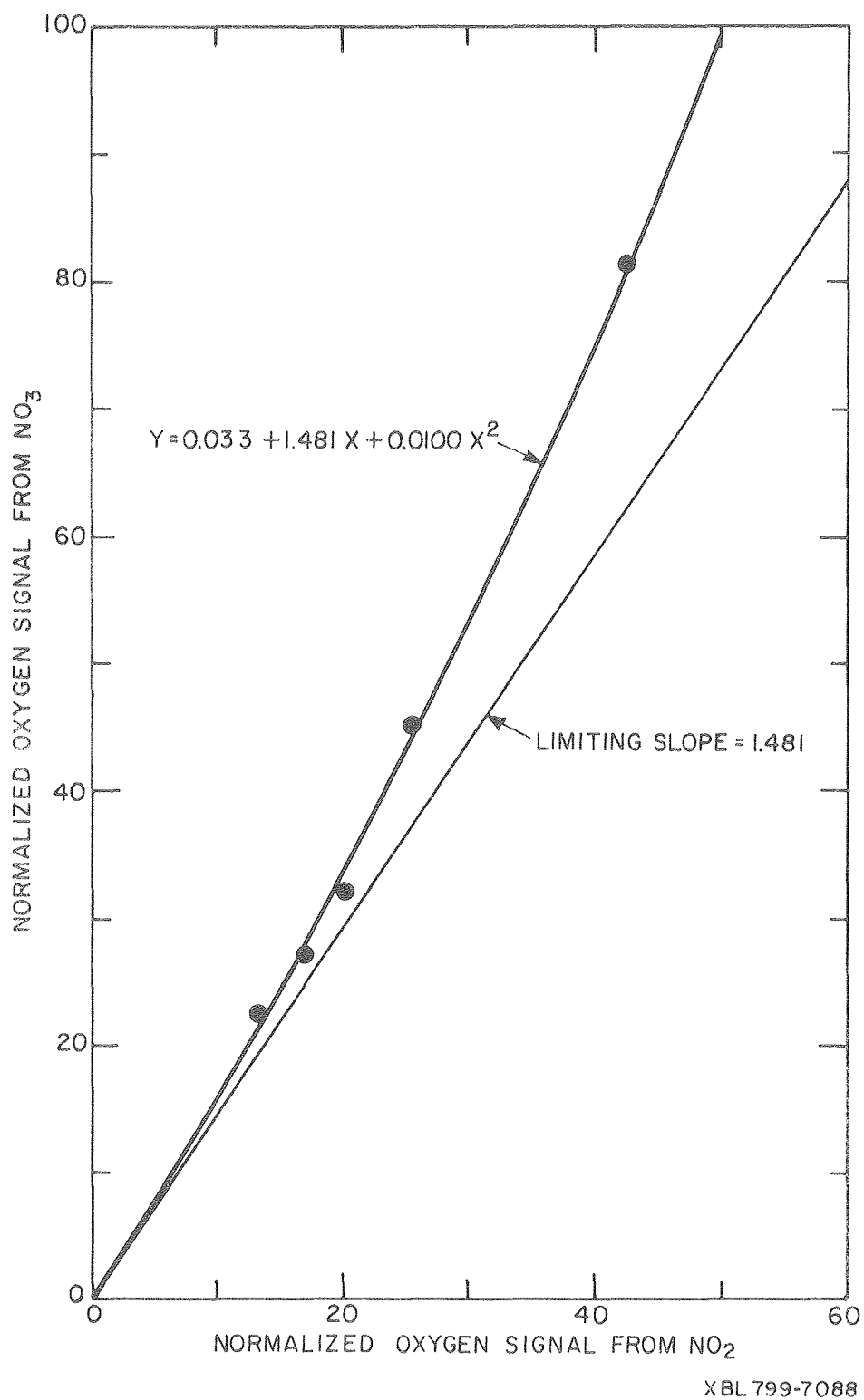


Figure 24. Determination of limiting normalized signal at zero lamp intensity.

first derivative to zero, results in the value of the limiting slope, at zero lamp intensity

$$\text{Limit } (I_{\text{lamp}} \rightarrow 0) \left[\frac{\left(\frac{[O]_{\text{NO}_2}}{[\text{NO}_2]_0 (1 - e^{-E\sigma})} \right)}{\left(\frac{[O]_{\text{NO}_3}}{[\text{NO}_3]_0 (1 - e^{-E\sigma})} \right)} \right] = 0.676 \quad (42)$$

This limiting value was used to correct the $[\text{NO}_3]$ concentrations determined at the standard lamp intensity. Due to the large activation energy of the N_2O_5 equilibrium constant,¹⁰ this correction amounts to an apparent temperature of 0.96°C higher than that measured by the temperature transducer attached to the photolysis cell. This correction procedure is valid, regardless of the actual mechanism which is operating.

In Figure 23, two data points using pure NO_2/N_2 are slightly higher than that from NO_2 in a N_2O_5 flow, due to a small absorption and/or quenching of resonance fluorescence by the cell constituents. In this same figure, it is seen that oxygen atom production in the lamp increases dramatically at higher microwave powers. Unfortunately this increased signal level could not be utilized because of the accompanying excess noise pickup by the infrared spectrometer due to microwave leakage from the cavity.

Since the normalized signals are in fact measures of relative quantum yield, it is immediately apparent that, even in the limit of zero lamp intensity, the absolute oxygen atom quantum yield from NO_3 calculated at 5850.0 Å is considerably greater than one. Having

measured corrected values of laser fluence, NO_2 concentration, and cross section, this could only result from an inaccurate value of the NO_3 cross section. To further investigate this, an experiment was performed in which oxygen signal was measured as a function of laser fluence at both 5850.0 and 5893.0 Å (Table 16). A plot of $\log\left(1 - \frac{[O]}{\phi_0[\text{NO}_3]}\right)$ versus laser fluence results in a slope equal to the NO_3 cross section. However, since the absolute quantum yield is also unknown, such a plot must be iteratively fit by a nonlinear least square procedure for both quantum yield and cross section.

The solution to the best fit parameters was a "u"-shaped function, which converged more quickly the further from the well the parameters were. However, approach to the actual best fit was achieved slowly and the paucity of data did not allow an extremely precise set of parameters to be determined. The best fit equations through points obtained at 5850.0 Å and 5892.9 Å are shown in Figures 25 and 26. At 5850 Å fixing the best fit cross section at $3.60 \times 10^{-18} \text{ cm}^2/\text{molecule}$ resulted in an absolute quantum yield value of 0.99 ± 0.05 . At 5892.9 Å, a best fit cross section of $8.18 \times 10^{-18} \text{ cm}^2/\text{molecule}$ was obtained with a quantum yield of 0.715 ± 0.08 . A line with a slope representing the cross section value obtained by Graham⁹ at 1 atmosphere pressure is also shown in each case. The ratios of cross sections at 5850.0 Å and 5893.0 Å are

$\lambda(\text{Å})$	$\frac{\sigma(\text{this work})}{\sigma(\text{Graham})}$
5850.0	1.46
5892.9	1.47

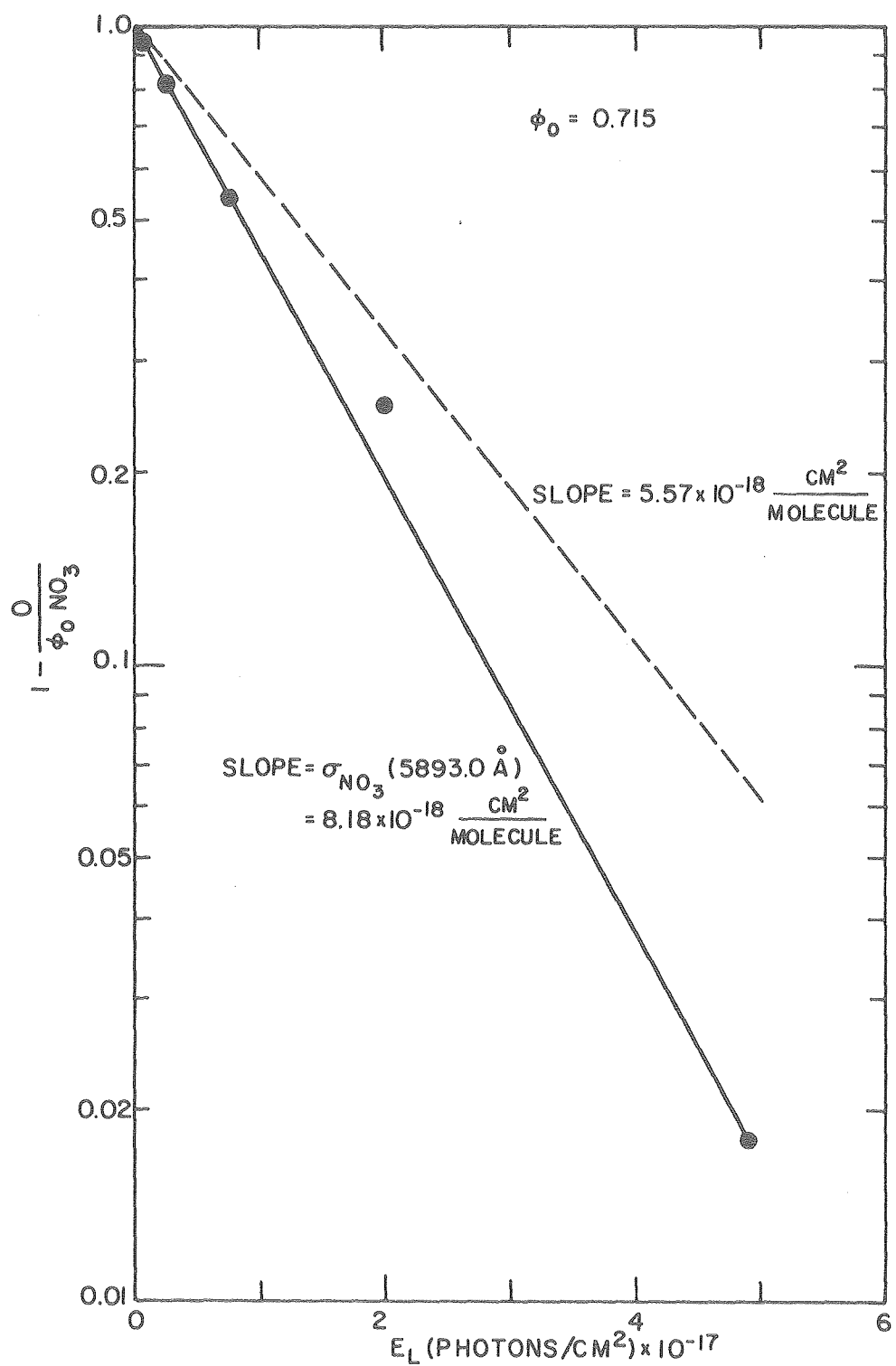
Table 16. [O] signal and $\left(1 - \frac{[O]}{[NO_3] \cdot \phi_0}\right)$ vs. laser fluence.

	$[NO_3]$ (molecules \cdot cm $^{-2}$)	$[O]^*$	Laser Fluence (Photons \cdot cm $^{-2}$)	$1 - \frac{[O]}{[NO_3] \cdot \phi_0}$
	$\times 10^{-12}$	$\times 10^{-10}$	$\times 10^{-16}$	
$\lambda = 5850.0 \text{ \AA}$				
	1.95	173	60.5	0.113
	1.91	115	25.5	0.396
	1.91	63.4	12.8	0.667
	1.92	21.9	2.97	0.886
	1.84	9.36	1.38	0.949
	2.03	2.32	0.421	0.985
	1.98	12.2	2.54	0.912
	1.98	6.04	1.21	0.960
	1.97	21.7	4.18	0.858
	1.98	97.2	27.9	0.366
	1.98	9.77	1.95	0.934
$\lambda = 5892.9 \text{ \AA}$				
	1.93	136	49.1	0.018
	1.92	103	40.1	0.253
	1.89	62.9	7.25	0.536
	1.92	25.7	2.65	0.813
	1.96	7.74	0.692	0.945
<hr/>				
$\lambda = 5850.0 \text{ \AA}$	$\sigma = 3.60 \times 10^{-18}$,		INCPT = 1.033,	$R^2 = 0.9993$
$\lambda = 5892.9 \text{ \AA}$	$\sigma = 8.18 \times 10^{-18}$,		INCPT = 0.996,	$R^2 = 0.99992$

*[O] from $NO_2 + 2h\nu$ is negligible (see Section III-F).



Figure 25. Plot $\text{Log} \left(1 - \frac{[\text{O}]}{\phi_{\text{O}} \cdot [\text{NO}_3]} \right)$ versus laser fluence at $\lambda_{\text{excite}} = 5850.0 \text{ \AA}$.



XBL799-7085

Figure 26. Plot of $\log \left(1 - \frac{[O]}{\phi_0 [NO_3]} \right)$ versus laser fluence at $\lambda_{excite} = 5892.9 \text{ \AA}$.

Also, the relative quantum yield at 5893.0 to 5850.0 Å determined in this experiment (0.72) matched that for the average ratio determined at low E_0 values, in subsequent experiments. Assuming a fast excited state dissociative channel, along with results from NO determinations (see Section IID.4) which indicate a total quantum yield of 1.02 and 1.03 at 5850.0 and 5893.0 Å, eliminated the possibility of interference from either 2-photon or saturation effects.

2. Oxygen Atom Quantum Yield Measurements

Determinations of absolute oxygen atom quantum yield were performed from 4700 to 6800 Å, in the low (Table 17) and moderate (Table 18) E_0 regime. Day to day reproducibility was typically better than 5% and the average of multiple determinations (Table 31) at each wavelength was used to construct the graphic representation shown in Figure 27 which consists entirely of data in the low E_0 limit. Overall estimation of uncertainty in quantum yield was ± 0.05 . The observed maximum in oxygen atom production occurs at 5850 Å and falls off rapidly at lower energies and more slowly at higher energies. The thermodynamic wavelength cutoff for production of $O + NO_2$ was calculated by Graham⁹ to be 5800 ± 30 Å in good agreement with the observed behavior.

Additional experiments were performed to investigate the behavior of NO_3 to varying levels of laser fluence. Data accumulated at 4 wavelengths consists of measurements of [O] atom intercept and quantum yield versus fluence and is shown in Table 19. At both 5850.0 and 5892.9 Å the oxygen atom signal rises linearly with fluence, then begins to roll off as the high energy limit is approached (Figures 28 and 29). This is precisely the behavior predicted by Equation (20),

Table 17. Oxygen Atom Quantum Yield versus Wavelength
Low ($E \times \sigma_{\text{NO}_3}$) regime: 0.79 cm^2 aperture.

λ_{laser} (Angstroms)	$[\text{N}_2\text{O}_5]$ $\times 10^{-15}$	$[\text{NO}_2]$ $\times 10^{-13}$	$[\text{NO}_3]$ $\times 10^{-12}$	$[\text{O}]$ $\times 10^{-10}$	Average Laser Fluence (Photons $\cdot \text{cm}^{-2}$) $\times 10^{-16}$	$\left(\frac{-E\sigma_{\text{NO}_3}}{1-e} \right)$	ϕ_{O}
	Units of molecules $\cdot \text{cm}^{-3}$						
6170.0	0.555	1.95	1.58	4.55	3.91	0.0911	0.316
5850.0	0.671	1.96	1.96	19.1	2.97	0.101	0.965
5850.0	0.646	1.96	1.88	9.39	1.38	0.0484	1.03
5892.9	0.628	1.91	1.86	24.0	2.65	0.194	0.665
5892.9	0.625	1.87	1.90	7.49	0.692	0.0550	0.718
5813.0	0.611	1.86	1.86	13.3	1.89	0.0845	0.846
5700.0	0.594	1.87	1.80	14.5	2.42	0.0857	0.941
5500.0	0.587	1.89	1.77	5.36	1.39	0.0445	0.680
5600.0	0.587	1.90	1.75	11.14	1.87	0.0848	0.749
5658.4	0.587	1.87	1.79	10.33	1.94	0.0707	0.819
6233.1	0.568	2.01	1.55	0*	0*	0.00*	0.076*
6233.1	0.568	2.01	1.55	1.51	0.682	0.113	0.0865
6270.0	0.541	1.86	1.60	1.48	0.982	0.0944	0.0979
5892.9	0.906	2.33	2.18	13.95	1.25	0.0959	0.667
6005.0	0.912	2.37	2.13	8.30	1.95	0.0669	0.582
5850.0	0.906	2.35	2.09	13.35	1.84	0.0640	1.00
6045.3	0.895	2.33	2.05	7.95	1.72	0.0976	0.396
5959.3	0.802	2.23	1.86	10.40	1.79	0.103	0.542

(continued. . .)

Table 17 continued.

5813.0	0.840	2.29	1.93	12.07	1.65	0.0746	0.839
5850.0	1.26	8.40	0.874	5.94	1.97	0.0686	0.992
5892.9	1.27	8.38	0.878	8.07	1.55	0.118	0.799
6005.0	1.29	8.44	0.867	3.48	1.90	0.0659	0.608
5959.3	1.30	8.81	0.839	5.48	1.77	0.102	0.641
6045.3	1.30	9.12	0.811	4.14	1.79	0.107	0.477
6095.0	1.31	8.99	0.823	.842	1.65	0.0318	0.322
5850.0	1.26	8.83	0.811	5.44	1.91	0.0665	1.01
5813.0	1.25	8.56	0.825	8.04	1.97	0.0881	1.05
5300.0	.473	1.16	2.26	6.16	1.28	0.0383	0.712
5100.0	.451	1.10	2.28	4.19	1.35	0.0253	0.728
4900.0	.442	1.07	2.29	4.09	1.95	0.262	0.681
5216.7	.433	1.10	2.18	5.83	1.57	0.0383	0.698
530010	.428	1.12	2.12	5.80	1.30	0.0391	0.700
4800.0	.424	1.07	2.20	2.58	1.65	0.0154	0.763
5100.0	.418	1.04	2.32	4.55	1.43	0.0268	0.732
4700.0	.414	1.03	2.40	2.29	1.75	0.0125	0.765
5288.7	.406	1.13	2.10	13.3	2.66	0.0784	0.805
5300.0	.397	1.07	2.10	7.32	1.66	0.0495	0.704
5000.0	.389	1.03	2.10	4.96	1.93	0.0273	0.866
5100.0	.378	1.02	2.05	5.89	1.80	0.0337	0.852
4800.0	.370	1.00	2.05	2.95	1.89	0.0176	0.819
6600.0	.358	.975	1.99	0*	0.00*	0.0*	0.00*
5589.5	.608	1.29	2.70	20.1	1.89	0.0907	0.764

(continued. . .)

Table 17 continued

5500.0	.423	1.17	2.09	9.62	1.87	0.0594	0.777
5300.0	.351	.990	2.01	8.03	1.82	0.0573	0.698
5400.0	.351	1.01	1.96	6.00	1.54	0.0400	0.767
5700.0	.351	1.02	1.94	6.70	0.990	0.0425	0.812
5589.5	.343	1.05	1.79	11.8	1.56	0.0752	0.880
5474.7	.338	1.05	1.83	13.5	2.20	0.0848	0.865
5688.0	.336	1.04	1.86	5.29	0.786	0.0278	0.953
5658.4	.328	1.02	1.83	15.7	2.48	0.0894	0.957
5959.3	.313	0.996	1.83	4.23	0.684	0.0407	0.567
5850.0	.310	0.982	1.83	2.69	0.421	0.0151	0.972
6095.0	.297	0.978	1.77	4.52	2.64	0.0505	0.507
6045.3	.291	0.968	1.75	11.8	2.64	0.146	0.459
6135.0	.289	0.968	1.72	4.16	2.37	0.0738	0.327
6250.0	.289	0.956	1.74	2.24	0.671	0.0814	0.159
6250.0	.289	0.941	1.77	4.03	2.55	0.276	0.195
6200.0	.289	0.941	1.77	4.17	2.64	0.0909	0.356
5813.0	.287	0.944	1.77	3.16	2.38	0.105	0.930
5893.0	.288	0.973	1.79	1.55	9.982	0.0768	0.735
6005.0	.288	1.02	1.77	2.35	1.49	0.0520	0.634
5850.0	.289	1.05	1.71	3.08	1.95	0.0680	1.05
5850.0	.301	0.978	1.79	7.16	1.21	0.0428	0.937
5850.0	.301	0.978	1.79	25.8	4.20	0.140	1.03

*Extrapolated to $E_L \rightarrow 0$ (see Figure 32).

Table 18. Oxygen Atom Quantum Yield versus Wavelength (moderate ($E \times \sigma_{\text{NO}_3}$) regime).

λ_{laser} (Angstroms)	$[\text{N}_2\text{O}_5]$	$[\text{NO}_2]^{**}$	$[\text{NO}_3]$	$[\text{O}]^*$	E(cell) (photons·cm ²) ×10 ⁻¹⁶	$\left(\frac{-E\sigma_{\text{NO}_3}}{1-e} \right)$	Φ_0
	Units of molecules·cm ⁻³						
	×10 ⁻¹⁵	×10 ⁻¹³	×10 ⁻¹²	×10 ⁻¹⁰			
4700.0	0.719	3.55	1.06	14.6	13.4	0.150	0.916
4800.0	0.719	3.50	1.08	31.8	19.8	0.267	1.10
4900.0	0.719	3.63	1.04	9.80	6.32	0.135	0.698
5000.0	0.719	3.55	1.06	36.0	20.4	0.390	0.871
5100.0	0.719	3.77	0.962	33.9	20.0	0.473	0.754
5200.0	0.718	3.53	1.07	36.9	13.5	0.381	0.909
5300.0	0.719	3.55	1.06	48.2	12.5	0.475	0.955
5450.0	0.708	3.42	1.09	47.7	14.3	0.434	1.01
5600.0	0.713	3.51	1.07	43.5	8.32	0.481	0.847
5850.0	0.701	3.36	1.09	102.5	45.5	0.937	1.00
6233.1	0.634	2.01	1.72	5.97	2.22	0.324	0.107
6233.1	0.616	2.01	1.67	18.6	6.87	0.702	0.158
6233.1	0.592	2.02	1.61	26.7	12.4	0.887	0.187
6600.0	0.356	0.952	2.07	20.2	27.7	0.874	0.112
6600.0	0.357	0.968	2.04	8.99	12.9	0.620	0.0712
6600.0	0.358	0.982	2.02	3.67	7.25	0.419	0.0433
6790.0	0.364	1.00	2.02	0.273	7.77	0.489	0.00275
6650.0	0.372	1.01	2.04	2.54	7.51	0.554	0.0225

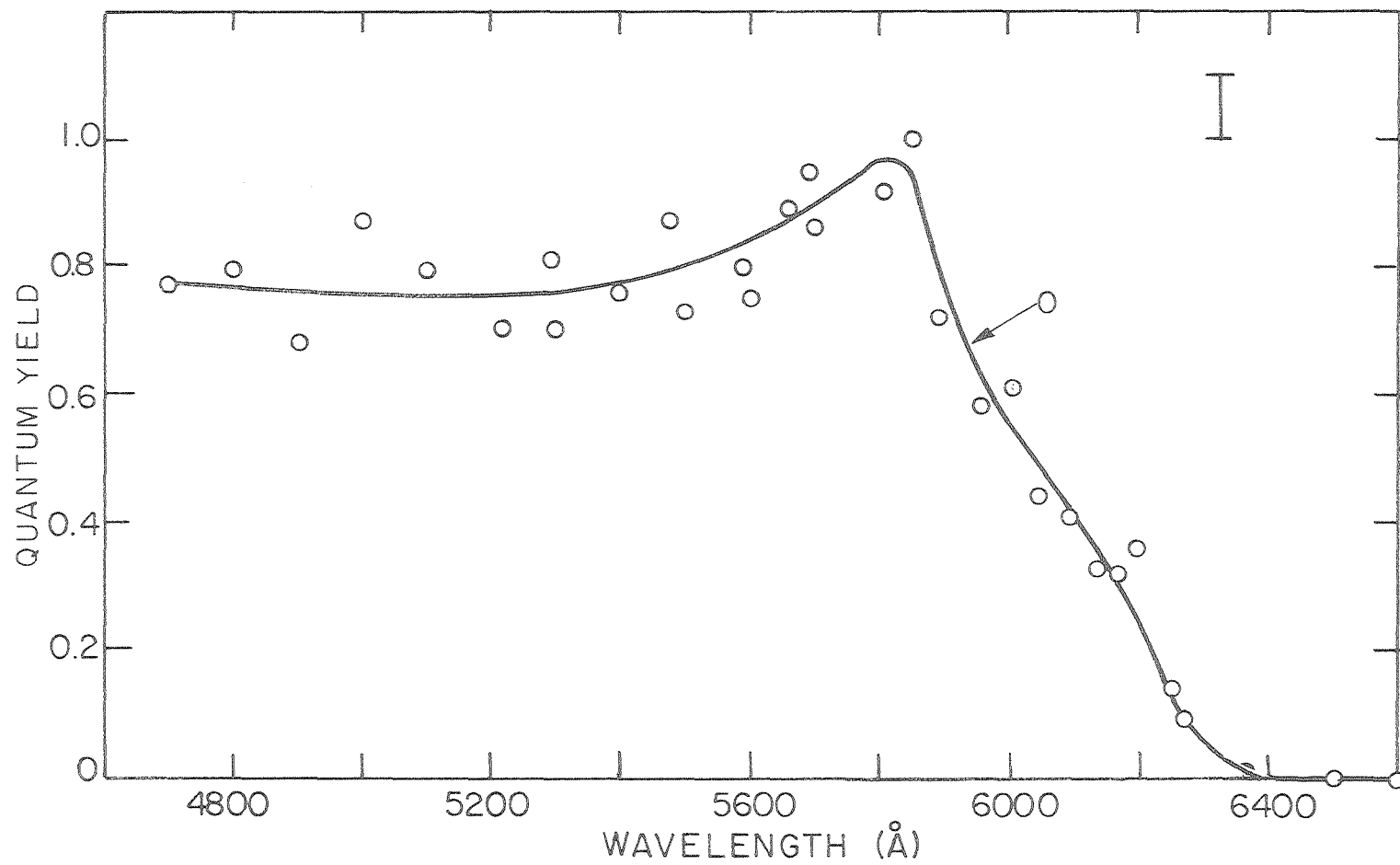
(continued . . .)

Table 18 continued.

6625.0	0.376	1.03	2.02	4.27	6.94	0.823	0.0256
6500.0	0.376	1.03	2.01	0.280	6.42	0.260	0.00537
6700.0	0.394	1.07	2.04	0.325	6.85	0.529	0.00302
6850.0	0.399	1.11	1.99	0.529	20.9	0.0152	(0.175)
6750.0	0.399	1.15	1.93	1.71	21.1	0.0884	(0.100)
6790.0	0.370	1.00	2.05	3.78	23.8	0.872	0.0211

* Corrected for [O] atom signal from 2 photon photodissociation of NO₂.

** Measured NO₂; additional NO₂ from NO₃ → NO₂ + O is negligible.



XBL 799-7077A

Figure 27. Averaged O quantum yield values versus wavelength (low Eσ).

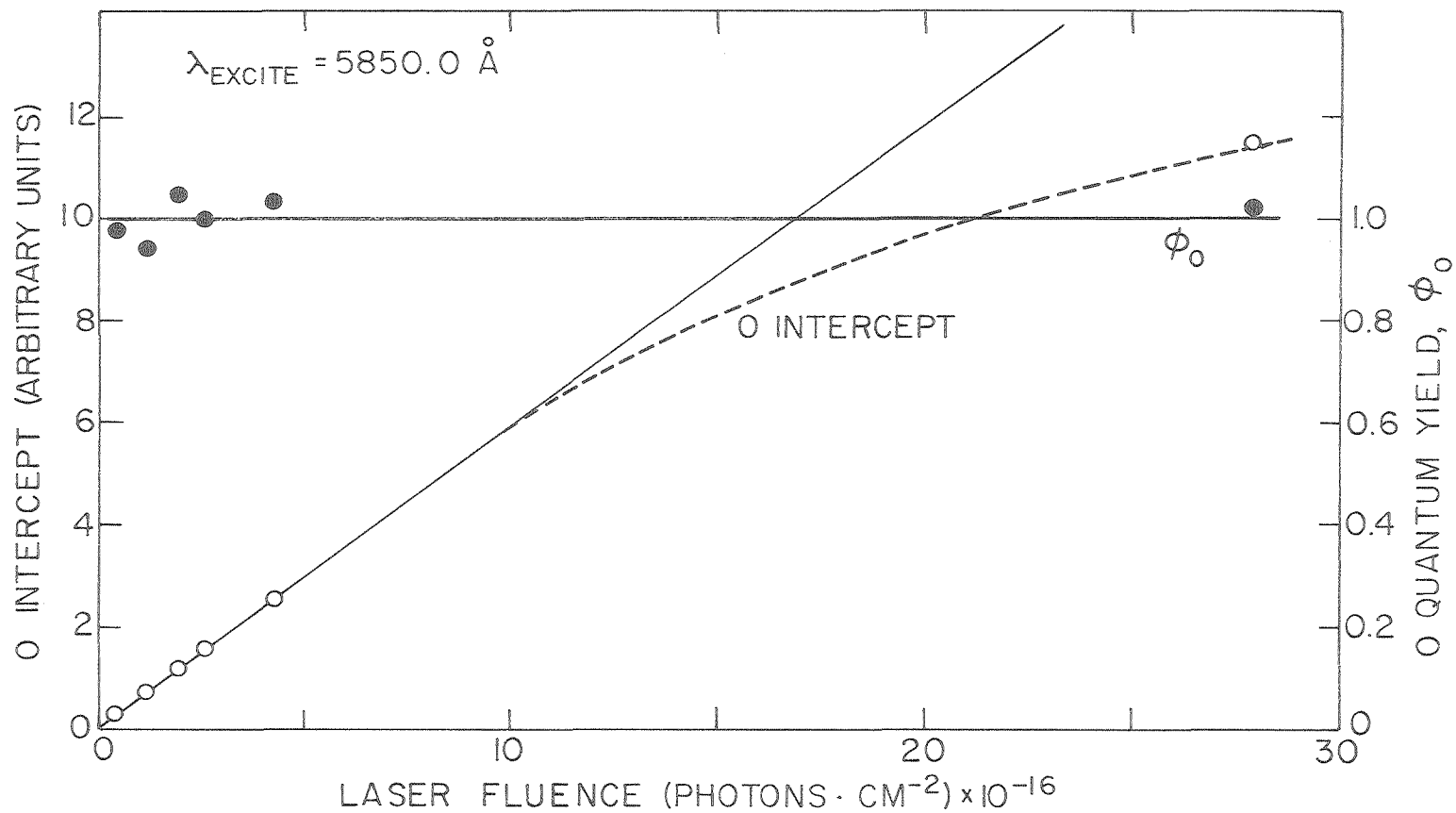
Table 19. [O] Signal and ϕ_0 vs. Laser Fluence

λ (Å)	Laser Fluence (photons·cm ⁻²) ×10 ⁻¹⁶	$\left(\frac{-E\sigma_{\text{NO}_3}}{1-e} \right)$	[O] Intercept ^{a,b)} (Arbitrary Units)	ϕ_0
5850.0	0.421	0.0151	0.274	0.972
"	1.21	0.0428	0.715	0.937
"	1.95	0.0680	1.15	1.05
"	2.54	0.0875	1.58	1.00
"	4.20	0.140	2.56	1.03
"	27.9	0.633	11.5	1.02
				(c,d) 1.002±(0.41)0.017
5892.9	0.692	0.0550	1.53	0.718
"	2.65	0.194	5.06	0.665
"	7.25	0.447	12.4	0.745
"	20.1	0.807	20.3	0.690
"	49.1	0.982	26.7	0.718
				(c,e) 0.707±(0.031)0.014
6233.1	0.682	0.113	0.75	0.0865
"	2.22	0.324	2.94	0.107
"	6.87	0.702	8.84	0.158
"	12.4	0.887	13.8	0.187
6600.0	3.35	0.222	0.746	0.0185
"	7.25	0.419	3.30	0.0433
"	12.9	0.620	8.09	0.0712
"	27.7	0.874	18.2	0.112

a) Normalized for [NO₃] concentration.b) [O] from NO₂ + 2hν is negligible.c) Average ± (σ_X)σ_{X̄}.

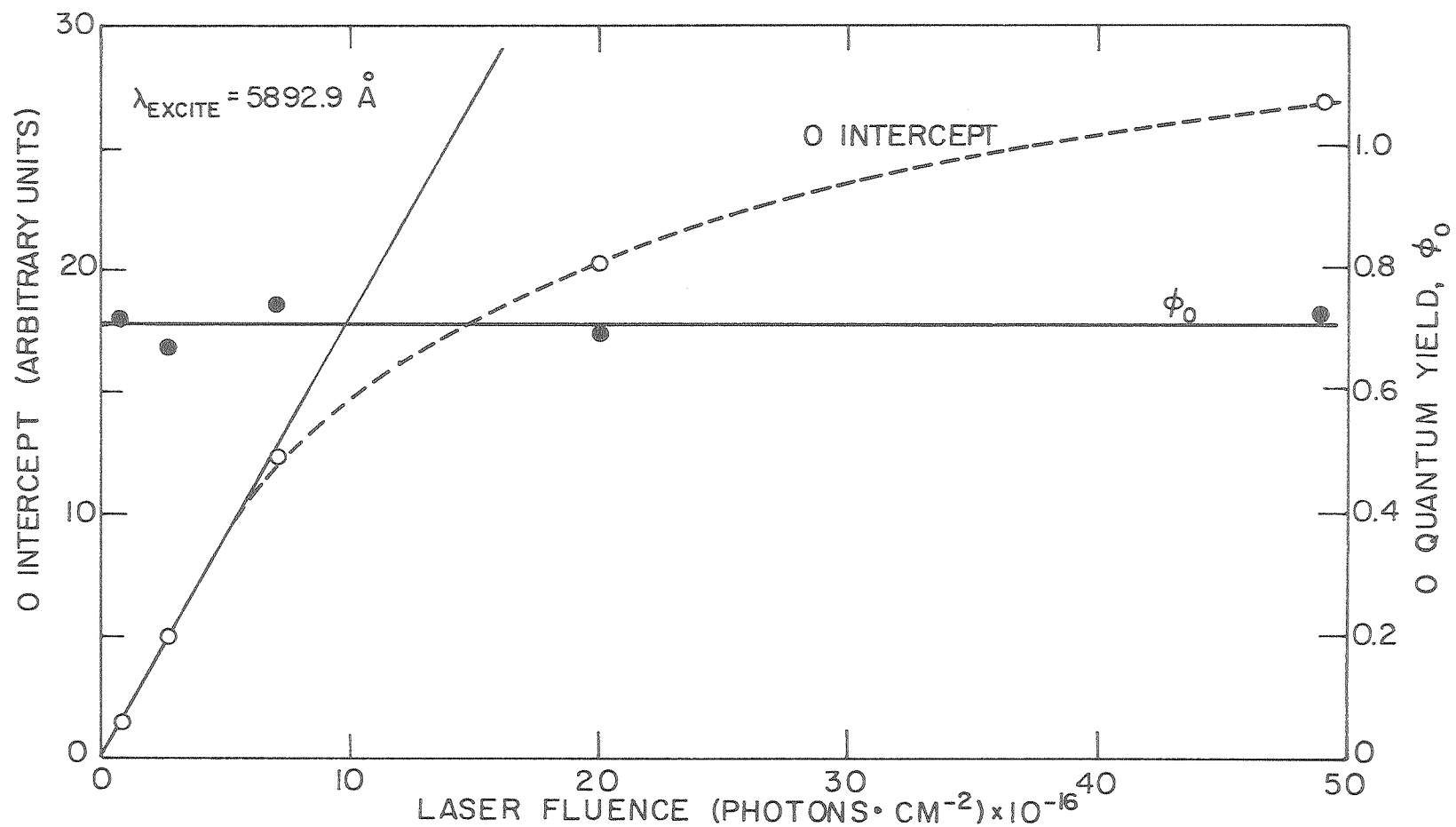
d) Slope = 0.00113 ± 0.0018

e) Slope = 0.000221 ± 0.00087



XBL799-7081

Figure 28. Oxygen fluorescence signal versus laser fluence and quantum yield at $\lambda = 5850.0 \text{ \AA}$.

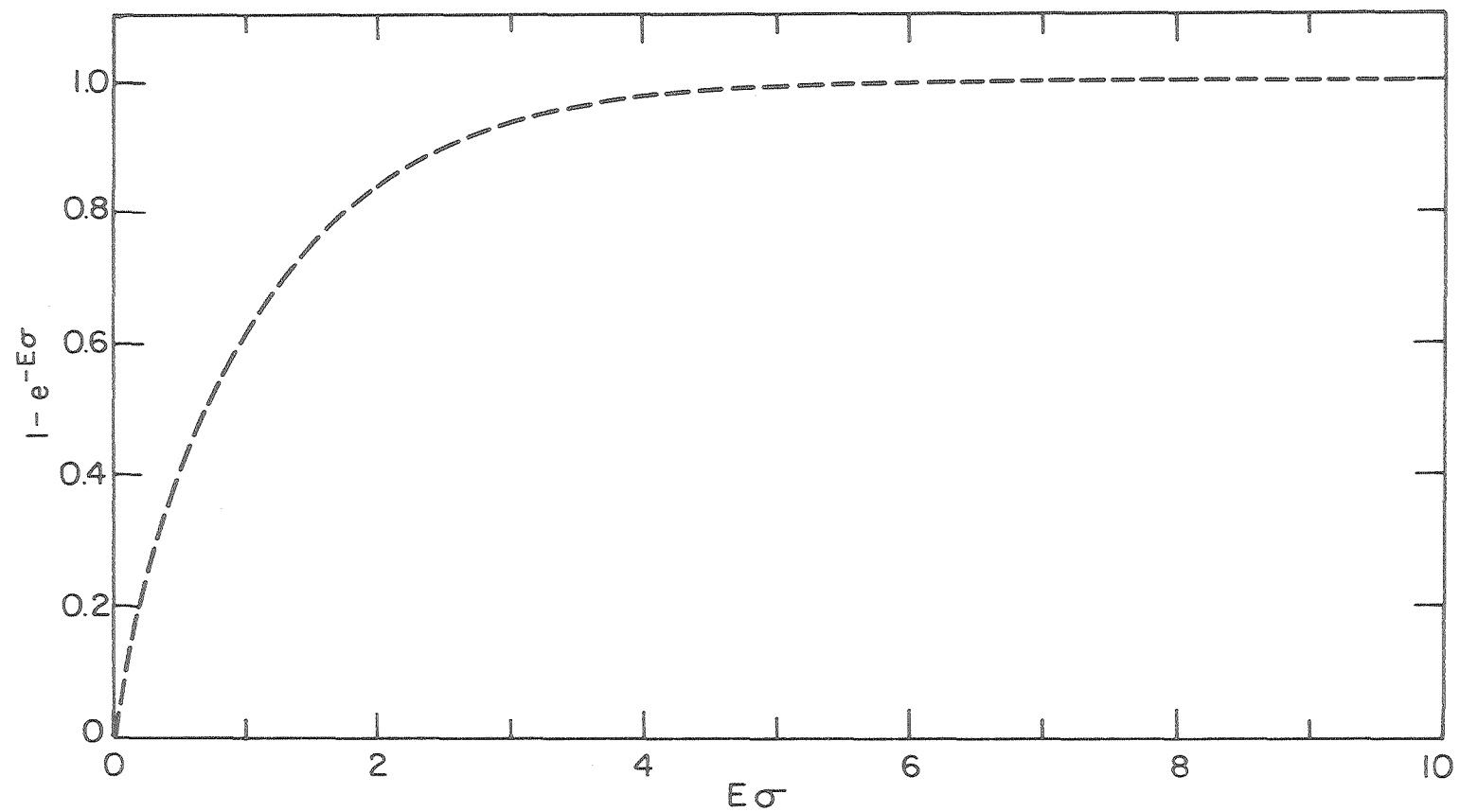


XPL 799-7080

Figure 29. Oxygen fluorescence signal versus laser fluence and quantum yield at $\lambda = 5892.9 \text{ \AA}$.

3. Nitric Oxide Calibration by NO₂ Photolysis

The reduced sensitivity of the NO detector, coupled with reduced quantum yield for NO production from NO₃, did not allow observation of product from both NO₂ and NO₃ at the same mole fraction. Increasing the NO₂ concentration, to levels where NO is observable from ultraviolet photolysis depletes NO₃ to a level where it can no longer furnish adequate NO under visible photolytic conditions. At the NO₂ levels utilized for calibration purposes, its maximum optical density was < 0.01, and N₂O₅ absorption still dominated any fluorescence attenuation. While the quenching efficiency of NO₂ for electronically excited NO A(v' = 0,1) is unknown, the assumption of a gas kinetic rate reduces the fluorescence efficiency from 0.96 and 0.79 at the maximum



XBL 799-7082

Figure 30. Graphical representation of low and high energy fluorescence signal behavior.

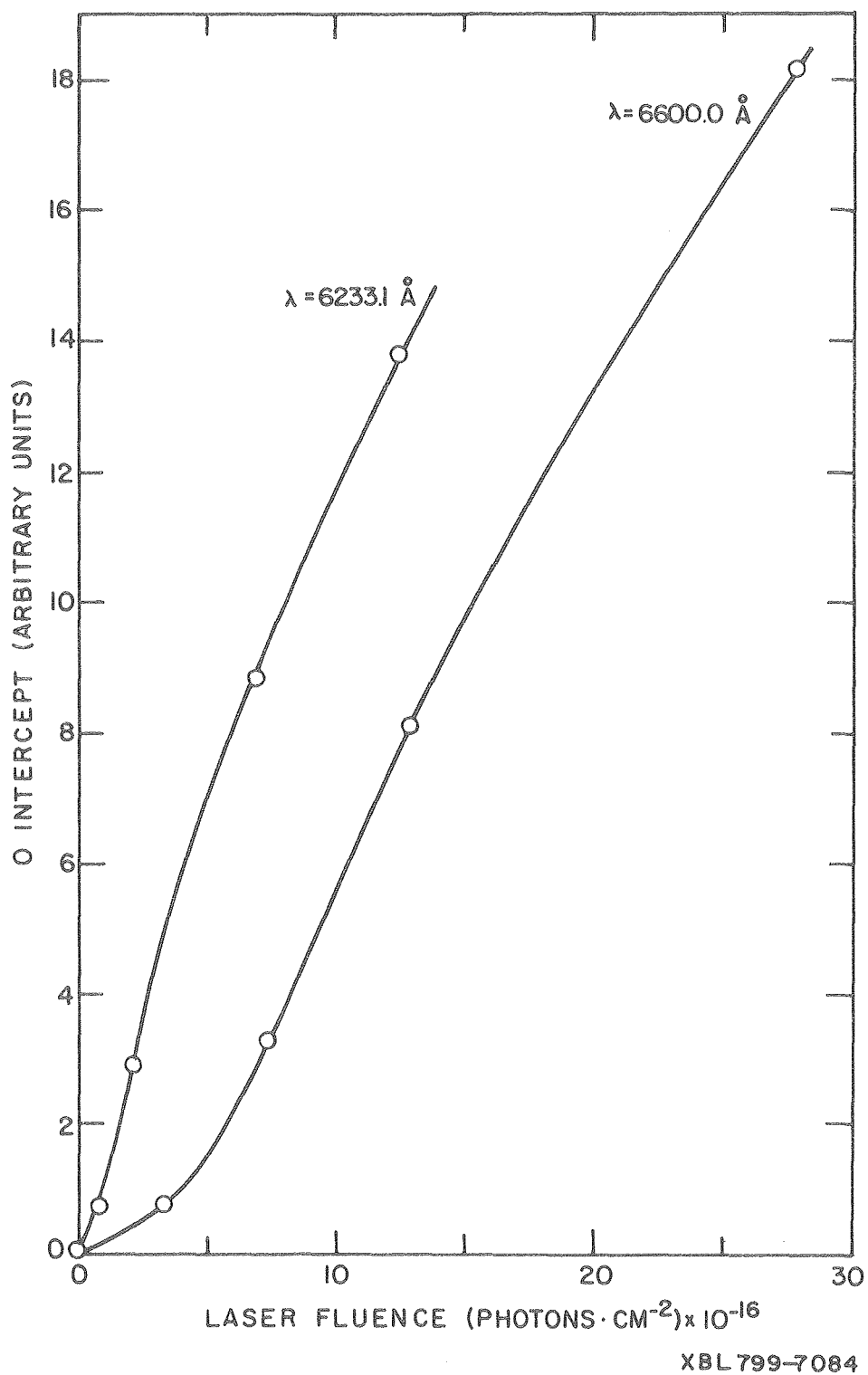
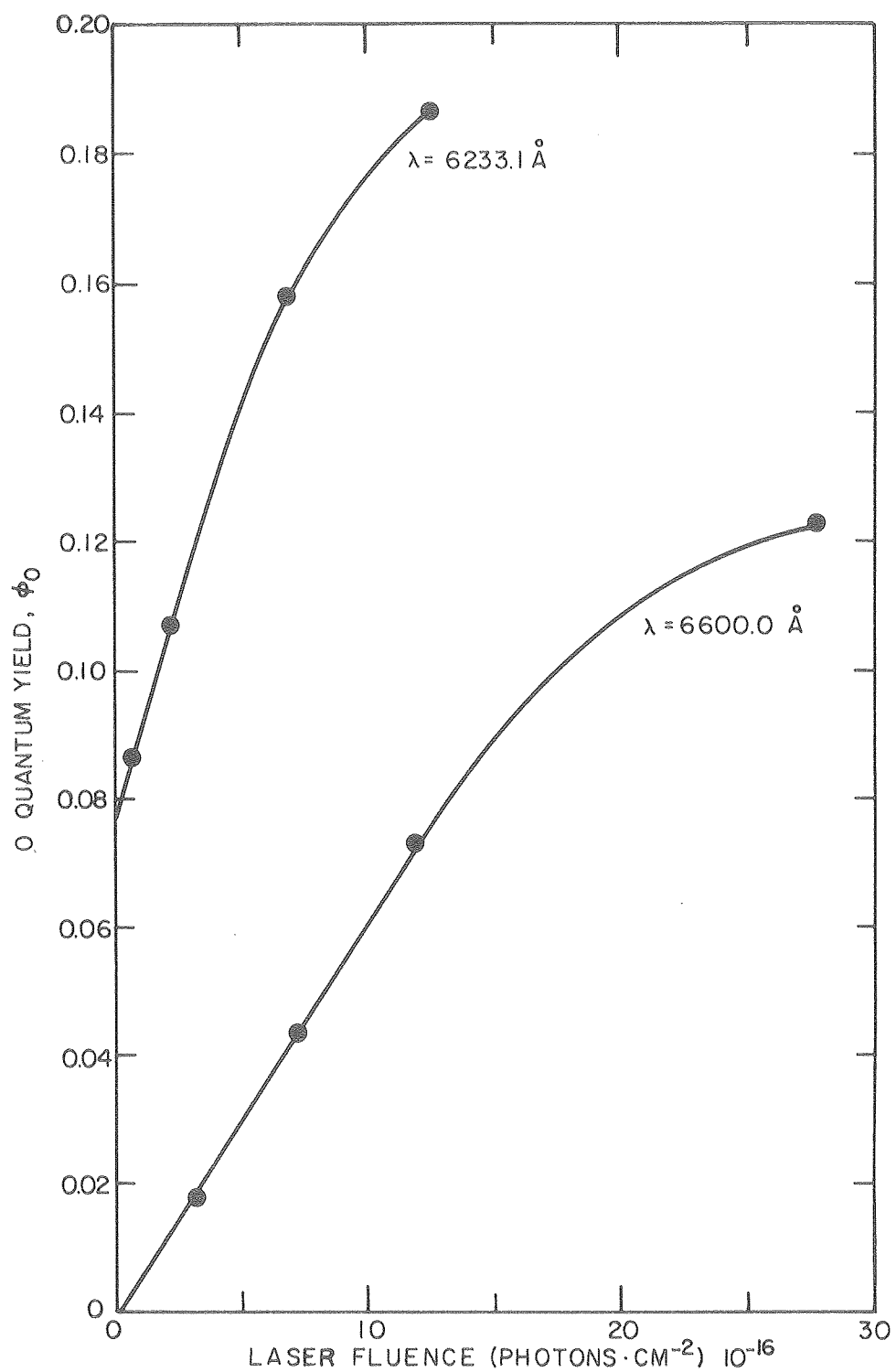


Figure 31. Oxygen fluorescence signal versus laser fluence at 6233.1 and 6600.0 Å.



XBL799-7090

Figure 32. Oxygen atom quantum yield versus laser fluence at 6233.1 and 6600.0 Å.

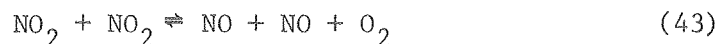


Figure 33. Two-photon behavior of NO_3 in the 6000–7000 Å region.

NO₂ concentration present.

Increased NO₂ concentrations in the presence of N₂O₅ and NO₃ were generated either by warming a 2" section of glass tubing leading from the saturator to the I.R. cell, or by separate injection of purified NO₂ from a second saturator into the N₂O₅ saturator. Temperatures of 298-308K were required to achieve usable NO₂ concentration without significantly depleting any N₂O₅. Better photon counting statistics were obtained, however, by separately injecting higher concentrations of NO₂ into the N₂O₅, both methods giving comparable results.

Attempts to photolyse pure NO₂/N₂ to observe NO were not successful, due to a constant amount of NO impurity in the stream resulting in low signal-to-noise ratios. Various methods of NO₂ purification consistently resulted in increasing the NO fluorescence background (versus N₂) to a level equivalent to a ~0.14% impurity, which was somewhat higher than that produced by laser photolysis. While this effect was originally thought to be due to NO₂ photolysis by the lamp, varying the flow rate by a factor of 50 had no effect. However, calculating the amount of NO present due to the Bodenstein⁷³ equilibrium:



resulted in a value of ~ 0.14% at the temperature and NO₂ concentration used. Therefore, either a fast heterogeneous reaction occurred during flow, or the original NO impurity in the NO₂ was not sufficiently oxidized during purification. Nitric oxide impurity is not a problem when N₂O₅ is present due to very fast scavaging by NO₃.

The use of increased NO_2 concentrations in this calibration was advantageous for two additional reasons. First, conditions could be easily adjusted such that the nitric oxide signal at zero time equaled twice that initially produced, due to the fast secondary reaction



being faster than diffusion out of the laser beam area (or flow past the lamp). At 10 torr total pressure, flow past the lamp and diffusion from the laser beam zone can both be calculated for 1-100% migration.

Table 20

	1%	10%	100%
Flow past lamp	1 ms	10 ms	100 ms
Diffusion (RMS displacement)	1 μs	100 μs	1 ms

The calculated half life for reaction 44 is $\leq 40 \mu\text{s}$, which coincides with typical channel dwell times used.

When NO_2 was photolysed at 3471 \AA , Busch and Wilson⁷⁵ found by photofragmentation spectroscopy an equal probability of recoil of the NO fragment in the $v''=0$ and $v''=1$ vibrational state. Since the relative sensitivity of the lamp/detection system to vibrationally excited ground state NO was not known, it was desirable to photo-lytically produce NO in $v''=0$ for calibration purposes. Fortuitously, at the NO_2 concentrations used, $\text{NO}(v''=1)$ from direct or secondary reaction was quenched in $\leq 200 \mu\text{s}$ by NO_2 (and possibly even faster

by the N_2O_5 present). The comparable intensities of ground state to hot band emission from the lamp suggest that the detection system was moderately (if not equally) sensitive to $v''=1$ nitric oxide, relaxing somewhat the quenching requirement.

NO_2 calibration data is presented in Table 21, and the detectivity defined represents the ratio of NO observed (based on bulk NO sensitivity) to that produced, based on $2[NO_2](1-e^{-E\sigma})$. This calibration factor, unlike that for bulk NO gas flow, determines the absolute sensitivity in the (0.79 cm^2) laser beam region. For high $E\sigma$ regime experiments, in which the 0.79 cm^2 beam aperture was not used (to increase signal level), a calibration factor of 0.38 was calculated based on the ratio of normalized signals with and without the aperture

$$\frac{\text{N.S. NO } (\infty \text{ aperture})}{\text{N.S. NO } (.79 \text{ cm}^2 \text{ aper.})} = \frac{1.68 \pm 0.15}{1.45 \pm 0.11} \quad (45)$$

Similarly, for non-apertured photolysis experiments, laser energy densities were calculated based on beam waist measurements (from burn patterns on photographic film) indicating a spot size of 0.91 cm^2 . However, for most runs in the high $E\sigma$ regime, the energy density was sufficiently large that $(1-e^{-E\sigma})$ was very close to 1 regardless of small variations in assumed beam area.

4. Nitric Oxide Quantum Yield Measurements

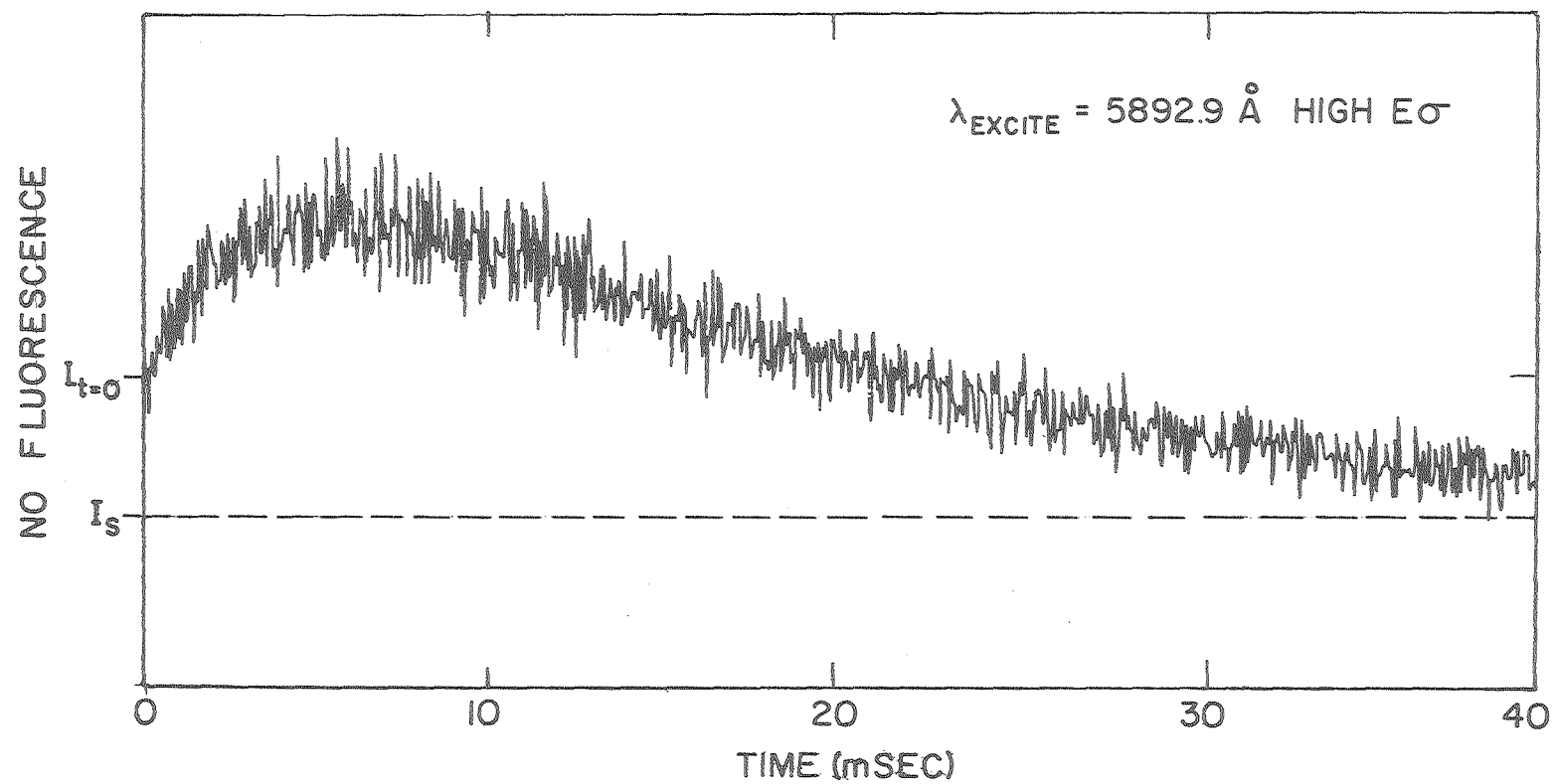
A typical temporal profile, resulting from detection of NO following NO_3 photolysis, is shown in Figure 34. The initial rise in signal is due to the fast secondary reaction of $O + NO_2 \rightarrow NO + O_2$ from the oxygen channel, which is operating concurrently.

Table 21. Nitric Oxide Calibration by NO₂ Photolysis
 ($\lambda_{\text{laser}} = 3518.3 \text{ \AA} - 0.79 \text{ cm}^2 \text{ aperture}$)

[N ₂ O ₅]	[NO ₂]	[NO ₃]	[NO] _a	[NO] _b	Average Laser Fluence (Photons·cm ⁻²) × 10 ⁻¹⁵	(1-e ^{-Eσ}) × 10 ⁴	Detectivity [NO] observed [NO] produced
× 10 ⁻¹⁵	units·molecules·cm ⁻³ × 10 ⁻¹⁵	× 10 ⁻¹⁰	× 10 ⁻¹²				
1.02	3.23	1.11	4.72	1.33	1.55	7.32	0.28
1.02	2.13	1.58	3.56	1.55	1.78	8.38	0.43
1.10	2.40	1.46	2.32	0.706	1.02	4.83	0.30
1.57	3.22	1.60	3.88	1.20	1.28	8.56	0.31
0.200	2.35	0.251	2.28	0.707	1.02	4.83	0.31
0.150	2.83	0.166	3.06	0.979	1.16	5.42	<u>0.32</u>
							0.325±.022

a) [NO] Produced = 2[NO₂](1-e^{-Eσ})

b) [NO] Observed = Bulk NO sensitivity⁻¹ × count rate|_{T=0}.



XBL 799-7107

Figure 34. NO fluorescence signal versus time at $\lambda = 5892.9 \text{ \AA}$.

Due to the low signal to noise ratio inherent in these measurements, the majority of NO data was obtained in the high energy limit (Table 22). The wavelengths investigated covered the range of 4700-6800 Å. One experiment was run in the low E₀ regime and that data is presented in Table 23. NO₃ concentrations were corrected using the same calibration factor determined for the 0 lamp, since the thermal effects from both lamps were found to be very similar. A comparison of averaged quantum yield values is plotted in Figure 35 and 35A. Included in Figure 35 is the relative absorption spectrum of NO₃ in this region.

At several wavelengths below 5800 Å, a small but definite amount of NO was observed, representing apparent quantum yields of ≤ 0.04 . This NO was later found to be entirely due to 2-photon photolysis of NO₂. In Section III E, the 2-photon cross sections for NO₂ have been measured and tabulated; the values obtained completely accounted for the NO production observed below 5800 Å.

While the zero time intercept defines the quantity of NO initially produced, the limiting initial slope contains information concerning the oxygen atom channel. The rate of change of NO with time is represented by the following production and loss terms.

$$\text{Slope} \Big|_{t=0} = \frac{d[\text{NO}]}{dt} \Big|_{t=0} = k_1[\text{O}]_0[\text{NO}_2]_0 - k_2[\text{NO}]_0[\text{NO}_3]_0 - k_{\text{diff}}[\text{NO}]_0$$

(46)

where the zero subscripts represent zero time concentrations.

Table 22. Nitric oxide quantum yield vs. wavelength (high E σ regime, 0.79 cm aperture).

λ_{laser} (Angstroms)	$\frac{[\text{N}_2\text{O}_5]}{\times 10^{-15}}$	$\frac{[\text{NO}_2]}{\times 10^{-13}}$	$\frac{[\text{NO}_3]}{\times 10^{-12}}$	$\frac{[\text{NO}]}{\times 10^{-11}}$	Average Laser Fluence (Photons $\cdot \text{cm}^{-2}$) $\times 10^{-17}$	$\left(\frac{-E\sigma_{\text{NO}_3}}{1-e} \right)$	ϕ_{NO}
6095.0	0.914	1.50	2.83	2.74	7.92	0.788	.123
5892.9	0.950	1.50	2.92	8.95	7.48	0.998	.307
6045.3	1.00	1.59	2.90	7.11	6.45	0.979	.243
5850.0	1.09	1.70	3.14	1.52	4.74	0.818	.0589
5959.3	1.14	1.98	3.10	11.3	3.60	0.889	.409
5892.9	1.14	2.07	2.78	6.58	3.08	0.918	.258
5959.3	1.22	1.90	2.61	3.55	.624	0.315	.432
5700.0	1.57	2.00	3.82	0	3.77	0.748	0
5700.0	1.35	1.89	3.35	0	2.29	0.567	0
5892.9	1.21	2.08	2.86	6.80	2.88	0.904	.253
5892.9	1.04	1.71	3.25	7.77	13.1	1.00	.239
5892.9	.949	1.30	2.77	9.78	5.49	.989	0.357
5892.9	1.05	1.52	2.73	6.79	1.89	.785	0.317
5892.9	.852	1.02	3.56	7.99	2.68	.887	0.253

(continued . . .)

Table 22 (continued, but at ∞ aperture)

λ_{laser}	$[\text{N}_2\text{O}_5]$ $\times 10^{-15}$	$[\text{NO}_2]$ $\times 10^{-13}$	$[\text{NO}_3]$ $\times 10^{-12}$	$[\text{NO}]^a$ $\times 10^{-11}$	$[\text{O}]^a$ $\times 10^{-12}$	Laser Fluence ^(b) $\times 10^{-17}$	$\left(\frac{-E\sigma_{\text{NO}_3}}{1-e} \right)$	ϕ_{NO}	ϕ_{O}
4900.0	.664	.969	2.91	~ 0	1.76	8.03	.665	0	.908
5200.0	.541	.890	2.48	$< .110$	1.44	9.34	.852	$< .006$.679
5100.0	.523	.875	2.43	~ 0	1.73	9.06	.821	0	.867
5000.0	.504	.882	2.35	~ 0	2.00	9.37	.739	0	1.15
4700.0	.464	.881	2.29	~ 0	5.70	5.88	.344	0	.724
4800.0	.448	.864	2.29	< 0.85	9.36	7.03	.481	$< .010$.851
5271.2	1.11	1.35	4.36	~ 0	2.46	7.41	.803	0	.704
5400.0	1.39	1.59	4.42	< 0.48	2.20	8.13	.883	$< .0014$.563
5500.0	1.45	1.70	4.28	~ 0	2.95	7.00	.895	0	.770
5600.0	1.41	1.74	3.71	~ 0	2.15	8.78	.984	0	.589
5700.0	1.37	1.75	3.59	~ 0	2.86	9.52	.969	0	.830
5800.0	1.41	1.79	3.57	~ 0	3.24	8.20	.999	0	.978
5892.9	1.05	1.81	2.95	8.41	1.76	5.86	.992	.295	.600
5892.9	1.12	2.06	2.97	9.61	2.36	6.93	0.996	.325	.797
6045.3	1.44	2.86	2.89	7.26	.958	4.46	0.931	.270	.356
5959.3	1.66	2.32	2.95	9.16	1.44	3.21	0.858	.362	.571
5959.3 ^c	1.72	4.07	2.51	7.14	1.14	3.62	0.889	.320	.510 ^{c)}
5892.9 ^c	1.93	4.14	2.69	6.68	1.79	5.26	0.986	.252	.626 ^{c)}
5892.9 ^d	0.920	4.15	1.31	(d)	(d)	3.82	0.956	(d)	--

(continued. . .)

Table 22 (continued)

λ_{laser}	$[\text{N}_2\text{O}_5]$ $\times 10^{-15}$	$[\text{NO}_2]$ $\times 10^{-13}$	$[\text{NO}_3]$ $\times 10^{-12}$	$[\text{NO}]^a$ $\times 10^{-11}$	$[\text{O}]^a$ $\times 10^{-12}$	Laser Fluence (b) $\times 10^{-17}$	$\left(\frac{-E\sigma_{\text{NO}_3}}{1-e} \right)$	ϕ_{NO}	ϕ_{O}
5945.0 ^c	0.736	1.41	2.94	9.46	1.95	11.7	.999	.322	.398 ^c
5850.0 ^c	0.808	1.62	2.88	0	3.81	11.2	.982	0	.726 ^c
6005.0 ^c	0.751	1.84	2.40	4.72	2.78	10.8	.979	.201	.360 ^c
6095.0 ^c	0.782	2.12	2.24	.751	.881	8.68	.818	.0410	.289 ^c
5813.0 ^c	0.815	2.33	2.20	0	2.98	11.3	.995	0	.816 ^c
5892.9 ^c	0.733	2.20	2.13	6.28	2.29	10.9	1.00	.295	.642 ^c
5892.9 ^c	0.653	2.05	2.07	6.31	2.30	10.3	1.00	.305	.645 ^c
6045.3 ^c	0.625	2.02	2.01	3.51	.767	8.04	.992	.176	.230 ^c
5959.3 ^c	0.594	2.02	1.93	5.45	1.67	9.74	.997	.283	.521 ^c
5813.0 ^{c,e}	0.923	13.8	.376	0	(f)	8.41	.981	0	(f)
6045.3 ^{c,e}	1.01	15.1	.368	.686	(f)	7.90	.991	.188	(f)
6095.0	1.00	1.07	4.08	6.49	1.03	13.2	.925	.172	.273
6005.0	1.16	1.23	4.14	11.1	1.88	13.7	.993	.271	.458
5850.0	1.40	1.41	4.44	1.37	3.92	13.4	.992	.0311	.891
5892.9	1.64	1.55	4.84	11.8	2.99	13.1	1.00	.243	.674
5813.4	1.74	1.56	5.14	.210	3.61	13.1	.998	.00410	.703
5959.4	1.25	1.37	4.22	14.1	2.41	12.7	1.00	.335	.570
6045.3	0.857	1.09	3.62	9.30	1.08	11.7	1.00	.257	.298
5945.0	0.702	.966	3.37	11.9	1.82	12.4	1.00	.353	.541
5892.9	0.550	.743	3.38	7.30	2.81	14.9	1.00	.216	.830
6600.0	0.907	.943	4.61	.186	1.45	11.2	1.00	.00403	.315

(continued. . .)

Table 22 (continued)

6625.5	1.15	1.17	4.90	.232	.868	8.66	1.00	.00474	.177
6650.0	1.04	1.07	4.69	0	.594	10.6	1.00	0	.127
6790.0	.982	1.14	4.39	0	.647	8.72	.529	0	.147
6135.0	.907	.987	4.06	3.95	1.46	12.3	.985	.0987	.365
6233.1	.977	1.08	4.09	4.54	1.65	12.1	1.00	.111	.404
6270.0	.844	1.02	3.79	2.55	.553	11.9	1.00	.0673	.146
6170.0	.675	.897	3.41	3.19	.703	11.2	.946	.0935	.218
6135.0	.380	.601	2.84	2.60	.485	10.5	.965	.0947	.177
6375.0	.329	.541	2.70	.604	0	10.6	.925	.0242	0
5813.4	.202	.623	1.82	0	1.95	13.6	1.00	0	1.07
5892.9	.202	.653	1.74	7.06	1.74	13.6	1.00	.406	1.00
5959.3	.236	.680	1.94	6.56	1.45	13.9	1.00	.338	.746
6045.3	.220	.678	1.82	5.73	.617	13.7	1.00	.315	.339
5850.0	.283	.483	3.27	8.44	(f)	9.83	.981	.0263	(f)
5892.9	.391	.702	3.11	8.24	(f)	13.8	1.00	.265	(f)

a) Corrected for $\text{NO}_2 + 2 \text{h}\nu \rightarrow \text{NO} + \text{O}$.

b) Beam spot size = 0.91 cm^2

c) CH_4 buffer gas — Φ_{O} corrected for $\text{O} + \text{CH}_4$

d) SF_6 buffer gas — Φ_{NO} not statistically significant

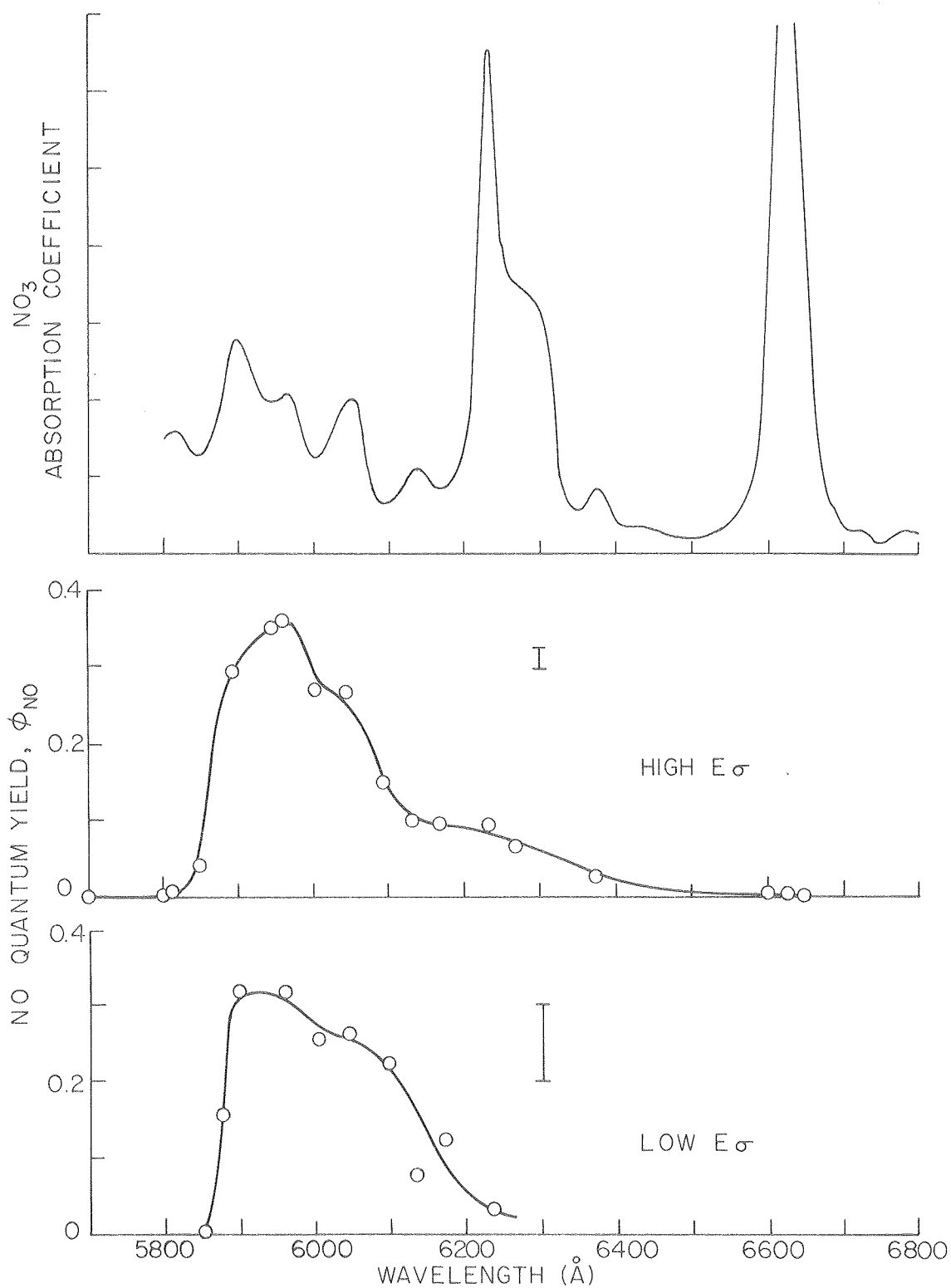
e) Low $[\text{NO}_3]$

f) Not measured

g) Calculated from $[\text{NO}]$ initial slopes.

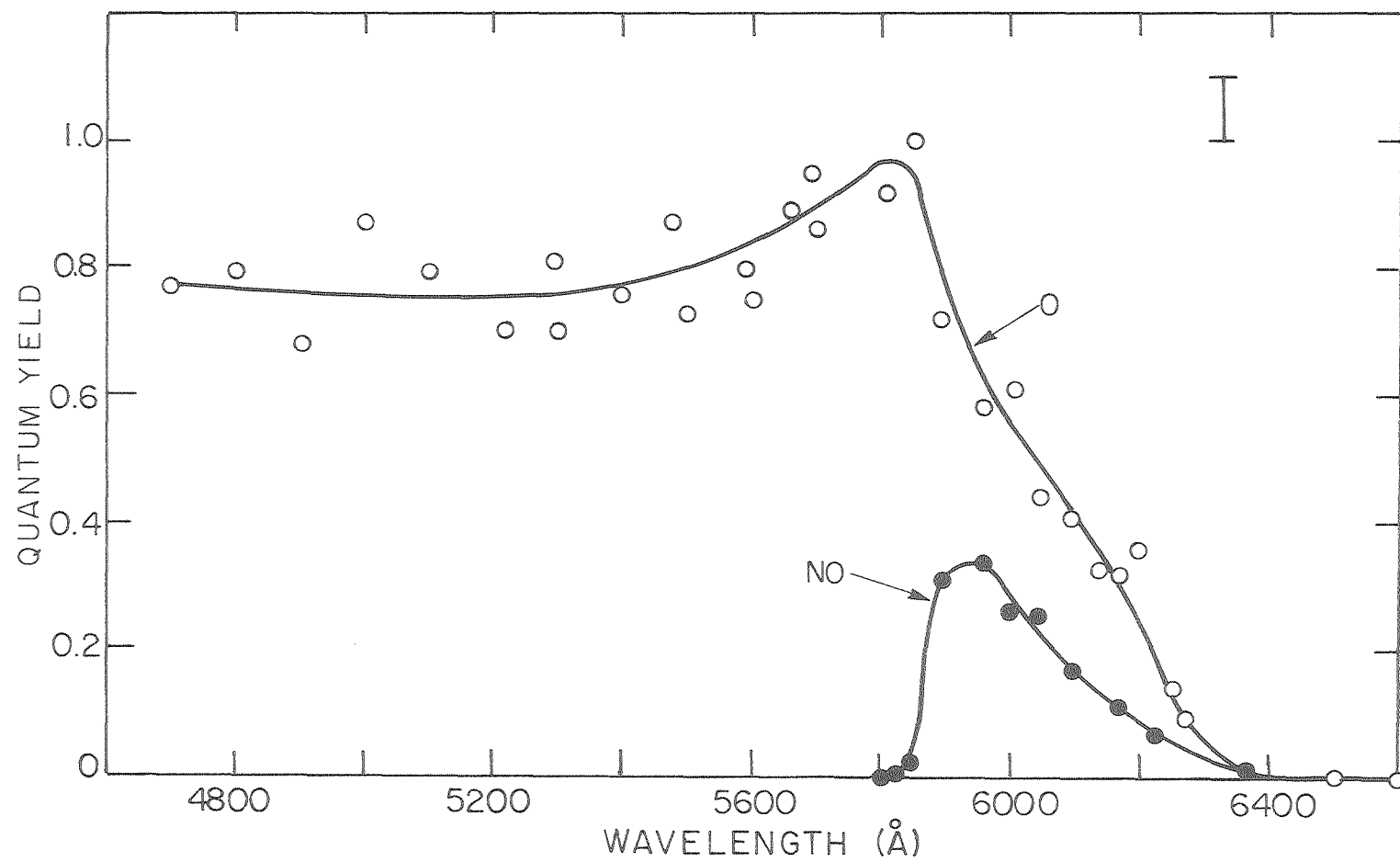
Table 23. Nitric Oxide Quantum Yield vs. Wavelength
(Low E σ Regime — 0.79 cm² Aperature)

λ_{laser} (Angstroms)	[N ₂ O ₅] × 10 ⁻¹⁵	[NO ₂] × 10 ⁻¹³	[NO ₃] × 10 ⁻¹²	[NO] × 10 ⁻¹⁰	Average Laser Fluence (Photons·cm ⁻²) × 10 ⁻¹⁶	$\left(\frac{-E\sigma_{\text{NO}_3}}{1-e} \right)$	ϕ_{NO}
	molecules·cm ⁻³						
5892.9	0.806	0.982	3.82	10.1	0.914	0.0718	0.366
5850.0	1.00	1.12	4.05	.463	6.48	0.208	0.0055
6005.0	1.27	1.28	4.19	22.1	5.15	0.169	0.312
5875.0	1.19	1.25	3.84	13.2	4.27	0.220	0.156
6095.0	0.648	0.909	3.19	12.2	7.79	0.142	0.269
6135.0	0.535	0.808	3.21	3.51	4.66	0.140	0.0781
6233.0	0.477	0.750	3.00	2.56	1.45	0.240	0.0355
6170.0	0.439	0.738	2.88	5.25	6.45	0.146	0.125
6095.0	0.883	1.06	3.73	10.5	8.55	0.154	0.183
5892.9	0.830	1.02	3.54	15.2	1.92	0.145	0.297
5892.9	0.811	0.998	3.22	34.6	4.94	0.332	0.323
5959.3	0.798	1.07	3.70	11.3	1.67	0.0961	0.317
6045.3	0.811	1.05	3.76	26.5	4.15	0.220	0.302
6005.0	0.817	1.05	3.79	13.3	5.69	0.184	0.191
5892.9	1.13	1.76	2.92	25.1	3.53	0.250	0.343
6095.0	1.32	1.92	2.78	4.12	3.60	0.0681	0.218
6045.3	1.17	1.86	2.77	12.4	3.73	0.200	0.224
6005.0	1.13	1.82	2.78	5.58	2.24	0.0772	0.260



XBL799-7078

Figure 35. Averaged NO quantum yield versus wavelength at high and low $E\sigma$.



XBL799-7077

Figure 35A. Comparison of absolute NO and O atom quantum yields.

$$[\text{NO}_2]_0 = [\text{NO}_2]_{\text{measured}} + [\text{O}]_0 \quad (47)$$

$$[\text{NO}_3]_0 = [\text{NO}_3]_{\text{measured}} - [\text{NO}]_0 - [\text{O}]_0 \quad (48)$$

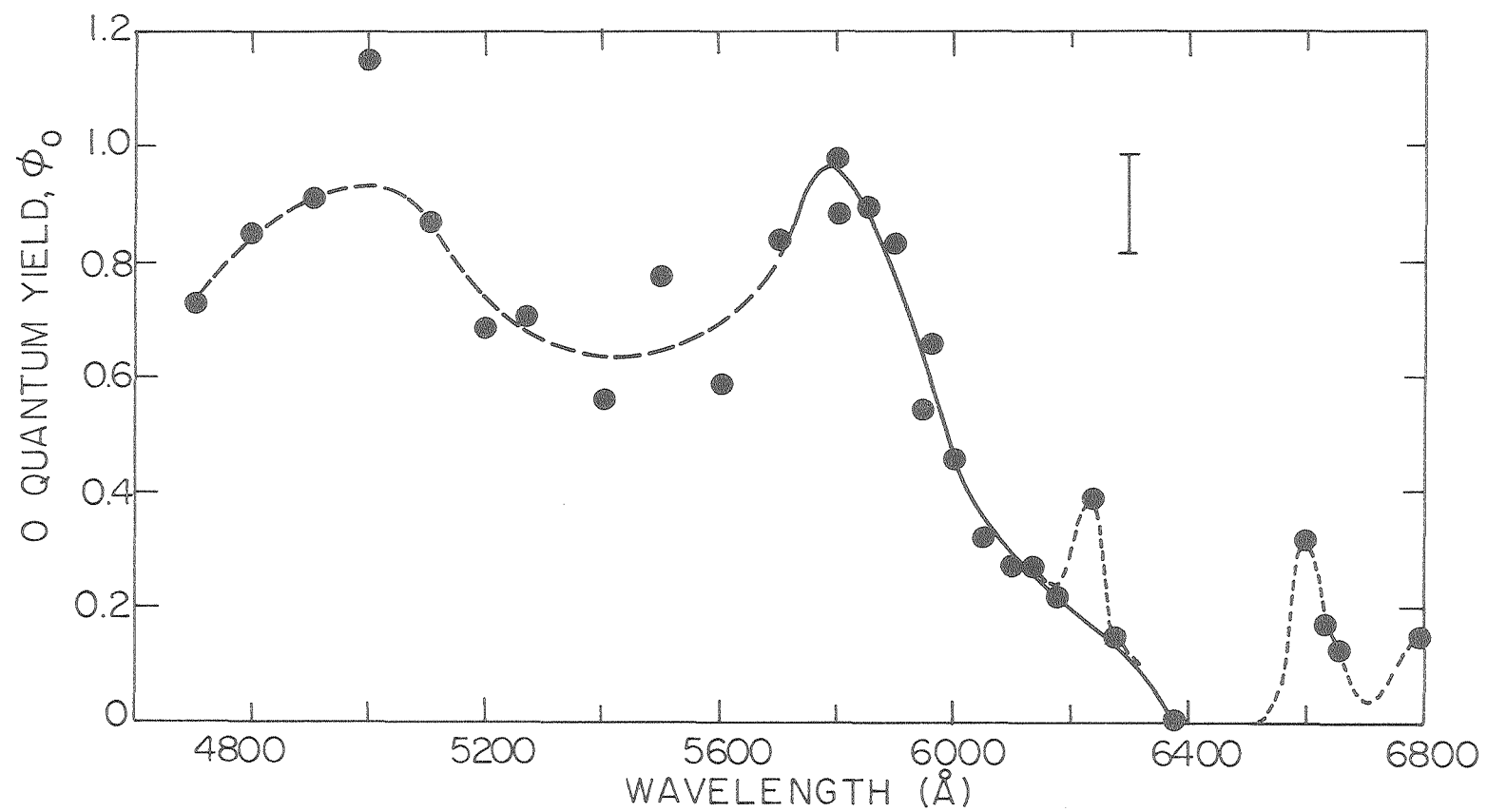
$$\text{Slope} \Big|_{t=0} \cdot \left(\frac{\text{Dwell Time}}{\text{Channel}} \right)^{-2} \cdot (\# \text{ shots})^{-1} \cdot (\text{NO sensitivity}) =$$

$$k_1[O]_0^2 + (k_1[NO_2] - k_2[NO]_0)[O]_0 + [NO]_0(k_2[NO]_0 - k_2[NO_3] - k_{\text{diff}})$$

$$(49)$$

$$\begin{aligned} \text{where } k_1 &= 1.03 \times 10^{-11} \text{ cm}^3 \cdot \text{molecule}^{-1} \cdot \text{sec}^{-1} \text{ (This work, see Sec.III F)} \\ k_2 &= 1.87 \times 10^{-11} \text{ cm}^3 \cdot \text{molecule}^{-1} \cdot \text{sec}^{-1} \text{ (Graham}^9\text{)} \\ k_{\text{diff}} &= 110 \text{ sec}^{-1} \text{ (This work)} \end{aligned}$$

Solving this quadratic expression results in oxygen-atom quantum yields which should correspond to those previously determined, if indeed the interpretation of the temporal profile presented is correct. Oxygen atom measurements obtained from nitric oxide initial slope information are shown in Table 22, and a plot of averaged quantum yield versus wavelength at the high E_0 limit is shown in Figure 36. Considering the even lower information content of slope data versus intercept data, the quantum yield curve is remarkably similar to that obtained by direct observation of oxygen atoms. The two-photon features, which occur under the mainly one photon inactive absorption peaks of NO_3 , are also clearly shown. The data below 5700 \AA are single determinations at inordinately low NO_3 concentrations, resulting in a decrease in precision. The initial positive slope observed in the



XBL 799-7103

Figure 36. O quantum yield versus wavelength from NO initial slope data.

high energy regime was not discernable at the low energy limit, due to very low S/N ratios.

Before it was apparent that the initial positive slope was indeed due to $O + NO_2$, several alternative explanations were proposed and investigated (see Section IVB-1). One such explanation involved the reaction sequence



in which a greater sensitivity of the detection system for ground vibrational state NO resulted in the initial signal rise. The decrease in NO quantum yield at shorter wavelength could be explained by assuming that increasingly larger fractions of NO are produced vibrationally excited and subsequently deactivated at a fixed rate by M gas (since N_2 is a very poor quencher, M must be assumed to be either N_2O_5 or HNO_3).

An experiment designed to test this possibility was to substitute the N_2 carrier gas with a very fast NO ground state vibrational quencher, which should eliminate the initial rise in slope and increase $[NO]_0$, especially at lower wavelengths. A second requirement for this quencher would be that it not quench the $NO(A^2\Sigma^+)$ electronic state, which could reduce the NO fluorescence signal. Several fast vibrational quenchers were found (NO_2, H_2O) but were obviously unsuitable. Gases such as O_2, N_2O , and CO_2 are rapid electronic quenchers while N_2 argon, CO and helium are very slow vibrational quenchers. Hydrocarbons, due to their near resonant bending (C-H) frequencies with NO, are rapid

vibrational quenchers, but no data could be found concerning their electronic quenching rates.

An experiment was performed with mixes of CH_4/NO , SF_6/NO (also no data available), and O_2/NO , to determine the degree of $\text{A}^2\Sigma$ state electronic quenching. The following results were obtained, along with several values from the literature.^{30,75}

Table 24. Electronic $\text{A}^2\Sigma$ quenching half pressure vs. M gas.

[M] Gas	NO signal sensitivity ⁻¹ $\frac{\text{molecules} \cdot \text{cm}^{-3}}{\text{count} \cdot \text{sec}^{-1}}$	Quenching half pressure k_f/k_Q (torr)	Quenching Probability/ Collision
N_2	2.82×10^7	1400 (lit) $v'=0$	3×10^{-4} (lit)
CH_4	3.78×10^7	27.81	0.015
SF_6	4.33×10^8	0.689	0.61
O_2	2.39×10^8	1.32	0.318
CO_2	not measured	0.31 (lit)	} $v'=0$ 1.2
O_2	not measured	0.58 (lit)	
N_2O	not measured	0.31 (lit)	

While SF_6 and O_2 were unsuitable, methane only produced a slight decrease in fluorescence signal while also being a very efficient ground state vibrational quencher (Table 25).

Using 10 torr of CH_4 quenches $\text{NO X}^2\Pi$ ($v''=1$) in the first signal channel (40 μsec). Subsequent experiments showed CH_4 to have only a negligible effect on NO_2 sensitivity (since N_2 buffer is itself a very efficient NO_2 quencher.) The N_2O_5 infrared cross section was assumed to be unchanged by the presence of CH_4 and the cross section at 743 cm^{-1}

Table 25. NO X²Π Vibrational Relaxation Rates^{31,76,77}

NO(ν=1) → NO(ν=0) + hν, τ = 80 msec.

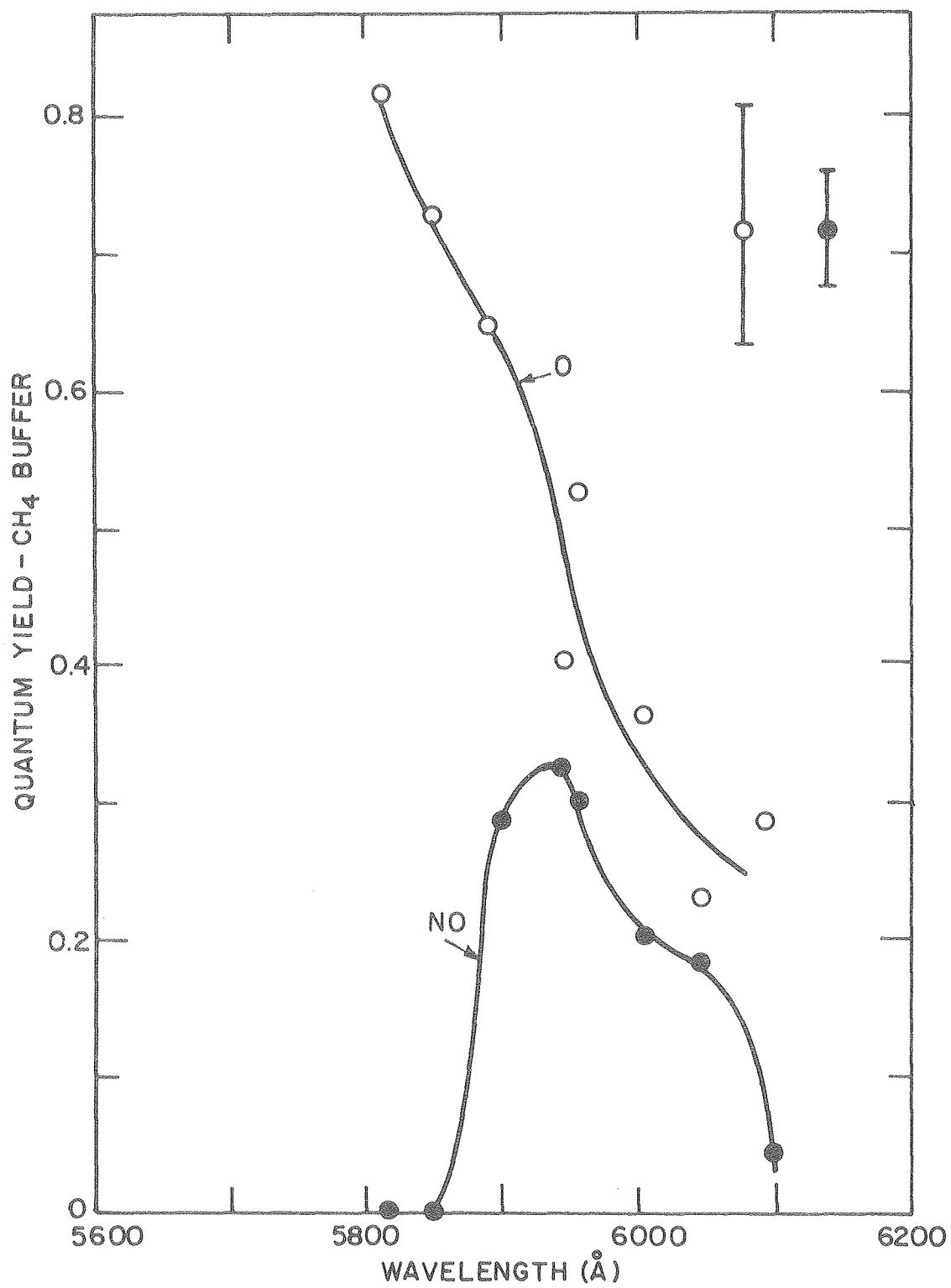
[M] Gas	k (300 K)	τ _{1/2} @ 10 torr	τ _{1/2} @ [M] _{ambient}	[M] _{ambient}
CH ₄	1.9x10 ⁻¹³	16 μsec	--	--
N ₂	1.37x10 ⁻¹⁶	23 msec	23 msec	3x10 ⁻¹⁷
CO ₂	4.10x10 ⁻¹⁴	76 μsec	--	--
NO	7.6x10 ⁻¹⁴	40 μsec	120 sec	~ 10 ¹¹
H ₂ O	1.85x10 ⁻¹²	1.7 μsec	--	0
NO ₂	2.05x10 ⁻¹²	1.6 μsec	230 msec	2x10 ¹²
CO	6.15x10 ⁻¹⁵	500 μsec	--	--
N ₂ O ₅	3x10 ⁻¹⁴	NA	100 msec	3x10 ¹⁴
IF	3x10 ⁻¹³	NA	10 msec	3x10 ¹⁴
	3x10 ⁻¹²	NA	1 msec	3x10 ¹⁴
HNO ₃	IF 3x10 ⁻¹³	NA	> 100 msec	1.5x10 ¹³

determined in this work, utilized to monitor its concentration (methane is transparent at 743 cm^{-1}).

Two photolysis experiments were performed duplicating the 5800-6095 Å region with CH_4 , and the results were qualitatively similar to the N_2 buffer results (Figure 37). Direct comparison shows the CH_4 quantum yields to be slightly lower than the N_2 experiments, but this may be an experimental artifact resulting from slight errors in two additional NO/CH_4 and NO_2/CH_4 calibrations which were performed. If the absolute quantum yields, however, are indeed different, this either rules out any formation of vibrationally excited NO and/or suggests that the NO detection system is slightly more sensitive to vibrationally excited NO if it is indeed present.

In attempts to resolve this question, an attempt was made to measure $\text{NO X}^2\Pi$ ($v''=0$) formation using a cadmium ion discharge line at 2144 Å . As expected, the sensitivity of this lamp was far too low to adequately measure NO using a reasonable number of laser flashes. Alternatively, the use of an NO gas filter between the lamp and cell to measure $\text{NO X}^2\Pi$ ($v''=0$) formation was not successful due to the loss in lamp intensity and sensitivity resulting from $1/R^2$ losses.

The behavior of the nitric oxide intercept and quantum yield was investigated as a function of laser fluence at 3 wavelengths. While results obtained at 5959.3 and 6045.3 Å are inconclusive for lack of sufficient data, the data obtained at 5892.9 Å clearly demonstrate adherence to the previously observed quantum yield expression. The average of the quantum yield data points (Table 25) is 0.292 ± 0.10 , while a linear least square fit results in a value of 0.302 ± 0.011 and a finite slope which is however not statistically significant (Figure 38).



XBL 799-7102

Figure 37. O and NO quantum yield results vs. wavelength using CH₄ buffer gas.

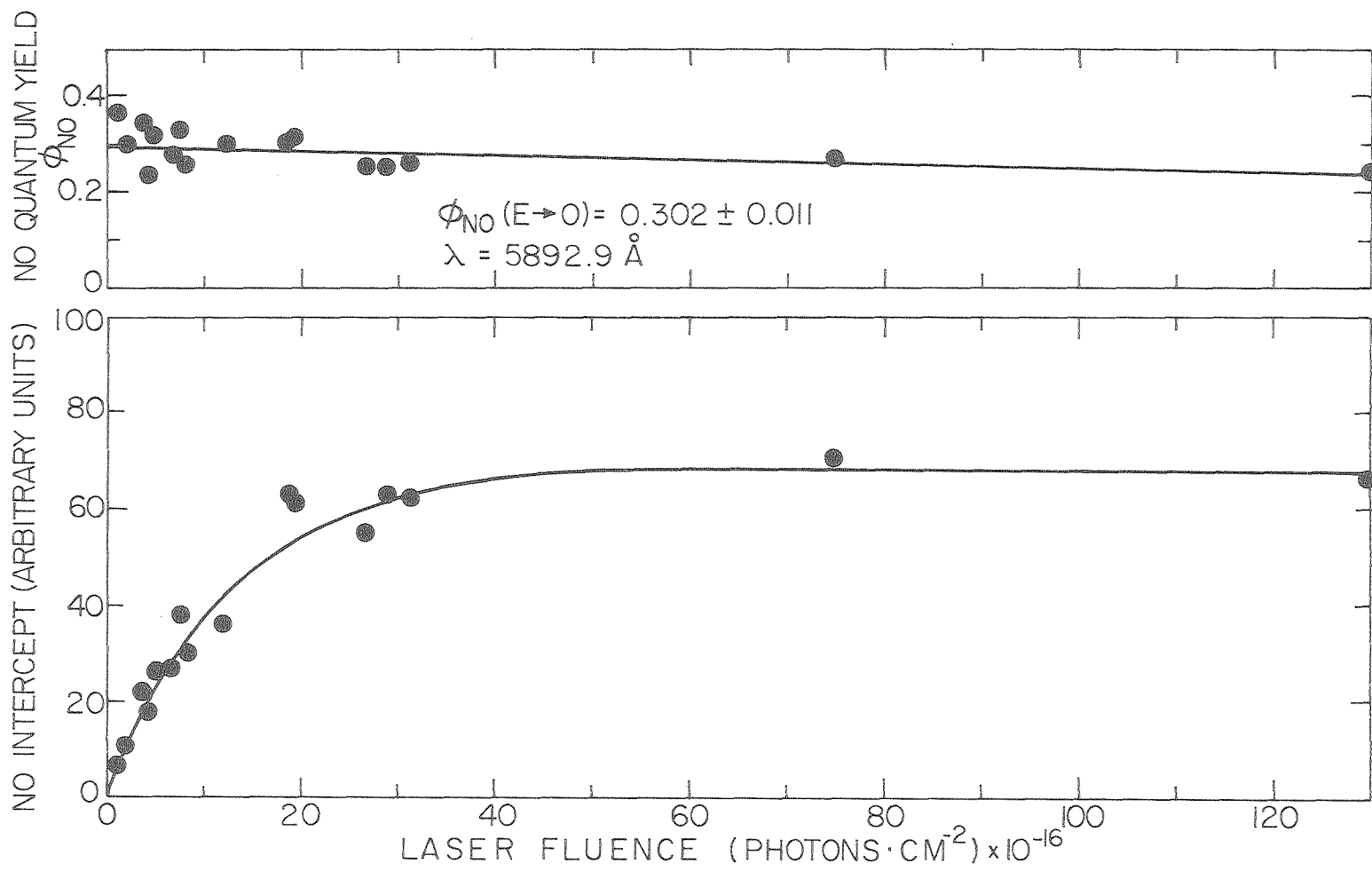
Table 26. [NO] Signal and ϕ_{NO} vs. Laser Fluence(Aperature = 0.79 cm^2)

	Laser Fluence (Photons $\cdot \text{cm}^{-2}$) 10^{-16}	$\left(\frac{-E\sigma_{\text{NO}_3}}{1-e} \right)$	[NO] Intercept (Arbitrary units) ^a	ϕ_{NO}
$\lambda = 5892.9 \text{ \AA}$	18.9	0.785	61.7	0.317
	1.92	0.145	10.4	0.297
	4.92	0.332	26.5	0.323
	8.00	0.479	30.0	0.257
	26.8	0.887	54.6	0.253
	6.53	0.413	26.2(b)	0.278(b)
	0.914	0.0718	6.70	0.366
	54.9	0.989	89.7	0.357
	18.9	0.785	61.7	0.308
	3.53	0.250	22.2	0.343
	7.60	0.462	38.4	0.326
	12.3	0.632	36.1(c)	0.298(c)
	74.8	0.998	70.0	0.269
	4.12	0.285	17.3	0.232
	30.8	0.918	61.9	0.258
	28.8	0.904	63.2	0.253
	131	1.00	66.2	0.239
				0.292 \pm .010
$\lambda = 6045.3 \text{ \AA}$	64.5	0.979	62.2	0.198
	0.997	0.0579	8.30	0.243
	3.33	0.181	9.40	0.306
				0.249 \pm .031
$\lambda = 5959.3 \text{ \AA}$	9.06	0.423	37.3	0.362
	1.67	0.0961	7.50	0.321
	6.24	0.315	35.1	0.437
				0.373 \pm .034

a) Adjusted for $[\text{NO}_3]$, NO sensitivity and number of laser shots/experiment.

b) 20 torr total pressure (N_2).

c) 25 torr total pressure (N_2).



XBL 799-7089

Figure 38. NO signal and quantum yield results vs. laser fluence.

5. Oxygen Atom Quantum Yields from N_2O_5 Photolysis

Complementing the recent work of Connell,¹⁷ several experiments were performed to measure directly primary photochemical products from ultraviolet photolysis of N_2O_5 . Referring to the relative cross sections for NO_2 and N_2O_5 (Figure 2), it is apparent that interference from NO_2 photolysis decreases with decreasing wavelength. To capitalize on this, photolysis was restricted to wavelengths below 3000 Å, where the maximum interference from NO_2 photolysis was less than 5%, minimizing the necessary correction.

Switching dyes and doubling crystals to $\lambda = 3518.3$ Å allowed in situ calibration of both O and NO by photolysis of NO_2 with negligible interference from N_2O_5 .

Several experiments were performed to detect NO as a product from N_2O_5 photolysis at 2950 Å. After sufficient laser shots to easily distinguish $\geq 2 \times 10^{10}$ molecules/cm³ of product, absolutely no deviation from a zero intercept was observed. At the N_2O_5 concentrations present, and an EO value of 2.3×10^{-4} , this represents an upper limit for primary NO production from N_2O_5 of $\phi_{NO} \leq 0.11$.

Subsequent experiments designed to detect oxygen atom were carried out at $2900 \text{ Å} < \lambda < 3000 \text{ Å}$, which was an optimum EO wavelength region. Small corrections for oxygen atom production from NO_2 were applied, and the observed product concentrations recorded in Table 27. Connell¹⁹ has shown that the observed oxygen atom quantum yield is a function of N_2O_5 and buffer gas pressures and of the rates of secondary reactions. Assuming a mechanism in which collisionally activated decomposition competes with deactivation of excited N_2O_5 , results in a first order

Table 27. Oxygen atom quantum yields from N_2O_5 Photolysis (concentrations in molecules $\cdot\text{cm}^{-3}$)

λ (Å)	$[\text{NO}_2] \cdot 10^{-14}$	$[\text{N}_2\text{O}_5] \cdot 10^{-15}$	$[\text{O}]_{t=0} \cdot 10^{-10}$	Laser Energy(mJ/Pulse)	$\phi_0(\text{N}_2\text{O}_5)^{\text{a,b)}$
2925.0	0.317	1.40	3.42	0.860	$0.36 \pm .07$
2925.0	0.324	1.38	2.84	0.723	$0.36 \pm .07$
2925.0	0.263	0.763	1.95	0.735	$0.44 \pm .10$
2925.0	1.27	1.59	5.58	1.32	$0.34 \pm .03$
3000.0	1.22	1.81	4.30	1.30	$0.33 \pm .03$
2950.0	1.78	1.05	4.28	1.54	$0.39 \pm .04$
2900.0	1.76	1.03	3.16	0.884	$0.38 \pm .09$

a) Error is uncertainty in measuring intercept.

b) Corrected for O atom from NO_2 photolysis.

dependence of quantum yield on N_2O_5 concentration. A rough extrapolation of Connell's data to adjust for the different buffer gas concentration used in this work was made and applied to his calculated expression for ϕ_0 versus $[\text{N}_2\text{O}_5]$. This adjusted expression is shown in Figure 39 along with the experimentally determined quantum yields determined here.

E. Detection of $\text{O}_2(^1\Sigma_g^+)$ and $\text{NO}_3(^2\text{B}_2)$ Fluorescence

The near coincidence of onset of NO_3 absorption with the thermodynamic limit for production of $\text{NO}(\text{X}^2\Pi_j) + \text{O}_2(^1\Sigma_g^+)$ suggests that this channel may be responsible for these photo products. However vibrationally excited ground state ($\text{X}^3\Sigma_g^-$) or excited state ($^1\Delta_g$) O_2 would appear reasonable, if O_2 is formed from a scissoring vibration in excited NO_3 .

Several attempts were made to observe $\text{O}_2(^1\Sigma_g^+)$ photoproduct following flash photolysis of NO_3 , over a 10^5 range of laser intensities, (100 mJ-1 μJ), using both photon counting and D.C. signal detection techniques. Calculated band shapes⁸⁸ for the $\text{O}_2(\text{b}^1\Sigma_g^+ \rightarrow \text{X}^3\Sigma_g^-)$ (0-0), (1-1), and (2-2) transitions at 300K are shown in Figure 40. The transmittance for the various filters used to isolate the emission, and the quantum efficiency of the photomultiplier tube (cooled RCA 31034A) are also shown. The detection optics were similar to those used for NO fluorescence measurements, but excluded much of the baffling so as to increase collection efficiency.

Due to the long radiative lifetime of $\text{O}_2(^1\Sigma_g^+)$ ($\tau_{\text{rad}} = 12$ sec) and its susceptibility to quenching, experiments were performed over several time regimes ranging from 1 μs to 20 msec time resolution.

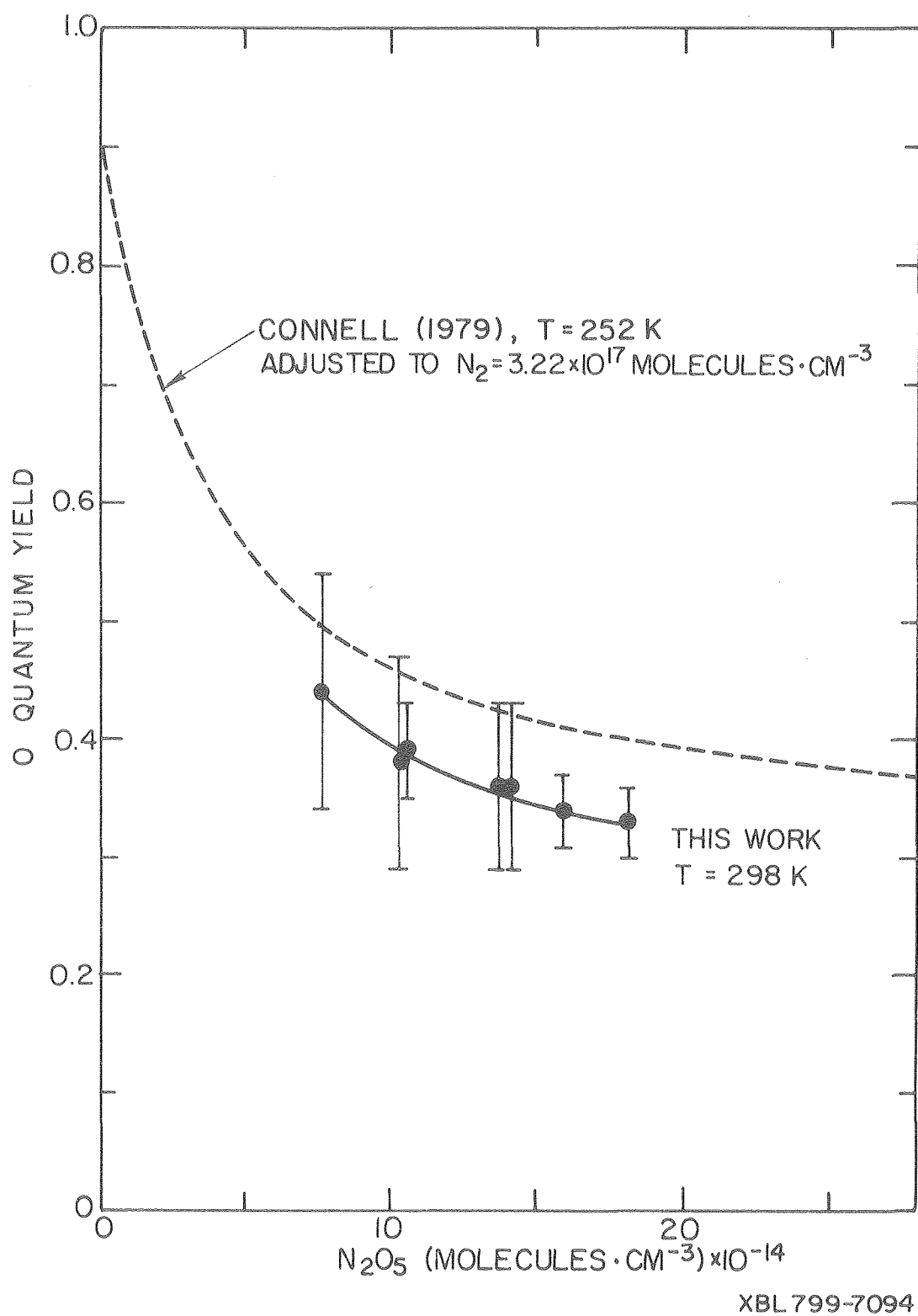
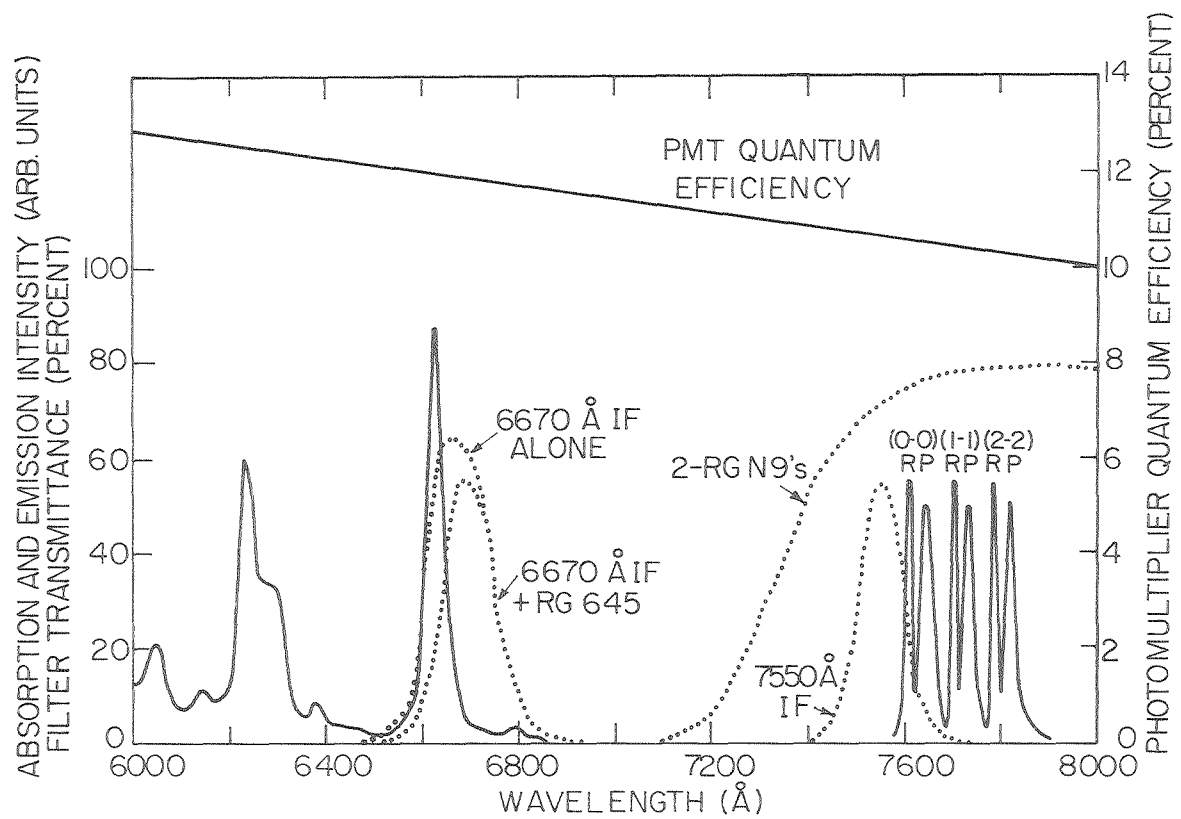


Figure 39. O quantum yield from photolysis of N_2O_5 at $2500 < \lambda < 3000 \text{ \AA}$.



XBL 799 -7101

Figure 40. Band shapes, PMT quantum yield and filter transmissions for $O_2(^1\Sigma_g^+)$ and NO_3^* fluorescence experiments.

The known quenching efficiency of N_2 results in an effective radiative lifetime of 1.7 ms for $O_2(^1\Sigma_g^+)$ and 170 ns for NO_2 (which also fluoresces in this region), under the conditions used. Fluorescence due to NO_2/N_2 was easily observed and was typically 3-4 times the scattered light level (N_2 alone). The large separation in the time regimes allowed NO_2 fluorescence to be subtracted from the first channel of the total signal.

Initial experiments utilized N_2 buffer gas and a 7550 Å interference filter (120 Å FWHM, 54% T), and scanned the wavelength region from 5850 to 6200 Å which covered the range of NO production. After corrections for NO_2 fluorescence (including the small amount of additional NO_2 from the flash), signal levels with and without NO_3 were virtually identical from 1 μs to 20 ms, and were equivalent to scattered light intensities. In an attempt to increase sensitivity, subsequent experiments utilized O_2 buffer which is 200 times less efficient than N_2 in quenching $O_2(^1\Sigma_g^+)$. However while the radiative lifetime with N_2 is 10 times faster than diffusion (1.7 ms), it now becomes ~10 times slower with O_2 , resulting in a potential signal enhancement of only ~10. A second advantage of O_2 is its ability to rapidly quench $^{87}O_2(^1\Sigma_g^+)$ $v=1,2$ to $v=0$, which are energetically possible and whose emission is not passed by the 7550 Å filter. The 7550 Å filter was subsequently replaced by two-RGN9 long pass filters to further increase collection efficiency. The band pass was closed by a rapid decrease in photomultiplier sensitivity at 8900 Å. Finally an excitation wavelength of 6050.0 Å was chosen, since NO_2 shows a minimum in absorption and virtually no emission in this region,⁸⁸ which further reduced background fluorescence. Emission from NO_2 (in O_2)

from a temperature controlled saturator was utilized as the background signal (vs. pure O_2) at an identical concentration to that present in the $NO_3/NO_2/O_2$ experiment. At 5850, 5893, 6050 and 6233 Å, fluorescence from NO_3 photolysis was again found to be essentially equal to the background (after correcting for NO_2 and laser fluence), throughout the various time and laser energy regimes.

An equally ambitious attempt was made to observe fluorescence from excited NO_3 as a function of excitation energy, below the photodissociation threshold. The excitation wavelengths investigated were 6005, 6135, 6170, 6233, 6270, 6375 (and 6600 Å). The detection optics were similar to those used for $O_2(^1\Sigma_g^+)$ observation, with an appropriate change in filtration. Initial experiments utilized a 6670 Å interference filter (64%T, 120 Å FWHM), and subsequent runs, added a Schott RG-645 long pass filter, to further reduce scattered light. The cell was not optimized to reduce scattered light from the laser making direct observation of NO_3 resonance fluorescence extremely difficult. However, scattered light was extremely low when the laser was tuned to shorter wavelengths, but increased rapidly beyond 6375 Å.

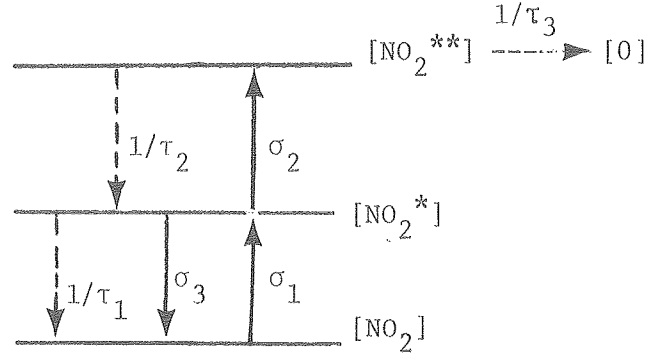
Analogous to the $O_2(^1\Sigma_g^+)$ experiments, both time regime and laser fluence was varied with wavelength, and fluorescence signals collected in digital (low E_L) and analog (high E_L) mode. Time constants were varied by terminating current pulses into a range of $50\Omega - 1M\Omega$ resistors, prior to a 9 bit A/D conversion or direct viewing on a 100 MHz storage oscilloscope. The majority of data was collected at the NO_3 , $v''=1$ absorption wavelength (6233.1 Å), where the total photodissociation quantum yield is 0.14 and E_0 is maximized. Emission due to NO_2/N_2 was easily observed and subtracted from $NO_3/NO_2/N_2$ data.

Results from excitation throughout the entire 6005-6375 Å region failed to produce any observable signal due to NO₃ fluorescence at 6600 Å < λ < 6800 Å. Calculation of detection sensitivity, limits of limiting values of molecular parameters and implications of both the NO₃^{*} and O₂(¹Σ_g⁺) studies will be presented in Section IV-C.

F. Nitrogen Dioxide Two Photon Cross Sections

In order to properly interpret results from high energy regime experiments, it was necessary to define the behavior of NO₂ under these laser intensities. Experiments were carried out at selected wavelengths between 4800 and 5850 Å, as well as several wavelengths in the red corresponding to regions exhibiting two photon behavior in NO₃. Laser fluences were approximately equal to those used in the previously described high energy experiments involving NO product yields. However, in the present experiments, oxygen atom was monitored, due to the higher resulting precision involved. Absolute oxygen atom sensitivity was determined from low energy NO₃ photolysis at 5850.0 Å, using the previously measured quantum yield of 1.00. The 100 ppm NO₂/N₂ calibration mixture was the source of flowing NO₂ at 10 torr total pressure, and a slight correction factor (see Figure 23) was applied to the observed signal, due to the absence of N₂O₅ and NO₃, which were present in the calibration runs.

Assuming a straightforward sequential two-photon pumping mechanism in the absence of coherence effects allows the use of rate equations to describe the process.⁷⁸⁻⁸¹ In a three level system, the following transitions are considered:



where $\frac{1}{\tau} = \frac{1}{\tau_{\text{rad}}} + \Sigma k_Q[Q]$ and $1/\tau_T = \frac{1}{\tau_1} + \frac{1}{\tau_2}$ (48)

The equations that govern the concentrations of NO_2 , NO_2^* , NO_2^{**} , and O , when the laser is on, are

$$\begin{aligned} \frac{d[NO_2]}{dt} &= -\sigma_1[NO_2]I + \sigma_3[NO_2^*]I + \frac{[NO_2^*]}{\tau_1} \\ \frac{d[NO_2^*]}{dt} &= \sigma_1[NO_2]I - \sigma_2[NO_2^*]I - \sigma_3[NO_2^*]I - \frac{[NO_2^*]}{\tau_1} \\ \frac{d[NO_2^{**}]}{dt} &= \frac{d[O]}{dt} = \sigma_2I[NO_2^*] - \frac{[NO_2^{**}]}{\tau_2} - \frac{[NO_2^{**}]}{\tau_3} \end{aligned} \quad (49)$$

While the possibility of using the steady state approximation exists, the exact solution for such systems has been solved repeatedly in journal articles and textbooks.⁸² Solving this set of coupled differential equations, results in an expression for $[O]$, immediately following the laser pulse (T_L)

$$[O] = \left(\frac{[NO_2]\sigma_1\sigma_2I^2}{(\sigma_2+\sigma_3-\sigma_1)I+1/\tau_T} \right) \left(\frac{\exp\{-(\sigma_2I+\sigma_3I+1/\tau_T)T_L\}-1}{\sigma_2I+\sigma_3I+1/\tau_T} - \frac{\exp\{-\sigma_1IT_L\}-1}{\sigma_1I} \right) \quad (50)$$

The comparable steady state expression yields:

$$[O] = \frac{[NO_2]\sigma_1\sigma_2I^2}{(\sigma_2+\sigma_3)I+1/\tau_1} T_L \quad (51)$$

Measurement of $[O]_{t=0}$, the laser intensity, and the one photon cross section results in σ_2 . Both the exact and steady state expression result in two photon cross sections, which deviate by less than 10%. Assuming fast vibrational relaxation of the first excited state⁸³ and a concomitantly low value for $I\sigma_3[NO_2^*]$, only affects the calculated values by about 1-2%.

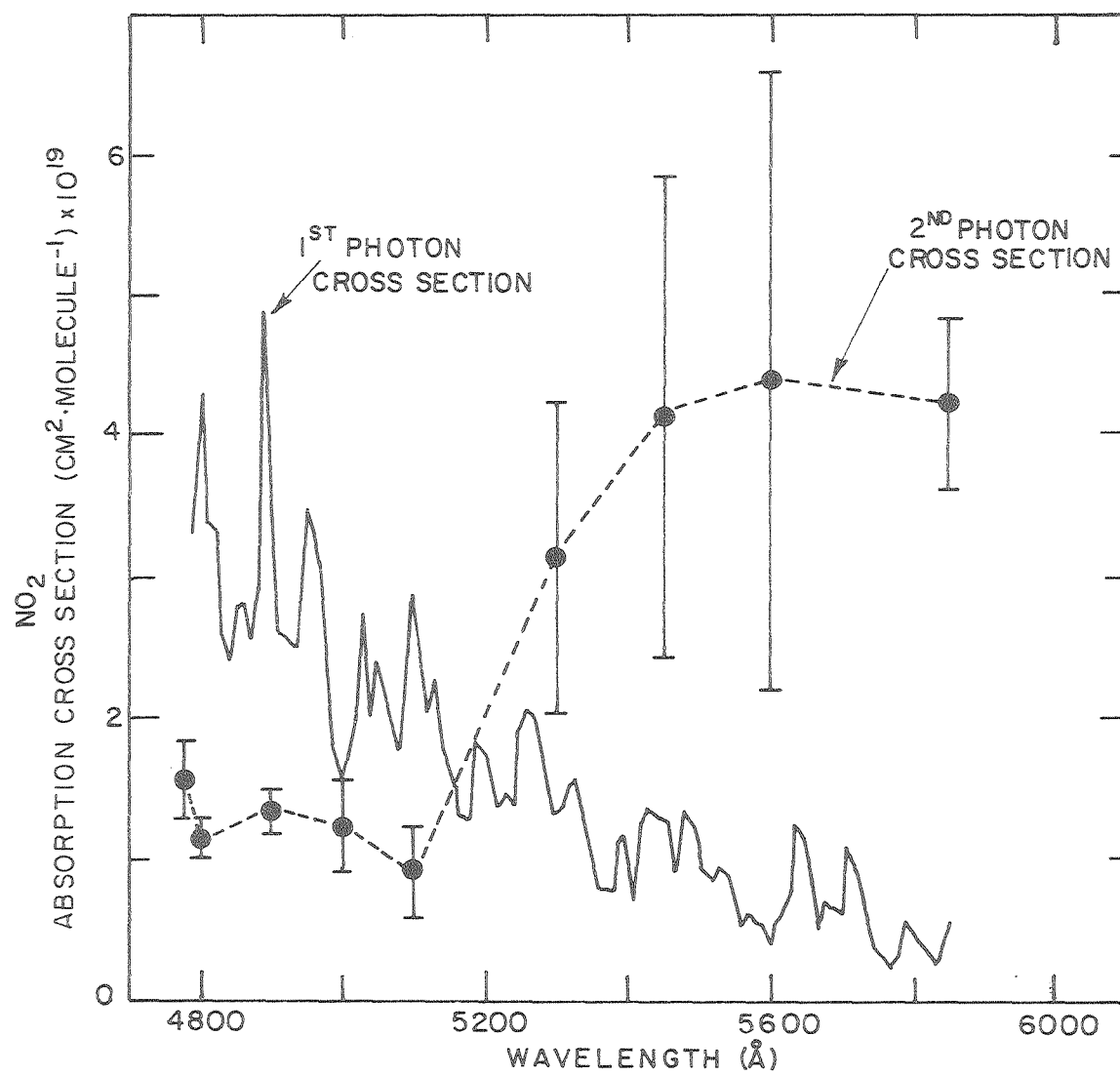
The exact expression (Equation 50) was solved iteratively for σ_2 for the various $[O]$ concentrations measured. One photon NO_2 cross sections were from unpublished measurements of Graham,⁸⁴ and the values of the following kinetic quantities used were

$$\begin{aligned} [NO_2] &= 3.7 \times 10^{13} \text{ molecules cm}^{-3} \\ [Q] = [N_2] &= 3.22 \times 10^{17} \text{ molecules cm}^{-3} \\ k_Q(N_2) &= 2.1 \times 10^{-11} \text{ molecules}^{-1} \cdot \text{cm}^3 \cdot \text{sec}^{-1} \\ 1/T_R &= 2.5 \times 10^4 \text{ sec}^{-1} \\ T_L &= 4 \times 10^{-7} \text{ sec (FWHM)} \\ I\sigma_3[NO_2^*] &\rightarrow 0 \end{aligned}$$

The resulting values of σ_2 (and $\sigma_1 \cdot \sigma_2$) are given in Table 28, where the standard deviations represent the uncertainty in measuring the 0 atom intercept. A plot of the first and second photon NO_2 cross sections is shown in Figure 41 versus wavelength, and Figure 42 shows the two photon cross section ($\sigma_1 \cdot \sigma_2$) versus wavelength. Due to the rapid decrease in $\sigma_1(NO_2)$ and increase in $\sigma(NO_3)$ with increasing wavelength, corrections for two photon photolysis of NO_2 become very

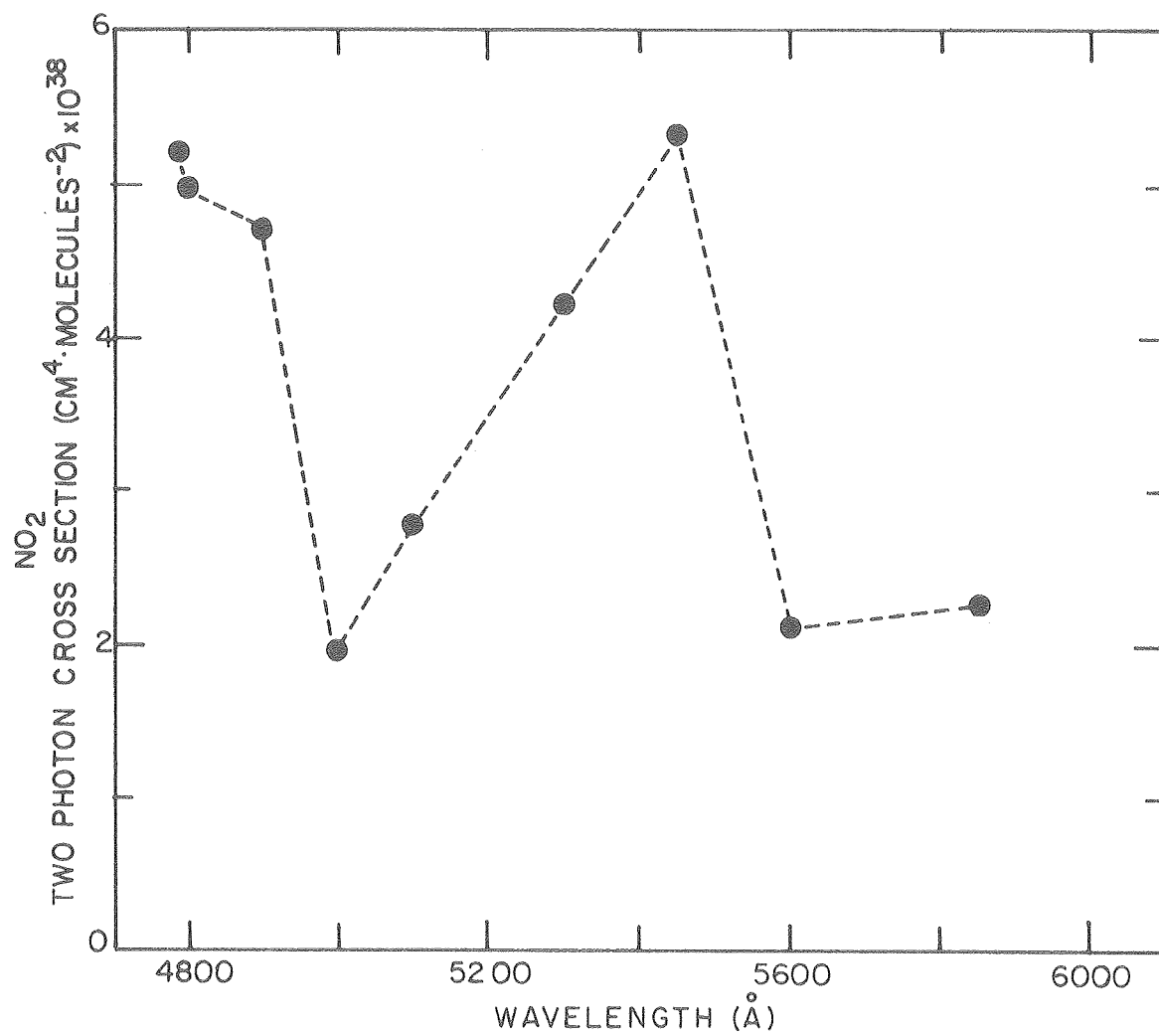
Table 28. NO₂ Two Photon Cross Sections

Wavelength (Å)	E_{laser} (Photons·cm ⁻²) ×10 ⁻¹⁷	$[O]_{t=0}$ (Molecules cm ⁻³) ×10 ⁻¹¹	σ_2 (cm ² ·molecules ⁻¹) ×10 ¹⁹	$\sigma_1 \cdot \sigma_2$ (cm ⁴ ·molecules ⁻²) × 10 ³⁸
4790.9	5.25	1.18±.24	1.55±.32	5.21
4800.0	5.35	1.12±.15	1.15±.15	4.98
4900.0	4.76	0.883±.11	1.37±.17	4.73
5000.0	4.47	0.341±.094	1.25±.134	1.96
5100.0	3.95	0.371±0.11	0.985±.30	2.81
5300.0	1.49	0.0846±0.031	3.24±1.15	4.34
5450.0	2.57	0.310±0.13	4.25±1.7	5.44
5600.0	1.81	0.0558±.028	4.00±2.2	1.93
5850.0	7.68	1.12±0.16	4.40±.61	2.26
6850.0	4.85	0.0901±0.0023	8.10±2.1	0.454



XBL 799-7093

Figure 41. First and second photon absorption cross section for NO₂ versus wavelength.



XBL 799-7092

Figure 42. Two-photon cross sections for NO₂ versus wavelength.

minor beyond $\sim 5600 \text{ \AA}$, at the conditions necessary for $(1 - e^{-E\sigma})$ to approach 1. Values of $\sigma_2(\text{NO}_2)$ at 6600, 6750 and 6850.0 \AA were estimated (due to lack of good $\sigma_1(\text{NO}_2)$ cross sections), and the corrections at these wavelengths were found to be negligible.

G. Rate of the $0 + \text{NO}_2$ Reaction

The decay of oxygen atom with time was determined mainly by its fast reaction with NO_2 and to a lesser extent ($< 5\%$) by $0 + \text{NO}_3$. The reaction of $0 + \text{N}_2\text{O}_5$ has been shown to be very slow,^{9,17,86} (as is $0 + \text{HNO}_3$)^{85,86} and can be ignored in this system.

During the course of measuring O atom quantum yields, a substantial amount of data was also accumulated, measuring the rate of O atom decay as a function of NO_2 and NO_3 . One hundred and forty-four data points obtained under pseudo first order kinetic conditions have been tabulated representing various modes of atomic oxygen generation, namely visible photolysis of $\text{NO}_3/\text{N}_2\text{O}_5$ mixtures, ultraviolet photolysis of a) pure NO_2 , b) NO_2 in N_2O_5 mixtures, c) N_2O_5 itself, and visible two-photon NO_2 photolysis. Subjecting this entire data base to a linear least squares analysis (after correcting for loss due to the reaction of $0 + \text{NO}_3$ ⁹) resulted in a rate constant for $0 + \text{NO}_2$ of

$$k_{0, \text{NO}_2} = 1.033 \pm 0.0084 \times 10^{-11} \text{ molecules}^{-1} \cdot \text{cm}^3 \cdot \text{sec}^{-1} \quad (R^2 = 0.991) \quad (52)$$

with an intercept of

$$k_{\text{diffusion}} = 102.7 \pm 8.4 \text{ sec}^{-1} \quad (53)$$

Attempts to identify correlated data sets based on mode of atomic

oxygen-atom generation were not successful, indicating the absence of unidentified channels of decay (possibly due to excited species, etc.).

Since the individual data points are closely clustered about a specific concentration present in each of the 14 runs, groups of data points have been averaged about a mean NO_2 concentration, for ease of graphical representation. Table 29 presents this clustered $\text{O} + \text{NO}_2$ rate data which is subsequently plotted in Figure 43. The linear least square fit to this grouped data resulted in

$$k_{\text{O},\text{NO}_2} = 1.029 \pm 0.012 \times 10^{-11} \text{ molecules}^{-1} \cdot \text{cm}^3 \cdot \text{sec}^{-1} \quad (R^2 = 0.998) \quad (54)$$

with an intercept of

$$k_{\text{diffusion}} = 102.5 \pm 17.5 \text{ sec}^{-1} \quad (55)$$

which is very close to that obtained from all of the individual data points. This value is compared to the accepted⁸⁶ value of

$$k_{\text{O},\text{NO}_2} = 9.3 \pm 0.93 \times 10^{-12} \text{ molecules}^{-1} \cdot \text{cm}^3 \cdot \text{sec}^{-1} \quad (56)$$

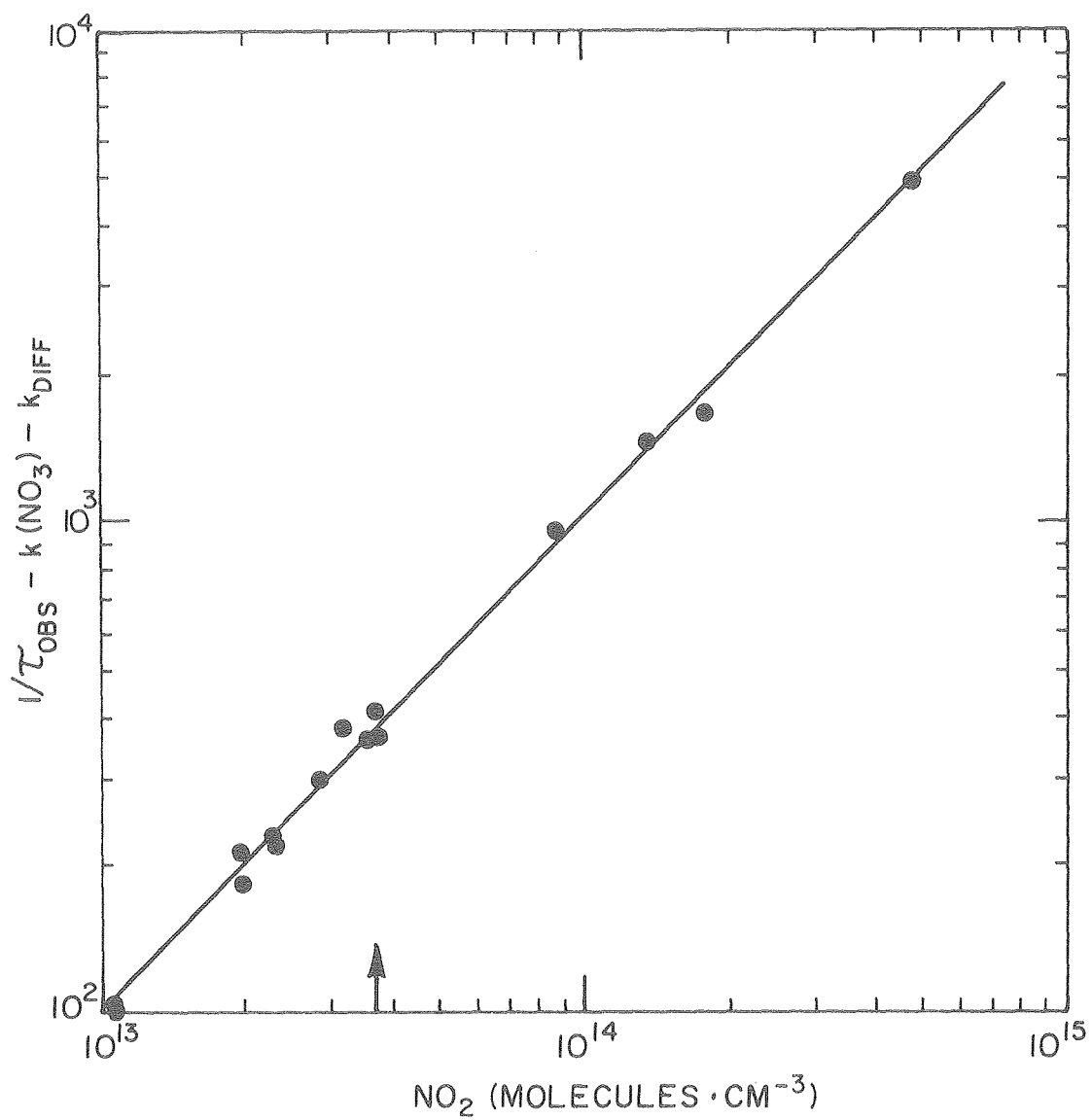
The complete data base of 144 points is given in Appendix H .

H. Calculation of Laser Heating

The thermal energy deposition per laser shot can be calculated using typical experimental parameters. Assuming a maximum laser energy of 1/2 Joule at 6000 Å, and a typical NO_3 absorbance of $1.7 \times 10^{-3}\%$, results in an absorbed energy of 17 μJoules. Thermalizing this with 10 torr of buffer gas, in an irradiated volume of $\sim 12 \text{ cm}^3$ results in:

Table 29. Clustered O + NO₂ Rate Data

$1/T_{\text{Obs}} - k(\text{NO}_3) \pm \sigma_y$	Average $[\text{NO}_2](\text{molecules cm}^{-3})$ $\times 10^{-13} \pm \sigma_x$	Data Points Averaged
1056±3	8.69±.09	10
202.3±10	1.05±.03	20
205.5±5	1.05±.01	28
286.1±8	1.98±.09	8
513.7±5	3.70±.01	2
321.7±4	2.30±.06	8
401.9±40	2.84±.51	8
485.5±33	3.17±.02	8
315.1±16	1.98±.10	12
329 ± 4	2.29±.05	2
1544 ± 5	13.7 ±.14	16
460 ± 128	3.6 ±.12	16
5065 ± 159	47.9 ±.22	4
1777 ± 3	17.8 ±.02	2
		144 total



XBL799-7099

Figure 43. Plot of $O + NO_2$ reaction rate.

Low E σ experiments produce ΔT values of $\sim 0.01^\circ\text{C}/\text{shot}$. Mixing of the irradiated gas within the total cell volume results in values of:

$$\Delta T(\text{low } E\sigma) = 8.3 \times 10^{-4} \text{ } ^\circ\text{C}/\text{shot} \quad . \quad (59)$$

In all experiments the cell contents were completely flushed between shots and no discernable temperature rise was ever observed in cell temperature due to laser heating.

IV. Results and Discussion

A. NO₃ Cross Sections

The only previous quantitative measurement of NO₃ cross sections result from work by Graham and Johnston⁹ and Schott and Davidson.⁵ Graham utilized a molecular modulation technique in which an absolute NO₃ absorption cross section was calculated from the ratio of modulation signals for N₂O₅ and NO₃. The NO₃ modulation was monitored at 627 nm, the center of a fairly broad absorption band that obeyed Beer's Law (at 1 atmosphere total pressure), and N₂O₅ was observed at its 8.03 μm infrared absorption peak. A complete CHEMK⁶⁰ computer simulation was used to determine a stoichiometric factor (SF) relating the NO₃ and N₂O₅ concentration modulations. The resulting cross section at 0.83 nm resolution was obtained from the following experimental quantities:

$$\sigma_{\text{NO}_3}(627 \text{ nm}) = \sigma_{\text{N}_2\text{O}_5}(8.03 \text{ } \mu\text{m}) \frac{1}{\text{SF}} \frac{A_{\text{NO}_3}}{A_{\text{N}_2\text{O}_5}} \frac{L_{\text{N}_2\text{O}_5}}{L_{\text{NO}_3}} \quad (58)$$

where L represents the optical path length. This value was then used to adjust relative cross section values obtained from optical absorption measurements in NO₂/O₃/N₂ mixtures, correcting for absorption due to O₃.

The work of Schott and Davidson involved a shock tube study in which flash spectrograms of N₂O₅ were observed as a function of time following the shock. From optical densities of NO₂ and N₂O₅ (corrected for temperature), measurements of NO₃ absorption were obtained in the presence of ca. 10⁻² mole/liter of argon and at a resolution of 3.6 nm.

A wavelength of 652 nm, which is between the two strongest bands of NO_3 (6233 and 662.5 nm), was chosen since it allowed simultaneous measurement of NO_2 and NO_3 . In addition, avoiding strong absorption peaks obviates difficulties which might arise from pressure and temperature broadening and departure from Beer's Law due to non-uniform absorption over a finite spectral interval. The data was obtained at elevated temperatures (650-1050K) and extrapolated to 300K, resulting in a value of $8.4 \times 10^{-19} \text{ cm}^2 \cdot \text{molecule}^{-1}$ at 652 nm. Graham and Johnston's value at this wavelength is $3.9 \times 10^{-19} \text{ cm}^2 \cdot \text{molecule}^{-1}$, and the present study resulted in a value of $5.7 \times 10^{-19} \text{ cm}^2 \cdot \text{molecule}^{-1}$.

While the inordinately high value obtained by Schott and Davidson is not easily explainable, the larger cross section obtained in this work compared to that obtained by Graham and Johnston may be due to a deviation from Beer's Law behavior. When the absorption band consists of fine rotational lines, a deviation from linear behavior is usually observed when the widths of the lines are much narrower than the spectral width of the light source. In a strong absorption feature, the line centers may be optically thick, resulting in a lowered apparent cross section. Either by substantially reducing the pressure of absorber or by broadening the lines by addition of sufficiently high pressure of buffer gas, the lack of resolution may be circumvented. The low optical density at the peak maximum in the present work ($\sim 5 \times 10^{-4}$) assures that line centers are not saturated. This is further confirmed by agreement in cross section measurements at 5850.0 and 5892.3 Å, which represent a local NO_3 absorption minimum and maximum respectively. The direct absorption performed by Graham

et al. necessitates large optical densities in the peak maxima in order adequately to measure the weaker spectral features. A further indication that spectral resolution is involved, was the observation by Graham et al. that a 7% increase in cross section resulted by (decreased time constant and) decreasing the resolution by a factor of ~ 4 . Finally, the use of Graham's cross sections to interpret the present work results in primary quantum yields of ~ 1.5 , which are chemically unrealistic. The cross section is defined by $\sigma = (1/NL) \ln_e (I_0/I)$.

NO_3 cross sections, adjusted by the factor of 1.46, are given in Table 30. For direct observation of atmospheric NO_3 by absorption, the question of total pressure and optical density may need to be carefully considered.

B. Quantum Yield Determinations

1. Nitric Oxide and Oxygen from Measurements from NO_3 Photolysis.

The quantum yields for NO and O production versus wavelength have been averaged (Table 31) and presented previously (Figure 35A). This table also lists the sum of both O and NO channel quantum yields, which is shown in Figure 44 superimposed on a relative NO_3 absorption spectrum. Interpolated values over each nm for both ϕ_{O} and ϕ_{NO} have been tabulated, as well as the product of quantum yield and cross section (Tables 32 and 33). The data from these tables have been plotted, showing the photochemically active bands associated with each channel (Figure 45).

The important photochemical parameter is the product of absorption cross section and quantum yield. Graham and Johnston³⁹ obtained this product from an averaged $\overline{\sigma_{\text{NO}_3}}$ and $\overline{\phi_{\text{O,NO}}}$ over an assumed

Table 30. NO_3 absorption cross sections ($\text{cm}^2 \cdot \text{molecule}^{-1}$, base e) at 10 torr and 297 K, averaged over each nm - corrected values from Graham.⁹

λ	$10^{19}\sigma$	λ	$10^{19}\sigma$	λ	$10^{19}\sigma$	λ	$10^{19}\sigma$
400	0.0	446	3.4	492	13.0	538	30.8
401	0.1	447	3.6	493	13.0	539	27.4
402	0.1	448	4.1	494	12.8	540	26.4
403	0.4	449	4.1	495	13.3	541	24.5
404	0.3	450	3.9	496	15.2	542	24.5
405	0.7	451	4.1	497	16.4	543	20.9
406	0.4	452	4.5	498	15.8	544	20.3
407	0.1	453	4.7	499	15.0	545	23.7
408	0.4	454	5.0	500	14.3	546	29.8
409	0.7	455	5.1	501	13.7	547	37.4
410	0.9	456	4.7	502	13.3	548	40.1
411	0.7	457	5.0	503	13.9	549	36.4
412	0.4	458	5.4	504	15.3	550	32.7
413	1.0	459	5.7	505	16.9	551	31.2
414	1.0	460	5.7	506	17.4	552	31.5
415	0.9	461	5.3	507	16.6	553	32.4
416	0.4	462	5.1	508	15.5	554	35.8
417	0.6	463	5.5	509	16.4	555	40.6
418	0.9	464	6.0	510	19.0	556	43.1
419	1.3	465	6.6	511	22.0	557	43.8
420	1.3	466	6.6	512	23.5	558	46.3
421	1.3	467	7.0	513	22.0	559	50.1
422	1.2	468	7.3	514	20.6	560	47.2
423	1.5	469	7.6	515	20.4	561	41.6
424	1.8	470	7.2	516	20.4	562	39.1
425	1.9	471	7.3	517	19.0	563	37.8
426	1.3	472	7.9	518	17.7	564	36.2
427	1.2	473	8.0	519	18.7	565	36.1
428	1.8	474	8.2	520	21.0	566	37.7
429	1.8	475	8.6	521	23.1	567	37.2
430	1.8	476	9.3	522	25.1	568	37.5
431	2.2	477	9.9	523	24.2	569	38.4
432	2.0	478	9.6	524	21.9	570	36.9
433	2.2	479	9.3	525	20.1	571	36.6
434	2.5	480	9.3	526	20.0	572	36.2
435	3.1	481	9.5	527	22.0	573	36.1
436	3.1	482	9.2	528	26.1	574	37.2
437	2.6	483	8.9	529	30.7	575	39.4
438	2.6	484	9.1	530	30.5	576	42.6
439	3.1	485	9.6	531	27.9	577	44.5
440	2.8	486	10.8	532	26.4	578	44.2
441	2.8	487	11.7	533	25.3	579	42.9
442	2.9	488	11.7	534	25.8	580	43.7
443	2.8	489	12.6	535	29.5	581	46.7
444	3.1	490	13.6	536	33.9	582	45.3
445	3.4	491	13.4	537	34.7	583	39.1

(continued. . .)

Table 30 (continued)

λ	$10^{19}\sigma$	λ	$10^{19}\sigma$	λ	$10^{19}\sigma$
584	36.1	630	93.6	676	4.5
585	35.9	631	73.3	677	5.8
586	40.1	632	47.7	678	8.0
587	50.8	633	29.1	679	8.6
588	65.4	634	19.3	680	7.2
589	80.6	635	15.5	681	5.1
590	82.8	636	18.0	682	3.6
591	75.8	637	23.9	683	2.3
592	70.5	638	25.7	684	1.3
593	63.1	639	19.6	685	0.7
594	57.2	640	14.3	686	0.4
595	57.1	641	11.4	687	0.3
596	60.7	642	9.9	688	0.6
597	59.7	643	10.1	689	0.3
598	51.7	644	10.4	690	0.1
599	42.2	645	9.8	691	0.0
600	35.8	646	8.2	692	0.0
601	35.8	647	7.2	693	0.1
602	41.5	648	6.3	694	0.1
603	49.5	649	5.4	695	0.3
604	58.4	650	4.7	696	0.6
605	61.0	651	4.8	697	0.6
606	49.3	652	5.7	698	0.6
607	33.9	653	6.9	699	0.6
608	23.2	654	8.3	700	0.4
609	19.4	655	10.1	701	0.3
610	19.7	656	13.0	702	0.3
611	20.9	657	17.2	703	0.1
612	24.7	658	24.5	704	0.0
613	31.7	659	40.3		
614	32.7	660	74.8		
615	29.1	661	148		
616	25.4	662	249		
617	24.4	663	249		
618	26.7	664	168		
619	29.5	665	107		
620	36.1	666	71.0		
621	58.1	667	43.4		
622	111	668	25.5		
623	176	669	15.6		
624	170	670	10.9		
625	126	671	8.8		
626	102	672	8.3		
627	101	673	6.9		
628	101	674	5.3		
629	97.8	675	4.4		

Table 31. Averaged NO and O quantum yields.

λ_{laser} (Angstroms)	$\phi_0^{(a)}$	$\phi_{\text{NO}}^{(a)}$	$\phi_{\text{NO}}^{(b)}$	$(\phi_0 + \phi_{\text{NO}})^{(c)}$
4700.0	.77	—	0	.77
4800.0	.79	—	< .010	.79
4900.0	.68	—	0	.68
5000.0	.87	—	0	.87
5100.0	.79	—	0	.79
5200.0	—	—	< .006	—
5216.7	.70	—	—	.70
5271.2	—	—	0	—
5288.7	.81	—	—	.81
5300.0	.70	—	—	.70
5400.0	.76	—	< .0014	.76
5474.7	.87	—	—	.87
5500.0	.73	—	0	.73
5589.5	.80	—	—	.80
5600.0	.75	—	0	.75
5658.4	.89	—	—	.89
5688.0	.95	—	—	.95
5700.0	.86	—	0	.86
5800.0	—	—	0	—
5813.4	.92	—	.0021	.92
5850.0	1.00	.0055	.039	1.02
5875.0	—	.156	—	—
5892.9	.72	.32	.29	1.03
5945.0	—	—	.35	—
5959.0	.58	.32	.36	.92
6005.0	.61	.25	.27	.87
6045.3	.44	.26	.27	.71
6095.0	.41	.22	.15	.63
6135.0	.33	.078	.097	.42
6170.0	.32	.13	.094	.43

(continued. . .)

Table 31 continued.

6200.0	.36	(.075) ^c	---	(.44)
6233.1	.076 ^d	.036	.097	.14
6250.0	0.14	(0) ^c	---	.14
6270.0	.098	---	.067	.17
6375.0	---	---	.024	---
6500.0	0 ^d	---	---	---
6600.0	0 ^d	---	.0040	.0040
6625.0	---	---	.0047	.0047
6650.0	---	---	0	0
6790.0	---	---	0	---

a) Low E σ regime.b) High E σ regime

c) Estimated value

d) Limit $E_{\text{laser}} \rightarrow 0$ e) ϕ_{NO} averaged: $((a)+(b))/2$.

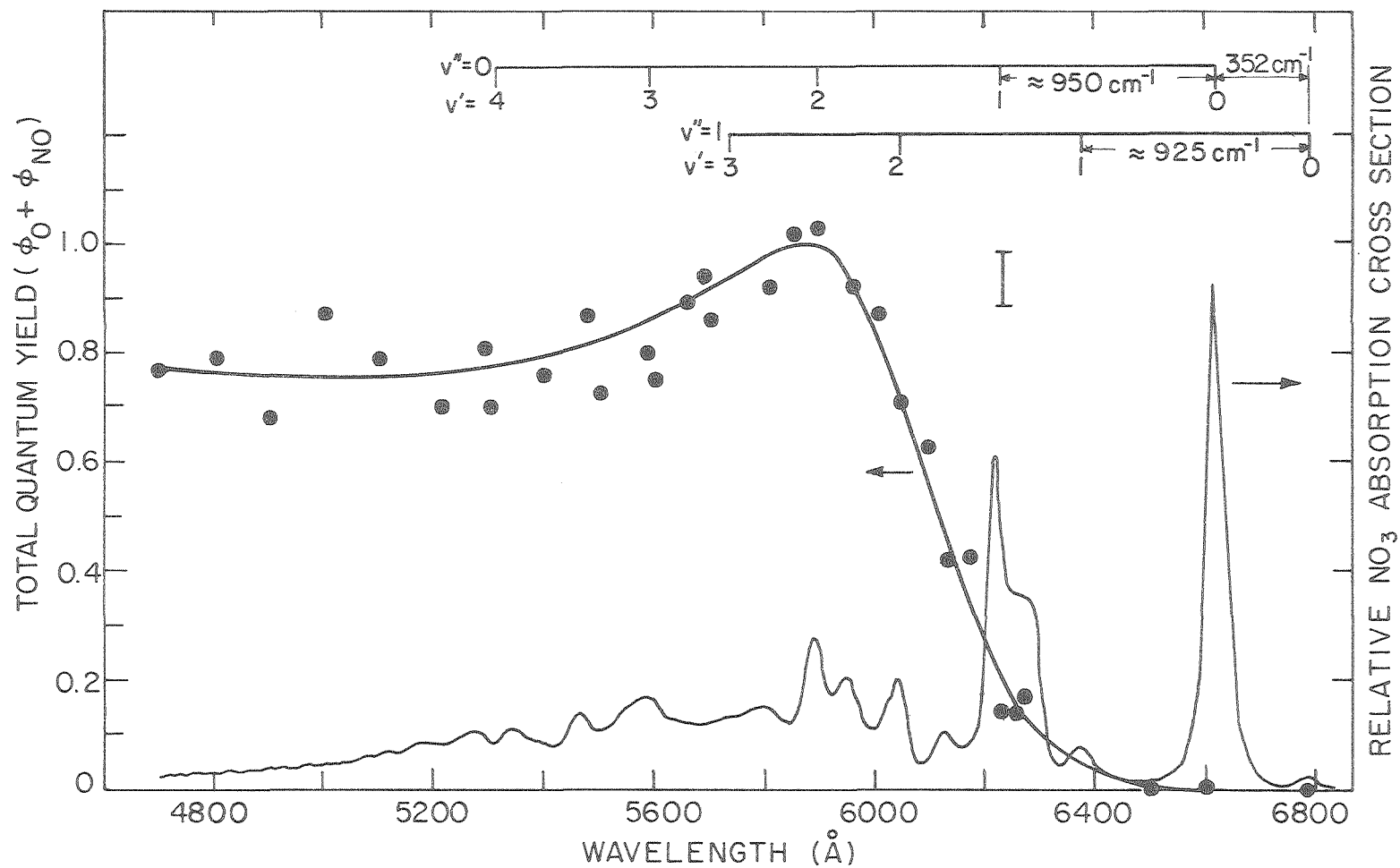


Figure 44. Total quantum yield for NO_3 photodissociation versus wavelength. XBL 799-7079

Table 32. Wavelength (nm) vs. non-zero values of ϕ_0 and $\phi_0 \sigma_{\text{NO}_3}$
 $(\text{cm}^2 \cdot \text{molecule}^{-1}) \cdot 10^{19}$, interpolated over each nm from
 470-685 nm.

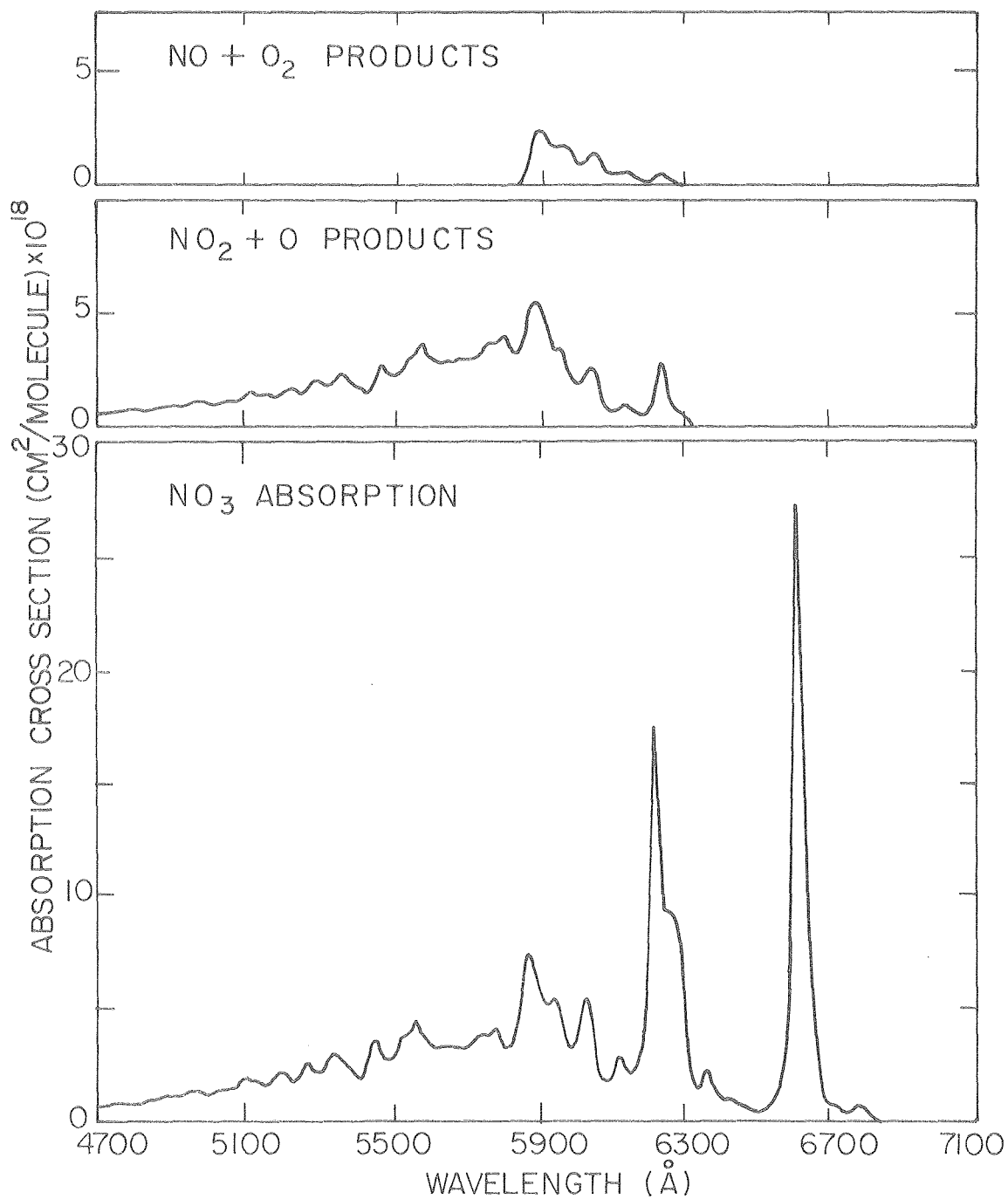
λ	ϕ_0	$\phi_0 \sigma_{\text{NO}_3}$	λ	ϕ_0	$\phi_0 \sigma_{\text{NO}_3}$	λ	ϕ_0	$\phi_0 \sigma_{\text{NO}_3}$
470	0.770	5.5	516	0.753	15.4	561	0.845	35.2
471	0.770	5.6	517	0.754	14.3	562	0.850	33.3
472	0.769	6.1	518	0.754	13.3	563	0.855	32.3
473	0.769	6.2	519	0.755	14.1	564	0.860	31.1
474	0.768	6.3	520	0.755	15.9	565	0.865	31.2
475	0.768	6.6	521	0.756	17.4	566	0.870	32.8
476	0.767	7.2	522	0.756	19.0	567	0.875	32.6
477	0.767	7.6	523	0.757	18.3	568	0.880	33.0
478	0.766	7.4	524	0.757	16.6	569	0.885	34.0
479	0.766	7.2	525	0.758	15.3	570	0.900	33.2
480	0.765	7.1	526	0.758	15.2	571	0.905	33.2
481	0.765	7.3	527	0.759	16.7	572	0.910	32.9
482	0.764	7.0	528	0.759	19.8	573	0.915	33.0
483	0.764	6.8	529	0.760	23.3	574	0.920	34.3
484	0.763	6.9	530	0.760	23.2	575	0.930	36.7
485	0.763	7.3	531	0.762	21.2	576	0.940	40.1
486	0.762	8.2	532	0.764	20.2	577	0.950	42.3
487	0.762	8.9	533	0.766	19.3	578	0.960	42.5
488	0.761	8.9	534	0.768	19.8	579	0.965	41.4
489	0.761	9.5	535	0.770	22.7	580	0.970	42.3
490	0.760	10.3	536	0.772	26.1	581	0.975	45.6
491	0.760	10.2	537	0.774	26.9	582	0.980	44.4
492	0.759	9.9	538	0.776	23.9	583	0.985	38.5
493	0.759	9.9	539	0.778	21.3	584	0.990	35.7
494	0.758	9.7	540	0.780	20.6	585	1.000	35.9
495	0.758	10.1	541	0.782	19.2	586	0.990	39.7
496	0.757	11.5	542	0.784	19.2	587	0.940	47.8
497	0.757	12.4	543	0.786	16.4	588	0.880	57.6
498	0.756	11.9	544	0.788	16.0	589	0.750	60.4
499	0.756	11.4	545	0.790	18.7	590	0.750	62.1
500	0.755	10.8	546	0.792	23.6	591	0.730	55.3
501	0.755	10.4	547	0.794	29.7	592	0.710	50.1
502	0.754	10.0	548	0.796	32.0	593	0.690	43.5
503	0.754	10.5	549	0.798	29.0	594	0.660	37.8
504	0.753	11.5	550	0.800	26.2	595	0.650	37.1
505	0.753	12.7	551	0.804	25.1	596	0.630	38.3
506	0.752	13.1	552	0.808	25.5	597	0.610	36.4
507	0.752	12.5	553	0.812	26.3	598	0.590	30.5
508	0.751	11.6	554	0.816	29.2	599	0.570	24.0
509	0.751	12.3	555	0.820	33.3	600	0.560	20.0
510	0.750	14.2	556	0.824	35.5	601	0.540	19.3
511	0.750	16.5	557	0.828	36.3	602	0.520	21.5
512	0.751	17.7	558	0.832	38.5	603	0.510	25.2
513	0.751	16.6	559	0.836	41.9	604	0.500	29.2
514	0.752	15.5	560	0.840	39.6	605	0.490	29.9
515	0.753	15.4						

TABLE 32 (continued)

λ	ϕ_{NO}	$\phi_{\text{NO}}^{\sigma_{\text{NO}_3}}$
606	0.470	23.2
607	0.460	15.6
608	0.440	10.2
609	0.430	8.3
610	0.410	8.1
611	0.400	8.4
612	0.380	9.4
613	0.370	11.7
614	0.360	11.8
615	0.340	9.9
616	0.320	8.1
617	0.280	6.8
618	0.270	7.2
619	0.250	7.4
620	0.230	8.3
621	0.200	11.6
622	0.190	21.1
623	0.180	31.6
624	0.150	25.5
625	0.120	15.2
626	0.090	9.2
627	0.080	8.1
628	0.070	7.0
629	0.060	5.9
630	0.050	4.7
631	0.040	2.9
632	0.030	1.4
633	0.020	0.6
634	0.020	0.4
635	0.010	0.1
636	0.005	0.1
637	0.003	0.1
638	0.001	0.0
639	0.000	0.0
640	0.000	0.0

Table 33. Wavelength (nm) vs. non-zero values of ϕ_{NO} and $\phi_{\text{NO}}\sigma_{\text{NO}_3}$ ($\text{cm}^2 \cdot \text{molecule}^{-1}$) $\times 10^{19}$, interpolated over each nm from 470–685 nm.

λ	ϕ_{NO}	$\phi_{\text{NO}}\sigma_{\text{NO}_3}$
585	0.000	0.0
586	0.050	2.0
587	0.120	6.1
588	0.250	16.4
589	0.300	24.2
590	0.310	25.7
591	0.315	23.9
592	0.319	22.5
593	0.315	19.9
594	0.313	17.9
595	0.310	17.7
596	0.305	18.5
597	0.300	17.9
598	0.290	15.0
599	0.280	11.8
600	0.270	9.7
601	0.265	9.5
602	0.260	10.8
603	0.260	12.9
604	0.255	14.9
605	0.250	15.3
606	0.245	12.1
607	0.240	8.1
608	0.230	5.3
609	0.220	4.3
610	0.210	4.1
611	0.200	4.2
612	0.185	4.6
613	0.170	5.4
614	0.150	4.9
615	0.130	3.8
616	0.100	2.5
617	0.085	2.1
618	0.070	1.9
619	0.060	1.8
620	0.050	1.8
621	0.045	2.6
622	0.040	4.4
623	0.035	6.1
624	0.030	4.2
625	0.025	2.5
626	0.020	1.5
627	0.015	1.0
628	0.010	0.5
629	0.005	0.0
630	0.000	0.0



XBL 799-7117

Figure 45. Photochemically active bands from NO₃ absorption.

photochemically active wavelength region. In this work, these products were determined directly and summed over each nm. This was accomplished by integrating the $\phi\sigma$ data and dividing by the active wavelength region.

$$\frac{\int_{\lambda_1}^{\lambda_2} \phi_{0,NO} \sigma_{NO_3} d\lambda}{\Delta\lambda} = (\phi_{0,NO} \sigma_{NO_3})_{AVE} \quad (59)$$

These data as well as the photochemically active areas are compared in Table 35. The ratio of $\sigma\phi$ and area sums are shown below

Table 34		
Ratio:		
<u>This work</u>		
Graham & Johnston		
$\phi_0 \sigma_{NO_3}$	=	1.24
$\phi_{NO} \sigma_{NO_3}$	=	1.27
$\sum_{O+NO} \text{area}$	=	1.25

This constant factor reflects partially offsetting differences due to higher average σ_{NO_3} and lower average ϕ values from this study.

The photolytic rate of NO_3 destruction (j value) can be calculated across the visible spectrum

$$j = \int_{\lambda_1}^{\lambda_2} \phi_{\lambda} \sigma_{\lambda} I_{\lambda} d\lambda \quad (60)$$

Gelinas et al.⁸⁹ have tabulated solar light fluxes (I_{λ}) for

Table 35. Comparison of NO₃ quantum yield data and j values.

	This work	Graham and Johnston ⁹
$\sigma_{\text{NO}_3 \cdot \phi_0}$ ($\Delta\lambda$)	$2.1 \times 10^{-18} \text{ cm}^2 \cdot \text{molecule}^{-1}$ ($470 \leq \lambda \leq 635 \text{ nm}$) ^a	$1.7 \times 10^{-18} \text{ cm}^2 \cdot \text{molecule}^{-1}$ ($470 \leq \lambda \leq 600 \text{ nm}$) ^b
$\sigma_{\text{NO}_3 \cdot \phi_{\text{NO}}}$ ($\Delta\lambda$)	$9.0 \times 10^{-19} \text{ cm}^2 \cdot \text{molecule}^{-1}$ ($585 \leq \lambda \leq 628 \text{ nm}$) ^a	$7.1 \times 10^{-19} \text{ cm}^2 \cdot \text{molecule}^{-1}$ ($520 \leq \lambda \leq 640 \text{ nm}$) ^b
$\sigma_{\text{NO}_3 \cdot \phi_0 \cdot \Delta\lambda}$	$3.42 \times 10^{-16} \text{ cm}^2 \cdot \text{nm} \cdot \text{molecule}^{-1}$	$2.21 \times 10^{-16} \text{ cm}^2 \cdot \text{nm} \cdot \text{molecule}^{-1}$
$\sigma_{\text{NO}_3 \cdot \phi_{\text{NO}} \cdot \Delta\lambda}$	$3.86 \times 10^{-17} \text{ cm}^2 \cdot \text{nm} \cdot \text{molecule}^{-1}$	$8.52 \times 10^{-17} \text{ cm}^2 \cdot \text{nm} \cdot \text{molecule}^{-1}$
$\Sigma \text{ Areas}$	$3.81 \times 10^{-16} \text{ cm}^2 \cdot \text{nm} \cdot \text{molecule}^{-1}$	$3.06 \times 10^{-16} \text{ cm}^2 \cdot \text{nm} \cdot \text{molecule}^{-1}$
$j(\text{NO} + \text{O}_2)$	$0.022 \pm 0.002 \text{ sec}^{-1}$	$0.040 \pm 0.008 \text{ sec}^{-1}$
$j(\text{NO}_2 + \text{O})$	$0.18 \pm 0.018 \text{ sec}^{-1}$	$0.099 \pm 0.020 \text{ sec}^{-1}$
$j(\text{Entire band})\phi=1$	0.39 sec^{-1}	0.27 sec^{-1}

a) Measured

b) Estimated active band region

overhead sun, averaged at 50 \AA intervals and correcting for ozone absorption, Rayleigh scattering and atmospheric particles. The quantum yields of the present study give:

$$j(\text{NO} + \text{O}_2) = 0.022 \pm 0.002 \text{ sec}^{-1}$$

$$j(\text{O} + \text{NO}_2) = 0.15 \pm 0.018 \text{ sec}^{-1}$$

$$j(\text{entire band})_{\phi=1} = 0.39 \text{ sec}^{-1}$$

compared to values from Graham and Johnston in Table 35.

The effect of internal energy contribution to the photolysis of NO_3 is evident in the extent of the product fall off region below the calculated thermodynamic band dissociation limit of $5800 \pm 30 \text{ \AA}$ (Figure 44). The amount of excess energy above 5800 \AA needed for dissociation is tabulated below for several of the experimentally determined points

Table 36

Wavelength (\AA)	ΔE Below 5800 \AA (cm^{-1})
5800.0	0
5813.0	39
5850.0	147
5892.9	272
5945.0	421
5959.3	461
6005.0	589
6045.0	700
6095.0	834
6135.0	942

In terms of vibrational excitation of NO_3 , if the ground state levels are similar in energy spacing to the excited state ($\sim 950 \text{ cm}^{-1}$), then approximately 0.8% of $v''=1$ is populated at 300K. However, if the small spectral featured at 6780 \AA is a hot band, indicative of a $\sim 385 \text{ cm}^{-1}$ ground state vibrational spacing (see Figure 44), then approximately 1.7% of $v''=1$ is populated. At 6135 \AA , the quantum yield for NO_2 production is 0.33, indicating that a substantial fraction of the molecules must then be rotationally excited.

To the high energy side of 5800 \AA , the total quantum yield slowly falls from ~ 1.0 to an average value of about 0.85. The remaining absorption must either result in fluorescence, quenching, or non-radiative decay. Another possibility exists, that being production of NO, which was not observed due to the particular choice of experimental conditions.

Most of the NO data acquired below 5800 \AA was at high laser fluence. A distinct possibility exists that some of the probability for NO production was funneled into two photon production of $\text{O} + \text{NO}_2$. Three pieces of evidence argue against this, however. First, O quantum yields, obtained at moderate energies by direct observation (Table 18) over the wavelength range $4700\text{--}5800 \text{ \AA}$, average around 0.91.^{a)} The analogous set of data, obtained from initial NO slope information at comparable laser fluence (Figure 36), closely parallels the O data and indicates an average quantum yield of significantly less than one over this range.

(a) These data unfortunately are very noisy, due to a malfunction in the high voltage PMT shield.

A third experiment in which ϕ_{NO} was obtained at both high and low $E\sigma$ values, demonstrates little or no loss in product over the range 5850–6150 Å as a function of fluence (Figure 35). A close analysis of the relative product difference under each curve shows a slightly higher product yield at high $E\sigma$ between 5850–6050 Å followed by an almost equally lower yield from 6050–6150 Å. However, the high $E\sigma$ results now show greater product yield above 6150 Å, in the region where sequential 2-photon transitions begin to compete significantly with one photon absorption.

A second mechanism exists which could possibly result in low apparent NO quantum yields. This entails a substantial fraction of the excess internal energy residing in the NO product as vibrational excitation, which might be insensitive to detection in the present experiment. If O_2 were produced vibrationally and electronically cold, up to 8 quanta of vibrational energy would reside in NO, minus that expended in relative translation (which according to Busch and Wilson^{37,38} could be substantial (40–60%)). However, scanning from 5800–4700 Å only encompasses a $\Delta v=2$ vibrational state change in NO. It is not expected that the hot band emission spectral intensity from the resonance lamp changes radically over a range of $\Delta v=2$. Furthermore, the experiments with CH_4 buffer gas suggest that NO is produced in a relatively low vibrational state, which is reasonable since intuitively it is expected that the O_2 fragment should possess a substantial portion of the excess energy. (That CH_4 had little effect on signal level may be due to an intrinsically fast vibrational quenching action by N_2O_5 (and/or HNO_3), which has a vibrational energy defect of only $\sim 170 \text{ cm}^{-1}$ versus $\sim 343 \text{ cm}^{-1}$ for CH_4 .) Finally, the close correspondence

in $\phi_{\text{NO}_3}^\sigma$ ratios for both O and NO (and total area ratios) between Graham's work and the present study (Table 34) strongly indicates that all of the NO produced has been accounted for.

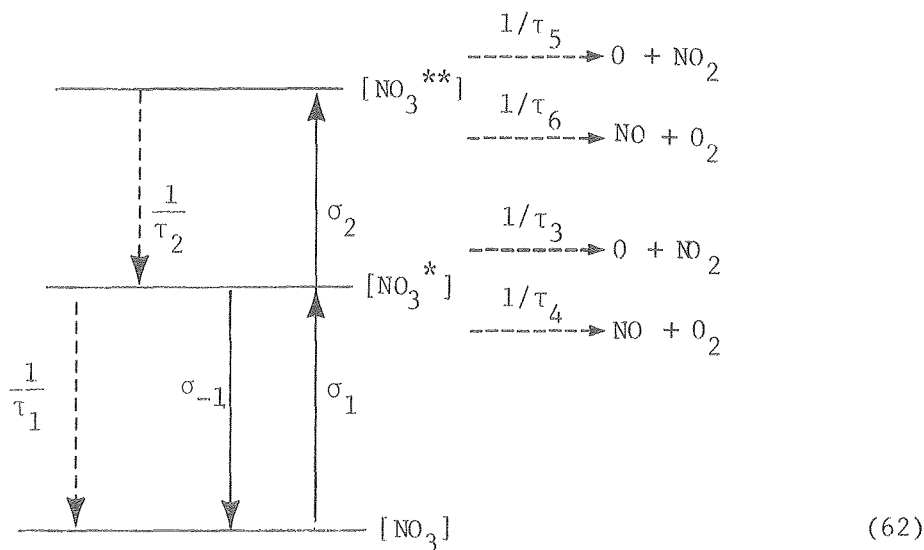
In Section III-D4, the observation of an initial increase in NO signal following photolysis, was interpreted in terms of the fast secondary reaction $\text{O} + \text{NO}_2 \rightarrow \text{NO} + \text{O}_2$. The excellent agreement between ϕ_0 values from direct observation versus analysis of the initial NO slope indicates the validity of this explanation. Several alternative explanations have previously been proposed which included the following:

- | | | |
|----|--|--------------------------|
| a) | $\text{NO}_2^{(*)} + \text{NO}_3^{(*)} \rightarrow \text{NO} + \text{NO}_2 + \text{O}_2$ | excited state reactions |
| b) | $\text{NO}_3^* + h\nu \rightarrow \text{NO} + \text{O}_2$ | } two-photon absorptions |
| c) | $\text{NO}_3^* + h\nu \rightarrow \text{O} + \text{NO}_2 \rightarrow \text{NO} + \text{O}_2$ | |
| d) | $\text{NO}_2^* + h\nu \rightarrow \text{NO} + \text{O}$ | |
| e) | NO diffusion into "hot" spot in viewing region . (61) | |

The approximate half life of $\text{O} + \text{NO}_2 \rightarrow \text{NO} + \text{O}_2$ in this system was ~ 30 msec, which was roughly consistent with the observed signal maximum of ~ 8 msec, taking into account the measured NO diffusion times of $\sim 110 \text{ sec}^{-1}$ out of the viewing zone. The ground state half life of (a) is $\sim 800 \text{ sec}$; in order to be on the 8 msec time scale, this reaction would have to be virtually gas kinetic (an enhancement of 10^5). Two photon absorptions are also an unlikely candidate, since varying the total energy fluence failed to show any effect except at 6233 and 6600 Å, where the two photon effect seen was correlated to the $\text{O} + \text{NO}_2$ reaction. As to the possibility of NO diffusing into a "hot"

spot in the viewing region, an experiment in which the beam size was doubled also failed to show any variation in either the hump or absolute $[\text{NO}]$ at time $t=0$. (Note: The NO detection system was designed to observe only the laser beam region.)

Analysis of the two photon behavior in NO_3 follows an analogous treatment already given for NO_2 . Since quantitative information is difficult to extract due to unknown quenching rates, radiative lifetimes, and 2 photon cross sections, the description will be limited to a steady state treatment. The following transitions in a simplified 3 level system are considered



where $\frac{1}{\tau_1}$ and $\frac{1}{\tau_2} = \frac{1}{\tau_{\text{rad}}} + \Sigma k_Q [Q]$; and $\frac{1}{\tau_T} = \Sigma \frac{1}{\tau}$

Assuming a steady state for $[\text{NO}_3^*]$ and $[\text{NO}_3^{**}]$ leads to the following expression

$$\frac{d[O]}{dt} = \frac{[\text{NO}_3] \sigma_1 \sigma_2 I_0 \tau_3}{(I_0 \sigma_{-1} + I_0 \sigma_2 + \tau_T^{-1}) \tau_3} + \frac{[\text{NO}_3] \sigma_1 I_0}{(I_0 \sigma_{-1} + I_0 \sigma_2 + \tau_T^{-1}) \tau_3} \quad (63)$$

after integrating and combining terms:

$$[O] = \frac{[NO_3] \sigma_1 I_0 (\sigma_2 I_0 \tau_3 + 1) \tau_{laser}}{(I_0 \sigma_{-1} + I_0 \sigma_2 + \tau_T^{-1}) \tau_3} \quad (64)$$

where $[NO_3]$ is the ground state concentration.

It is clear from Eq. (63) that the production of O consists of a single photon and a two photon contribution. This expression describes the competition between one and two photon behavior shown in Figure 32, in which excitation at 6600 Å is strictly a two photon process, while at 6233.1 Å the two channels compete. It is expected that the O signal will depend linearly (large I_0) or quadratically (small I_0) on the intensity of the laser pulse. This is demonstrated in Figure 31, in which quadratic behavior is clearly visible at 6600 Å while much less so at 6233.1 Å. An analogous expression follows immediately for production of NO from each of the two channels. If the lifetime (τ_3), of the excited state (NO_3^*) were known, Equation (64) could be used to deduce the two photon cross section (or vice versa).

Two final details concerning O production need to be considered. First is the question of possible contamination by O_3 in the system, which might originate from its being trapped in or on the N_2O_5 during synthesis. While infrared analysis placed an upper limit of less than 0.1% of the N_2O_5 , this could still represent 10-20% of the NO_3 concentration. The most convincing argument for the absence of O_3 comes from consideration of its absorption spectrum which is photochemically active ($\phi_0 = 1$) throughout the visible region (Figure 3). The cross section difference between 5850 and 6600 Å changes by a factor of 2, while the O quantum yield goes from 1 to 0 in the low

EO limit. Model calculations indicate further that O_3 would not survive the 10 minute transit time in the N_2O_5 saturator at the ambient NO_2 concentrations present.

The second question pertaining to O production concerns the possibility of simultaneous 2 photon dissociation of N_2O_5 , which might account for the apparent increase in NO_3 cross section over that previously measured. However, if 2-photon excitation of N_2O_5 were occurring, the production of O at 5850 Å (where ϕ_O (measured) = 1) would continue to increase with laser fluence and this was not observed (up to a maximum intensity of 1.3 MW). Furthermore the excess production of O from NO_3 over that from NO_2 continued to occur even in the low EO limit.

2. Nitric Oxide and Oxygen Atom from N_2O_5 Photolysis

The following results from this study concerning the photodynamics of N_2O_5 concur with recent findings by Connell¹⁷ (see Figure 39).

- (a) The primary photoproducts include an oxygen atom and possibly a minor amount of NO which represents less than 11% photolytic conversion.
- (b) The reduced quantum yield is apparently due to quenching of electronically excited N_2O_5 by ground-state N_2O_5 and to a lesser extent by buffer gas.

Furthermore the current experiments at $2900 < \lambda < 3000 \text{ Å}$ show little dependence of quantum yield on wavelength. The dotted curve in Figure 39 results from solving a steady state expression for $N_2O_5^*$ in terms of quantum yield and solving for the various parameters by a least square fit to the data. Connell's actual data fall somewhat below this line, by about 0.05 units, and agree quite well with this work after correction for the effect of buffer gas.

C. Detection of $O_2(^1\Sigma_g^+)$ and $NO_3(^2B_2)$ Fluorescence

A search for either emission from $O_2(^1\Sigma_g^+)$ or NO_3^* proved unsuccessful. In both cases, it is possible to calculate expected emission levels and put an upper limit on yield of production or quenching efficiency.

Emission from $O_2(^1\Sigma_g^+)$ is very long lived ($\tau \sim 12$ sec) and relatively susceptible to quenching, two of the fastest quenchers being O_3 and H_2O . While O_3 was demonstrated to be absent, the presence of N_2O_5 insures existence of an extremely dry system. The rates of quenching by N_2O_5 and HNO_3 , unfortunately, are not known.

In the initial $O_2(^1\Sigma_g^+)$ experiments which employed an interference filter before the detector, the relative fluorescence signal due to NO_2 versus $O_2(^1\Sigma_g^+)$ was calculated to be

$$\frac{E_f(NO_2)}{E_f(O_2(^1\Sigma_g^+))} \cong \frac{2.3 \times 10^9 \text{ counts}}{4.8 \times 10^7 \text{ counts}} \cong \frac{48}{1} \quad (71)$$

Assuming $\phi_f(O_2(^1\Sigma_g^+)) = 0.5$,

$$(1 - e^{-E\sigma}) = 0.8$$

% filter transmission = 50

$$k_Q(N_2) = 2 \times 10^{-15} \text{ cm}^3 \cdot \text{molecule}^{-1} \cdot \text{sec}^{-1} \text{ (for } O_2(^1\Sigma_g^+))$$

$$E_{\text{laser}} = 200 \text{ mJ/cm}^2 \text{ (at } \lambda = 6050 \text{ \AA)}$$

However, emission from NO_2 is broadband, with approximately 1/50 falling within the bandpass of the filter. Similarly, only 10% of the $O_2(^1\Sigma_g^+)$ emission is captured by the filter, resulting in a signal ratio ($NO_2/O_2(^1\Sigma_g^+)$) of 10/1 which is on the limit of detectability. Removing the

filter results in an expected signal of $\sim 3 \times 10^4$ counts after 60 (50 mJ/cm²) laser pulses, and fewer than 20 counts were observed. This is explainable by a quantum yield for $O_2(^1\Sigma_g^+)$ production of $< 6.7 \times 10^{-4}$. However assuming a maximum quenching rate of 10^{-11} cm³·molecule⁻¹·sec⁻¹ and typical N₂O₅ concentrations (in O₂ buffer), reduces the total signal to ~ 18 counts, in 100 μ s, which is again considerably below the detectivity level.

Photon counting is only useful for count rates less than $\sim 10^7$ sec⁻¹, because pulse pile up and subsequent paralysis of the discriminator result in either reduced or total loss of signal. While counting mode techniques were utilized to search for NO₃ emission (in the event of an anomalously long lifetime), most of the work involved D.C. detection due to the large expected photocurrent.

The integrated absorption coefficient for NO₃ was estimated, utilizing the entire absorption band (from 4000–6750 Å) and an averaged cross section of 2.61×10^{-18} cm²/molecule. The maximum calculated radiative lifetime was

$$\tau_0 \text{ (abs. coeff)} \approx 4.3 \times 10^{-7} \text{ sec} \quad (72)$$

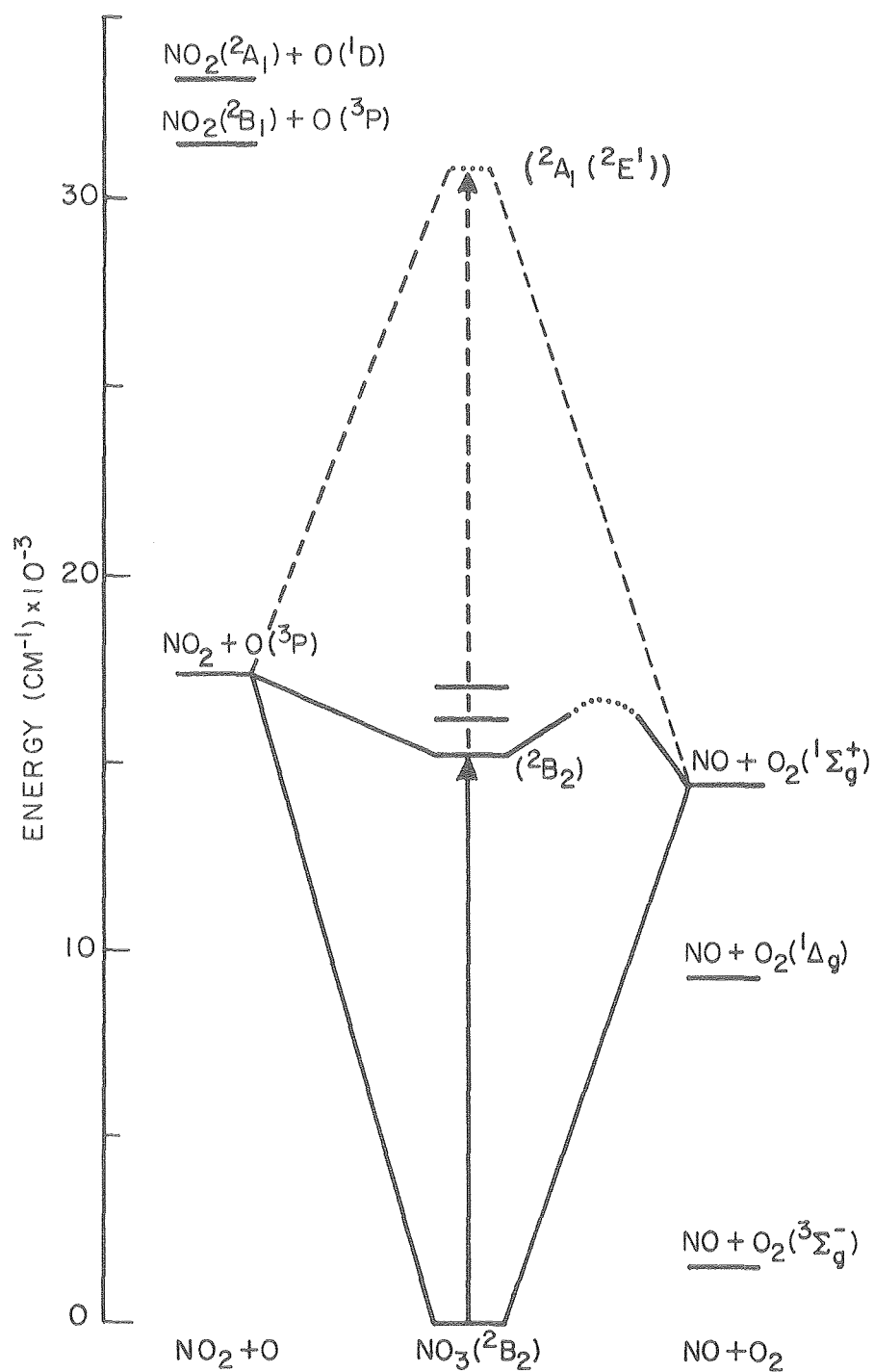
From estimates of the oscillator strength ($f \approx 0.013$) derived from calculations by Olsen, et al.,¹⁴ a second estimate can be calculated

$$\tau_0 \text{ (oscillator st.)} \approx 4.5 \times 10^{-7} \text{ sec} \quad (73)$$

While the agreement is probably fortuitous the results indicate the magnitude of the time region of the fluorescence. A better estimate results from multiplying this lifetime by the wavelength-dependent fluorescence quantum yield.

Anomalous long lifetimes in small polyatomics (NO_2 , CS_2 , and SO_2) have been previously observed and Bixon and Jortner⁹⁸ have concluded that no intramolecular electronic relaxation processes occur in such molecules. The lifetime anomaly has been explained by Douglas⁹⁹ to be due to an extensive interaction (coupling) between the initially formed excited state and another state, either metastable or the ground state. The possibility of rapid resonance fluorescence could not be experimentally verified, due to an inordinant amount of scattered laser light, in the present cell.

Figure 1 depicts schematically the energetics for single photon excitation of the NO_3 system including various electronic and vibrational states of possible photofragmentation products. Figure 46 indicates

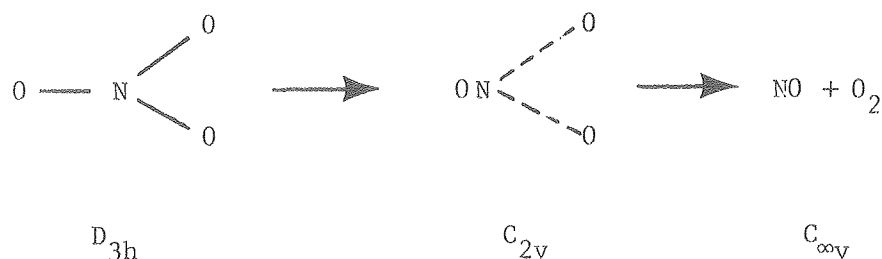


XBL 799-7091

Figure 46. Energy level diagram for the NO_3 system. Laser excitation indicated by arrows for one (solid) and two-photon (dashed) transitions. Correlations allowed by conservation of orbital and spin symmetry by one- and two-photon excitation are similarly indicated. NO_3 terms shown are those of Olsen.¹⁴

some correlations between photochemical fragments based on considerations of conservation of orbital and spin symmetry along the appropriate reaction coordinates.⁹⁰ It was constructed on the basis that transitions including the same symmetry species do not cross each other.

The multiplicities of all products indicated are allowed from doublet NO_3 , by spin correlation rules, where the NO_x products are ground state $\text{NO}(\tilde{X}^2\Pi_j)$ and $\text{NO}_2(\tilde{X}^2A_1)$. When the symmetry of the excited state is known, it becomes possible to apply symmetry correlation rules between the excited state and dissociation products.¹⁰⁰ However an unambiguous determination of the geometry of NO_3 has not yet been achieved. Assuming a C_{2v} excited-state NO_3 configuration due to a Jahn-Teller perturbation, the longest wavelength transition should be an allowed z-polarized transition ${}^2B_2 \leftarrow {}^2B_2$. The main primary process in this region is formation of $\text{NO}_2(X^2A_1)$ and $\text{O}({}^3P)$ while the secondary product above 5850 Å is $\text{NO}({}^2\Pi_j) + \text{O}_2$. The 2B_2 state correlates to the production of O atom in a P or D state. Furthermore the symmetry axis of C_{2v} (z axis) is assumed to correspond to the axis of the NO molecule (z→z) from which B_2 is shown to correlate to Π symmetry. If however NO_3 occurs in a symmetric D_{3h} symmetry, the ground state term becomes ${}^2A'_2$ (after Walsh⁹¹) which does not correlate to $\text{NO}_2({}^2A_1)$. The dissociation of NO_3 to $\text{NO} + \text{O}_2$ can likewise be assumed to occur in the molecular plane via a C_{2v} intermediate (i.e., $\sigma_h \rightarrow \sigma_v(yz)$).



In this case, the $A_2' \rightarrow B_2$ transition is allowed, followed again by another allowed transition to either NO or NO_2 . If, however the excited state is also of D_{3h} symmetry, the predominance of the NO_2 product channel suggests either an A_1' or E' term correlating to the 2A_1 NO_2 product. Now, going through a C_{2v} intermediate configuration (to produce $\text{NO} + \text{O}_2$) is only allowed in E' if that state is B_2 .

Analogous arguments based on each assumed symmetry type for a sequential 2 photon absorption are as follows. The excited state located near 3300 Å, has been calculated to be 2A_1 . Now, the transition ${}^2B_2 \rightarrow {}^2A_1$ only correlates to Σ^+ or Δ linear products, which are energetically not possible. The corresponding transition leading to NO_2 , only correlates with S or D state oxygen atoms. Since $\text{O}({}^3\text{P})$ was observed at 6600 and 6233 Å, and the threshold for $\text{NO}_2 + \text{O}({}^1\text{D})$ is ~ 6024 Å, it is doubtful whether 2A_1 represents the second excited state.

From the calculations of Olsen *et al.*¹⁴ it is apparent that for angles larger than 120° the slightly more stable configuration is a 2B_2 state. However the trigonally arranged wavefunction does not transform to an irreducible representation of the D_{3h} point group, but rather to the C_{2v} subgroup, indicating that the state is actually $2E'$. Based on this assignment, the allowed transition to ${}^2E'$ now correlates

to A_1 or B_2 in C_{2v} , which allows both Σ^+ or π linear products. Similarly, E' allows both A_1 and/or B_2 states of NO_2 .

The low probability of NO production upon one photon absorption suggests a similarly low rate of formation upon 2-photon excitation, even though both channels are allowed. The low quantum yield for NO implies a moderate potential barrier for the dissociation, arising from the energy required to bring two O atoms together to form a bond.

E. Nitrogen Dioxide Two Photon Cross Sections

Only one other study has investigated the 2-photon photolysis of NO_2 . Gerstmayr, Harteck and Reeves,⁹² using a Q-switched ruby laser at 6943 Å, measured the production of O_2 from NO_2 photolysis. Using several simplifying assumptions, they obtained a cross section value for absorption of the second photon of

$$\sigma_2 = 1.3 \times 10^{-19} \text{ cm}^2/\text{molecule} \quad (65)$$

(Assuming their Beer's Law calculation was to the base, e). At 6850 Å (using an estimated one photon (σ_1) cross section) a value of

$$\sigma_2 = 8.10 \pm 2.1 \times 10^{-19} \text{ cm}^2/\text{molecule} \quad (66)$$

was obtained from this study resulting in a two photon cross section of

$$\sigma_1 \cdot \sigma_2 = 4.54 \times 10^{-39} \text{ cm}^4 \cdot \text{molecule}^{-2} \quad (67)$$

The measurement at 6850 Å extends the observed trend towards larger σ_2 values as σ_1 gets smaller (see Figures 40, 41). At longer

wavelengths this effect is not due to decreased quenching efficiency since several workers^{93,94} have demonstrated a small increase in quenching efficiency with increasing wavelength.

F. Rate of the $O + NO_2$ Reaction

The reaction rate of $O + NO_2$, due to its criticality in atmospheric modeling, has been thoroughly studied (see references 1-9).⁹⁵ Values ranging from 4×10^{-12} to 3×10^{-11} $cm^3 \cdot molecule^{-1} \cdot sec^{-1}$ have been reported with little or no activation energy. The most recent recommendation for the rate constant from JPL publication #79.27⁸⁶ is based on the results of Davis et al.,⁹⁶ Bemand et al.,⁹⁷ and Slanger et al.,⁹⁵ resulting in a value of

$$k_{O,NO_2} = 9.3 \pm 0.93 \times 10^{-12} \text{ cm}^3 \cdot \text{molecule}^{-1} \cdot \text{sec}^{-1}, \quad (68)$$

with the possibility of a slight negative temperature coefficient.

The value obtained in this work is

$$k_{O,NO_2} = 1.03 \pm 0.008 \times 10^{-11} \text{ cm}^3 \cdot \text{molecule}^{-1} \cdot \text{sec}^{-1} \quad (69)$$

which falls marginally within the recommended limits, but is high, considering the degree of previous replication. While the value in Eq. (69) is the apparent rate of the $O + NO_2$ reaction in this experiment (and the value used to extract ϕ_O values from the temporal NO profiles), the question of its accuracy will be discussed in this section.

The fact that 144 data points were averaged over 14 experimental runs resulted in a reported precision ($\pm\sigma$) of 0.8%. The effect of lamp heating, at the lowest NO_2 concentration studied, caused a bulk increase of ~10% as measured by the NO_2 fluorescence detector vs.

lamp off conditions. If the lamp effect caused a locally high (instead of uniform) NO_2 concentration, the measured values at low $[\text{NO}_2]$ would be too low, causing the measured rate constant to be even higher. To test this out, a least squares line was fit to the 34 data points with $[\text{NO}_2] \geq 8 \times 10^{13} \text{ molecules}\cdot\text{cm}^{-3}$, where the lamp heating effect represented less than a 2% increase in NO_2 . This resulted in a rate constant value of

$$k'_{\text{O},\text{NO}_2} = 1.02 \pm 0.02 \times 10^{-11} \text{ cm}^3\cdot\text{molecule}^{-1}\cdot\text{sec}^{-1} \quad (69)$$

and a diffusion coefficient of

$$k_{\text{diff}} = 151.1 \pm 44.9 \text{ sec}^{-1} \quad (70)$$

which is not significantly different from that obtained using the complete data base. Furthermore, values obtained from pure NO_2/N_2 (see arrow on abscissa--Figure 42) agree quite well with those from the N_2O_5 system measurements.

Several other factors investigated included calibration of (a) NO_2 concentration, (b) multichannel scaler time base and (c) absolute pressure. The details of the NO_2 calibration have been described previously (Section IIIC). The time base of the multichannel scaler was checked, using a pulse generator and a counter equipped with an externally available calibrated oscillator. The resulting dwell times values (corrected for dead time) at various nominal switch positions were found in all cases to be slightly slow. This effect when corrected for, results in a still higher rate constant.

Table 37

Nominal Dwell Time	Measured Error
4.00 ms	-0.025%
400 μ s	-0.21%
40 μ s*	-2.2%

(70)

*Dwell time used to collect
O + NO₂ rate data

A dead time of 2 μ sec existed in each channel, due to a fixed reset time. However, by numerical calculation, it is easily shown that this in no way affects the calculated decay times.

The capacitance manometer used has a stated accuracy of 0.15% at 10 torr. This unit was checked against a similar unit and was found to agree within 1% across the entire usable range. Since the NO₂ detector is physically located downstream from the photolysis cell results in a local pressure somewhat lower than that in the cell. However, all NO₂ calibrations were carried out under the same pressure/flow conditions as the rate measurements, which negated any effect due to pressure differential.

The use of a calcium fluoride window in this experiment could be critical since it blocks Lyman- α radiation. The rate of H + NO₂ is an order of magnitude faster than O + NO₂, and photolytic production of H from possible low levels of hydrocarbon impurities would result in an erroneously high rate constant measurement. In this study, both CaF₂ and MgF₂ windows were used with no resulting differences in observed rate constant.

Fluctuations in laser pulse intensity do not affect this measurement nor do variations in temperature. Flowing the photolysis mixture (and thereby flushing the cell completely between shots) results in a significant advantage over previous static experiments, and it tends to minimize absorption losses of NO_2 to the walls. In situ monitoring of NO_2 concentration is another benefit, rarely enjoyed by previous workers.

V. Summary

This study measured several photochemical parameters, important in elucidating the roles of NO_3 and N_2O_5 in the atmosphere. Among the goals achieved were the following:

1. Development of sensitive in situ detection systems for NO , O and NO_2 .
2. Measurement of channel-specific absolute photofragmentation quantum yields for NO_3 in the visible and N_2O_5 in the ultra-violet region.
3. Investigation of the two-photon photolytic behavior of NO_3 .
4. Redetermination of NO_3 , NO_2 , and NOCl absorption cross sections at specified wavelengths.
5. Measurement of NO_2 two-photon absorption cross sections.
6. Reinvestigation of the rate constant for reaction of oxygen atoms with NO_2 .

Acknowledgments

This study was carried out under the guidance and direction of Professor Harold S. Johnston, to whom I am deeply indebted. His wealth of knowledge and patient manner, allows the student to reap the benefits of pursuing his own interests and goals. The excitement and motivation I've acquired throughout the course of this work, is a direct reflection of his constant concern for his students.

I wish to thank my co-workers for making this experience an enjoyable one. Special thanks are due to Jim Podolske for availing his computer expertise, Dave Littlejohn, for his assistance in laser modification, and to Herbert Nelson, who was always available as a sounding board for questions, problems and ideas.

Gratitude is also extended to the personnel of the Department of Chemistry and of Lawrence Berkeley Laboratory for excellent support and assistance. Special thanks go to the personnel of the machine, electronic and glass blowing shops, for their fine craftsmanship and dedication to the students needs. I also wish to acknowledge Ms. Nancy Monroe and Ms. Gloria Pelatowski for their fine work in preparing the graphics and to Mrs. Carol Hacker, who was able to decipher the original draft and transform it into typed manuscript.

I especially wish to thank Camille for her patience and encouragement in this work.

I would also like to thank the U.S. Department of Energy for their funding of this research through the Materials and Molecular Research Division of the Lawrence Berkeley Laboratory under Contract W-7405-ENG-48.

APPENDICES

The following chemical reactions were used to model and optimize the operating conditions of the photochemical system. The rate constants are given in units of $(\text{cm}^3/\text{molecule}) \cdot \text{sec}^{-1}$ where the reaction order is given by:

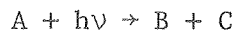
x = 3 for trimolecular

and activation energies are in units of temperature (K).

		$\sigma_{\text{eff}}(\text{cm}^2)$	ϕ
1.	$\text{NO}_3 + h\nu = \text{NO} + \text{O}_2$	2.0E-18	.22
2.	$\text{NO}_3 + h\nu = \text{NO}_2 + \text{O}$	2.0E-18	.78
3.	$\text{NO}_2 + h\nu = \text{NO}_2^*$	2.0E-19	1.00
4.	$\text{O}_3 + h\nu = \text{O}_2 + \text{O}$	3.0E-21	1.00
		A	E _a
5.	$\text{N}_2\text{O}_5 + \text{M} = \text{NO}_2 + \text{NO}_3$	4.7E-20	---
6.	$\text{NO}_2 + \text{NO}_3 + \text{M} = \text{N}_2\text{O}_5 + \text{M}$	8.5E-31	---
7.	$\text{NO}_2 + \text{NO}_3 = \text{NO} + \text{NO}_2 + \text{O}_2$	2.5E-14	+1220
8.	$\text{O}_2 + \text{NO} + \text{NO}_2 = \text{NO}_2 + \text{NO}_3$	8.0E-14	- 400
9.	$\text{NO}_3 + \text{NO}_3 = \text{NO}_2 + \text{NO}_2 + \text{O}_2$	8.5E-13	2435
10.	$\text{N}_2\text{O}_5 = \text{HNO}_3 + \text{HNO}_3$	3.0E-03	---
11.	$\text{NO}_2 + \text{O} = \text{NO} + \text{O}_2$	9.3E-12	---
12.	$\text{NO}_3 + \text{O} = \text{NO}_2 + \text{O}_2$	1.0E-11	---
13.	$\text{O} + \text{O} + \text{M} = \text{O}_2 + \text{M}$	5.0E-33	---

		A	E _a
14.	$O + O_2 + M = O_3 + M$	4.6E-35	-1050
15.	$O_3 + M = O + O_2 + M$	1.65E-19	11430
16.	$O + O_3 = O_2 + O_2$	1.90E-11	2300
17.	$NO + O_3 = NO_2^* + O_2$	1.26E-12	2104
18.	$NO + O_3 = NO + O_2$	9.0E-13	1200
19.	$NO_2^* + M = NO_2 + M$	2.0E-10	--
20.	$NO_2 + O_3 = NO_3 + O_2$	1.34E-13	2450
21.	$N_2O_4 + M = NO_2 + NO_2 + M$	3.70E-7	5550
22.	$NO_2 + NO_2 + M = N_2O_4 + M$	4.70E-35	860
23.	$NO_2 + NO_2 = NO + NO + O_2$	3.30E-12	13540
24.	$NO + NO + O_2 = NO_2 + NO_2$	1.87E-11	--
25.	$NO + O + M = NO_2 + M$	3.00E-33	- 940
26.	$NO + O + M = NO_2 + M + HV1$	7.00E-32	---
27.	$NO + O = NO_2 + HV2$	4.20E-18	---
28.	$NO_2 + O + M = NO_3 + M$	1.00E-31	---
29.	$NO_2^* = NO_2^* + HV3$	5.40E+04	---
30.	$NO_2^* + NO_2 = NO + NO + O_2$	4.2E-14	---
31.	$NO_2^* + NO_2 = NO_2 + NO_2$	9.8E-12	---

APPENDIX B:

DERIVATION OF QUANTUM YIELD EXPRESSION AND DEMONSTRATION
OF NON-DEPENDENCE ON TEMPORAL BEAM PROFILE

$$\frac{dA}{dt} = -\frac{I_a}{\ell} = -\frac{I_0 - I}{\ell} = -\frac{I_0}{\ell} (1 - e^{-\sigma[A]\ell})$$

$$\frac{dB}{dt} = -\frac{I_a \phi}{\ell} = -\frac{I_0 - I \phi}{\ell} = \frac{I_0 \phi}{\ell} (1 - e^{-\sigma[A]\ell})$$

For optically thin samples:

$$(1 - e^{-\sigma[A]\ell}) \rightarrow \sigma[A]\ell$$

and

$$\frac{d[A]}{dt} = -\sigma[A]I_0$$

$$\frac{d[B]}{dt} = \sigma[A]I_0\phi$$

$$\frac{d[A]}{A} = -\sigma \int I_0(t) dt$$

NOTE: $[A]_t$ is $[A]$ at time t

$$\begin{aligned} \ln \frac{[A]_t}{[A]_0} &= -\sigma \int_0^t I_0(t) dt \\ &= -\sigma \int_0^t I_0(t) dt \\ \therefore [A]_t &= [A]_0 e^{-\sigma \int_0^t I_0(t) dt} \end{aligned}$$

$$\frac{d[B]}{dt} = \sigma[A]_t I_0(t)\phi$$

$$\frac{d[B]}{dt} = \sigma\phi \left([A]_0 e^{-\sigma \int_0^t I_0(t) dt} \right) I_0(t) dt$$

$$[B]_t = \sigma \phi [A]_0 \int_0^t I_0(t) e^{-\sigma \int_0^t I_0(t) dt} dt$$

Let $E(t)$ be the laser fluence from time 0 to time t and $E_f = E(\text{final})$.

$$E(t) = \int_0^t I_0(t) dt \quad ; \quad \frac{dE}{dt} = I_0(t)$$

$$[B]_f = \sigma \phi [A]_0 \int_0^{E_f} e^{-\sigma E} dE$$

$$[B]_f = \sigma \phi [A]_0 \left[-\frac{1}{\sigma} e^{-\sigma E} \right]_0^{E_f}$$

$$[B]_f = \phi [A]_0 (1 - e^{-\sigma E})$$

Rearranging:

$$\phi = \frac{[B]}{[A]_0 (1 - e^{-E\sigma})}$$

APPENDIX C

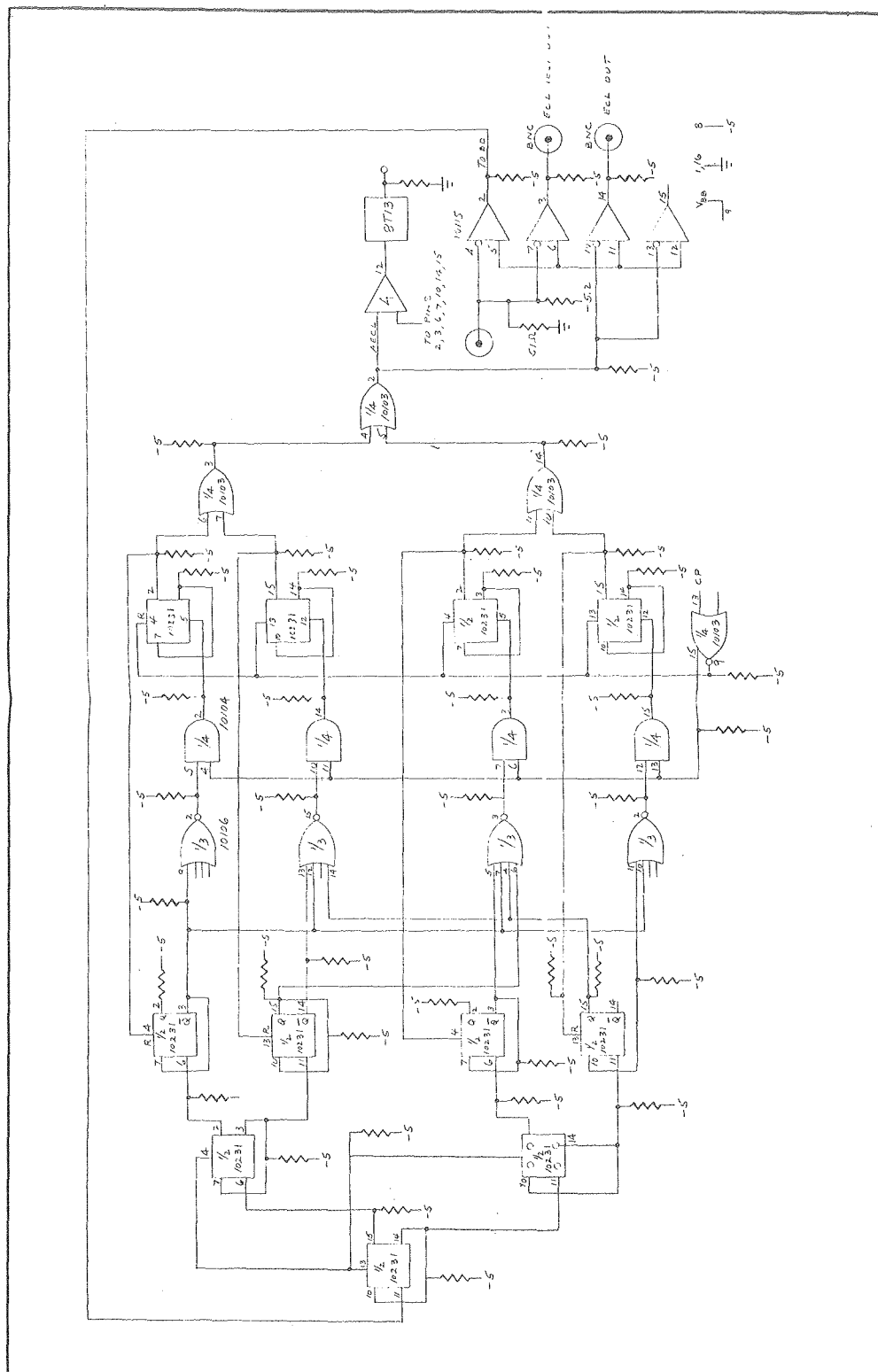


Figure C-1. Pulse pile-up counter-prescaler.

APPENDIX D:
HIGH SPEED PULSE COUNTER/INTERFACE

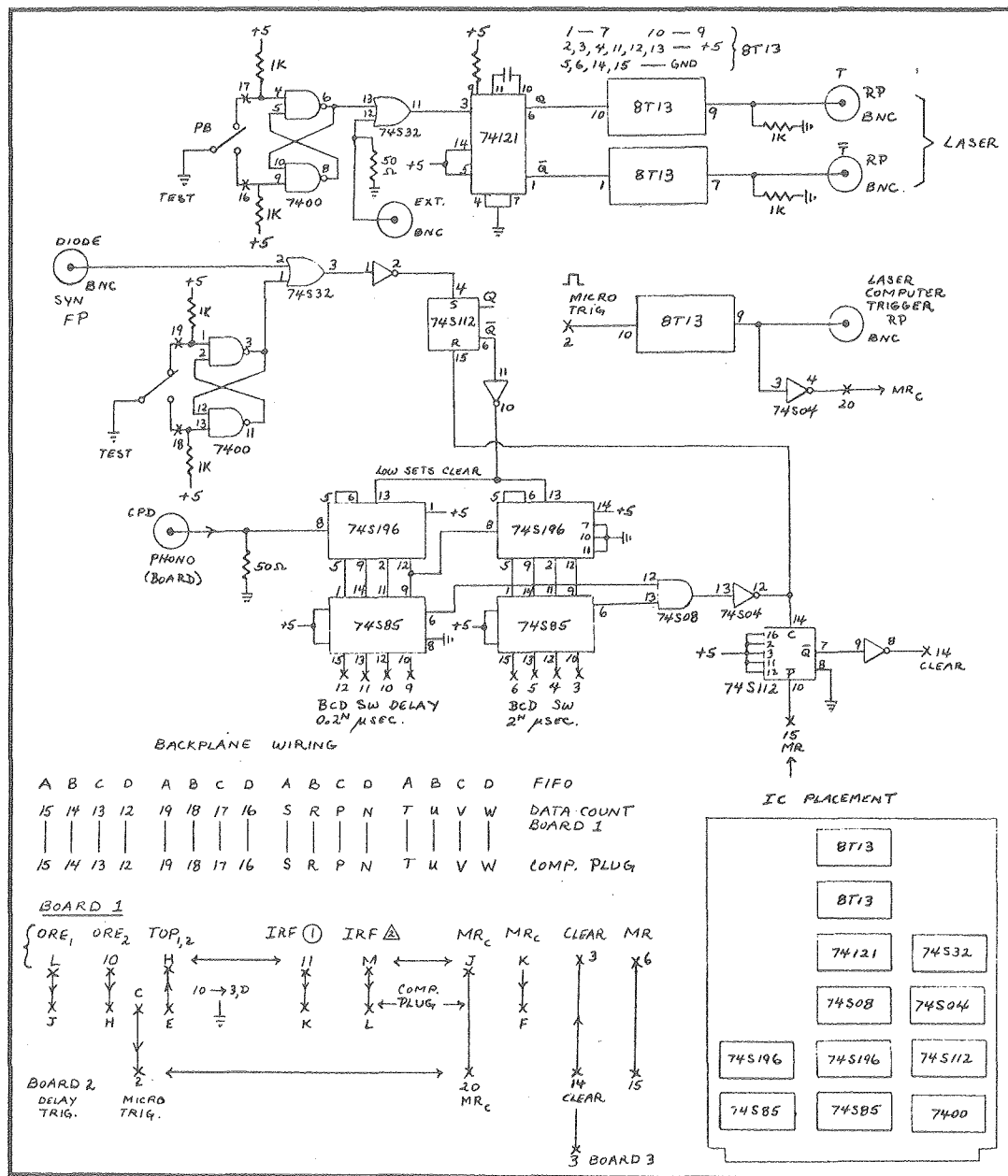


Figure D-2. Pulse interface delay trigger - Board 2.

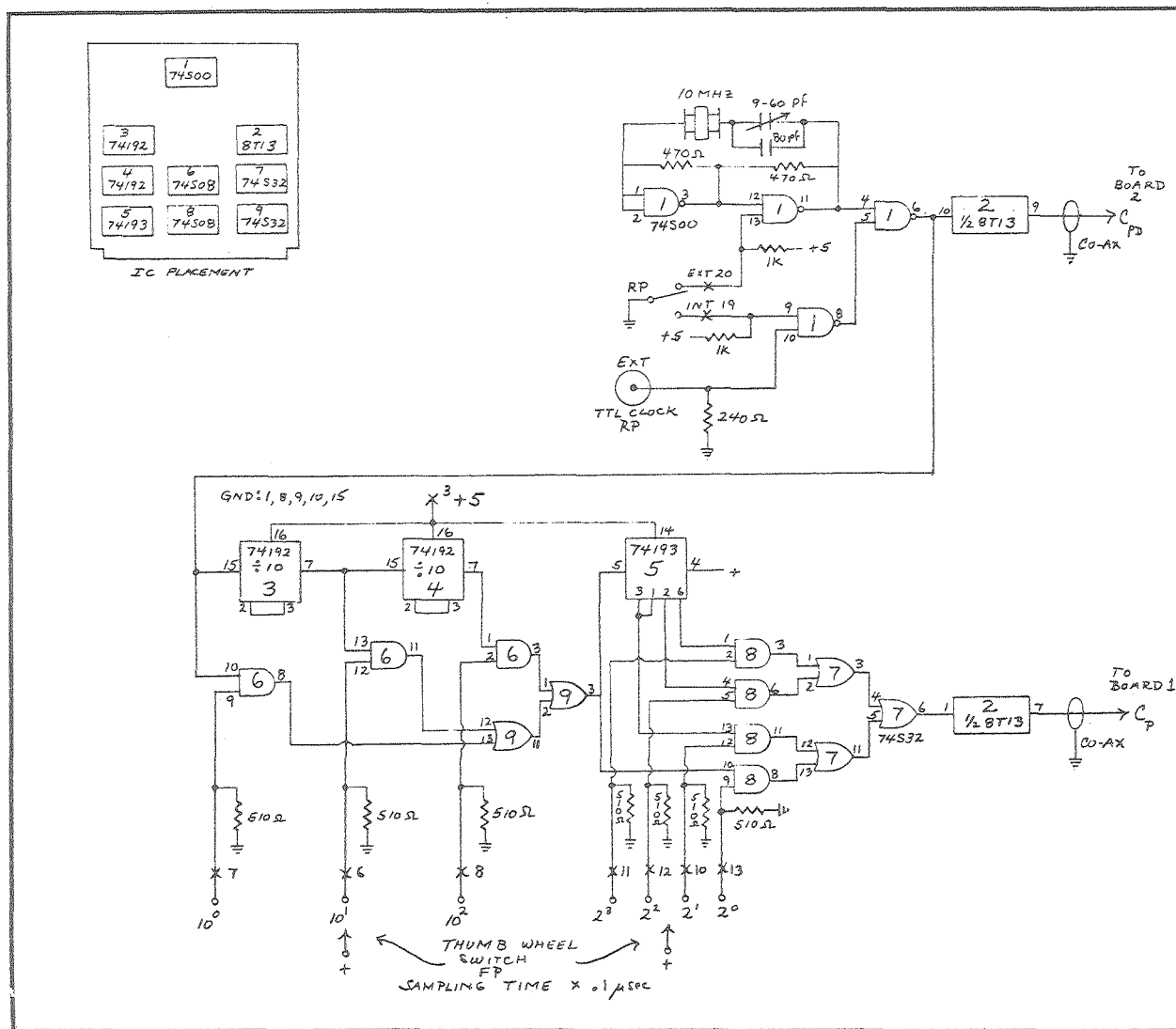
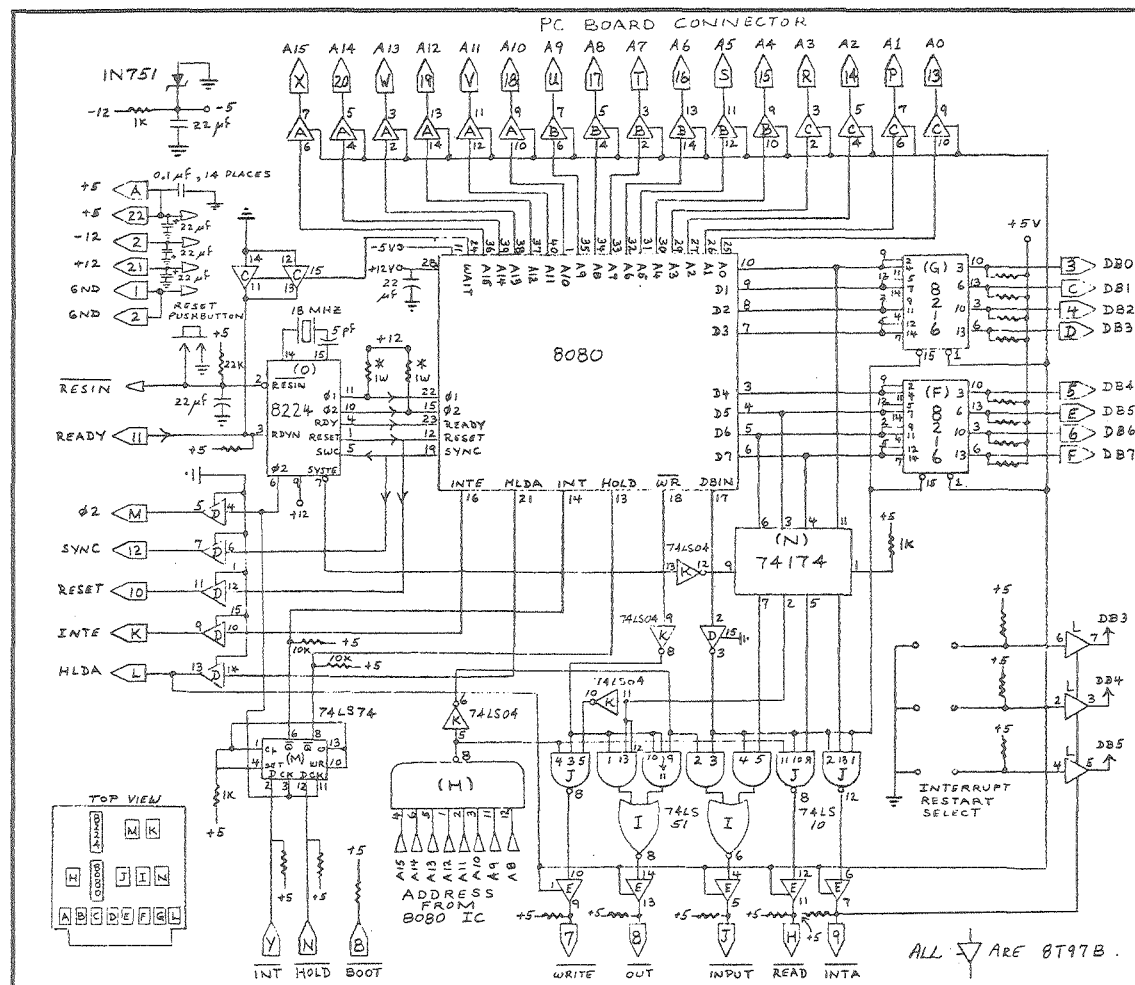
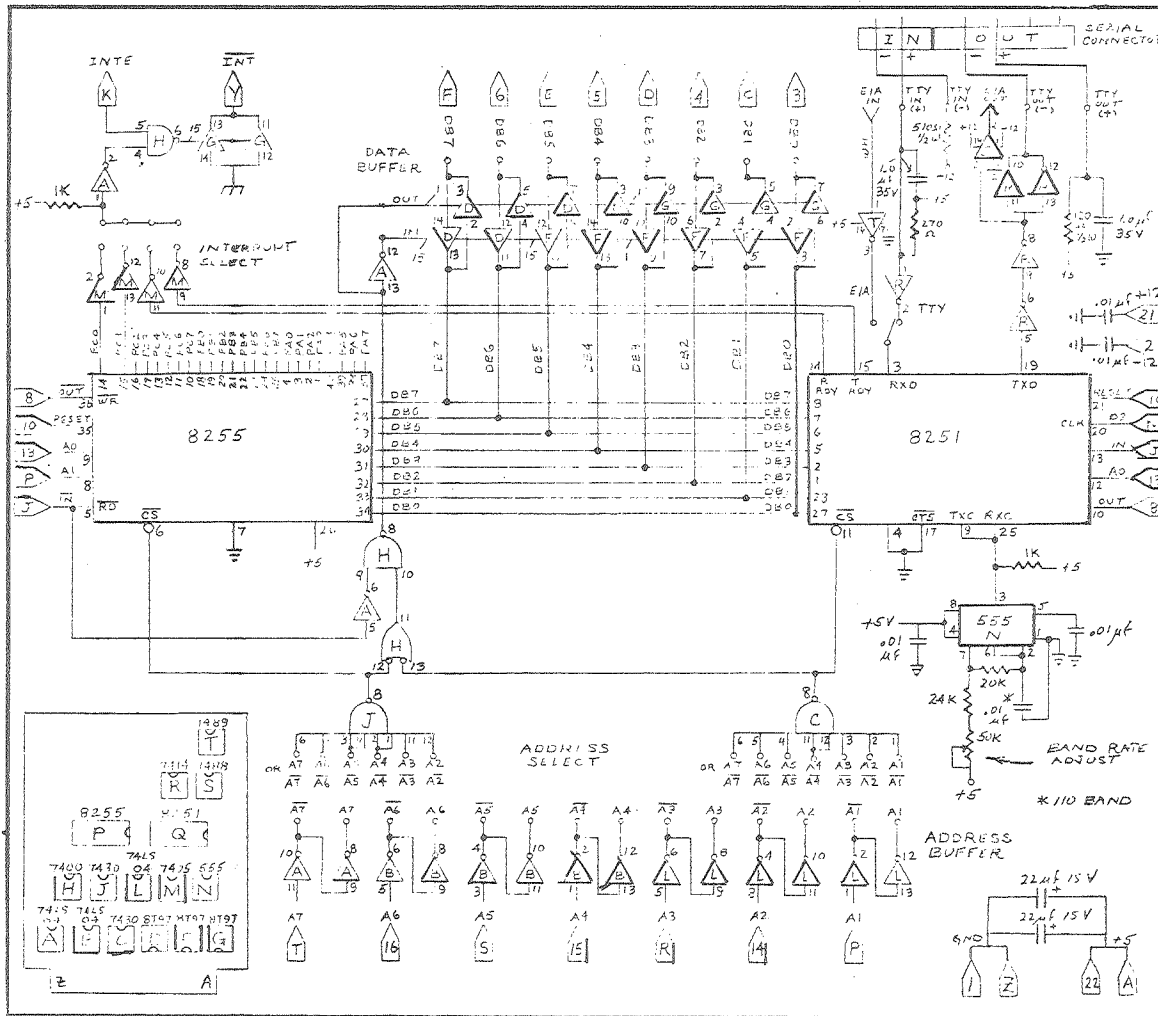
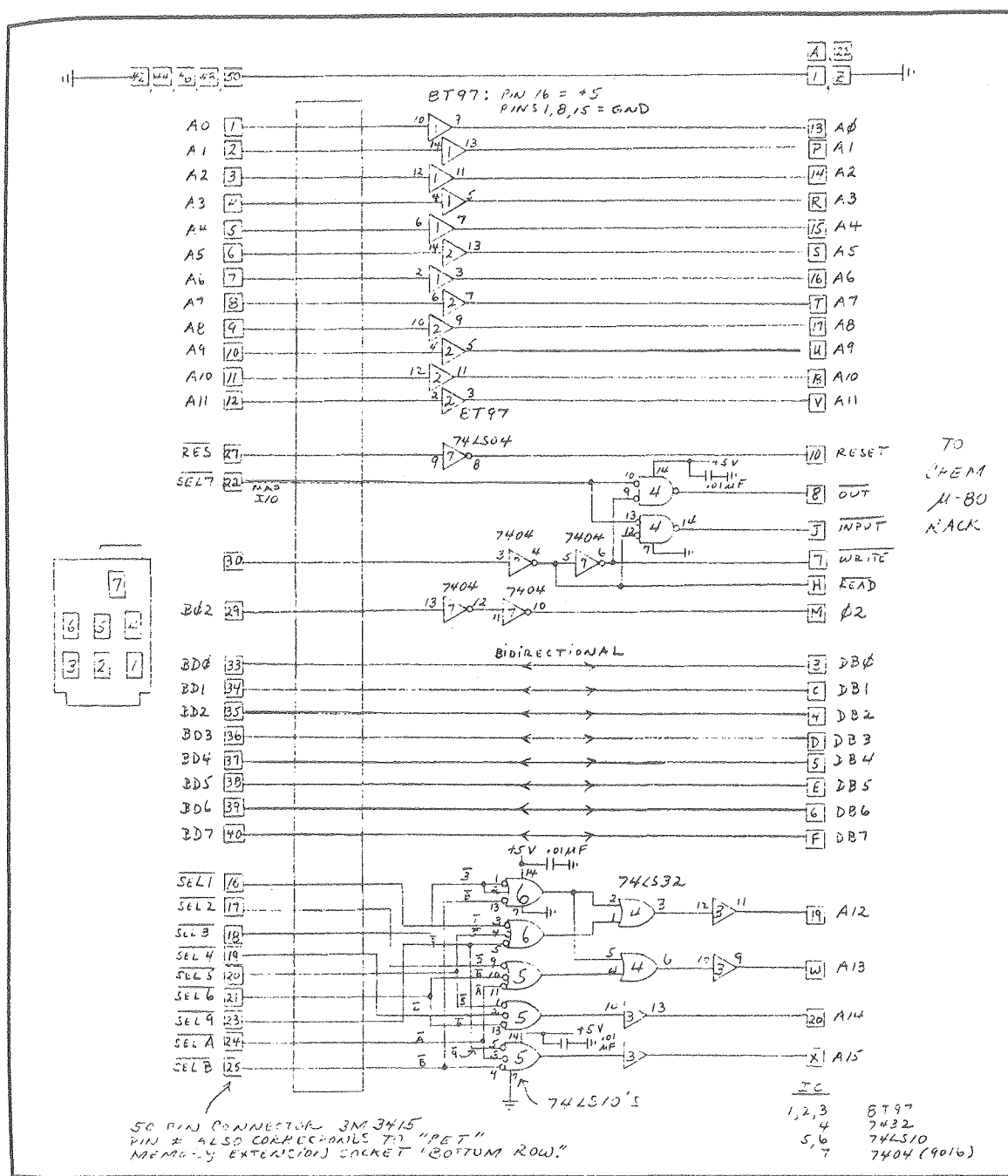


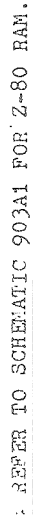
Figure D-3. Pulse interface clock board (#3).

200







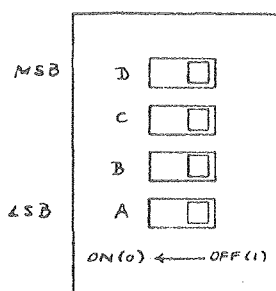


ADDRESS SELECT
WITH SWITCHES:

ON = 0

OFF = 1

DECODE TO 16 DIFFERENT 4K BLOCKS.



D	C	B	A	BANK
0	0	0	0	PAGES 00→0F
0	0	0	1	PAGES 10→1F
0	0	1	0	PAGES 20→2F
0	0	1	1	PAGES 30→3F
0	1	0	0	PAGES 40→4F
0	1	0	1	PAGES 50→5F
0	1	1	0	PAGES 60→6F
0	1	1	1	PAGES 70→7F
1	0	0	0	PAGES 80→8F
1	0	0	1	PAGES 90→9F
1	0	1	0	PAGES A0→AF
1	0	1	1	PAGES B0→BF
1	1	0	0	PAGES C0→CF
1	1	0	1	PAGES D0→DF
1	1	1	0	PAGES E0→EF
1	1	1	1	PAGES F0→FF*

WITH JUMPERS:

0 = WITH JUMPER

1 = WITHOUT JUMPER

* NOTE: PAGE FF IS RESERVED
FOR MEMORY MAP I/O.

REFER TO SCHEMATIC 903A1 FOR Z-80 RAM.



CHEM u80 BUS CALL-OUTS

Bottom or
Foil Side

1	GND
2	-12V
3	DB0
4	DB2
5	DB4
6	DB6
7	<u>Write</u>
8	<u>Out</u>
9	<u>In</u> ta
10	Reset
11	Ready
12	Sync
13	A0
14	A2
15	A4
16	A6
17	A8
18	A10
19	A12
20	A14
21	+12V
22	+5V

Top or Component
Side from right to left

A	+5V
B	<u>Hold</u>
C	DB1
D	DB3
E	DB5
F	DB7
H	<u>Read</u>
J	<u>Input</u>
K	<u>In</u> te
L	Hlda
M	<u>Q2</u>
N	<u>Eoot</u>
P	A1
R	A3
S	A5
T	A7
U	A9
V	A11
W	A13
X	A15
Y	<u>In</u> t
Z	Ground

APPENDIX F:

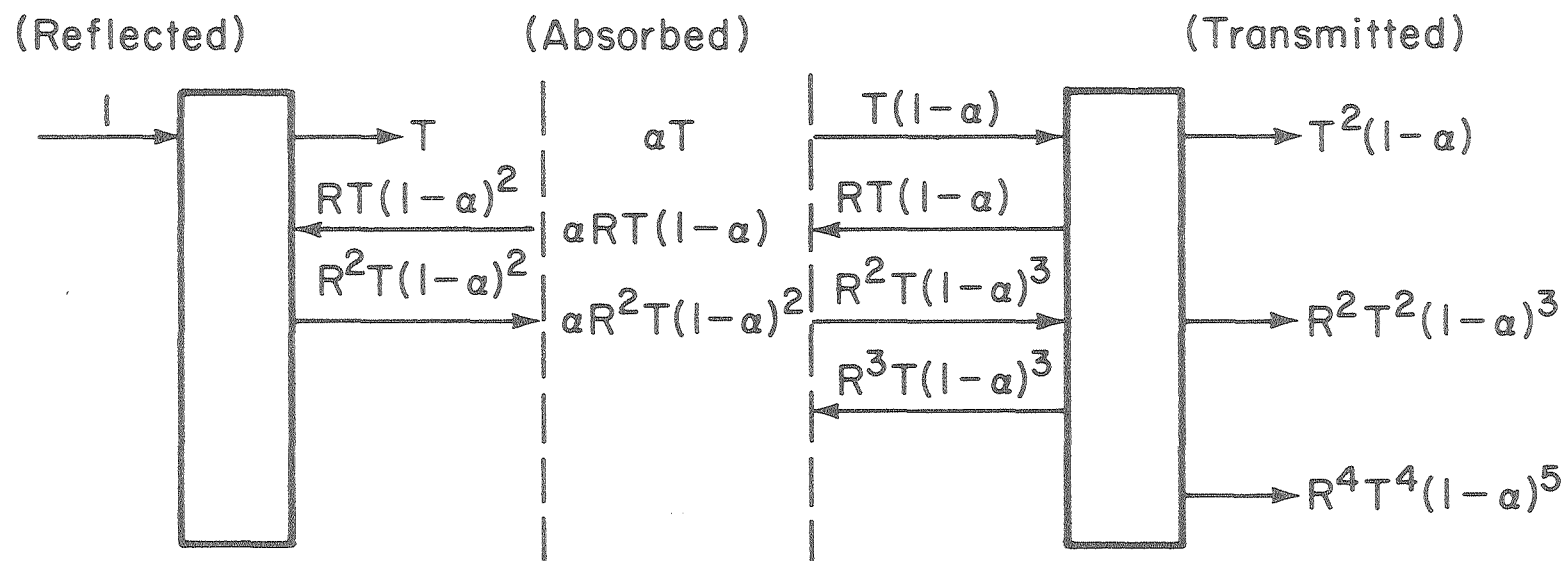
CALCULATION OF ABSORBED INTENSITY IN PHOTOMETRIC EXPERIMENTS^{56,57}

The following derivation closely follows Hunt and Hills⁵⁷ calculation of absorbed intensity in photometric experiments, but modified to obtain the total intensity (I_0^i) present directly behind the front entrance window. Figure 47 represents the radiation terms which are reflected, absorbed and transmitted by a cell with plane parallel windows, containing a substance absorbing (in a single pass) a fraction α of the light incident upon it.

Summing two infinite series, the following expression result:

$$\frac{I_t}{I_0} = \sum T^2 [(1-\alpha) + R^2(1-\alpha)^3 + R^4(1-\alpha)^5 + \dots] = \frac{T^2(1-\alpha)}{1-(1-\alpha^2)R^2}$$

$$\frac{I_0^i}{I_0} = \sum T (1 + R(1-\alpha) + R^2(1-\alpha)^2 + R^3(1-\alpha)^3 + \dots) = \frac{T}{1-R(1-\alpha)}$$



XBL 7910-12206

Figure 47. Reflected, absorbed and transmitted radiation terms, from two plane-parallel windows.

and

$$\frac{I_O^i}{I_t} = \frac{\left(\frac{T}{1-R(1-\alpha)} \right)}{\left(\frac{T^2(1-\alpha)}{1-(1-\alpha)^2 R^2} \right)}$$

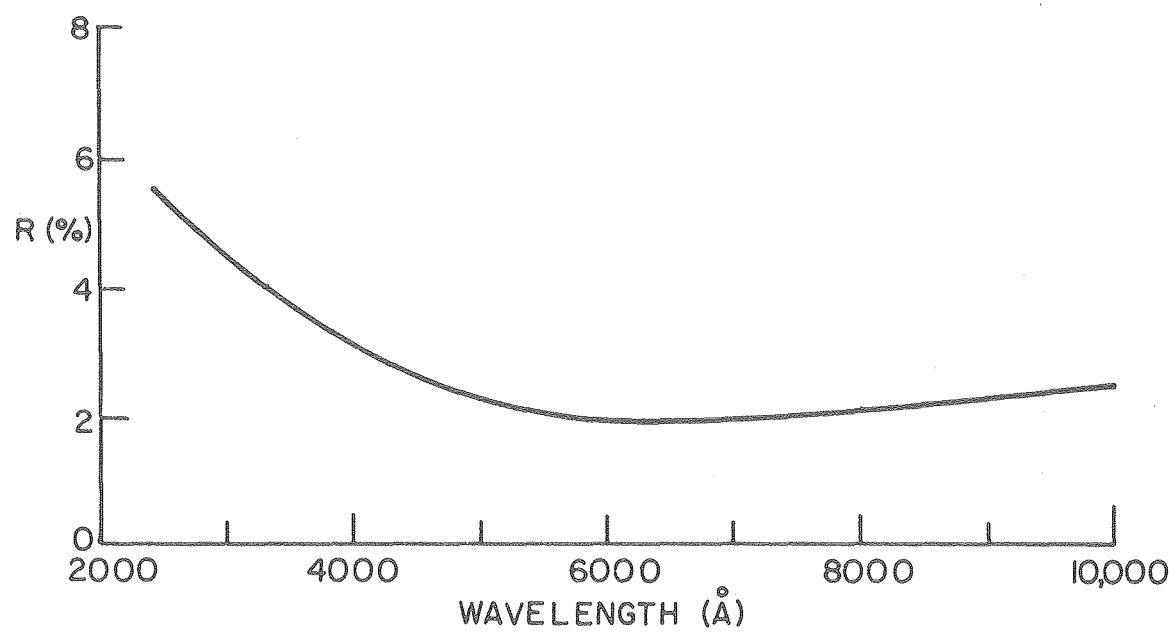
for the empty cell, $\alpha=0$ and

$$\frac{I_t}{I_0} = \frac{T^2}{1-R^2}$$

which is solved assuming noabsorption (or scattering) by the windows
(A=0)

$$T + R + A = 1$$

APPENDIX G



X B L 799-7104

Figure G-1. Gen-Tec joulemeter surface coefficients of reflection versus wavelength.

Appendix H

Values of NO₂ concentration and ($k_{\text{OBS}} - k_{0, \text{NO}_3}$) for the reaction O + NO₂; 144 points fit with $R^2 = 0.991$ by a line with slope $1.033 \pm .0084 \times 10^{-11} \text{ cm}^3 \cdot \text{molecule}^{-1} \cdot \text{sec}^{-1}$ and intercept $102.7 \pm .84 \text{ sec}^{-1}$.

(Captions for columns of figures)

$$k_{\text{OBS}} - k_{0, \text{NO}_3}$$

Values of NO_2 concentration and $(k_{\text{OBS}} - k_{\text{O},\text{NO}_3})$ for the reaction $\text{O} + \text{NO}_2$.

$[\text{NO}_2] \times 10^{-13}$	$k_{\text{OBS}} - k_{\text{O},\text{NO}_3}$	$[\text{NO}_2] \times 10^{-13}$	$k_{\text{OBS}} - k_{\text{O},\text{NO}_3}$
0.3630E+01	0.3980E+03	0.1870E+01	0.3100E+03
0.3550E+01	0.3180E+03	0.4320E+01	0.4860E+03
0.3550E+01	0.3560E+03	0.4650E+01	0.5940E+03
0.3500E+01	0.3960E+03	0.4760E+01	0.6020E+03
0.3530E+01	0.3890E+03	0.2360E+01	0.3910E+03
0.3550E+01	0.5050E+03	0.2060E+01	0.3460E+03
0.3510E+01	0.4390E+03	0.2010E+01	0.3300E+03
0.3420E+01	0.3820E+03	0.2010E+01	0.4200E+03
0.3360E+01	0.3640E+03	0.2300E+01	0.3390E+03
0.3700E+01	0.5580E+03	0.2500E+01	0.3790E+03
0.1200E+02	0.1631E+04	0.2680E+01	0.4130E+03
0.1090E+02	0.1594E+04	0.3000E+01	0.4430E+03
0.1250E+02	0.1515E+04	0.3360E+01	0.4680E+03
0.1320E+02	0.1695E+04	0.3760E+01	0.4620E+03
0.1440E+02	0.1327E+04	0.2810E+01	0.3240E+03
0.1510E+02	0.1629E+04	0.2320E+01	0.3560E+03
0.3700E+01	0.4620E+03	0.2330E+01	0.3110E+03
0.1270E+02	0.1565E+04	0.2370E+01	0.3270E+03
0.1220E+02	0.1484E+04	0.2350E+01	0.3490E+03
0.1230E+02	0.1527E+04	0.2330E+01	0.3450E+03
0.1290E+02	0.1325E+04	0.2310E+01	0.2950E+03
0.1390E+02	0.1352E+04	0.2290E+01	0.2960E+03
0.1500E+02	0.1364E+04	0.2230E+01	0.3330E+03
0.1580E+02	0.1517E+04	0.2200E+01	0.3210E+03
0.1500E+02	0.1606E+04	0.3700E+01	0.5140E+03
0.2200E+01	0.3300E+03	0.3700E+01	0.5140E+03
0.2380E+01	0.3270E+03	0.1530E+01	0.2740E+03
0.2390E+03	0.2772E+05	0.1670E+01	0.2680E+03
0.2230E+01	0.3300E+03	0.2050E+01	0.2740E+03
0.2130E+01	0.3190E+03	0.2290E+01	0.2650E+03
0.2020E+01	0.3090E+03	0.2090E+01	0.2640E+03
0.1960E+01	0.3390E+03	0.2160E+01	0.2870E+03
0.1960E+01	0.3350E+03	0.2020E+01	0.2950E+03
0.1970E+01	0.3010E+03	0.2040E+01	0.3310E+03
0.1970E+01	0.3110E+03	0.1290E+01	0.2030E+03
0.1970E+01	0.3250E+03	0.1380E+01	0.2450E+03
0.1910E+01	0.3130E+03	0.1460E+01	0.2070E+03
0.1870E+01	0.3740E+03	0.1300E+01	0.1990E+03
0.1860E+01	0.3860E+03	0.1170E+01	0.2090E+03
0.1870E+01	0.4070E+03	0.9900E+00	0.1850E+03
0.1890E+01	0.2910E+03	0.1010E+01	0.1900E+03
0.1900E+01	0.2970E+03	0.1020E+01	0.2000E+03

(continued. . .)

$[\text{NO}_2] \cdot 10^{-13}$	$k_{\text{OBS}} - k_{\text{O}, \text{NO}_3}$	$[\text{NO}_2] \cdot 10^{-13}$	$k_{\text{OBS}} - k_{\text{O}, \text{NO}_3}$
0.1050E+01	0.1940E+03	0.1030E+01	0.2320E+03
0.1050E+01	0.1860E+03	0.1020E+01	0.2090E+03
0.1040E+01	0.1930E+03	0.1000E+01	0.2020E+03
0.1020E+01	0.2030E+03	0.9520E+00	0.2010E+03
0.9960E+00	0.2160E+03	0.9680E+00	0.2210E+03
0.9820E+00	0.2380E+03	0.9820E+00	0.2530E+03
0.9780E+00	0.1910E+03	0.1000E+01	0.2250E+03
0.9780E+00	0.1890E+03	0.1010E+01	0.2310E+03
0.9780E+00	0.1890E+03	0.1030E+01	0.2030E+03
0.9780E+00	0.1870E+03	0.9070E+01	0.1025E+04
0.9780E+00	0.2120E+03	0.8370E+01	0.1004E+04
0.9680E+00	0.1920E+03	0.8490E+01	0.9390E+03
0.9680E+00	0.1990E+03	0.8400E+01	0.1110E+04
0.9560E+00	0.2340E+03	0.8380E+01	0.1094E+04
0.9410E+00	0.2270E+03	0.8810E+01	0.1097E+04
0.9410E+00	0.2270E+03	0.3770E+01	0.3500E+03
0.9440E+00	0.1840E+03	0.8440E+01	0.1187E+04
0.9730E+00	0.1840E+03	0.9120E+01	0.1022E+04
0.1020E+01	0.2020E+03	0.8830E+01	0.9600E+03
0.1050E+01	0.1970E+03	0.8560E+01	0.1058E+04
0.1160E+01	0.1820E+03	0.8440E+01	0.1187E+04
0.1100E+01	0.2080E+03	0.9120E+01	0.1028E+04
0.1070E+01	0.2070E+03	0.8830E+01	0.9600E+03
0.1100E+01	0.2140E+03	0.8560E+01	0.1058E+04
0.1120E+01	0.2070E+03	0.4680E+02	0.4791E+04
0.1070E+01	0.2330E+03	0.5030E+02	0.5372E+04
0.1040E+01	0.2080E+03	0.4920E+02	0.5307E+04
0.1030E+01	0.2030E+03	0.4540E+02	0.4789E+04
0.1130E+01	0.2060E+03	0.1780E+02	0.1780E+04
0.1070E+01	0.2040E+03	0.1780E+02	0.1774E+04

References

1. H. S. Johnston, *Science*, 173, 517 (1971).
2. G. Sprenger, *Z. Elektrochem.* 37, 674 (1931).
3. E. J. Jones and O. R. Wulf, *J. Chem. Phys.* 5, 873 (1937).
4. D. A. Ramsay, *Proc. Colloq. Spectroscopy Int.*, 10th, 583 (1962).
5. G. Schott and N. Davidson, *J. Am. Chem. Soc.*, 80, 1841 (1958).
6. R. A. Graham and H. S. Johnston, *Can. J. Chem.* 52, 1415 (1974).
7. H. S. Johnston, G. E. McGraw, T. T. Paukert, L. W. Richards, and J. van den Bogaerde, *Proceedings of the National Academy of Science* 57(5) 1146 (1967).
8. H. S. Johnston, E. D. Morris, Jr., and J. van den Bogaerde, *J. Am. Chem. Soc.* 91, 7712 (1969).
9. R. A. Graham and H. S. Johnston, *J. Phys. Chem.* 82, 254 (1978).
10. R. A. Graham, Lawrence Berkeley Laboratory Report #4147 (1975).
11. F. Magnotta, *Electro-optical Systems Design* 10, 24 (1978).
12. G. W. Chantry, A. Horsfield, J. R. Norton, and D. H. Whiffen, *Mol. Phys.* 5, 589 (1962).
13. L. Dogliotti and E. Hayon, *J. Phys. Chem.* 71, 3802 (1967).
14. J. F. Olsen and L. Burnelle, *J. Am. Chem. Soc.* 92(12) 3659 (1970).
15. H. H. Holmes and F. Daniels, *J. Am. Chem. Soc.* 56, 630 (1934).
16. R. Murphy, Doctoral Thesis, University of California at Los Angeles, (University Microfilms, Ann Arbor, 1969).
17. P. S. Connell, Doctoral Thesis, University of California at Berkeley, Lawrence Berkeley Laboratory Report #9034 (1979).
18. D. Garvin and R. F. Hampson, Eds., "Chemical Kinetics Data Survey", NBSIR 74-430, (1974).

19. G. Z. Whitten, Rate Constant Evaluation Using a New Computer Modeling Scheme, presented at the ACS National Meeting (Spring 1974).
20. A. C. Hindmarsh, Lawrence Livermore Laboratory Report #UCID-30001, Rev. 1 (1972).
21. E. D. Morris, Jr., and H. Niki, J. Phys. Chem. 77, 613 (1974).
22. G. E. Streit, J. S. Wells, F. C. Fehsenfeld and Carleton J. Howard, J. Chem. Phys. 70, 3439 (1979).
23. C. L. Creel and John Ross, J. Chem. Phys. 64(9) 3560 (1976).
24. Keith Schofield, J. Quant. Spectrosc. Radiat. Transfer 17, 13 (1977).
25. M. A. A. Clyne and H. W. Cruse, JCS Faraday Trans. II 68, 1281 (1972).
26. W. L. Wiese, M. W. Smith and B. M. Glennon, Natl. Std. Ref. Data Ser. NBS Vol. 4 (1966).
27. K. R. German, R. N. Zare and D. R. Crosley, J. Chem. Phys. 54, 4039 (1971).
28. A. B. Callear and I. W. M. Smith, Trans. Faraday Soc. 59, 1720 (1963).
29. L. A. Melton and W. Klemperer, Planet. Space SCI 20, 157 (1972).
30. A. B. Callear and I. W. M. Smith, Trans. Faraday Soc. 59, 1735 (1963).
31. R. L. Taylor, Can. J. Chem. 52, 1436 (1974).
32. D. C. Jain and R. C. Sahni, Trans. Faraday Soc. 64, 3164 (1968).
33. R. J. Spindler, Jr., L. Issacson and T. Wentink, Jr., JQSRT 10, 621 (1970).
34. H. P. Broida and T. Carrington, J. Chem. Phys. 38, 136 (1963).

35. P. P. Bemand and M.A.A.Clyne, J. Chem. Soc. Far. Trans. II, 69, 1643 (1973).
36. James Podolske, private communication.
37. G. E. Busch and K. R. Wilson, J. Chem. Phys. 56(7) 3626 (1972).
38. G. E. Busch and K. R. Wilson, J. Chem. Phys. 56(7) 3655 (1972).
39. R. T. Watson, private communication.
40. J. A. Gelbwachs, M. Birnbaum, A. W. Tucker and C. L. Fincher, Opto-Electron. 4, 155 (1972).
41. A. W. Tucker, A. Petersen, and M. Birnbarm, Appl. Opt. 12, 2036 (1973).
42. A. W. Tucker, M. Birnbaum, and C. L. Fincher, Appl. Opt. 14, 1418 (1975).
43. C. L. Fincher, A. W. Tucker, M. Birnbaum, R. J. Paur, and W. A. McClenny, Appl. Opt. 16, 1359 (1977).
44. E. F. Hughes, J. Chem. Phys. 35, 1531 (1961).
45. A. J. Illies and G. A. Takacs, J. Photochem. 6, 35 (1976/77).
46. N. M. Ballash and D. A. Armstrong, Spect. Acta, 30A, 941 (1974).
47. C. F. Goodeve and S. Katz, Proc. Roy. Soc. A172, 432 (1939).
48. H. Martin and R. Gareis, Z. Elektrochemie 60, 959 (1956).
49. A. M. Bass, A. E. Ledford, Jr., and A. H. Laufer, J. Rev. NBS,-A 80A(2) 143 (1976).
50. T. C. Hall and F. E. Blacet, J. Chem. Phys. 20, 1745 (1952).
51. A. B. Harker, W. Ho and J. J. Ratio, Chem. Phys. Letters 50(3), 394 (1977).
52. F. H. Ver Hoek and F. Daniels, J. Am. Chem. Soc. 53, 1250 (1931).
53. Matheson Gas Data Book, Matheson Co.

54. L. J. Beckham, W. A. Fessler and M. A. Kise, Chem. Rev. 48, 319 (1951).
55. P. G. Ashmore and M. S. Spencer, Trans. Faraday Soc. 55, 1868 (1959).
56. J. G. Calvert and J. N. Pitts, Jr., Photochemistry (John Wiley, and Sons, Inc., New York, 1967), pp. 793-795.
57. R. E. Hunt and T. L. Hill, J. Chem. Phys. 15(2) 111 (1947).
58. M. J. Digman and D. J. Leroy, J. Chem. Phys. 26, 964 (1957).
59. J. A. Davies and P. P. Manning, J. Am. Chem. Soc., 79, 5148 (1957).
60. G. Z. Whitten and J. P. Meyer, CHEMK: A Computer Modeling Scheme for Chemical Kinetics (Systems Applications, Inc., 1979).
61. J. N. Pitts, Jr., J. H. Sharp and S. I. Chan, J. Chem. Phys. 40, 3655 (1964).
62. H. Gaedtke, H. Hippler and J. Troe, Chem. Phys. Letters 16, 177 (1972).
63. H. Gaedtke and J. Troe, Buns. Ber. Phys. Chemie 79, 184 (1975).
64. G. B. Kistiakowsky, J. Am. Chem. Soc. 52, 102 (1930).
65. N. Basco and R. G. W. Norrish, Nature 189, 455 (1961).
66. N. Basco and R. G. W. Norrish, Proc. Roy. Soc. A268, 291 (1962).
67. G. L. Natanson, ACTA Physiocochem. USSR. 11, 521 (1939).
68. R. P. Wayne, Nature 203, 517 (1964).
69. C. R. Bailey and A. B. D. Cassie, Proc. Roy. Soc. (London) A145, 336 (1934).
70. P. G. Ashmore and J. Chanmugam, Trans. Faraday Soc. 49, 265 (1953).

71. G. H. Myers, D. M. Silver and F. Kaufman, J. Chem. Phys. 44, 718 (1966).
72. F. Daniels, R. A. Alberty, J. W. Williams, C. D. Cornwell, P. Bender, J. E. Harriman, Experimental Physical Chemistry (McGraw-Hill Book Company, N.Y., 1970), pp. 385-387.
73. M. Bodenstein and I. Ramsteiter, Z. Physik. Chem. 100, 68, 106 (1928).
74. G. E. Busch and K. R. Wilson, J. Chem. Phys. 56, 3626 (1972).
75. A. B. Callear and I. W. M. Smith, Trans. Faraday Soc. 59, 1720 (1963).
76. J. C. Stephenson, J. Chem. Phys. 59, 1523 (1973).
77. J. C. Stephenson, J. Chem. Phys. 60, 4289 (1974).
78. J. R. Ackerhalt and J. H. Eberly, Phys. Rev. A 14, 1705 (1976).
79. D. P. Hodgkinson and J. S. Briggs, Chem. Phys. Lett. 64, 511 (1979).
80. S. Leasure and R. E. Wyatt, Chem. Phys. Lett. 61, 625 (1979).
81. W. M. Jackson, J. B. Halpern and C. S. Lin, Chem. Phys. Lett. 55, 254 (1978).
82. H. S. Johnston, Gas Phase Reaction Rate Theory, (Ronald Press Co., N.Y., 1966), p. 329-332.
83. V. N. Donnelly, D. G. Keil and F. Kaufman, J. Chem. Phys. 71, 659 (1979).
84. H. S. Johnston, private communication.
85. R. F. Hampson, Jr., and D. Garvin, Reaction Rate and Photochemical Data for Atmospheric Chemistry--1977, (NBS, U.S. Department of Commerce, May, 1978).

86. Chemical Kinetic and Photochemical Data for Use in Stratospheric Modeling, Evaluation #2, (NASA-Jet Propulsion Laboratory, Pasadena, California, April 15, 1979).
87. L. C. Lee and T. G. Slanger, J. Chem. Phys. 69, 4053 (1978).
88. R. E. Smalley, B. L. Ramakrishna, D. H. Levy and L. W. Harton, J. Chem. Phys. 61, 4383 (1974).
89. R. J. Gelinas, R. P. Dickinson and K. E. Grant, Solar Flux and Photodissociation Calculations for LLL Physics Programs, University of California, Lawrence Livermore Laboratory, Livermore, CA., 94550 (1973).
90. G. Herzberg, Electronic Spectra of Polyatomic Molecules, (Van Nostrand, New York, 1966), Chapter III.
91. A. D. Walsh, J. Chem. Soc., 2301 (1953).
92. J. W. Gerstmayr, P. Harteck and R. R. Reeves, J. Phys. Chem. 76, 474 (1972).
93. S. Braslavsky and J. Heiklen, J. Photochem. 1, 203 (1973).
94. G. H. Myers, D. M. Silver and F. Kaufman, J. Chem. Phys. 44, 718 (1966).
95. T. G. Slanger, B. J. Wood and G. Black, Int. J. Chem. Kin. 5, 615 (1973).
96. D. D. Davis, J. T. Herron, and R. E. Huie, J. Chem. Phys. 58, 530 (1973).
97. P. P. Bemand, M. A. A. Clyne and R. T. Watson, J. Chem. Soc. Far. Trans. II. 70, 564 (1974).
98. M. Bixon and J. Jortner, J. Chem. Phys. 50, 3284 (1969).
99. A. E. Douglas, J. Chem. Phys. 45, 1007 (1966).
100. H. Okabe, Photochemistry of Small Molecules, (Wiley Interscience, N.Y., 1978) Chapter III.

